X-ray Crystallography of G Protein-coupled Receptors

Exploring Interactions with Drug Molecules

Dissertation

zur

Erlangung des Doktorgrades (Dr. rer. nat.)

der

Mathematisch-Naturwissenschaftlichen Fakultät

der

Rheinischen Friedrich-Wilhelms-Universität Bonn

vorgelegt von

Tobias Claff

aus Bad Honnef

Bonn 2022

Angefertigt mit Genehmigung der Mathematisch-Naturwissenschaftlichen Fakultät
der Rheinischen Friedrich-Wilhelms-Universität Bonn.

Gutachterin: Prof. Dr. Christa E. Müller
Gutachter: Prof. Dr. Michael Gütschow

Tag der Promotion: 13.12.2022
Erscheinungsjahr: 2023

Die vorliegende Arbeit wurde von Februar 2018 bis Juni 2022 am Pharmazeutischen Institut der Rheinischen Friedrich-Wilhelms-Universität Bonn unter der Leitung von Prof. Dr. Christa E. Müller angefertigt.

Für meine Eltern

Table of Contents

List of Abbreviations

A_1AR	Adenosine A_1 receptor
A_{2A}AR	Adenosine A_{2A} receptor
A_{2B}AR	Adenosine A_{2B} receptor
A_3AR	Adenosine A_3 receptor
ATP	Adenosine triphosphate
BODIPY	Boron-dipyrromethene
bRIL	Apocytochrome b_{562}RIL
BSA	Bovine serum albumin
CD	Cluster of differentiation
CHO	Chinese hamster ovary
CHS	Cholesteryl hemisuccinate
CNS	Central nervous system
COMT	Catechol-*O*-methyl-transferase
CPM	*N*-[4-(7-Diethylamino-4-methyl-3-coumarinyl)phenyl]maleimide
cryo-EM	Cryogenic electron microscopy
CTLA-4	Cytotoxic T-lymphocyte-associated protein 4
DAG	Diacylglycerol
DDM	Dodecyl-β-D-maltopyranoside
DESY	German Electron Synchrotron
DMSO	Dimethyl sulfoxide
DOP	δ-Opioid receptor
DTT	Dithiothreitol
E. coli	*Escherichia coli*
ECL	Extracellular loop
ER	Endoplasmic reticulum
ERK	Extracellular-signal regulated kinase
FAD	Flavin adenine dinucleotide
FDA	Food and Drug Administration
GABA	γ-Aminobutyric acid
GDP	Guanosine-5′-diphosphate
GP64	Glycoprotein 64
GPCR	G protein-coupled receptor
GRK	G protein-coupled receptor kinase

GTP	Guanosine-5′-triphosphate
HEPES	4-(2-Hydroxyethyl)piperazine-1-ethanesulfonic acid
HRP	Horseradish peroxidase
ICL	Intracellular loop
IP_3	1,4,5-Inositol trisphosphate
KOP	κ-Opioid receptor
LCP	Lipidic cubic phase
MAO-B	Monoamine oxidase B
Monoolein	1-oleoyl-*rac*-glycerol
MOP	μ-Opioid receptor
Nb	Nanobody
NECA	5′-*N*-Ethylcarboxamide adenosine
NMR	Nuclear magnetic resonance
NR2B	*N*-Methyl-D-aspartate receptor subtype 2B
PD	Parkinson's Disease
PD-1	Programmed cell death protein 1
PDB	Protein Data Bank
PD-L1	Programmed death-ligand 1
PEG	Polyethylene glycol
PEG400	PEG with the average molecular mass of 400
PIP_2	Phosphatidylinositol-4,5-bisphosphate
PLCβ	Phospholipase Cβ
PSB	Pharmaceutical Sciences Bonn
RGS	Regulators of G-protein signaling
SD	Standard deviation
SDS-PAGE	Sodium dodecyl sulfate polyacrylamide gel electrophoresis
SEM	Standard error of the mean
Sf9	*Sf9* cell line from *Spodoptera frugiperda*
StaR	Stabilized receptor
T_M	melting temperature
VHH	Variable domain of the heavy-chain antibody
wt	Wildtype

List of Figures

List of Tables

List of Appendices

1 Introduction

1.1 G Protein-coupled Receptors

G protein-coupled receptors (GPCRs) represent the largest class of membrane proteins in the human body.[1] They are integral membrane proteins comprised of seven transmembrane α-helices. Physiologically, GPCRs can be activated by a variety of diverse agonists ranging from photons[2] and small ions[3], over small molecule hormones[4] and neurotransmitters,[5] to peptides[6] and even proteins.[7] GPCRs are classified into six main families, based on evolutionary, structural, and functional homology: class A (rhodopsin-like receptors), class B (secretin receptors), class C (metabotropic glutamate receptors), class D (fungal mating pheromone receptors), class E (cyclic adenosine monophosphate [cAMP] receptors), and class F (frizzled/smoothened receptors).[8,9] Class A includes the olfactory receptors and represents the largest group of GPCRs. They are further divided into four sub-branches, designated α, β, γ, and δ branches.[10] The GRAFS system provides an alternative classification for vertebrate GPCRs into five families since class D and E are not found in vertebrates: **G**lutamate, **R**hodopsin, **A**dhesion, **F**rizzled/Taste2 and **S**ecretin (Figure 1).[11,12]

A significant amount of approximately 34 % of all drugs that are currently approved by the US Food and Drug Administration (FDA) target GPCRs.[1] Importantly, 224 non-olfactory GPCRs have not yet been investigated in clinical trials,[1] representing a huge potential for future drug development.

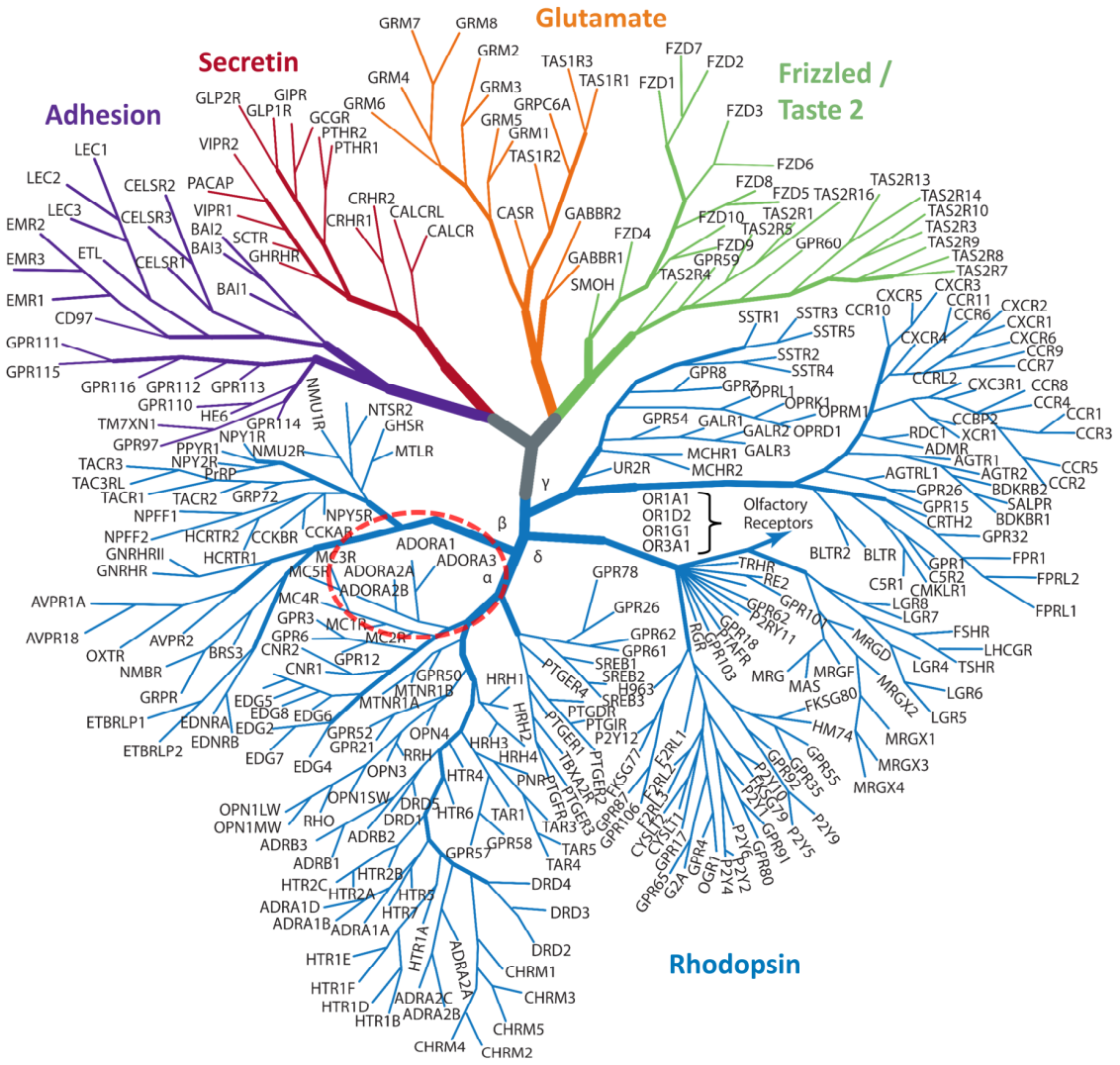

Figure 1. Phylogenetic tree of GPCRs.
GPCRs are named according to their Uniprot entry name.[13] The dotted red circle highlights the family of adenosine receptors. The figure was modified based on Stevens et al.[14]

1.1.1 Signaling Pathways

The canonical signaling pathway of GPCRs describes the transduction from signals to different effectors via the activation of heterotrimeric guanine nucleotide-binding proteins (G-proteins). G-protein heterotrimers consist of three widely-expressed subunits with various different combinations (20α-, 6β-, and 11γ-subunits).[15] One β-subunit typically forms a constitutive heterodimer with another γ-subunits that cannot be dissociated under physiological conditions.[16] In the inactive, heterotrimeric state of G-proteins, α-subunits are bound to guanosine-5′-diphosphate (GDP). G-protein activation leads to the exchange of GDP for guanosine-5′-triphosphate (GTP) which conformationally separates the α-subunit from the βγ-subunits (Figure 2).[17] Importantly, both the α- and γ-subunits are post-translationally modified to attach several different lipids (e.g., palmitoylation or myristylation for α-subunits and isoprenylation for γ-subunits) which restricts their localization to the plasma membrane, even in the active and separated state.[16] While the βγ dimer is capable of regulating different downstream effectors on its own through protein-protein interactions (e.g., with potassium or calcium channels),[18] the α-subunit generally determines the canonical signaling pathway of GPCRs. However, the G-protein signal is also terminated by the α-subunit through its own GTPase activity that hydrolyzes GTP to GDP (Figure 2). GTP hydrolysis can be accelerated by so-called regulators of G-protein signaling (RGS) proteins.[17] Moreover, GPCR activation leads to intracellular phosphorylation through G protein-coupled receptor kinases (GRKs).[19] The phosphorylated receptor attracts so-called arrestins that desensitize GPCR activation by internalization of the GPCR through clathrin-mediated endocytosis (Figure 2).[20]

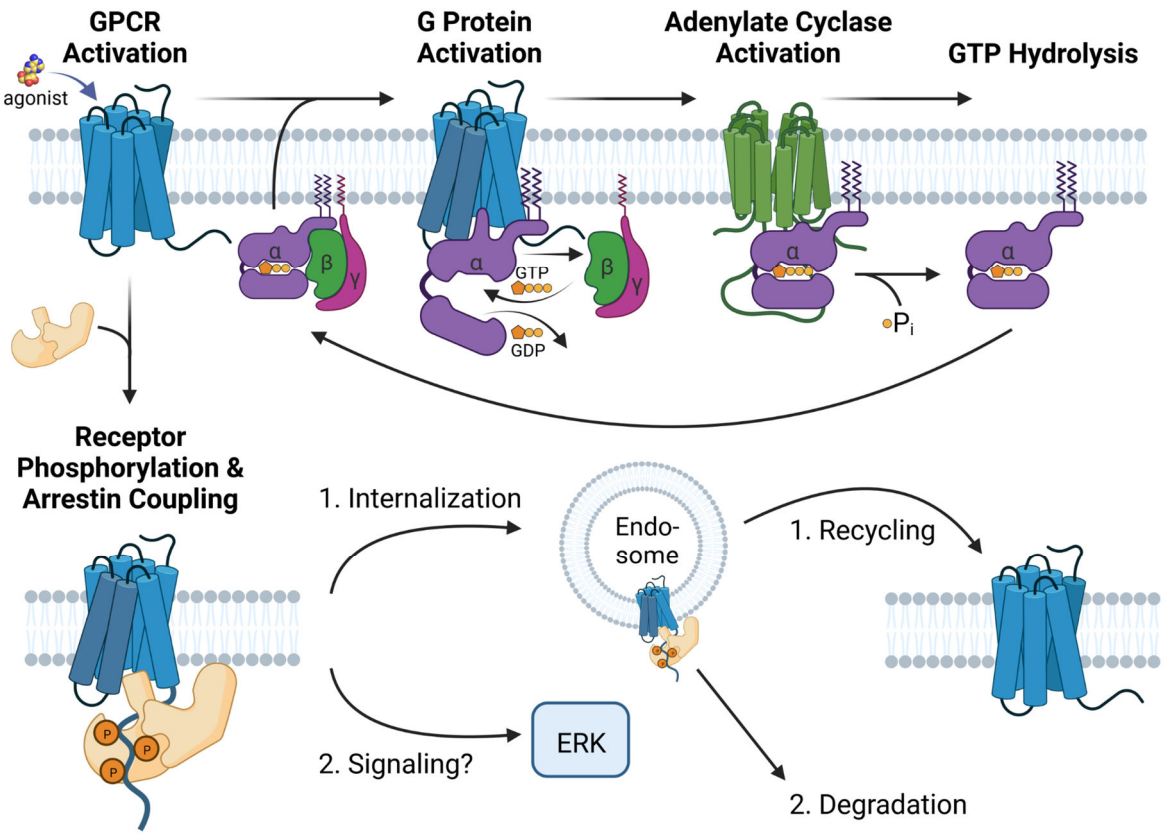

Figure 2. GPCR activation, desensitization and the G-protein cycle.
Top panel: The figure depicts the activation of a GPCRs, following movement of helices V and VII that triggers GDP-GTP exchange in the G-protein α-subunit. The α-subunit dissociates from the βγ-subunit and activates effector proteins (here shown for adenylate cyclase). GTP hydrolysis inactivates the Gα-protein following reassembly of the Gαβγ-trimer. Bottom panel: Receptor desensitization is initiated by receptor phosphorylation and arresting coupling.

G-proteins can be classified into four different subfamilies depending on their α-subunits: $G\alpha_s$, $G\alpha_{i/o}$, $G\alpha_{q/11}$ and $G\alpha_{12/13}$. $G\alpha_s$ and $G\alpha_{i/o}$ proteins regulate cAMP production either by stimulation ($G\alpha_s$) or inhibition ($G\alpha_{i/o}$) of adenylate cyclase. $G\alpha_{q/11}$ activation leads to the hydrolysis of the membrane phospholipid phosphatidylinositol-4,5-bisphosphate (PIP_2) to diacylglycerol (DAG) and 1,4,5-inositol trisphosphate (IP_3) through stimulation of phospholipase Cβ (PLCβ). While DAG remains in the cell membrane and is capable of activating membrane-bound protein kinase C, IP_3 can freely diffuse to the endoplasmic reticulum (ER) and is responsible for calcium release from the ER into the cytosol by activation of ligand-gated calcium channels. The activation of $G\alpha_{12/13}$ leads to the stimulation of small GTPases like Ras.[15]

Recent publications have suggested the existence of G-protein-independent signaling pathways mediated by arrestins.[21–24] Thus, extracellular-signal regulated kinases (ERK) may be activated solely by the interaction with activated arrestins or by GPCR-arresting complexes. ERK activation generally triggers a large downstream cascade that leads to various physiological effects including proliferation, differentiation and growth.[25] However, arrestin-dependent signaling remains one of the most controversial topics in GPCR signaling,[26] as studies showed that any downstream signaling was abolished without the presence of active G-proteins.[27,28]

1.1.2 Adenosine Receptors

Adenosine receptors belong to the α-branch of class A GPCRs[29] (Figure 1, red circle) activated by the purine nucleoside adenosine (Figure 3). Adenosine is omnipresent in the human body and can be formed by dephosphorylation of its respective nucleotides (e.g., starting from adenosine triphosphate [ATP]) by various ectonucleotidases.[30]

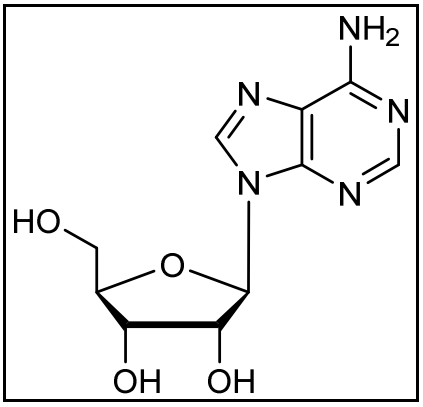

Figure 3. Chemical structure of adenosine.

Adenosine mainly acts by extracellular activation of four different subtypes of adenosine receptors, namely adenosine A_1, A_{2A}, A_{2B}, and A_3 receptor (A_1AR, A_{2A}AR, A_{2B}AR, and A_3AR, respectively). Importantly, adenosine displays different affinities for the receptor subtypes with very low affinity for the A_{2B}AR compared to the A_{2A}AR (~1000-fold difference).[31]

A_1 and A_3ARs mainly couple to G_i proteins and thereby inhibit intracellular cAMP synthesis, while A_{2A} and A_{2B}ARs are G_s-coupled thereby enhancing cAMP production. Adenosine receptors play important roles in the body, e.g. in the regulation of the central nervous system, the cardiovascular system, and immune functions.[32,33] This implies their involvement in several pathophysiological conditions and diseases, underlining the importance of the discovery of selective ligands.

1.2 Therapeutic Relevance of the Adenosine A_{2A} Receptor

In the brain, the A_{2A}AR is almost exclusively expressed at high levels in the caudate putamen (striatum) whereas, in the periphery, high A_{2A}AR expression is found in cells of the cardiovascular system and in immune cells.[34] A_{2A}AR activation results in vasodilatation and suppression of the immune system. While A_{2A}AR agonists have been developed as short-acting diagnostics for coronary artery imaging (Regadenoson, Figure 4),[35] A_{2A}AR antagonists can improve symptoms of neurodegenerative diseases (e.g. Istradefylline for Parkinson's Disease [PD], Figure 4)[36] and are clinically investigated as novel checkpoint inhibitors for the treatment of cancers.[37]

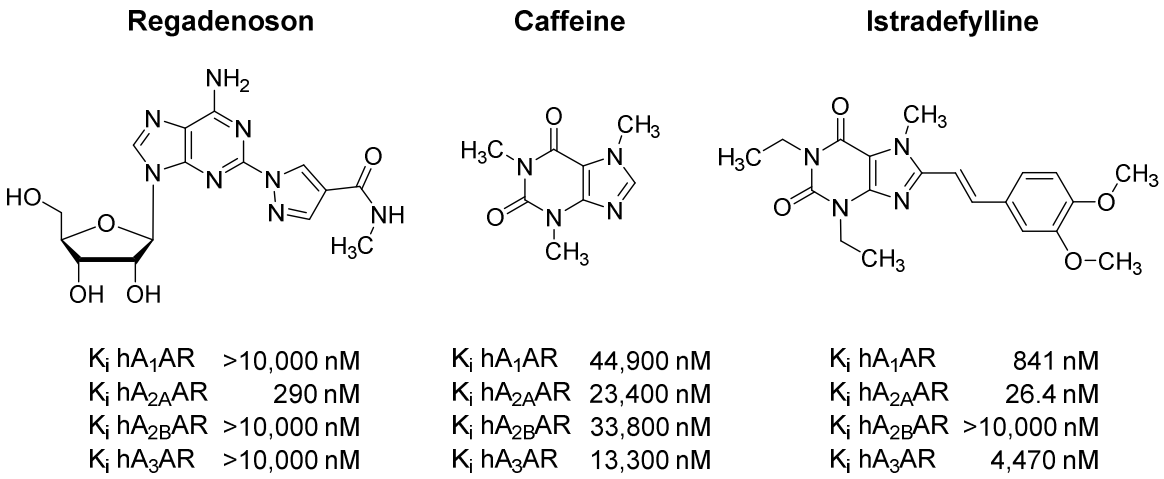

Figure 4. Chemical structures of approved A_{2A}AR ligands.
A_{2A}AR agonist Regadenoson (left), (non-selective) adenosine receptor antagonist Caffeine (center), and A_{2A}AR antagonist Istradefylline (right).[32,38]

1.2.1 Neurodegenerative Diseases

Neurodegenerative diseases represent a variety of disorders that can be characterized by a loss of functional neurons in the central nervous system (CNS).[39] Although a genetic predisposition is likely, the comprehensive origin of neurodegenerative diseases is often not fully understood. However, the risk of suffering from a neurodegenerative disease increases dramatically with age and may frequently result in dementia.[40] With growing life expectancies,

neurodegenerative diseases represent an ever-increasing challenge for health care and require the development of new therapies and diagnostics.[41] The A_{2A}AR has evolved as a suitable target for the treatment of neurodegenerative diseases like PD and Alzheimer's disease.[42]

1.2.1.1 Parkinson's Disease

PD is the second most prevalent neurodegenerative disease worldwide and the most common movement disorder.[43] The main hallmarks of PD are a loss of dopaminergic neurons in the substantia nigra and decreased dopamine signaling leading to major symptoms namely tremor, rigidity and bradykinesia.[44] Current treatment options are principally based on increasing the synaptic dopamine concentration using its precursor Levodopa in combination with the inhibition of metabolic enzymes.[45]

The degradation of dopamine mainly takes place via two physiological enzymes: catechol-*O*-methyl-transferase (COMT) and monoamine oxidase B (MAO-B).[45] MAO-B is one of two MAO isoforms (A and B) which are covalently linked to flavin adenine dinucleotide (FAD) and located in the outer mitochondrial membrane. While both enzymes catalyze the oxidative deamination of biogenic amines including dopamine, MAO-B is predominantly expressed in the basal ganglia, and upregulated in PD patients.[46] Elevated MAO-B activity under levodopa treatment is associated with an increased production of reactive oxygen species which may contribute to neuronal cell death and PD progression.[47,48] Moreover, recent studies have suggested that MAO-B increases the biosynthesis of γ-aminobutyric acid (GABA), thereby inhibiting dopaminergic neurons.[49,50] A MAO-B blockade can be achieved by irreversible or competitive inhibition using approved drugs that improve motor symptoms of PD patients.[48] However, PD patients may experience "off time" (i.e. periods when Parkinson's symptoms intensify) potentially resulting from the main therapy focus on enhancing dopaminergic signaling. Therefore, additional disease-modifying drugs that either delay PD progression or help reduce Levodopa consumption are urgently needed.

The blockade of the A_{2A}AR by antagonists is established as an attractive non-dopaminergic treatment for PD. Moreover, the A_{2A}AR is an emerging target for

neurodegenerative diseases in general[42] with the additional potential benefit of neuroprotection.[51] In the brain, the A_{2A}AR is almost exclusively expressed in the caudate-putamen (striatum) at high levels.[44] Moreover, the A_{2A}AR was observed to be upregulated in early-stage PD patients[52] which correlated with the severity of the disease.[53] The concomitantly increased A_{2A}AR activation directly inhibits dopamine D_2 receptor signaling by A_{2A}/D_2 receptor heterooligomer formation[54] and the G_s-coupled A_{2A}AR additionally counteracts G_i-coupled D_2 receptor signaling on the second messenger level, i.e. cyclic adenosine monophosphate production.[55]
The first and to date only FDA-approved and selective A_{2A}AR antagonist is the xanthine derivative Istradefylline (Nourianz™) which is structurally related to Caffeine (Figure 4). In combination with Levodopa, Istradefylline improved motor symptoms and reduced “off time” in PD patients without the risk of worsening dyskinesia that can occur at peak dopamine levels.[36]

1.2.2 Cancer Immunotherapy

Conventional methods for the treatment of cancer include surgical tumor removal, chemotherapy, radiation therapy and, in most cases, a combination of these methods. While non-targeted methods can be effective in the eradication of malignant cells, a major downside is the lack of selectivity because it also targets healthy cells and therefore results in with severe adverse effects.[56] Emerging strategies in the therapy of cancer are based on the activation of the endogenous immune system thereby removing malignant cells. Cancer cells have evolved to evade the human’s immune response and can modulate so-called immune checkpoints, i.e., regulators of the immune system.[57] Therapeutically relevant immune checkpoints include the cytotoxic T-lymphocyte-associated protein 4 (CTLA-4), the programmed cell death protein 1 (PD-1) and its ligand PD-L1. These immune checkpoints can be blocked by checkpoint inhibitors in order to reduce immune evasion of tumor cells. All currently approved checkpoint inhibitors are monoclonal antibodies.[58]

The A_{2A}AR represents a novel target for cancer immunotherapy that can be efficiently blocked by small molecules.[59] The A_{2A}AR is highly expressed on lymphocytes, and its activation leads to immunosuppression (Figure 5).[60,61] While extracellular adenosine concentrations are typically low, an adenosine upsurge can

occur in the microenvironment of tumors, mainly due to induced cell death by increased cellular stress and chemotherapy.[59,62] Dying cells release intracellular ATP that is rapidly metabolized to adenosine through ectonucleotidases (e.g., CD39 and CD73; CD refers to cluster of differentiation). Thereby, high concentrations of adenosine are formed in close proximity to tumor cells, capable of inhibiting the human immune response and protecting cancer cells from an attack by the immune system.[63] A blockade of the A_{2A}AR would counteract the upsurge of adenosine in the tumor microenvironment and support classical methods for the treatment of cancer.[59] Currently, multiple clinical trials of A_{2A}AR antagonists for the treatment of malignancies are ongoing.[64]

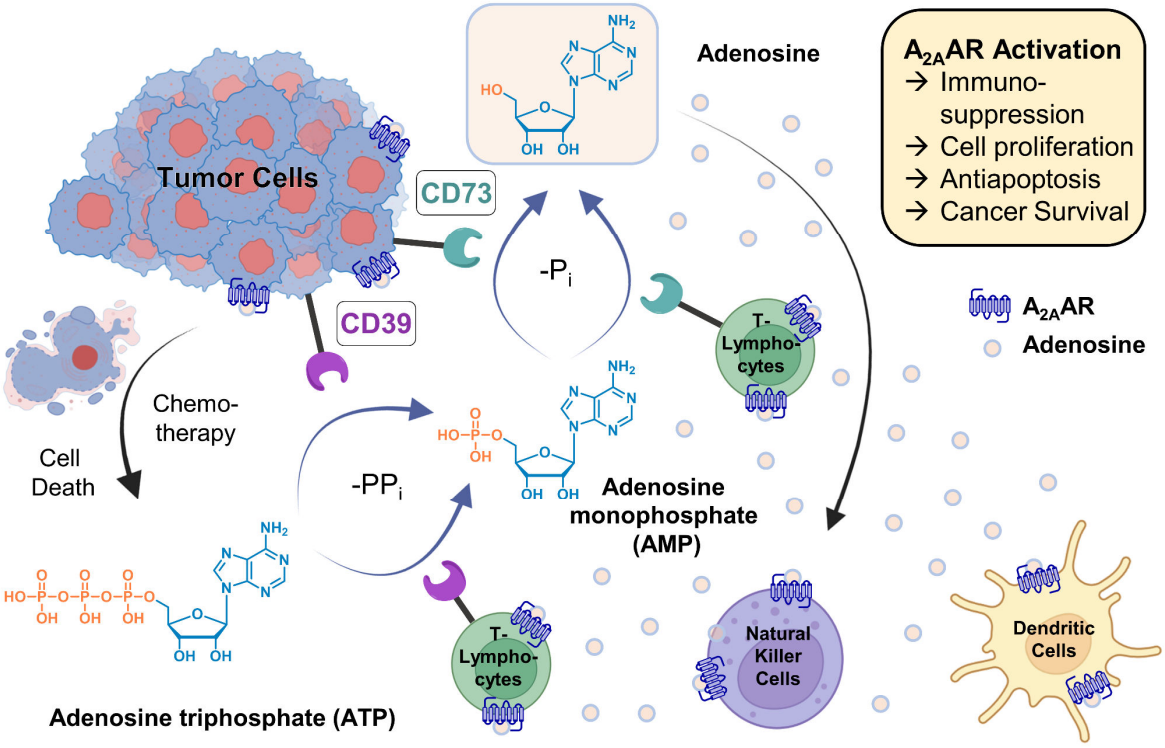

Figure 5. The A_{2A}AR as immune checkpoint.
The figure depicts the formation of adenosine as a metabolic product of ATP that is extensively released as a result of cell death. Adenosine activates A_{2A}ARs on the surface of cancer and immune cells promoting cancer survival.

1.2.3 Polypharmacology

In contrast to the development of highly selective drugs that act at one specific target, polypharmacology represents an emerging strategy to design drugs that mediate their effects through multiple pharmaceutical targets.[65] Although off-target effects of drugs are frequently associated with toxicity and adverse effects, it has been shown that various so-called 'dirty drugs' that act on many different targets, for example the antipsychotic drugs Clozapine or Aripiprazole, are difficult to replace with a target-selective substance.[66] Especially CNS disorders, neurodegenerative diseases and malignancies are complex and multifactorial, and therefore difficult to effectively target by a single selective drug.[67] The approval of one drug that engages multiple targets in contrast to multiple drugs that each acts on one target bears the potential advantage of less adverse effects due to a reduced metabolic burden to the human body, i.e., less potential to interact with metabolic enzymes or other drugs. Nevertheless, polypharmacology still remains a challenge for drug discovery as different targets often represent different protein families, each with a fundamentally different binding pocket architecture.[67,68]

Polypharmacology is highly relevant to this study, as we discovered dual-targeting A_{2A}AR antagonists and MAO-B inhibitors that have great potential for the treatment of PD,[69] and elucidated their binding mode on both targets using X-ray crystallography. Moreover, we solved the A_{2A}AR crystal structure of two dual A_{2A} and A_{2B}AR antagonists that are clinically relevant for cancer immunotherapy.[70] One of these antagonists (Etrumadenant) is currently under investigation in clinical trials for the treatment of different cancers. [71]

1.3 Structural Biology of G Protein-coupled Receptors

The very first GPCR crystal structure was determined of the light-sensitive photoreceptor Rhodopsin in 2000.[72] Nevertheless, it took seven more years for the elucidation of the first non-Rhodopsin crystal structures: the β_2-adrenergic receptor in 2007,[73] followed by the β_1-adrenergic receptor in 2008.[74] This represented a tremendous discovery that was awarded with the Nobel Prize in Chemistry in 2012.[75]

Crystallographic procedures for membrane proteins require protein extraction from and purification out of their membranes, which generally results in destabilization and aggregation of the receptor.[76] Importantly, there is a correlation between high receptor expression, increased receptor thermostability and successful GPCR crystal formation.[77] This has led to various strategies for the optimization of GPCR crystallization, and specifically for restraining GPCRs in a desired state to enhance its stability and increase the crystallization success: 1) Stabilizing point mutations: Suitable mutations have to be identified experimentally by investigating many different mutations for receptor expression and stability. However, the design of thermostabilizing mutations can also be facilitated by directed-evolution,[78–80] or by computational methods through knowledge from existing crystal structures.[81] 2) Complex formation with antibodies or nanobodies: These can be used to stabilize the inactive[73,82,83] or active state of GPCRs.[84,85] 3) Stabilizing ligands: Different GPCR conformations are stabilized by high-affinity ligands, ideally with long residence time, to reduce flexibility.[86] 4) Detergents: Solubilization with detergents is required to isolate GPCRs from their native membranes. Several different detergents are now commercially available and are continuously improved for their efficiency, mildness and micelle size.[87,88] 5) Fusion proteins: Although detergents are used to isolate GPCRs from their membranes, crystal growth generally requires hydrophilic crystal contacts[89] that are mostly lacking in hydrophobic GPCRs. Hence, hydrophilic fusion proteins can be inserted into the intracellular or extracellular surface of the receptor.[90] The N-terminus or the intracellular loop (ICL) 3 represent the most frequent fusion sites, but also the ICL2 has been replaced with a fusion partner in the crystallization of class B GPCRs.[91] 6) Lipidic cubic phase (LCP): Crystallization techniques have greatly advanced, and crystallization in LCP has facilitated the structure elucidation of GPCRs.[92]

Cryo-EM methods have recently become increasingly feasible for the structure elucidation of GPCRs,[93,94] especially in the active state and in complex with intracellular effectors like G-proteins,[95] arrestins,[96] or RGS.[97] While X-ray crystallography thus far still remains the gold standard for obtaining inactive state GPCR structures, mainly due to size limitations in cryo-EM without GPCR signaling complexes,[98] upcoming publications (preprints) present different strategies for overcoming the hurdles of cryo-EM for solving inactive state GPCR structures.[99–101]

1.3.1 The Structure of the Adenosine A_{2A} Receptor

The human A_{2A}AR consists of 412 amino acids and comprises a long and presumably flexible C-terminal domain whereas the N-terminus starts with transmembrane helix I (Figure 7). Eight cysteine residues of the A_{2A}AR form four extracellular disulfide bridges that connect the extracellular loop (ECL) 2 with helix III and the ECL3 with helix VI (Figure 7). While the A_{2B}AR represents the closest homolog of the A_{2A}AR,[102,103] the ECL2 shows the largest variety and has been identified as important determinant for subtype selectivity and for the adenosine affinity difference observed between A_{2A} and A_{2B}ARs.[31,104]

The A_{2A}AR was the fourth GPCR that had been successfully crystallized yielding a crystal structure in 2008,[105] but by now reached over 60 Protein Data Bank (PDB) entries.[106] These include structures in complex with 20 different A_{2A}AR antagonists,[107] one partial agonist (in the inactive state),[108] (see Table 1 for an overview) and four different A_{2A}AR agonists (including adenosine,[109] 5′-*N*-ethylcarboxamide adenosine [NECA],[109] UK-432097[110] and CGS21680[111], please refer to Figure 9 for chemical structures). Moreover, two A_{2A}AR structures have been solved in complex with the full agonist NECA and either together with a mini-$G\alpha_s$ protein by X-ray crystallography[112] or with the full mini-$G\alpha_s\beta_1\gamma_2$ heterotrimer and the stabilizing nanobody (Nb) 35 by cryogenic electron microscopy (cryo-EM) (Table 2).[95]

A comparison of three A_{2A}AR structures in different activation states is shown in Figure 6. The binding pocket of A_{2A}AR antagonists and agonists share similarities but also distinct differences. For example, both antagonists and agonists show similar hydrogen bonding interactions to $N253^{6.55}$. In the active conformation,

W246$^{6.48}$ and S277$^{7.32}$ adopt different conformations.[113] The ribose moiety of adenosine and its derivatives forms direct hydrogen bonding to S277$^{7.32}$, an interaction that has never been observed for A_{2A}AR antagonists (Figure 6b and d). It is well understood that GPCR activation results in an outward movement of helix VI which is necessary in order to make room for the accommodation of the C-terminal helix of G-proteins.[114] However, the extent of helix VI movements significantly varies for different GPCRs, especially for the intermediate-active states.[115] Intermediate-active GPCR states are mostly observed for structures obtained without the presence of a signaling partner.[116] Although the outward movement of helix VI is significantly smaller in the intermediate-active state of the A_{2A}AR (Figure 6c), the binding pocket of A_{2A}AR intermediate-active state structures is nearly identical to the binding pocket of the fully-active, G-protein-bound structures (Figure 6b and d). In the presence of $G\alpha_s$, helix VI shows an outward movement of approximately 14 Å away from the receptor core in the A_{2A}AR.[112]

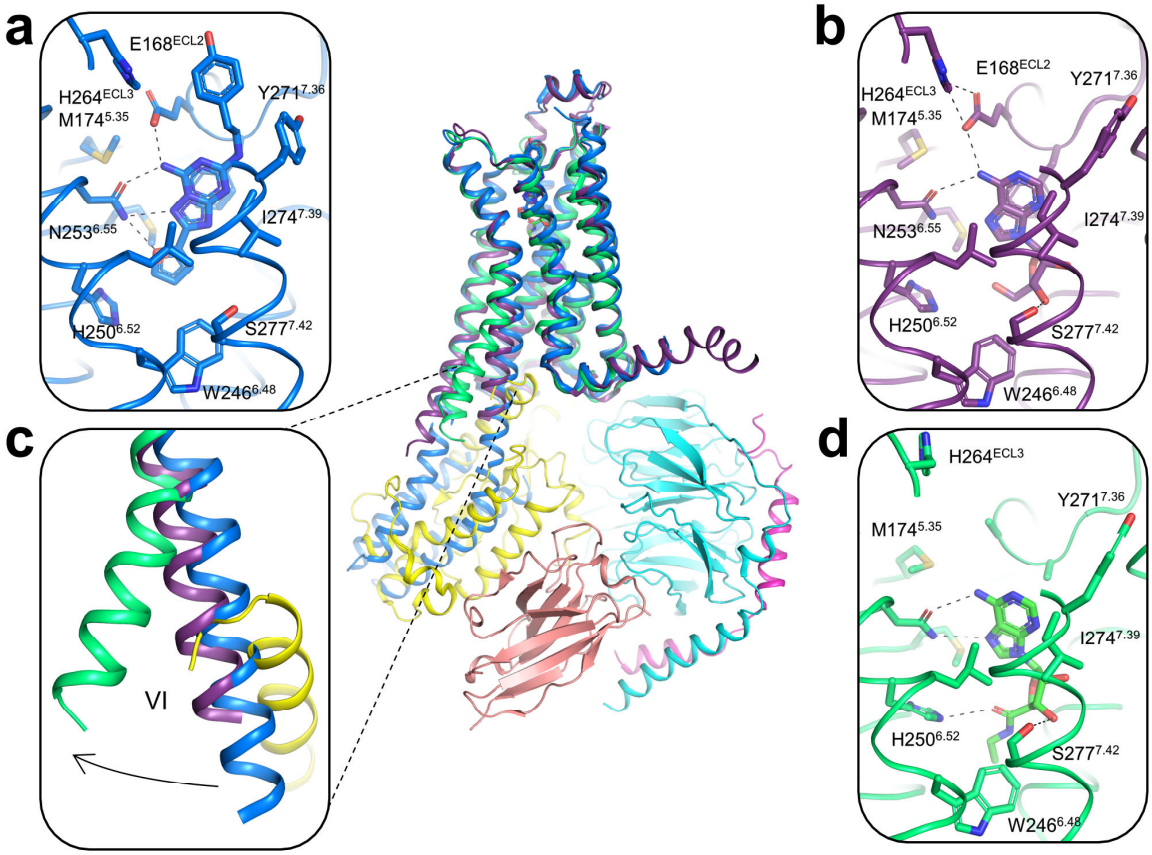

Figure 6. Structural comparison of the different A_{2A}AR conformational states. Overlay of three different A_{2A}AR structures (middle) and their binding pockets in the a) inactive state (in complex with antagonist ZM241385, PDB 4EIY, blue), b) the agonist-

bound intermediate state (in complex with adenosine, PDB 2YDO, purple) and d) the G-protein-bound fully active state (in complex with NECA, PDB 6GDG, green). The G-proteins are represented in yellow ($G\alpha_s$), cyan ($G\beta_1$) and pink ($G\gamma_2$). Nb35 is shown in red. c) Conformational changes of helix VI upon activation. The yellow helix represents the C-terminal helix of $G\alpha_s$.

To date, the co-crystal structures of 22 different A_{2A}AR antagonists have been published (please refer to Figure 8 for chemical structures), however, the majority (18) was exclusively co-crystallized using the so-called “stabilized receptor” (StaR) A_{2A}-StaR2 (Table 1), either with or without the intracellular fusion partner[90] apocytochrome b_{562}RIL (bRIL). This A_{2A}AR mutant comprises nine additional point mutations (Figure 7), two of which are directly located inside the orthosteric ligand binding pocket (T88$^{3.36}$A and S277$^{7.42}$A). These mutations were not only shown to abolish agonist binding[117] but may also negatively affect the affinity of certain antagonist scaffolds.[118] We recently established a putative new gold standard for the structure elucidation of the A_{2A}AR in its inactive state by developing the single A_{2A}AR mutant A_{2A}-PSB1-bRIL (with PSB referring to Pharmaceutical Sciences Bonn).[107] Importantly, although the mutational load is significantly reduced, this construct evolved with superior thermostability compared to the A_{2A}-StaR2 and the previously established A_{2A}AR crystallization construct that does not contain additional point mutations but also has the long and flexible A_{2A}AR C-terminus truncated (designated A_{2A}-ΔC-bRIL). The development of A_{2A}-PSB1-bRIL is discussed in detail in section 3.2.

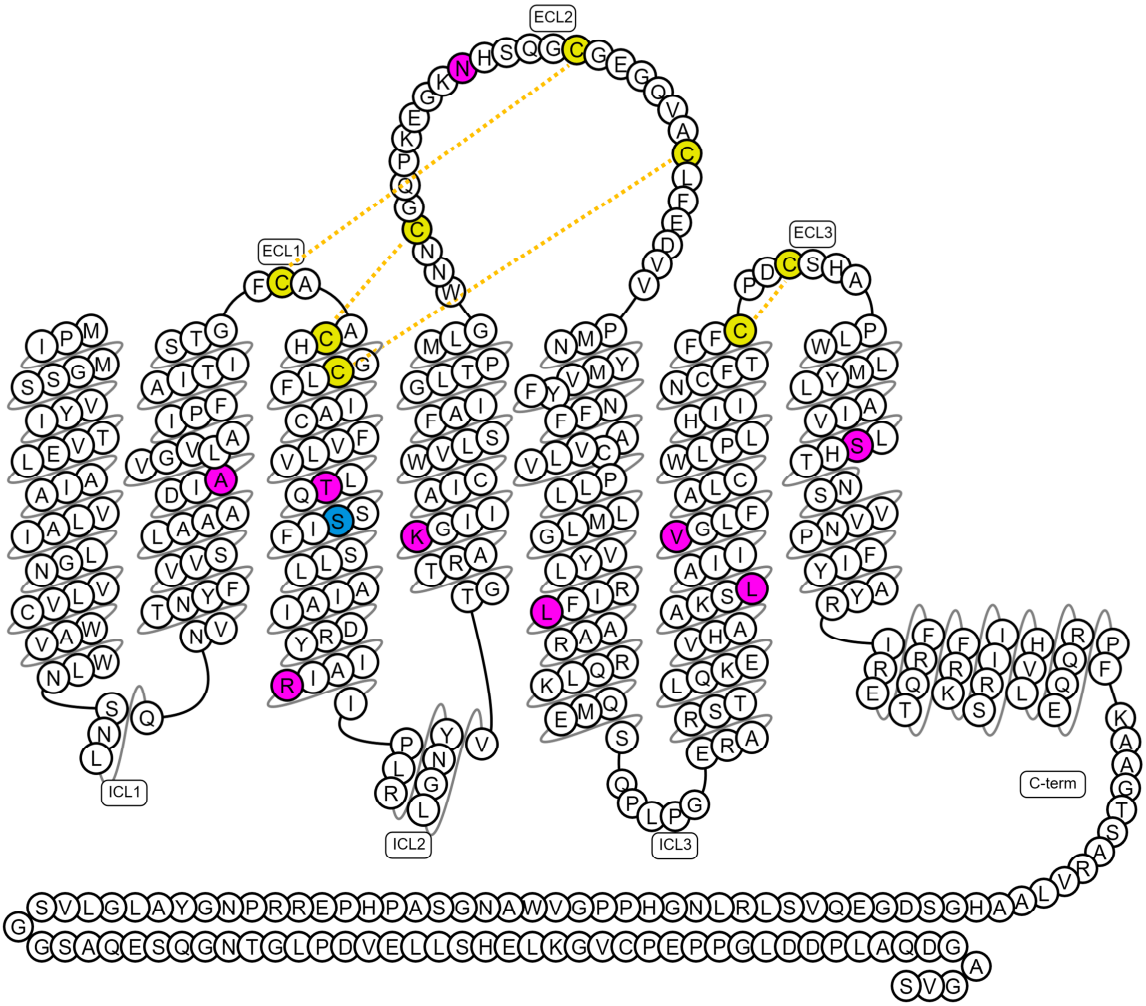

Figure 7. Snake-plot of the human A_{2A}AR.
The snake plot was generated using the GPCRdb database.[119] Cysteines that form disulfide bridges are highlighted in yellow and connected by yellow dotted lines. The $S91^{3.39}$K mutation in the thermostabilized construct A_{2A}-PSB1-bRIL is shown in blue. All point mutations in the A_{2A}-StaR2 are highlighted in pink.

Table 1. Complete list of all published inactive-state A_{2A}AR structures in the PDB as of June 2022.
The table was modified from Claff et al.[107] and complemented with new structures. All structures were obtained by X-ray diffraction with 7RM5 as an exception whose crystal structure was determined using microcrystal electron diffraction.

PDB Identifier	Ligand	A_{2A}AR construct	Resolution (Å)	Method	H264-E169 ionic lock	pH value during crystallization	Ref.
3EML	ZM241385	A_{2A}-ΔC-T4L	2.60	LCP	intact	5.5 – 6.5	[105]
4EIY 5JTB 6WQA 5K2A 5VRA 6LPJ 5K2B 6AQF 6LPK 5K2C 6MH8 6LPL 5K2D 6JZH 7RM5 5UVI 6PS7	ZM241385	A_{2A}-ΔC-bRIL (+ N154Q in 6AQF)	1.80 – 4.20	LCP	intact	4.8 – 5.0	[120–131]
3PWH	ZM241385	A_{2A}-StaR2	3.30	vapor diffusion	open	8.0 – 8.75	[117]
3VGA 3VG9	ZM241385	A_{2A}-ΔC + N154Q	2.70 – 3.10	LCP	intact/open	6.5	[82]
5IU4 5NM4 6S0L 5NLX 5OLG 6S0Q 5NM2	ZM241385	A_{2A}-StaR2-bRIL	1.72 – 2.14	LCP	intact	5.0 – 5.4	[132–134]
3REY	Xanthine amine congener (XAC)	A_{2A}-StaR2	3.31	vapor diffusion	open	8.0 – 8.75	[117]
3RFM	Caffeine	A_{2A}-StaR2	3.60	LCP	open	8.0 – 8.75	[117]
5MZP	Caffeine	A_{2A}-StaR2-bRIL	2.10	LCP	intact	5.0	[135]
3UZA	4g	A_{2A}-StaR2	3.27	vapor diffusion	open	8.0 – 8.75	[136]
3UZC	4e	A_{2A}-StaR2	3.34	vapor diffusion	open	8.0 – 8.75	[136]
5OLZ	4e	A_{2A}-StaR2-bRIL	1.90	LCP	intact	5.3 – 5.4	[134]
5OM1	4e	A_{2A}-StaR2-bRIL	2.10	LCP	intact	5.3 – 5.4	[134]
5OM4	4e	A_{2A}-StaR2-bRIL	2.00	LCP	intact	5.3 – 5.4	[134]

Table 1. (continued)

PDB Identifier	Ligand	A_{2A}AR construct	Resolution (Å)	Method	H264-E169 ionic lock	pH value during crystallization	Ref.
5IU7	12c	A_{2A}-StaR2-bRIL	1.90	LCP	intact	5.3 – 5.4	[132]
5IU8	12f	A_{2A}-StaR2-bRIL	2.00	LCP	intact	5.5	[132]
5IUA	12b	A_{2A}-StaR2-bRIL	2.20	LCP	intact	5.3 – 5.4	[132]
5IUB	12x	A_{2A}-StaR2-bRIL	2.10	LCP	intact	5.5	[132]
5MZJ	Theophylline	A_{2A}-StaR2-bRIL	2.00	LCP	intact	5.1	[135]
5N2R	PSB-36	A_{2A}-StaR2-bRIL	2.80	LCP	open	5.1	[135]
5OLH	Vipadenant	A_{2A}-StaR2-bRIL	2.60	LCP	intact	5.3 – 5.4	[134]
5OLO	Tozadenant	A_{2A}-StaR2-bRIL	3.10	LCP	open	5.3 – 5.4	[134]
5OLV	LUAA47070	A_{2A}-StaR2-bRIL	2.00	LCP	intact	5.3 – 5.4	[134]
5UIG	Cmpd-1	A_{2A}-ΔC-bRIL (Modified N- and C- terminus	3.50	vapor diffusion	intact	6.5	[137]
6GT3	Imaradenant	A_{2A}-StaR2-bRIL	2.00	LCP	intact	5.3 – 5.4	[138]
6ZDR	Chromone 4d	A_{2A}-StaR2-bRIL	1.92	LCP	intact	4.7 – 5.4	[139]
6ZDV	Chromone 5d	A_{2A}-StaR2-bRIL	2.13	LCP	intact	4.7 – 5.4	[139]
7ARO	LUF5833 (Partial agonist)	A_{2A}-StaR2-bRIL	3.12	LCP	open	5.3 – 5.4	[108]
7XP4	PSB-2113	A_{2A}-PSB1-bRIL	2.25	LCP	Intact	5.2	[107]
7PYR	PSB-2115	A_{2A}-PSB1-bRIL	2.60	LCP	intact	5.2	[107]

Table 2. Complete list of all published agonist-bound A_{2A}AR structures in the PDB as of June 2022.
6GDG was obtained by cryo-EM whereas all other structure were determined using X-ray diffraction.

PDB Identifier	Ligand	A_{2A}AR construct	Complex proteins	Resolution (Å)	Method	H264-E169 ionic lock	pH value during crystallization/ cryo-EM	Ref.
2YDO	Adenosine	A_{2A}-GL31[a)]	-	3.00	vapor diffusion	Intact	7.6	[109]
2YDV	NECA	A_{2A}-GL31[a)]	-	2.60	vapor diffusion	intact	6.4	[109]
3QAK	UK-432097	A_{2A}-ΔC-T4L	-	2.71	LCP	open	5.0 – 5.5	[110]
4UG2	CGS21680	A_{2A}-GL31[a)]	-	2.60	LCP	Intact	7.0	[111]
4UHR	CGS21680	A_{2A}-GL31[a)]	-	2.60	LCP	intact	4.8	[111]
5G53	NECA	A_{2A}-ΔC +N154^{ECL2}A	Mini-Gα_s	3.40	vapor diffusion	Intact	5.7	[113]
5WF5	UK-432097	A_{2A}-ΔC-T4L +S91$^{3.39}$A	-	2.60	LCP	open	5.0	[126]
5WF6	UK-432097	A_{2A}-ΔC-T4L +D52$^{2.50}$N	-	2.90	LCP	open	5.0	[126]
6GDG	NECA	N-Thioredoxin-A_{2A}-ΔC +N154^{ECL2}A	Mini-G$\alpha_s\beta_1\gamma_2$ + Nb35	4.11	Cryo-EM	unresolved	7.5	[95]
7EZC	UK-432097	A_{2A}-ΔC-bRIL +I92$^{3.40}$N, L95$^{3.43}$A, I238$^{6.40}$Y	-	3.80	LCP	open	8.2	[140]

[a)] The A_{2A}-GL31 construct contains five point mutations: L48$^{2.46}$A, A54$^{2.52}$L, T65$^{2.63}$A, Q89$^{3.37}$A, N154^{ECL2}A.

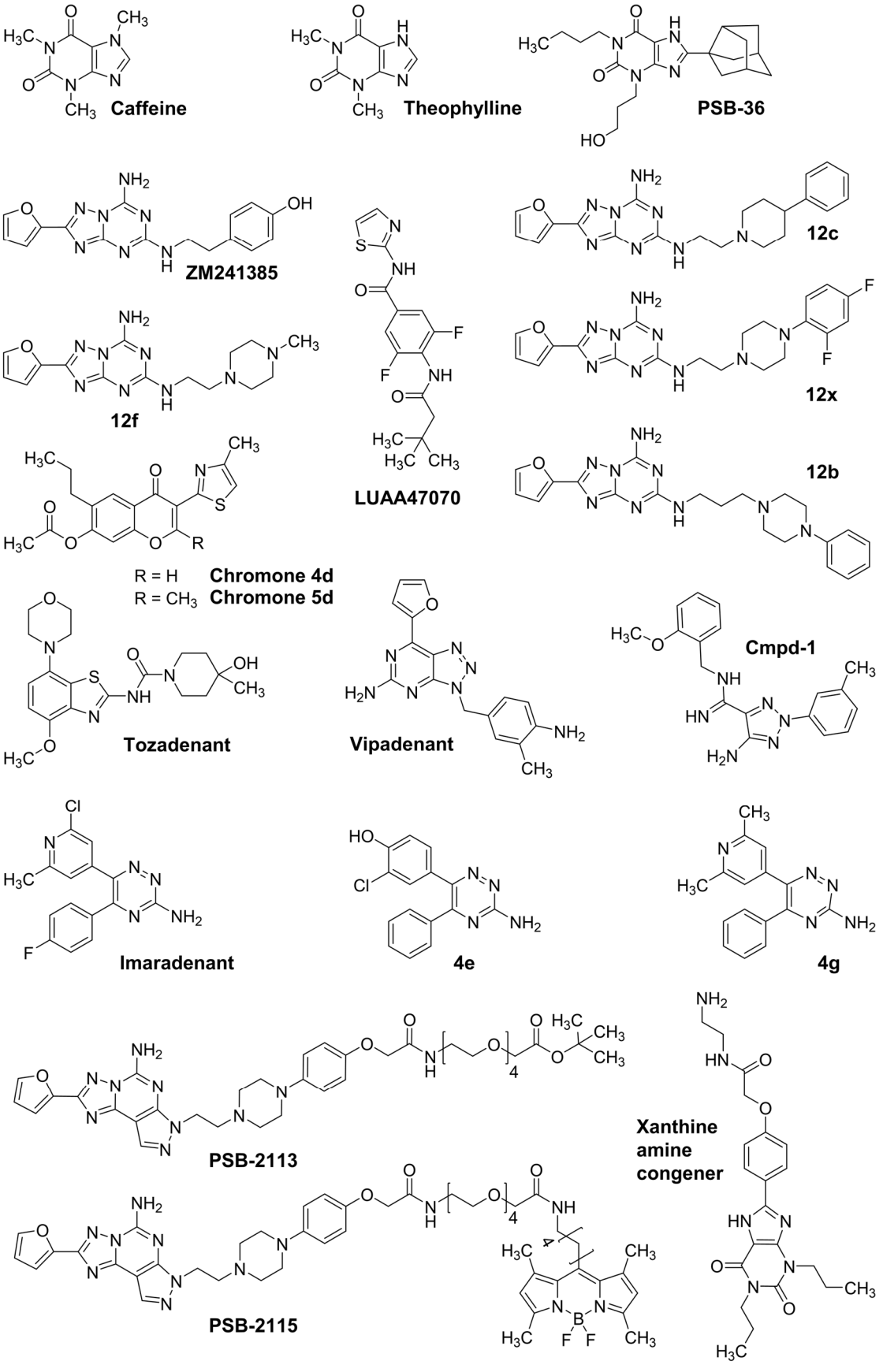

Figure 8. List of all co-crystallized A_{2A}AR antagonists as summarized in Table 1.

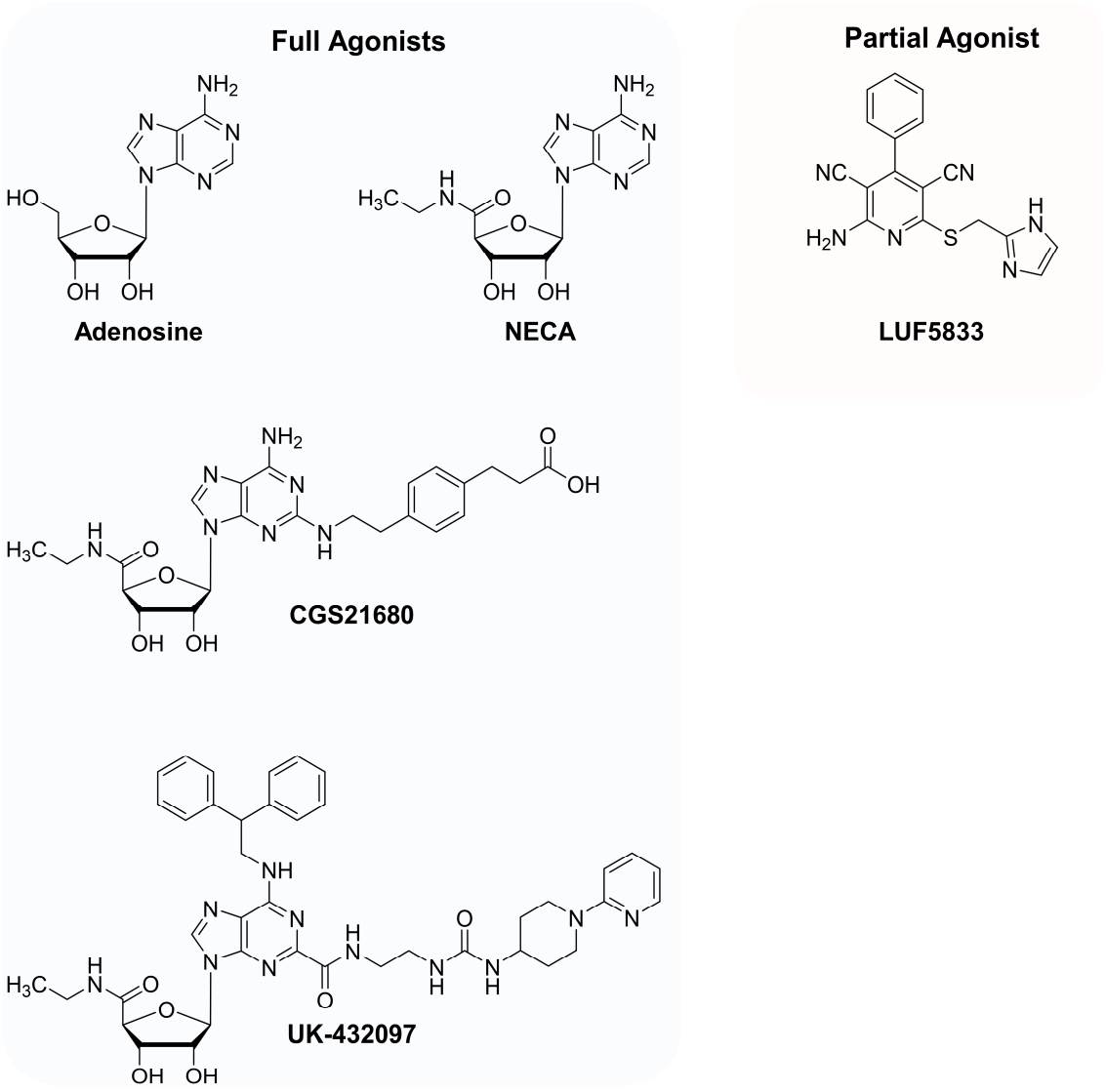

Figure 9. List of all co-crystallized A_{2A}AR agonists as summarized in Table 2.

1.3.2 Allosteric Sodium Binding Pocket

It is well understood that sodium ions can regulate several class A GPCRs and act as negative allosteric modulators.[137] Thereby, sodium ions can decrease agonist binding without greatly affecting the affinity of antagonists[120,137] or partial agonists.[138] Up to now, several crystal structures have been solved featuring a sodium ion bound within the seven transmembrane bundle in a pocket that is highly conserved in many class A GPCRs.[137] In fact, in these structures, the sodium binding pocket residue positions were almost identical (within 0.5 – 1.5 Å). Even the

positioning of structural water molecules within the sodium binding pocket were found to be conserved among functionally distant receptors such as the A_{2A}AR, the β_1-adrenergic receptor or the δ-opioid receptor, emphasizing the structural conservation of the sodium binding pocket within class A GPCRs.[3] Additionally, it has been shown that the sodium binding pocket is crucial for a functional receptor to initiate downstream signaling[126], and due to its location close to the ligand binding pocket, it is also available for ligand design.[3,80,139]

The A_{2A}AR was the first GPCR with structural evidence of a sodium binding pocket.[120] Residues of helices I, II, III, VI and VII are involved in the formation of that pocket, partly due to water-mediated interaction over a longer distance rather than direct effects on the sodium ion. Although A_1AR crystal structures have been solved,[135,140] the resolution of these structures was not sufficiently high to resolve a structural sodium ion. However, the superposition of A_{2A} and A_1AR structures shows that the residues which interact with the sodium ion in the adenosine receptors are virtually in the same conformation as the respective residues in the A_1AR (Figure 10), indicating that it may also contain an intact sodium binding pocket in the inactive state. These findings are consistent with pharmacological studies showing that the agonist affinity at the A_1AR decreases with high sodium concentrations.[141] Even in cases where high sodium concentrations do not interfere with the binding affinity of GPCR ligands, it cannot be ruled out that the respective GPCR has an allosteric sodium binding pocket. This was shown for the β_1-adrenergic receptor at which high sodium concentrations did not impact on agonist affinity, nevertheless, a sodium ion could be observed in the crystal structure reported in the same framework showing a highly conserved positioning and water network.[137,142]

The amino acid alignment of residues that are involved in the binding of an allosteric sodium ion in the A_{2A}AR shows that all amino acids are conserved among adenosine receptors and in various species including in human, rat and mouse species (Figure 10), suggesting that all adenosine receptors are allosterically regulated by sodium ions. Moreover, pharmacological evidence for a potential sodium regulation of adenosine receptors is available for all subtypes: A_1[141], A_{2A}[120,143], A_{2B}[138,144], and A_3[145,146].

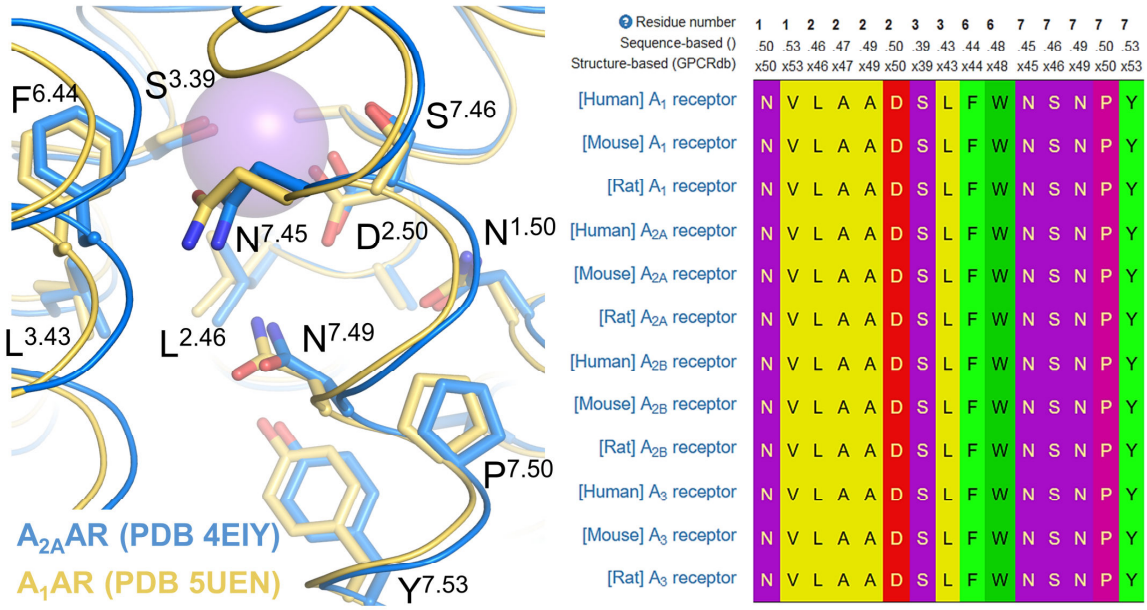

Figure 10. Potential sodium binding pocket in adenosine receptor subtypes.
Left: Superposition of the A_{2A}AR sodium binding pocket (orange, PDB 4EIY)[120] and the same residues in the A_1AR crystal structure (cyan, PDB 5UEN).[140] The sodium ion in PDB 4EIY is shown as a purple sphere. Right: Sequence alignment of residues that form the sodium binding pocket in the A_{2A}AR crystal structure are conserved among A_1, A_{2A}, A_{2B}, and A_3ARs of human, rat and mouse. Sequence alignment of sodium binding pocket residues was done with the GPCRdb online tool.[119]

1.4 Methods

1.4.1 *Spodoptera frugiperda Sf9* Insect Cell Expression

All A_{2A}AR constructs were expressed using a modified Bac-to-Bac baculoviral insect cell expression system (ThermoFisher, Cat. #10359016). The A_{2A}AR constructs are sub-cloned into a pFastBac1 expression vector that has the original polyhedrin promoter exchanged to the baculoviral glycoprotein 64 (GP64) promoter (GP64-pFastBac1).[147] The A_{2A}AR gene is transposed into the baculoviral genome using *Escherichia coli* (*E. coli*) strain DH_{10BAC} prior to the transfection of the *Sf9* cell line from *Spodoptera frugiperda* (*Sf9*) insect cells. Thereby, a recombinant baculoviral genome is achieved (so-called Bacmid) that can be purified and transfected directly into *Sf9* insect cells. This system has the advantage that no subsequent separation of the wildtype (wt) baculoviral genome from the recombinant genome has to be performed which is the case for other baculoviral expression systems.[148] The baculovirus is yielded from the cell supernatant four days after transfection (designated P0 viral stock). The P0 virus is then used to infect a larger amount of *Sf9* insect cells. The supernatant of 40 mL of infect insect cell culture yields a P1 viral stock with higher viral titers than the P0 viral stock. *Sf9* insect cell transfection and infections were performed as previously described.[107,149] A transfection and expression control is carried out using flow cytometry based assays as described in the next sections.

1.4.1.1 Transfection Control

A transfection control can be achieved by detecting the baculoviral protein GP64 that is expressed on the surface of infected insect cells. The detection of GP64 is performed using flow cytometry (Guava easyCyte HT, Merck) and a fluorescence-labeled antibody (GP64 coupled to Phycoerythrin, Expression Systems Cat. #97-201). Successfully transfected insect cells express GP64 in their surface and show yellow fluorescence whereas wt insect cells are non-fluorescent. The fluorescence shift can be detected and quantified (Figure 11). The GP64-assay is routinely

determined to measure the transfection efficiency of *Sf9* insect cell transfections prior to utilizing the result virus for subsequent infections.

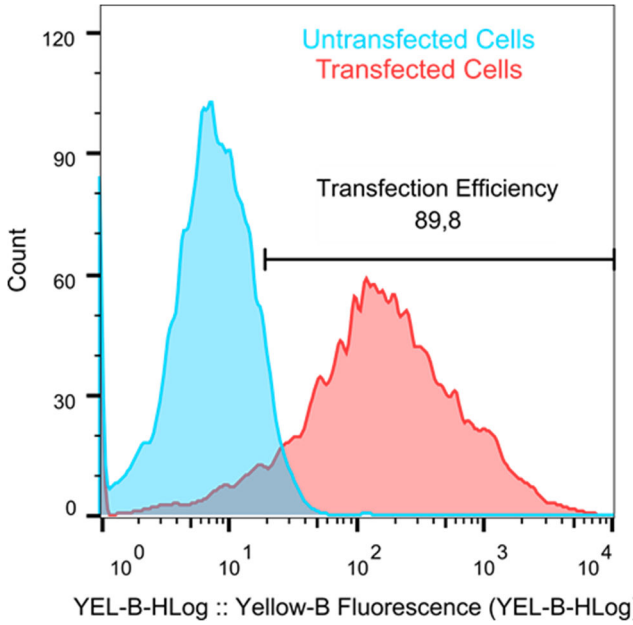

Figure 11. GP64-assay result to measure the transfection efficiency of *Sf9* insect cells.
In this particular control measurement, the transfection efficiency was determined to be 89.8%.

1.4.1.2 Expression Control

The abovementioned GP64-assay does not provide any information on the expression rate of the desired recombinant protein. Therefore, another flow cytometry-based assay is employed in order to detect an N-terminal FLAG epitope tag[150] that is attached to all A_{2A}AR constructs. While the original FLAG tag consisted of the amino acids DYKDDDDK,[150] our A_{2A}AR constructs contain the reduced sequence DYKDDDD that is still recognized by an anti-FLAG antibody conjugated to fluorescein isothiocyanate (FITC) (GenScript Cat. #A01632). The FLAG-assay is performed on a Guava easyCyte HT (Merck). Wt *Sf9* insect cells are non-fluorescent whereas cells that express the desired recombinant protein show green fluorescence due to the FITC fluorophore (Figure 12a). The surface expression is measured with intact cells whereas a representative total expression can be determined by the addition of Octoxinol 9 (Triton X-100) to permeabilize the

cell membrane (Figure 12b). 7-Aminoactinomycin is used to determine cell viability as it strongly binds to DNA and shows red fluorescence. Thus, Triton X-100 treated cells represent dead cells due to its cell permeability (Figure 12c and d).

The FLAG expression assay is routinely performed to control the successful expression of A_{2A}AR constructs prior to purification. In the example shown in Figure 12 for A_{2A}AR construct A_{2A}-PSB2-bRIL, more than 90 % of the *Sf9* insect cells are shown to be expressing the FLAG-tagged A_{2A}AR. Additionally, the total expression measurement did not increase the expression level, indicating that the receptor is completely expressed on the cell surface.

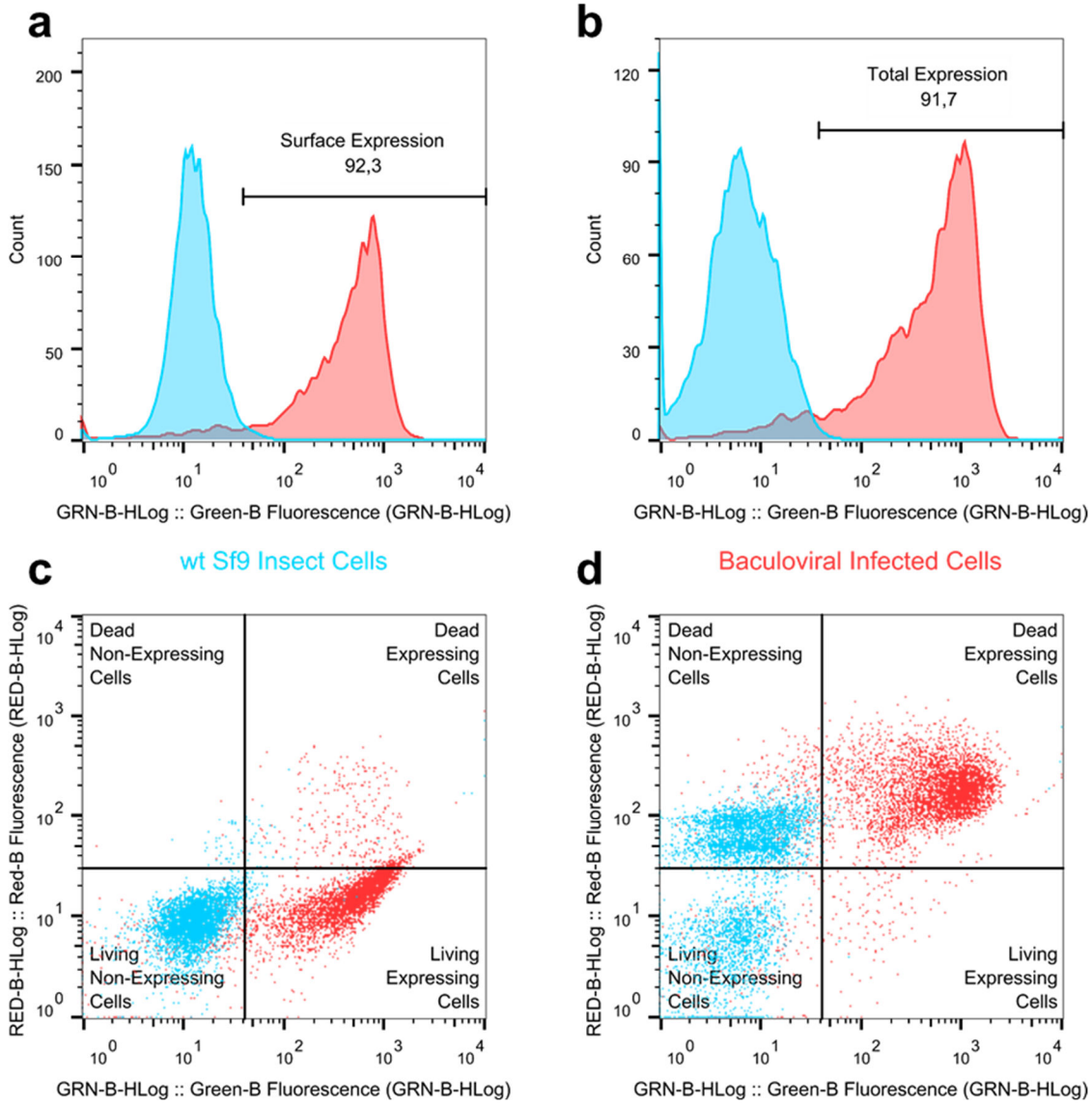

Figure 12. FLAG-assay to determine the surface and total expression of A_{2A}AR constructs.
a) Surface expression (92.3 %) and b) total expression (91.7 %) of A_{2A}-PSB2-bRIL (red) compared to untransfected wt *Sf9* insect cells (blue). c) Surface expression and d) total expression of the same cells but with living and dead cell differentiation.

1.4.2 GPCR Purification by Immobilized Metal Ion Affinity Chromatography

In their work in 1975, Porath et al. laid out the fundamental principles for immobilized metal ion affinity chromatography (IMAC) and demonstrated that certain human serum proteins exhibit affinity for heavy metal ions.[151] In the early days, proteins that naturally contain a high amount of aromatic amino acids on their surface (e.g. bovine pancreatic ribonuclease, human albumin, interferons or avidin) were purified using IMAC. Due to great methodology advances in molecular biology, recombinant proteins were successfully engineered to contain IMAC affinity tags (e.g. multiple histidine residues) that are able to form stable complexes with heavy metal ions such as Ni^{2+} or Co^{2+}.[152,153] Thus, IMAC would allow for the preparation of highly pure recombinant proteins using different insoluble matrices that are linked to heavy metal ions.[154,155] The immobilized protein would subsequently be washed and finally eluted by competitive displacement using imidazole, chelating agents, or pH gradients. [156]

All discussed $A_{2A}AR$ constructs in this thesis contain a C-terminal polyhistidine-tag (10 histidine repetitions) and were purified by IMAC (Co^{2+} matrix) using imidazole as the elution reagent. No further purification steps were performed in order to yield the purified $A_{2A}AR$ protein.

1.4.3 Sodium Dodecyl Sulfate Polyacrylamide Gel Electrophoresis

Sodium dodecyl sulfate polyacrylamide gel electrophoresis (SDS-PAGE) is used to determine the protein purity of the purified $A_{2A}AR$. We utilize homemade 10 % SDS-PAGE gels casted using *bis*-2-amino-2-(hydroxymethyl)propane-1,3-diol (*bis*-Tris) buffer due to their extended shelf life and higher band resolution. Figure 13 shows an SDS-PAGE control gel using bovine serum albumin (BSA). The control was performed to show that dithiothreitol (DTT) can successfully be used to reduce disulfide bonds in our gel setting. The non-reduced BSA sample shows two bands: 1. higher molecular weight band that corresponds to a BSA dimer (arrow in Figure 13)[157] and 2. a monomer band that elutes at lower molecular weight compared to reduced BSA samples due to multiple intact intramolecular disulfide bonds.

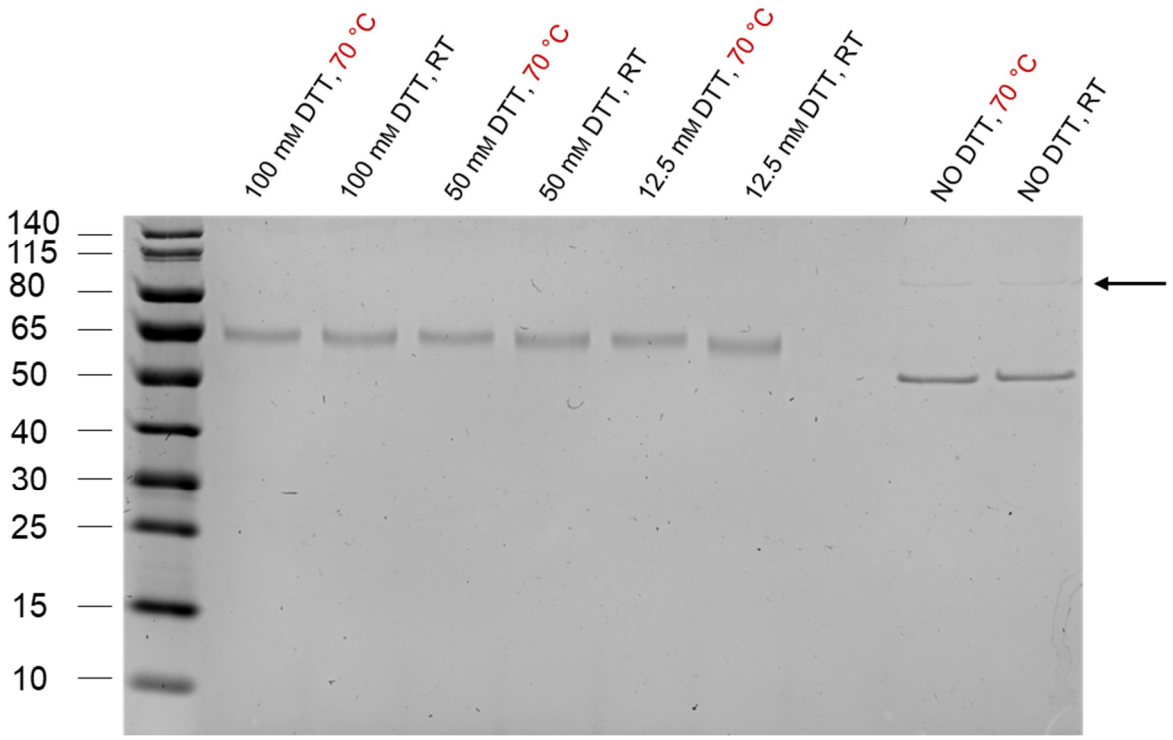

Figure 13. SDS-PAGE of BSA using homemade *bis*-Tris gels.
300 ng BSA were applied per well using different incubation procedures with and without the reducing agent DTT. BSA dimers (arrow) can be observed in the two wells from the right that were incubated without DTT. Proteins were detected using a Coomassie blue staining solution.

The BSA control was important as multiple bands can also be observed at some conditions for the A_{2A}AR or purified GPCRs in general. High molecular weight bands are frequently observed for membrane proteins with very different explanation approaches.[158–163] Briefly, these references imply 1. incomplete detergent binding, 2. metal gel-shift by multiple histidine residues, 3. incomplete reduction of highly stable disulfides, 4. aggregates by high incubation temperatures in loading dye, 5. glycosylation or 6. possible GPCR dimers. Therefore, it was initially presumed that multiple bands in SDS-PAGE gels of GPCRs may exist due to the formation of GPCR oligomers, similarly to BSA. In fact, the larger GPCR bands are often shown to be twice the size of the monomer band and multiple publications refer to the larger molecular weight GPCR bands as dimers or oligomers.[134,164,165] We tested the effect of DTT and loading dye incubation by western blot analysis using anti-His and anti-A_{2A}AR antibodies (ThermoFisher, Cat. #MA1-21315 and antibodies-online, Cat. #ABIN1535559) on purified proteins of the A_{2A} and A_{2B}AR (Figure 14). Different concentrations of DTT did not seem to change the SDS-PAGE pattern. However, higher incubation temperatures with loading dye (70 °C compared to 37 °C) did slightly increase the amount of high molecular weight bands for the A_{2B}AR (Figure 14a). It is unlikely that more GPCR oligomers form at 70 °C and therefore, multiple GPCR bands could be attributable to irreversible GPCR aggregation at higher temperatures. The addition of DTT did not change the amount of high molecular weight bands for both receptors. The A_{2A}AR western blot clearly showed that the high molecular weight bands are reactive to specific A_{2A}AR antibodies, therefore clearly contain the A_{2A}AR ECL2 peptide sequence. Furthermore, it was discovered that the dilution of a purified A_{2A}AR sample for crystallization from a concentrated protein did show a significant reduction of higher molecular weight bands on the SDS-PAGE gel (please refer to Figure 26c). Therefore, it is likely that high salt and high detergent concentrations in the purification buffers facilitate protein aggregation when the sample is incubated with loading dye, especially at higher temperatures. Taken all evidence together, it is likely that higher molecular weight bands in SDS-PAGE do not correspond to possible GPCR oligomer formations. Hence, the SDS-PAGE analysis in this thesis will not refer to these bands as oligomers or impurities.

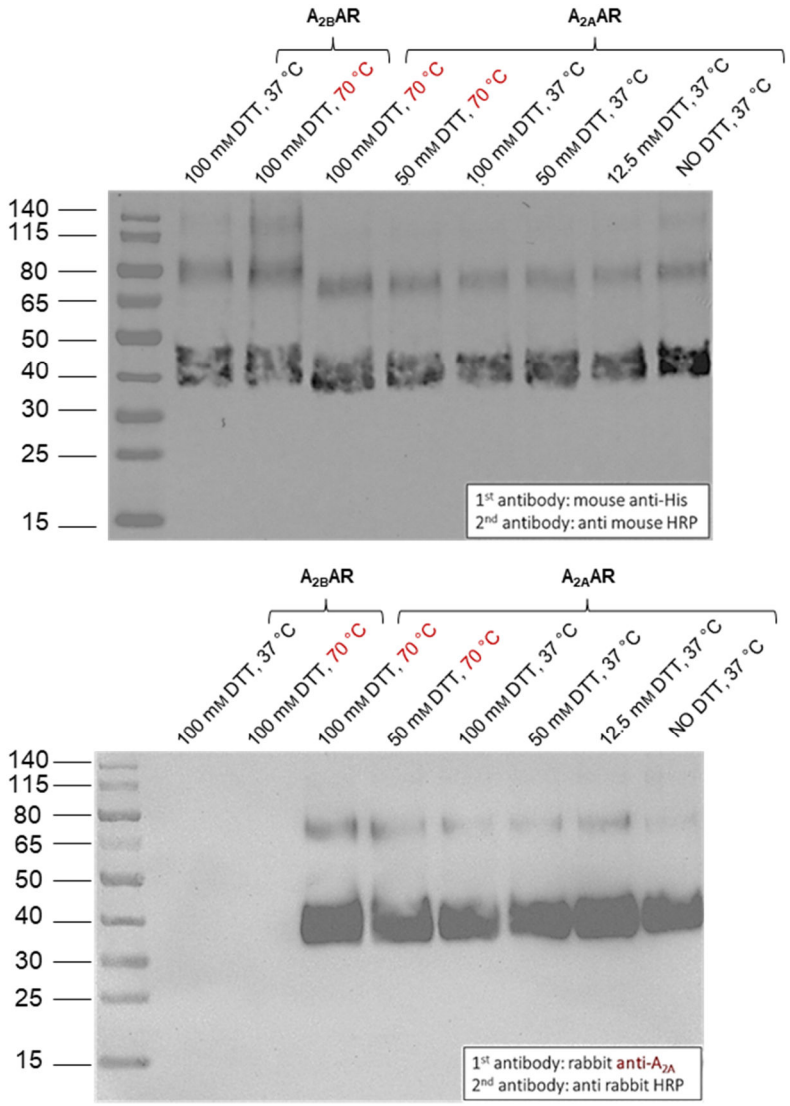

Figure 14. Western blot of purified A_{2A} and A_{2B}ARs.
Top: Western blot using anti-His antibodies. Bottom: Western blot using anti-A_{2A}AR antibodies. The epitope for the latter antibody is the A_{2A}AR ECL2. Similar protein amounts were applied to each lane. HRP refers to horseradish peroxidase.

1.4.4 Size-Exclusion Chromatography

In this thesis, size-exclusion chromatography (SEC) is used to assess the amount of protein aggregation in the final protein sample. The first separation of peptides and amino acids by SEC was performed by Lindqvist and Storgårds in 1995 who used a starch column as a molecular sieve. [166] Nowadays, SEC columns are packed with porous particles that are available with a variety of sizes to cover a wide molecular weight range for different protein preparations.[167] The size and hydrodynamic volume of a protein determines its elution profile during SEC. Larger molecules can pass by the pores of the SEC column whereas smaller proteins enter the pores and get restrained. Therefore, larger proteins (e.g. aggregates) exhibit a shorter elution time than smaller proteins.[167] Routinely, proteins can be detected using a UV detector at 280 nm absorption.

In this thesis, SEC is used to determine the monodispersity (or i.e., uniformity) of the GPCR protein sample by assessing its protein aggregation. Therefore, SEC is used as a final quality control step prior to crystallization experiments. A typical SEC profile of a protein sample compared to its buffer produced by our methods is shown in Figure 15. Here, the monodisperse protein fraction elutes at approximately 4.2 min which represents the GPCR in detergent micelles. Here, no protein aggregation peak is visible right before the protein. Further SEC analyses will only focus on showing the elution time range between 2 and 6 min that represents the $A_{2A}AR$ and other proteins (Figure 15). The peak height of the GPCR peak serves as an indicator for protein yield whereas routine protein quantification is not performed in order to avoid the loss of valuable protein sample.

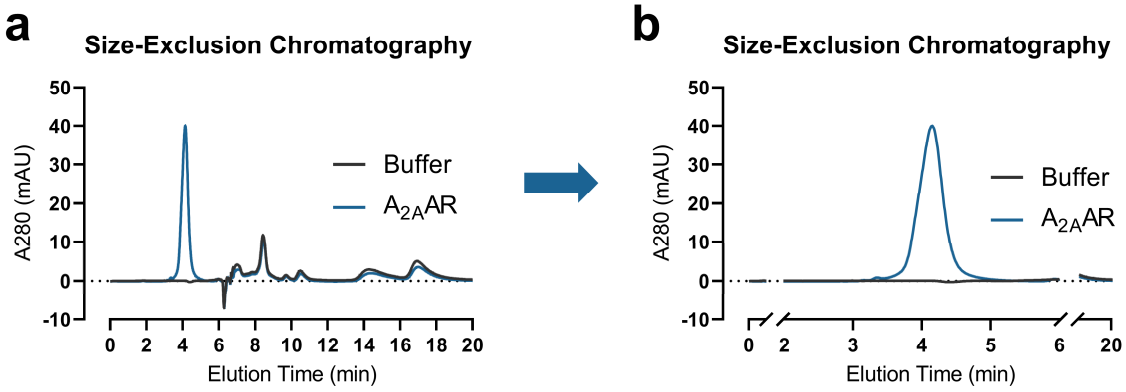

Figure 15. Size-exclusion chromatography analysis example.
a) Full size-exclusion chromatogram of the $A_{2A}AR$ compared to a buffer control. b) Zoomed section of the SEC result displaying the important and discussed protein signal.

1.4.5 Thermostability Assessment

It is of great importance to utilize a reliable pre-crystallization assay to determine receptor stability and hence choose only the most promising candidates for crystallization trials.[168,169] In this thesis, a fluorescence-based thermal stability assay is used to assess the thermostability of purified proteins.[168] The assay is performed using a real-time PCR cycler in a low volume format (50 µL total volume). The assay relies on the reagent *N*-[4-(7-diethylamino-4-methyl-3-coumarinyl)phenyl]maleimide (CPM) which exhibits weak fluorescence in its unbound form. However, when CPM reacts with nucleophiles (e.g., cysteines), it forms a covalent bond and emits fluorescence light upon excitation (Figure 16).

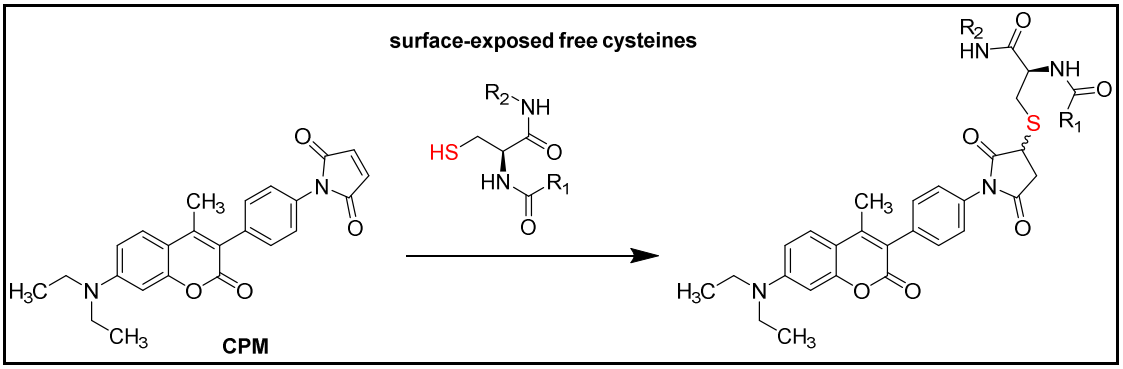

Figure 16. Reaction scheme of the thiol-specific reaction of CPM with solvent-exposed cysteines.

In buffer systems with physiological pH values (pH 7.4), CPM mostly targets free thiols that naturally occur in cysteines. In membrane proteins and specifically in GPCRs, hydrophobic cysteines are often buried inside the transmembrane domain and are not surface-exposed. Thus, these cysteines are not accessible for the reaction with CPM as long as the protein is folded correctly. In the CPM-based thermostability assay, the protein solution is gradually heated, which results in the unfolding of the protein and, ultimately, in its denaturation. Upon progressive unfolding, formerly buried cysteines become surface-exposed and react with CPM which generates a fluorescence signal (Figure 17). The advantage of this thermostability assay is its small-scale format which utilizes only small amounts of protein.

The melting temperature (T_M) is used to compare the thermostability of different protein preparations. It represents the temperature at 50 % protein unfolding, i.e., the temperature at 50 % of the fluorescence signal (Figure 17). It is determined by a Boltzmann-sigmoidal fit of the measured data. The top value of the sigmoidal fit has to be constrained to 100 % due to the characteristic negative gradient of the thermostability curve when approaching 100 °C.

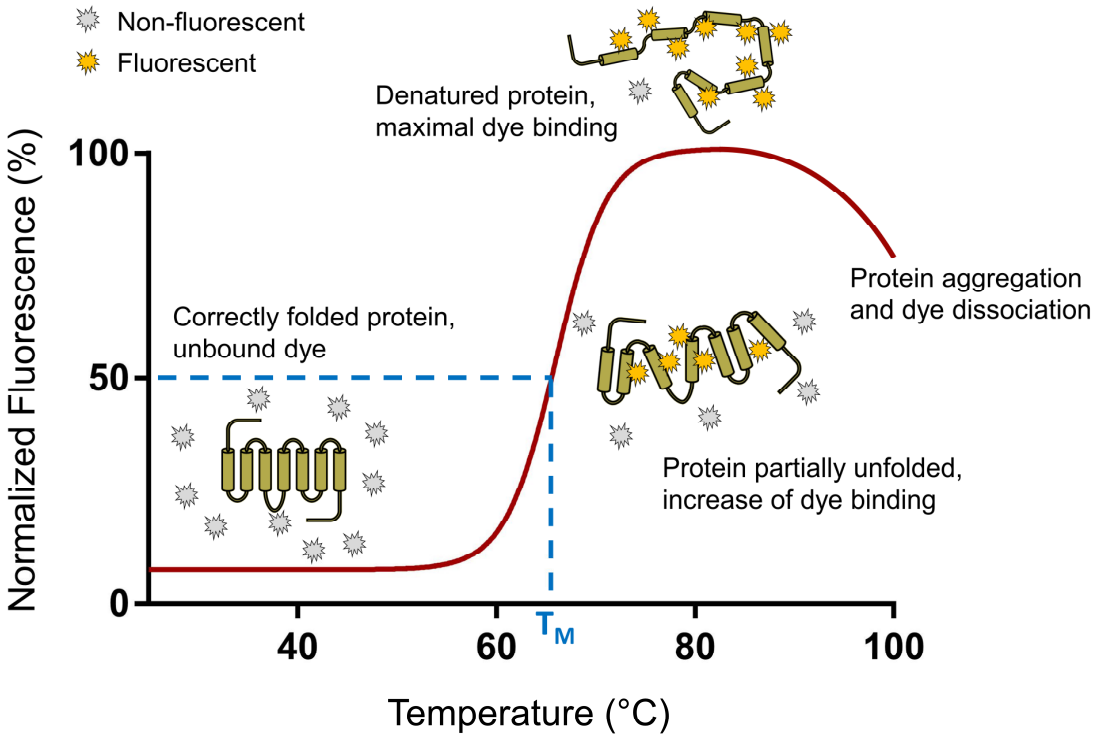

Figure 17. Principle of the CPM-based thermal shift assay.
The protein sequence of the GPCR is shown in green cylinders. Non-fluorescent CPM is depicted in grey stars whereas covalently-bound and fluorescent CPM is shown in yellow stars.

1.4.6 Crystallization of Membrane Proteins in Lipidic Cubic Phase

Protein crystallography has been used for many decades to yield reliable structural information of proteins at near atomic resolution.[170] However, crystallography of membrane proteins is often more challenging than crystallizing soluble proteins and has only recently become accessible.[171] Membrane proteins can be crystallized using (1) *in-surfo* or (2) bilayer methods.[172] *In-surfo* methods use the solubilized protein solution directly for vapor-diffusion type crystallization whereas bilayer methods rely on an artificial cell membrane that imitates the bilayer lipid phase. LCP crystallization represents a bilayer method that is also known as *in-meso* crystallization and requires the solubilized membrane protein to be reconstituted into a biscontinuous lipidic mesophase.[173] Landau and Rosenbusch pioneered the development of LCP crystallization methods and demonstrated the first crystallization of a membrane protein in LCP in 1996.[174] Their crystals diffracted up to 3.7 Å but no structure was reported. Ever since, LCP methods have been continuously optimized and enabled the elucidation of many GPCRs in the following decades.[169] A stable LCP forms after mixing protein solution with lipids in a 2 to 3 ratio at 20 °C (water content 40 % [w/w]) (refers to Pn3m in Figure 18). The monoacylglycerol monoolein (1-oleoyl-*rac*-glycerol) represents the most popular lipid for GPCR crystallography.[175] Precipitant solution is added to the LCP bolus during crystallization experiments. The additional water in the precipitant solution is capable of diffusing into the protein-containing mesophase (labeled with B in Figure 18 – Pn3m + water).[173]

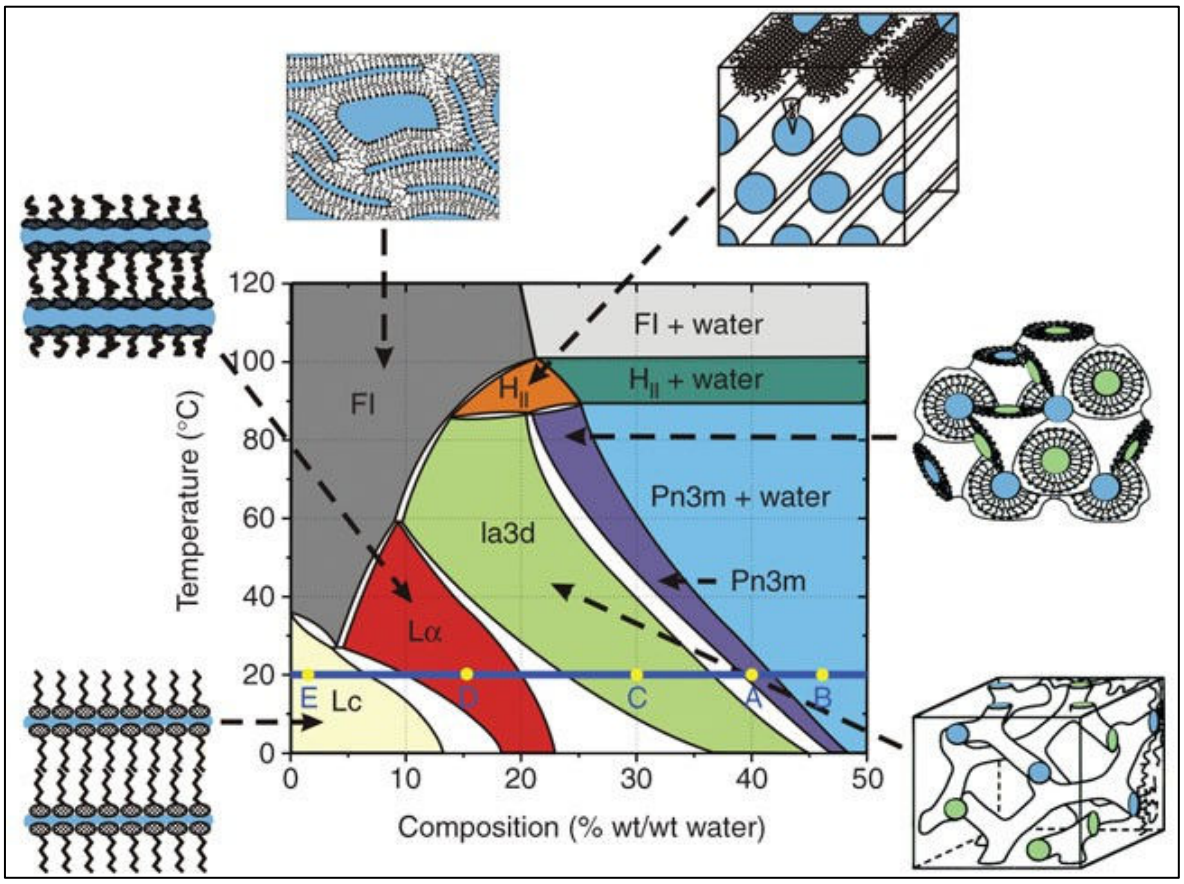

Figure 18. Phase diagram of lipid-water compositions at different temperatures. The blue dash represents phase changes that may happen due to phase composition modifications during crystallization experiments at 20 °C: **A** cubic phase type Pn3m, **B** two-phase system with a type Pn3m cubic phase and second phase of water, **C** cubic phase of type Ia3d, **D** lamellar liquid crystalline phase, **E** solid phase. Figure was taken without modifications from Caffrey and Cherezov.[173]

The exact mechanism for crystal formation in LCP is still not fully understood. However, Martin Caffrey has formulated the hypothesis that the precipitant solution destabilizes the LCP system and enables the formation of aqueous channels throughout the mesophase.[176,177] This so-called molecular sponge allows the protein to diffuse into lamellar phases which ultimately leads to crystal nucleation (Figure 19). The theory is supported by the fact that LCP protein mobility correlates with successful crystal growth.[178] Several factors influence the probability of successful crystal nucleation in LCP such as protein stability and purity, precipitant composition (polyethylene glycol [PEG], pH, salts, additives) and environmental conditions (temperature and humidity).[179]

One key advantage of crystallizing GPCRs in LCP represents the fact that some membrane proteins are more stable when embedded into LCP.[180]

Moreover, the artificial membrane environment during LCP crystallization is closer to the natural setting of a GPCR in the lipid bilayer of the cell membrane when compared to a solubilized GPCR in detergent micelles.[181] LCP crystallization experiments were found to be more robust to protein contamination than *in-surfo* methods and therefore require less extensive purification procedures.[182] However, the handling of the viscous and sticky cubic phase represents one limitation in LCP crystallization and requires a certain amount of expertise.[175]

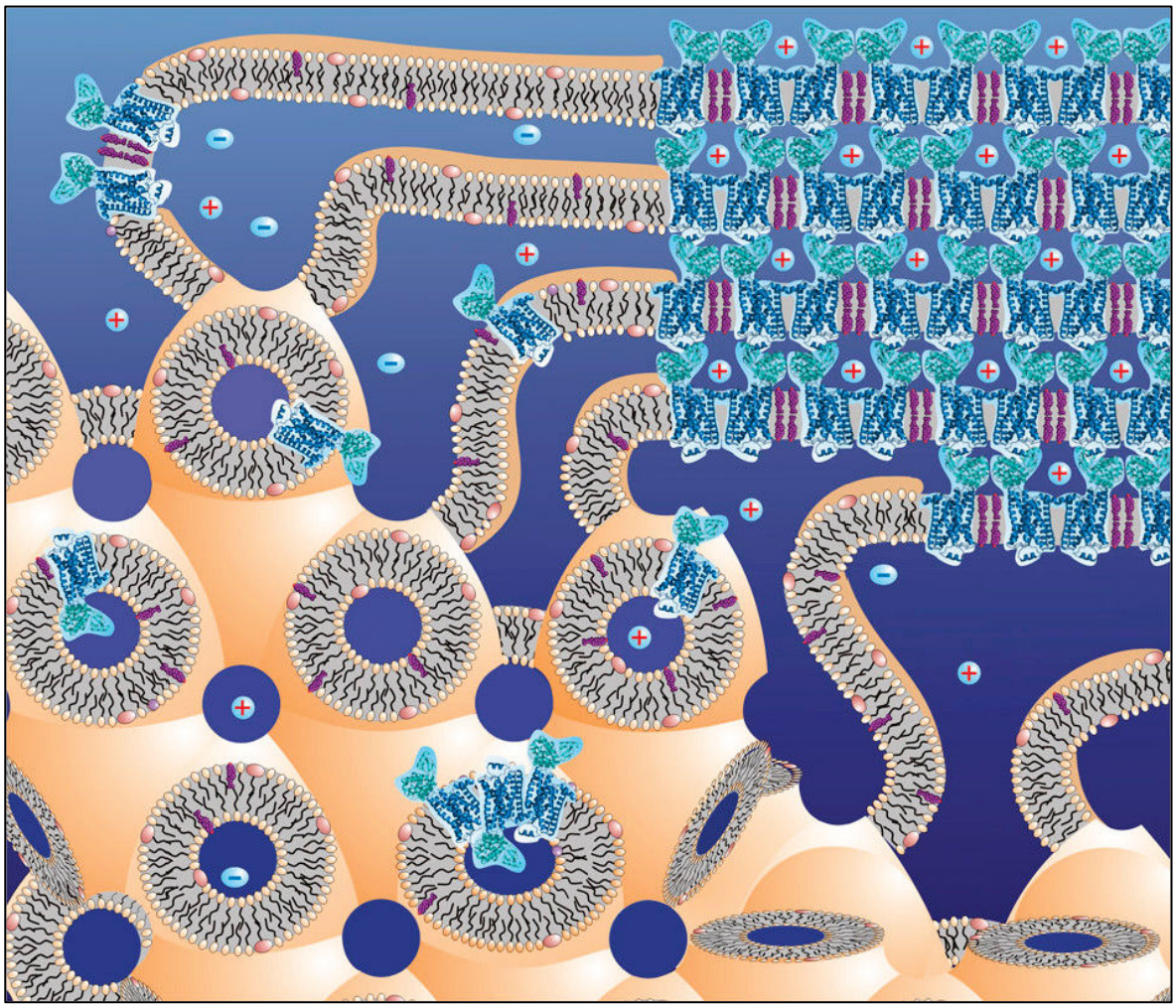

Figure 19. Illustration of the proposed mechanism taken place during LCP crystallization.
The yellow to brown colored structure represents lipid, the GPCR is depicted in blue and its fusion protein in green, purple depicts cholesterol. Figure taken without modifications from Cherezov et al.[178]

2 Aim of the Thesis

Tremendous technical and methodological advances over the past two decades have greatly advanced GPCR structural biology, and structural insights into ligand binding sites have been indispensable for the understanding of how ligands block or activate GPCRs.[183,184]

The aim of this thesis was divided into three research goals:

1. Continue the master thesis effort to solve agonist-bound δ-opioid receptor crystal structures.

2. Establish methods for membrane protein purification, protein analysis and (membrane) protein crystallization at the Pharmaceutical Institute of the University of Bonn.

3. These methods should then be applied to structural studies on adenosine receptors, and specifically on the A_{2A}AR as a proof-of-principle study.

Crystallization and structure determination of the A_{2A}AR in complex with one or more proprietary ligands would not only prove the successful implementation of all relevant structural biology methods, but also provide valuable insight into the binding mode of new A_{2A}AR ligands. This information could subsequently be used to optimize the new chemical classes of adenosine receptor ligands and increase both their potency and selectivity. Moreover, this could accelerate the translational development of novel drugs, e.g., for neurodegenerative diseases and for the immunotherapy of cancer.

3 Results and Discussion

3.1 Publication I: Elucidating the Active δ-Opioid Receptor Crystal Structure with Peptide and Small-molecule Agonists

3.1.1 Publication Details

The results of this chapter were published in the journal *Science Advances* in November 2019 with the title “Elucidating the active δ-opioid receptor crystal structure with peptide and small-molecule agonists”.[80] The publication was co-authored by the following people: Tobias Claff, Jing Yu, Véronique Blais, Nilkanth Patel, Charlotte Martin, Lijie Wu, Gye Won Han, Brian J. Holleran, Olivier Van der Poorten, Kate L. White, Michael A. Hanson, Philippe Sarret, Louis Gendron, Vadim Cherezov, Sebold Katritch, Steven Ballet, Zhi-Jie Liu, Christa E. Müller, and Raymond C. Stevens. Please refer to Appendix I for the publication’s full text and supplementary materials.

While parts of this effort were exerted during the framework of my Master of Science graduate thesis, a substantial amount of work including crystal optimization, structural analysis and manuscript preparation was performed as part of my doctoral thesis. All of my experimental contribution for this publication was performed at the ShanghaiTech University in Shanghai, China.

3.1.2 Previous Work

Within the framework of my Master of Science graduate thesis titled “Lipidic Cubic Phase Crystallization of the Human δ-Opioid Receptor”, I had substantially optimized the δ-opioid receptor for protein crystallization experiments and was able to generate initial crystal hits in LCP. This work was done during a research stay at the iHuman institute of the ShanghaiTech University in Shanghai (China). The thesis concluded with initial crystals diffracting to 3.4 Å resolution and crystal hits in complex with two additional, structurally diverse ligands. However, a crystal structure of the δ-opioid receptor had not yet been solved during the course of the master’s program.

3.1.3 Publication Summary and Contributions

Opioids (e.g., morphine) are well-known powerful analgesics and indispensable for global health care. However, the unrivaled analgesic potency is accompanied with potentially lethal adverse effects such as respiratory depression.[185] Moreover, the United States is currently facing an opioid epidemic with drug overdose to become the main cause of accidental deaths.[186] The opioid family consists of three GPCR subtypes: the μ-, κ-, and δ-opioid receptors (MOP, KOP, and DOP). While the analgesic potency and the side effects of opioids are largely attributed by the MOP,[187] DOP activation has become an attractive target to develop safer analgesics for the treatment of chronic pain.[188]

While crystal structures of the DOP in the inactive state and in complex with antagonists had been solved, the binding pocket of agonists remained elusive. In this work, we reported the first crystal structures of the DOP in complex with two structurally diverse agonists. For this purpose, the human wt DOP was genetically-engineered to stabilize the agonist-bound conformation for crystallization experiments. The mutation design was inspired by a directed evolution study performed on the KOP that showed great stabilization of the agonist-bound state.[189] This yielded a crystallization construct of the DOP bearing nine thermostabilizing point mutations. Three of these mutations (N90$^{2.45}$G, D95$^{2.50}$G, and N131$^{3.35}$S) are located in or close to the allosteric sodium binding pocket and facilitated the expulsion of sodium and the collapse of the pocket. These mutations were crucial for very high thermostability of the DOP construct in the complex of agonists. However, none of the nine point mutations affected the high-affinity binding of both crystallized agonists.

With the optimized DOP construct in hands, we solved the crystal structure of the thermostabilized DOP in complex with the peptide agonist KGCHM07 at 2.8 Å resolution and in complex with the small-molecule agonist DPI-287 at 3.3 Å resolution. We extensively analyzed the binding pose of both ligands and their activation states including a comparison to previously published opioid receptor structures. Thereby, we identified key factors for opioid receptor activation involving polar networks around the conserved D128$^{3.32}$ and a deeper penetration of agonists into the opioid receptor binding pocket, when compared to antagonists. Our findings were supported by a comprehensive mutagenesis study (Binding and

functional assays were performed by co-authors). Furthermore, we were able to describe crucial differences between small molecule and peptide ligand recognition. For instance, we revealed a large side chain rotation of residue W284$^{6.58}$ that is necessary to accommodate the large peptide ligand in the binding pocket. Residue R291 of the ECL3 was found to substantially change its conformation during DOP activation. We proposed R291^{ECL3} as a cationic counterpart for the carboxylate function of naturally occurring opioid peptides, the so-called “address” moiety according to the “message-address concept”.[190] The ECL3 is particularly diverse between opioid receptors and has been suggested as important factor for opioid selectivity.[191] In fact, we provided a structural understanding for selectivity determinants of DOP selective *N*,*N*-diethylbenzamide derivatives involving residues of the ECL3 and the adjacent ends of helices VI and VII.

The DOP construct optimization, the thermostability assessment of the optimized protein construct in complex with suitable DOP agonists, and the screening for suitable precipitant conditions for LCP crystallization experiments were conducted during the course of my abovementioned master thesis and this work is therefore not considered part of this doctoral thesis. Initial crystal hits of the thermostabilized DOP in complex with different ligands were generated during my master thesis but only showed X-ray diffraction to 3.4 Å resolution with incomplete datasets.

Thus, the effort was continued during my doctoral thesis. I started to optimize the crystal hits in order to yield well-diffracting crystals. Consequently, multiple rounds of crystallization experiments were performed to generate crystals of DOP in complex with the peptide agonist KGCHM07 that were used to solve its crystal structure to 2.8 Å resolution. Additionally, new crystals of the DOP in complex with DPI-287 were generated. The diffraction data for this co-crystal structure could then be completed and the resolution slightly increased to 3.3 Å. For this publication, I generated the DOP crystals, processed the initial datasets of the DOP-DPI-287 complex and was able to solve an initial structure by molecular replacement. However, the final structure determination of both structures and their refinements were conducted by co-authors with minor contributions from my side. Furthermore, I performed structural analysis, the comparison with previously solved crystal structures and created all publication figures. Finally, I was responsible for manuscript writing and editing with contribution from all co-authors.

3.2 Publication II: Single Stabilizing Point Mutation Enables High-resolution Co-Crystal Structures of the Adenosine A_{2A} Receptor with Preladenant Conjugates

3.2.1 Publication Details

The results of this chapter were published in the journal *Angewandte Chemie* in April 2022 with the title “Single stabilizing point mutation enables high-resolution co-crystal structures of the adenosine A_{2A} receptor with Preladenant conjugates”.[107] The publication was co-authored by the following people: Tobias Claff, Tim A. Klapschinski, Udaya K. Tiruttani Subhramanyam, Victoria J. Vaaßen, Jonathan G. Schlegel, Christin Vielmuth, Jan H. Voß, Jörg Labahn, and Christa E. Müller. Please refer to Appendix II for the publication’s full text and supplementary materials. The publication was designated as a “hot paper” by *Angewandte Chemie*, and featured on the inside cover of the respective issue.

3.2.2 Publication Summary and Contributions

This publication marks an important milestone as it represents the very first crystal structures solved by crystals generated in the Müller lab at the University of Bonn; it thus confirms the successful establishment of GPCR structural biology methods in Bonn. Herein, we solved crystal structures of the A_{2A}AR in complex with two conjugates of the important A_{2A}AR antagonist Preladenant. Preladenant bears a novel tricyclic scaffold and had been previously discovered possessing unrivalled potency and selectivity towards the A_{2A}AR.[192] It was the first non-xanthine antagonist that entered the clinical development as an antiparkinsonian drug and was evaluated in phase III clinical trials.[193] However, Preladenant ultimately failed to provide sufficient evidence for efficacy, presumably due to an imperfect trial design, and its development was therefore discontinued.[194] Nevertheless, Preladenant still represents one of the most potent and most selective A_{2A}AR antagonists, but its co-crystal structure and exact binding mode had remained elusive. We modified Preladenant to attach PEG linkers of different lengths. The most potent derivative bearing 4 PEG units (PSB-2113) was then conjugated to a

boron-dipyrromethene (BODIPY) fluorophore to yield a fluorescence-labeled A_{2A}AR antagonist (PSB-2115) that could potentially be used to visualize the A_{2A}AR in living cells.

In parallel, we optimized the previously published A_{2A}AR crystallization construct (A_{2A}-ΔC-bRIL) that had not contained additional point mutations to improve its stability and therefore facilitate its co-crystallization with different A_{2A}AR antagonists. We mutated a serine residue (S91$^{3.39}$) inside the highly conserved allosteric sodium binding pocket to the basic lysine (S91$^{3.39}$K) which had previously been observed to be beneficial for GPCR stability.[195,196] We showed that the basic amine of the lysine side-chain mimics the protonated sodium ion inside the allosteric sodium binding pocket and additionally displaces three structural water molecules without affecting overall helix geometry. Thereby, the mutation significantly reduced protein flexibility and locks the GPCR in its inactive state, which is beneficial for antagonist co-crystallization. This resulted in a substantial thermostability increase by the introduced mutation. Importantly, the stability of the new A_{2A}AR crystallization construct (designated A_{2A}-PSB1-bRIL) was even higher than the stability of the so-called stabilized receptor (StaR) A_{2A}-StaR2-bRIL[117,132] that had represented the best and most stable A_{2A}AR crystallization construct. The A_{2A}-StaR2 construct has been indispensable for our understanding of A_{2A}AR antagonist binding pockets but bears nine point mutations, two of which (T88$^{3.36}$A and S277$^{7.42}$A) are located directly inside the orthosteric ligand binding pocket interfering with agonist binding[109] and, in case of S277$^{7.42}$A, possibly also with the binding of antagonist scaffolds.[118] With our work, we provided a new gold standard for the crystallization of the A_{2A}AR in complex with antagonists bearing a significantly reduced number of mutations.

Subsequently, we used A2A-PSB1-bRIL to crystallize both of our new Preladenant conjugates, PSB-2113 and PSB-2115, and solved their high-resolution crystal structures at 2.25 and 2.60 Å resolution. The new structures revealed that the tricyclic scaffold of Preladenant displaces an “unhappy water molecule”[197] from the ligand binding pocket providing an explanation for the enhanced potency of Preladenant. Moreover, we suggested that the more restricted tricyclic scaffold is responsible for its high A_{2A}AR selectivity as the exit vector of the side-chain attached to N7 is sterically fixed and therefore less flexible when compared to the bicyclic and less selective A_{2A}AR antagonist ZM241385.

Although we were able to fully resolve the Preladenant core of PSB-2113 and PSB-2115, only weak electron density could be observed for the PEG linker and no density was detected for the BODIPY fluorophore in PSB-2115 suggesting high flexibility of the respective moieties. Nevertheless, we could show for the first time that the addition of a rather large fluorophore does not interfere with the binding mode of the antagonist scaffold itself.

For this publication, I took the lead on investigation, methodology, validation and manuscript writing. Therefore, I cloned the A_{2A}AR constructs, expressed them in *Sf9* insect cells, purified and analyzed the proteins, crystallized A_{2A}-PSB1-bRIL in LCP, and prepared crystals for data collection that was then performed in collaboration with the group of Prof. Dr. Jörg Labahn. The structures were solved using molecular replacement and refined by Dr. Udaya K. Tiruttani Subhramanyam. Moreover, I performed the thermostability assessment of A_{2A}-PSB1-bRIL and related constructs. I analyzed, interpreted and compiled results and generated the figures.

3.3 Discovery and Crystal Structure-guided Optimization of Dual Adenosine A_{2A} Receptor and Monoamine Oxidase B Blockers

3.3.1 3*H*-Imidazo[4,5-*b*]pyridines as Dual-target Lead Compounds Blocking both A_{2A}AR and MAO-B

3.3.1.1 Previous Work

During a high-throughput screening campaign that was previously carried out by colleagues on both A_{2A}AR and MAO-B, a 3*H*-imidazo[4,5-*b*]pyridine scaffold was discovered and subsequently used as a lead to develop dual-targeting drugs that blocks both targets (Figure 20).

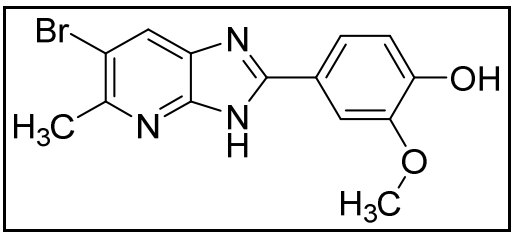

Figure 20. Hit compound discovered by high-throughput screening on the A_{2A}AR and MAO-B.

The hit compound was (moderately) potent on both A_1 and A_{2A}AR but showed only micromolar MAO-B inhibitory potency (hA_{2A} IC_{50} 0.20 µM, hA_1 IC_{50} 0.40 µM, MAO-B IC_{50} 6.3 µM). Subsequently, the novel scaffold was characterized and extensively optimized in order to increase affinity, inhibitory potency, and drug-like properties on both targets, ultimately leading to the indazole-substituted 3*H*-imidazo[4,5-*b*]pyridine that was used for the structural biology in this study. Table 3 provides an overview of all discussed 3*H*-imidazo[4,5-*b*]pyridines that were previously characterized. The complete optimization procedure and the synthesis of these compounds is not part of this thesis and will be published elsewhere.

3.3.1.2 Pharmacological Characterization of Selected Compounds

The indazole-imidazo[4,5-*b*]pyridines were modified in positions C5, C6 and *N*4′ in order to create a preliminary structure-activity relationship. While substituents at the N4′ positions were not required for high A_{2A}AR affinity, both larger substituents (propan-2-ol and methoxyethyl) were able to increase the MAO-B IC_{50} by 4- to 5-fold. On the other hand, the substitution pattern at the C5- and C6-positions were essential for A_{2A}AR affinity and MAO-B inhibition. The removal of the C5-methyl group was detrimental for A_{2A}AR affinity regardless of the tested combination of C6-substitutions whereas the C5-methyl group removal is tolerated by MAO-B when combined with a cyclopropyl in 6 position. Moreover, three different halogen substitutions (F, Cl, Br) were investigated at the C6-position. The MAO-B inhibitory potency increased with atom radius in the order of F, Cl, and Br whereas the A_{2A}AR affinity showed a negative trend in the same sequence.

All investigated imidazo[4,5-*b*]pyridines with triple-substitutions additionally showed low to moderate binding affinity at other adenosine receptor subtypes but the optimization of the imidazo[4,5-*b*]pyridines scaffold yielded several potent blockers of both the A_{2A}AR and MAO-B. Specifically, larger *N*4′-substitution disfavored A_{2B}AR binding and increased selectivity.

However, sub-nanomolar affinities or potencies could not be reached. Therefore, we started a structural biology campaign to obtain co-crystal structures with both targets to identify the exact binding mode of the imidazo[4,5-*b*]pyridines scaffold and employ structure-based optimization to further enhance the properties of the dual-target inhibitors. PSB-21007 was chosen for structural studies as it showed the highest dual-potency and superior selectivity towards the A_1AR.

Table 3. Affinities for the human ARs and inhibitory potencies towards MAO-B of novel 3*H*-imidazo[4,5-*b*]pyridine derivatives.[a)]

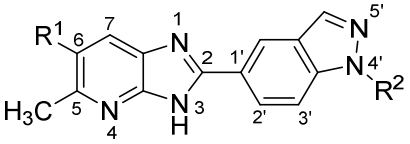

1 - 6

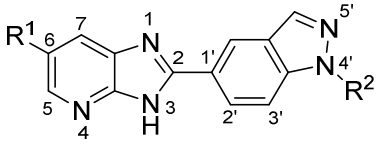

7 - 9

		Target	Human A_1AR	Human A_{2A}AR	Human A_{2B}AR	Human A_3AR	Human MAO-B IC_{50} ± SEM (nM)
			K_i ± SEM (nM) (or % inhibition at 1 µM, n = 2) vs. radioligands				
Cmpd.	**R^1**	**R^2**	[^{3}H]CCPA	[^{3}H]MSX-2	[^{3}H]PSB-603	[^{3}H]PSB-11	
1	F	H	**136** ± 19	**35.0** ± 5.2	**37.8** ± 9.8	**223** ± 28	**419** ± 20
2	F	CH_3	**1,420** ± 342	**47.2** ± 7.4	**65.8** ± 32.4	**142** ± 46	**442** ± 26
3	F	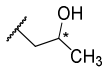	**763** ± 109	**69.8** ± 9.2	**208** ± 41	**132** ± 18	**118** ± 23
4 (PSB-21007)	F	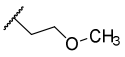	**1,900** ± 652	**50.3** ± 7.1	**183** ± 8	**292** ± 22	**83.3** ± 14.9
5	Cl	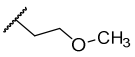	**650** ± 142	**89.4** ± 21.8	**303** ± 41	**88.5** ± 7.0	**6.25** ± 1.09
6	Br	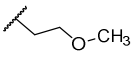	**759** ± 42	**105** ± 3	**158** ± 15	**51.7** ± 7.0	**3.62** ± 0.20
7	F	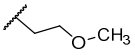	(9 %)	**521** ± 138	(30 %)	(32 %)	**800** ± 81
8	cyclo-propyl	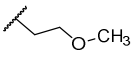	(10 %)	**1,660** ± 237	(19 %)	**291** ± 41.9	**37.1** ± 4.5
9	SO_2CH_3	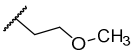	(-5 %)	**5,320** ± 892	(32 %)	(40 %)	**475** ± 63

[a)] K_i and IC_{50} values were determined as means from three independent experiments ± standard error of the mean (SEM), performed with the purified human MAO-B enzyme or on Chinese hamster ovary (CHO) cell membranes expressing the respective human wt adenosine receptor. Radioligand binding experiments were performed by Christin Vielmuth. MAO-B inhibitions assays were performed by Dr. Miriam Schlenk and Dr. Meryem Köse.

3.3.2 Crystal Structure of the A_{2A}AR in Complex with PSB-21007

3.3.2.1 Removal of a Glycosylation Site to Reduce Protein Microheterogeneity

We previously developed the optimized A_{2A}AR crystallization construct A_{2A}-PSB1-bRIL that contains a single point mutation (S91$^{3.39}$K) inside the allosteric sodium binding pocket to stabilize the inactive conformation which significantly enhanced protein thermostability.[107] For the co-crystallization of PSB-21007, we used the same construct but with the addition of another point mutation (N154^{ECL2}A) with the aim to remove a putative glycosylation site in the ECL2 of the A_{2A}AR. This construct is from now on referred to as A_{2A}-PSB2-bRIL.

Mutations of the asparagine in position 154 to either alanine or glutamine had previously been used for A_{2A}AR crystallization to eliminate post-translational N-linked glycosylation that is expected to inhibit crystal growth due to micro-heterogeneity[82,117] (for an overview of all published A_{2A}AR crystal structures, please refer to Table 1 and Table 2). Evidence of N-linked glycosylation is missing in available A_{2A}AR crystal structures and N154^{ECL2} is largely modeled to be buried inside the ECL2. In fact, N154^{ECL2} from A_{2A}AR PDB accession code 4EIY[120] only shows 5.2 Å² of solvent-accessible surface in the modeled conformation (Figure 21). This indicates that the non-glycosylated form of the A_{2A}AR is the one that predominantly crystallizes. However, we employed SDS-PAGE to demonstrate that A_{2A}-PSB1-bRIL (bearing the wt N154^{ECL2}) is still partially glycosylated whereas A_{2A}-PSB2-bRIL (bearing N154^{ECL2}A) successfully lost N-linked glycosylation (Figure 22). Glycosylated proteins typically

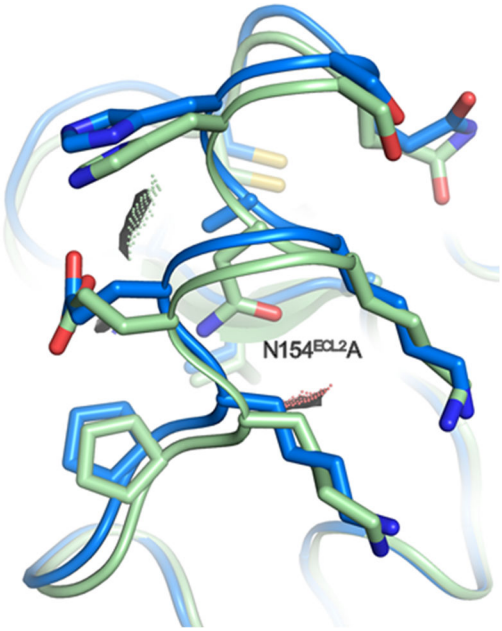

Figure 21. Residue N154^{ECL2} is buried inside the ECL2 in the A_{2A}AR crystal structure with the PDB accession code 4EIY
The A_{2A}-PSB2-bRIL-PSB-21007 complex is shown in blue and PDB 4EIY in green. The solvent accessible surface is shown in black and its area calculated from the colored dot surface.

migrate more slowly in SDS-PAGE and generate higher molecular weight smearing.[198] In fact, despite having only a single glycosylation site, smearing could be observed for the A_{2A}-PSB1-bRIL while a sharper band was detected for the $N154^{ECL2}$ mutants indicating the effective loss of glycosylation (Figure 22). Moreover, the glycosylation of A_{2A}-PSB1-bRIL could be prevented during expression by the glycosylation inhibitor Tunicamycin[199] or cleaved off by the enzyme peptide-N-glycosidase F (PNGase F)[200] applied to the purified protein.

The affinity of PSB-21007 to A_{2A}-PSB1-bRIL is nearly identical compared to the wt A_{2A}AR (K_i 89.9 ± 30.5 nM vs. 50.3 ± 12.3 nM; ΔpK_i 0.27; p = 0.1132 using the paired two-tailed t-test) demonstrating that the $S91^{3.39}K$ mutation virtually does not alter ligand binding. The affinity of PSB-21007 to A_{2A}-PSB2-bRIL has not been tested separately but it is not expected that the glycosylation removal ($N154^{ECL2}A$) affects A_{2A}AR affinity as the residue is not located close to the ligand binding pocket.

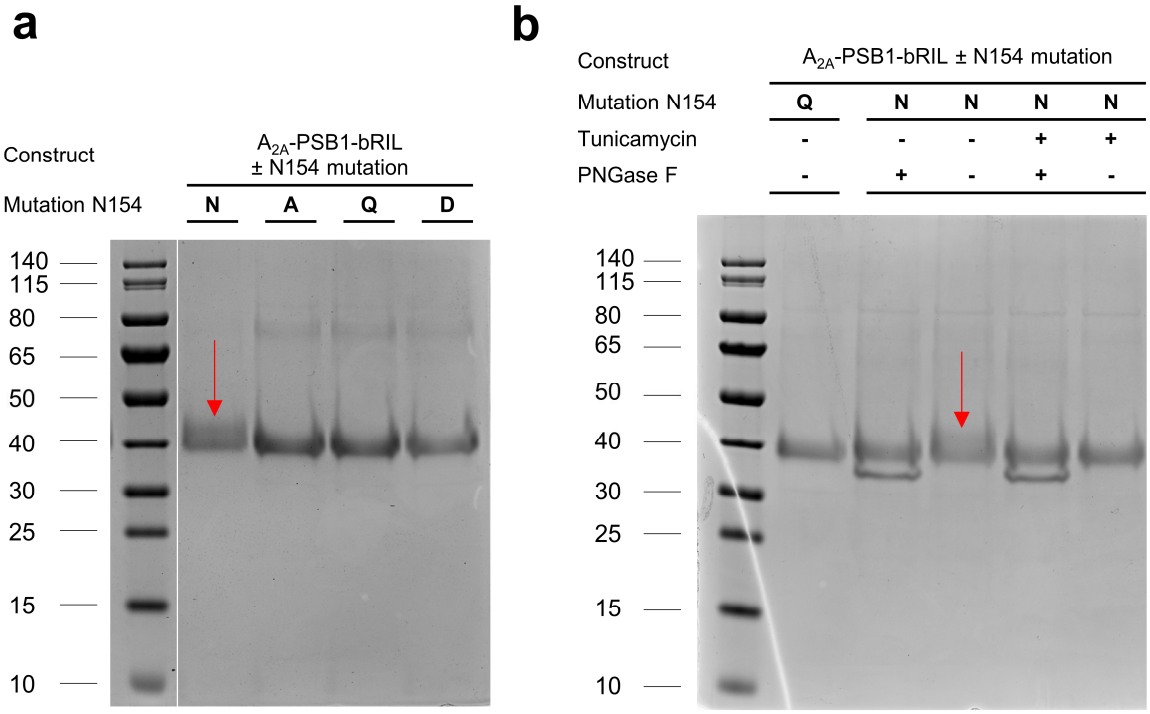

Figure 22. SDS-PAGE analysis of the A_{2A}AR glycosylation state.
a) SDS-PAGE of A_{2A}-PSB1-bRIL compared to different N154 mutations in the same protein background to remove N-linked glycosylation. The red arrow points to the characteristic glycosylation smear. A_{2A}-PSB1-bRIL plus N154A indicates the crystallization construct A_{2A}-PSB2-bRIL. The protein marker originated from the same SDS-PAGE gel. b) The effect of Tunicamycin and PNGase F on the SDS-PAGE mobility of A_{2A}-PSB1-bRIL, compared to N154Q in A_{2A}-PSB1-bRIL. Equal protein amounts were loaded onto the gel. Both the addition of Tunicamycin during A_{2A}-PSB1-bRIL expression or PNGase F treatment of the purified protein resulted in the removal of the characteristic glycosylation smear. The band for PNGase F (≈36 kDa) is visible directly under the A_{2A}AR band (≈48 kDa). The glycosylation SDS-PAGE analysis was performed by Jonathan G. Schlegel.

3.3.2.2 Purification and Crystallization of the A_{2A}-PSB2-bRIL-PSB-21007 Complex

The A_{2A}-PSB2-bRIL-PSB-21007 complex was purified and analyzed according to section 1.4. The size-exclusion chromatogram and the SDS-PAGE showed high purity and monodispersity of the purified protein (Figure 23a and c). The T_M of the complex was determined to be 72.4 °C (Figure 23b). Diffraction quality crystals are shown in Figure 23d with an average size of 50 µm. The crystals grew in the following precipitant condition: 30 % (w/v) PEG with the average molecular mass of 400 (PEG400), 400 mM $(NH_4)_2HPO_4$ (pH 7.4 at 25 °C).

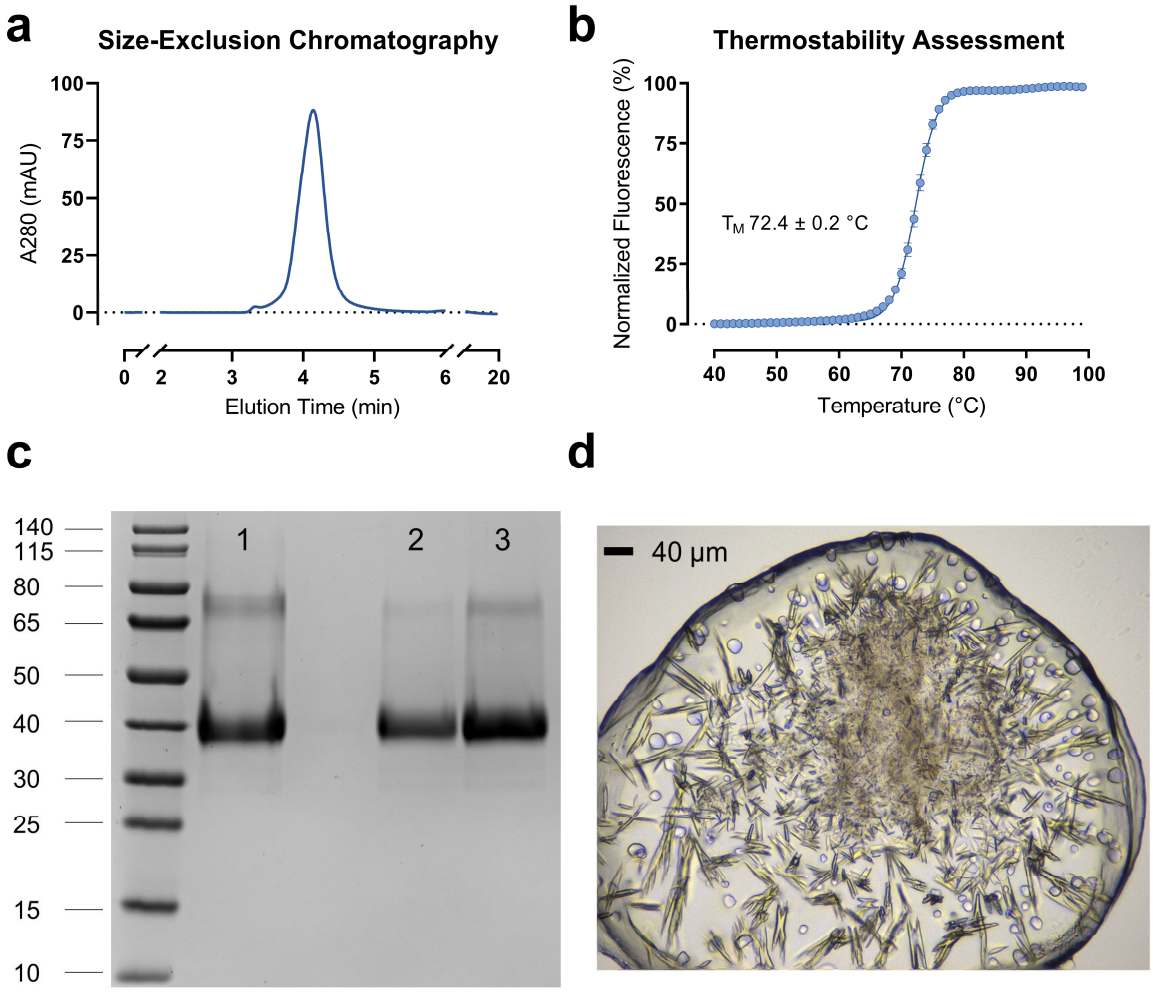

Figure 23. Protein analysis and crystallization of A_{2A}-PSB2-bRIL-PSB-21007.
a) SEC of the final protein sample used for crystallization (diluted 80-fold, injection volume 30 µL), b) thermostability assessment (in the presence of 12.5 µM PSB-21007) and c) SDS-PAGE of the purified A_{2A}-PSB2-bRIL-PSB-21007 complex. The data points in the melting curve and the T_M in panel b are shown as means ± SEM from three independent experiments. The SDS-PAGE was loaded with three different samples (1 protein sample before concentration, 2 and 3 final protein sample used for crystallization, but diluted ~200- and ~100-fold with water; equal sample volumes were applied). d) Crystals of A_{2A}-PSB2-bRIL-PSB-21007 in LCP used to obtain high-resolution diffraction data.

3.3.2.3 The A_{2A}AR Binding Pocket of PSB-21007

We obtained the structure of A_{2A}-PSB2-bRIL-PSB-21007 at 2.65 Å resolution. Data collection and structure determination were performed in collaboration by Prof. Jörg Labahn and Dr. Udaya K. Tiruttani Subhramanyam from the Centre for Structural Systems Biology in Hamburg. PSB-21007 was well resolved inside the orthosteric binding pocket of the A_{2A}AR (Figure 24). The *N*4 of PSB-21007 (for atom numbering please refer to Figure 24c) forms a direct but relatively weak hydrogen bond (N-H distance 2.42 Å, 168°) to N253$^{6.55}$ (Figure 24b), which represents a key anchor interaction similarly observed for other A_{2A}AR antagonists, e.g. ZM241385[120] (Figure 24e) and agonists, e.g. adenosine and its derivatives.[109] The interaction of PSB-21007 to N253$^{6.55}$ is further supported by water-mediated hydrogen bonds to *N*3 and *N*4 whereas ZM241385 forms direct hydrogen bonding to N253$^{6.55}$ via its N^7 amino group (for ZM241385 atom numbering please refer to Figure 24f). Therefore, the hydrogen bond network to N253$^{6.55}$ is somewhat stronger for ZM241385 compared to PSB-21007 and also extends to E169^{ECL2} (Figure 24e), which likely contributes to the higher affinity of ZM241385 compared to PSB-21007 (K_i 0.8 nM[201] vs. 50.3 nM). The *N*1 of PSB-21007 is involved in a water network work that couples the ligand to helices I and II. We were able to resolve five structural water molecules connecting *N*1 to Y9$^{1.35}$ and H278$^{7.43}$ as well as to the backbones of A59$^{2.57}$ and A63$^{2.61}$ (Figure 24b and e). This very space can potentially be targeted during the optimization of PSB-21007 to enhance A_{2A}AR affinity. PSB-21007 might be additionally substituted in its C7 position to achieve this goal. On the contrary, further extension of ZM241385 at its *N*3 position to target this pocket might be more difficult to achieve.

The 5-methyl group is located inside a partially hydrophobic pocket formed by M177$^{5.38}$, L249$^{6.51}$, H250$^{6.52}$, and N253$^{6.55}$ (Figure 24b and d). We observed that the 5-methyl group is essential for A_{2A}AR affinity in this series of 3*H*-imidazo[4,5-*b*]pyridines. Its removal possibly creates energetically unstable water molecules as the pocket may not be favorable for water. The fluorine in position 6 occupies another hydrophobic pocket formed by V84$^{3.32}$, L85$^{3.33}$, and W246$^{6.48}$ (Figure 24d and e) which also tolerates slightly larger substituents like chlorine or bromine. More voluminous substituents like cyclopropyl or SO_2CH_3 would not fit into the same binding pose explaining their detrimental effect on A_{2A}AR affinity.

The 3*H*-imidazo[4,5-*b*]pyridines and the indazole of PSB-21007 are not ideally coplanar but rotated by ≈30° to each other through the rotatable C2-C1′ bond. Their aromatic core structures are stabilized by π-π stacking interactions to F168^{ECL2} (Figure 24b and d). Additionally, the indazole forms hydrophobic contacts to I66$^{2.64}$, S67$^{2.65}$, E169^{ECL2}, M270$^{7.35}$, and I274$^{7.39}$ (Figure 24d and e). The *N*4′-methoxyethyl residue extends towards the extracellular surface of the A_{2A}AR and is stabilized by L167^{ECL2} and L267$^{7.32}$ (Figure 24b, d and e). Its location close to the receptor's surface may contribute to the fact that the *N*4′-extension is not essential but also not disruptive for A_{2A}AR affinity.

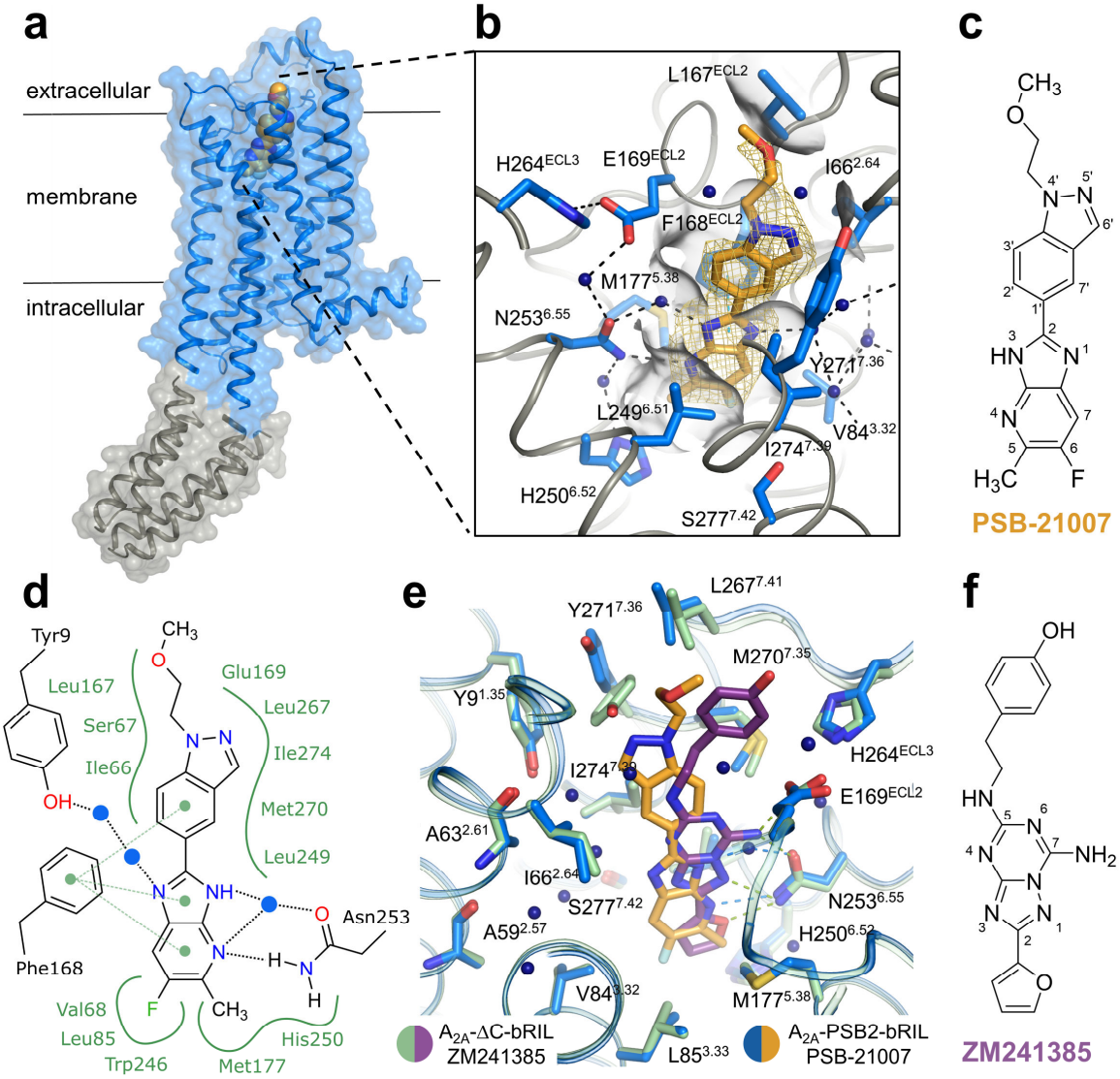

Figure 24. Crystal structure of the A_{2A}AR in complex with PSB-21007.
a) Overview of the structure of A_{2A}-PSB2-bRIL. b) Zoom into the A_{2A}AR ligand binding pocket of PSB-21007. The $2F_o - F_c$ electron density of PSB-21007 is shown in yellow mesh, contoured at 1 σ. Residues A265^{ECL3} to M270$^{7.35}$ were hidden for enhanced visualization

but the respective residues can be observed in panel e. c) Chemical structure of PSB-21007 including atom numbering. d) 2D-interaction diagram of the A_{2A}-PSB2-bRIL-PSB-21003 binding pocket with blue spheres representing water molecules. Black dashed lines represent hydrogen bonds and green dashed lines represent π-π interactions. Solid green lines outline the binding pocket surface. e) Ligand binding pocket comparison between the A_{2A}AR binding pockets of PSB-21007 and ZM241385 (PDB 4EIY). The binding pocket view is rotated by 180° compared to panel b. Residues $C166^{ECL2}$ to $F168^{ECL2}$ were hidden for better binding pocket visualization. f) Chemical structure of ZM241385 including atom numbering. Protein figures were created with PyMOL 2.4.1.

3.3.3 Crystal Structure of MAO-B in Complex with PSB-21007

The crystal structure of MAO-B in complex with PSB-21007 was obtained in collaboration by Prof. Claudia Binda and Andrea Gottinger at the Università di Pavia (Italy). The structure was solved at 1.4 Å resolution now representing the highest resolution MAO-B structure available. MAO-B crystallized as a homodimer consisting of two subunits that are rotated against each other by approximately 180° (Figure 25a). The C-terminal hydrophobic helix of MAO-B is considered to be its anchor to the outer mitochondrial membrane resulting in a perpendicular orientation of MAO-B to the membrane plane (Figure 25a and c).[202]

PSB-21007 could be well resolved inside the binding pocket with its indazole ring occupying the substrate cavity and the 3*H*-imidazo[4,5-*b*]pyridine bound in the entrance cavity. The *N*4′-methoxyethyl extension of PSB-21007 shows direct contact with the covalent co-factor FAD (Figure 25b). Importantly, this moiety partially occupies a sub-pocket formed by Y398, T399, G434, Y435 and FAD thereby displacing one structural water molecule that is typically observed between inhibitor and FAD in co-crystal structures of MAO-B with irreversible[203] or reversible[204] inhibitors. The same sub-pocket harbors another water molecule forming hydrogen bonds to C172, Y188, and Y435 whose displacement could potentially be targeted in lead optimization, especially since we showed that the A_{2A}AR tolerates different *N*4′-substitutions. The removal of the methoxyethyl side-chain of PSB-21007 resulted in a ≈5-fold potency loss at MAO-B consistent with the observed interactions. The indazole ring is additionally stabilized by π-π interactions to F343 (T-shaped) and Y398 (stacked) as well as hydrophobic contacts to Y60, L171, Q206 and Y326 (Figure 25b and c).

On the other hand, Y326 engages in T-shaped π-π interactions to the 3*H*-imidazo[4,5-*b*]pyridine scaffold in the entrance cavity and forms a weak hydrogen bond to its *N*1 atom (H-N distance 2.8 Å) (Figure 25b and c). The position of C172

is favorable for a weak π-sulfur interactions to both aromatic core structures (with distances from 5.0 – 5.9 Å). The *N*1 is connected to E206 and the backbones of P102 and I199 via structural water molecules (Figure 25b and c). A loop spanning from F99 to Y112 closes the entrance cavity in proximity to the mitochondrial membrane and was previously termed “gating switch” as it likely opens up the binding pocket for the substrate.[205] The 5-methyl group occupies a hydrophobic pocket formed by P104, W119, L164, and F168, thereby stabilizing the dynamic gating switch in the closed conformation. The 6-fluorine atom additionally forms hydrophobic contacts to P104 of the gating switch and to I316. Similarly to the A_{2A}AR binding pose, the C7 of the 3*H*-imidazo[4,5-*b*]pyridine ring faces towards a cavity that is occupied by five water molecules and connected to the surface of the gating switch through a solvent channel. This cavity may potentially be targeted by C7-derivatization with polar residues to enhance MAO-B affinity of 3*H*-imidazo[4,5-*b*]pyridines. At the same time, the exploration of C7 substituents may improve the dual activity as it also bears potential for increased A_{2A}AR affinity as described above.

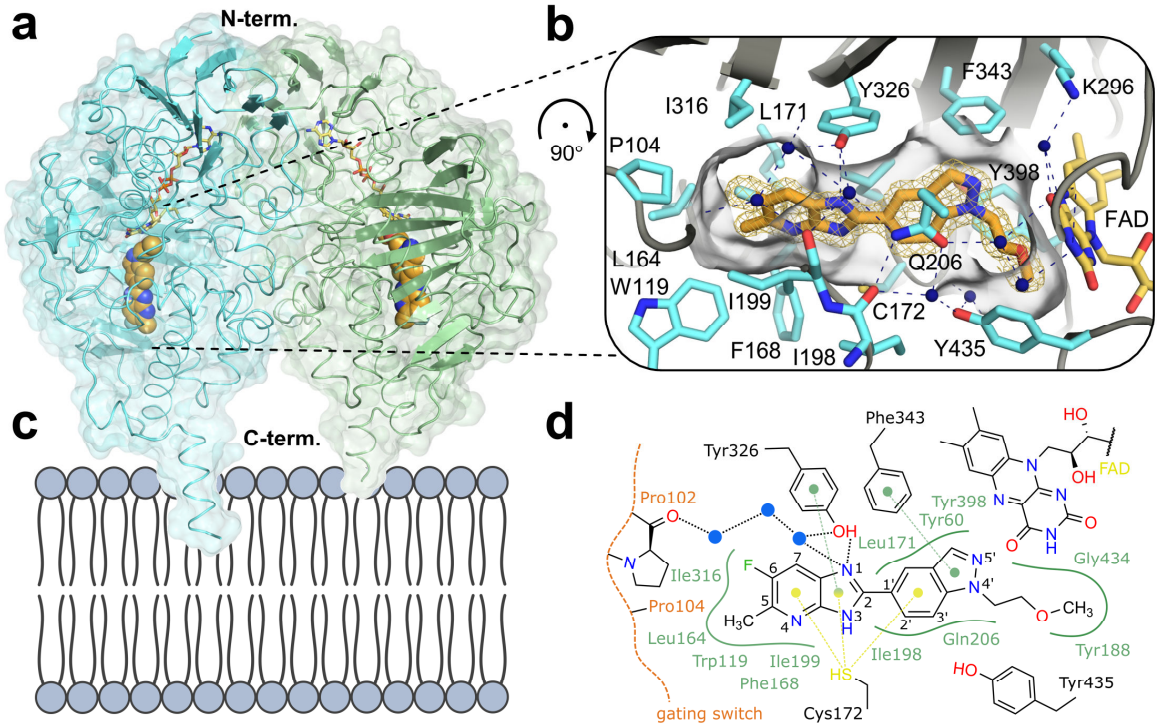

Figure 25. Crystal structure of MAO-B in complex with PSB-21007.
a) Structural overview of the MAO-B homodimer. PSB-21007 is shown in orange spheres and the covalently linked FAD is shown in yellow stick representation. b) MAO-B ligand binding pocket of PSB-21007. The $2F_o - F_c$ electron density is shown in orange mesh, contoured at 1.0 σ. c) Illustration of the MAO-B anchor in the outer mitochondrial membrane

with its C-terminus (C-term.). The C-terminal anchor has not been completely resolved in the crystal structure but is better resolved in chain A (left). d) 2D-interaction diagram of the MAO-B-PSB-21003 binding pocket with blue spheres representing water molecules. Green dashed lines represent π-π interactions, yellow dashed lines represent π-sulfur interactions and black dashed lines depict hydrogen bonds. Solid green lines outline the binding pocket surface. The orange dashed line illustrates the gating switch that covers the binding pocket entrance. Protein figures were created with PyMOL 2.4.1.

3.3.4 Summary

Novel 3*H*-imidazo[4,5-*b*]pyridine derivatives were discovered as dual-targeting A_{2A}AR antagonists and MAO-B inhibitors. Moreover, two new crystal structures were obtained of the derivative with the highest dual potency (PSB-21007) in complex with the A_{2A}AR on the one hand and MAO-B on the other hand. Hence, we were able to elucidate the binding mode of PSB-21007 to both targets. This structural information provides valuable insights into ligand binding pocket interactions and will greatly facilitate the optimization of this promising lead compound in order to increase the inhibitory potency at the MAO-B and the affinity at the A_{2A}AR.

3.4 The Adenosine A_{2A} Receptor Crystal Structure in Complex with the Novel Dual A_{2A}/A_{2B}AR Antagonist PSB-20327

3.4.1 Purification and Crystallization of the A_{2A}-PSB2-bRIL-PSB-20327 Complex

The A_{2A}-PSB2-bRIL-PSB-21007 complex was purified and analyzed according to section 1.4. The size-exclusion chromatogram and the SDS-PAGE showed high purity and monodispersity of the purified protein (Figure 26a and c). The T_M of the complex was determined to be 74.1 °C (Figure 26b). Diffraction quality crystals are shown in Figure 26d with an average length of 50 µm. The crystals grew in the following precipitant condition: 30 % (w/v) PEG400, 5 % (w/v) Tacsimate[206] pH 7.0 (pH 7.4 at 25 °C).

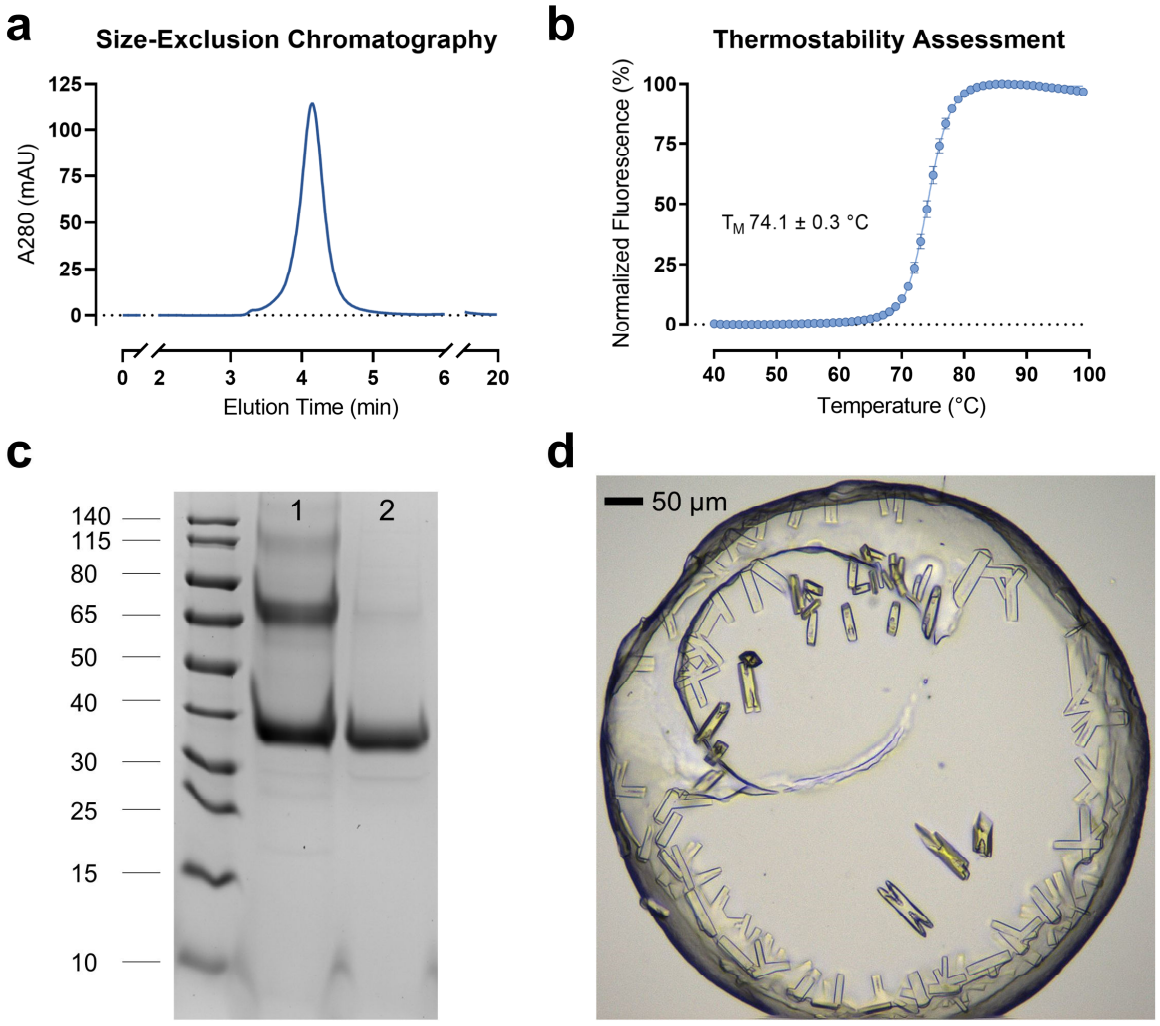

Figure 26. Protein analysis and crystallization of A_{2A}-PSB2-bRIL-PSB-20327.

a) SEC of the final protein sample used for crystallization (diluted 80-fold, injection volume 30 µL), b) thermostability assessment (in the presence of 25 µM PSB-20327) and c) SDS-PAGE of the purified A_{2A}-PSB2-bRIL-PSB-20327 complex. The data points in the melting curve and the T_M in panel b are shown as means ± SEM from three different experiments. The SDS-PAGE was loaded with different samples (1 protein sample before concentration, 2 final protein sample used for crystallization, but diluted ~100-fold with water; equal sample volumes were applied). d) Crystals of A_{2A}-PSB2-bRIL-PSB-20327 in LCP used to obtain high-resolution diffraction data.

3.4.2 The PSB-20327 Binding Pocket

We obtained the structure of A_{2A}-PSB2-bRIL in complex with PSB-20327 at 2.14 Å resolution. Data collection and structure determination were performed by Prof. Norbert Sträter and Dr. Renato Weiße from the University of Leipzig. PSB-20327 is a xanthine-based dual A_{2A}/A_{2B}AR antagonist exhibiting nanomolar affinities for the A_{2A} and A_{2B}ARs (K_i A_{2A}AR 23.1 ± 6.2, K_i A_{2B}AR 16.6 ± 3.6) and display high selectivity towards the A_1 and A_3ARs (K_i > 1000 nM). PSB-20327 was generally well-resolved within the orthosteric binding site of the A_{2A}AR. However, the terminal pyridine moiety is surface-exposed resulting in ambiguous electron density due to high flexibility.

The structure reveals that PSB-20327 is anchored inside the A_{2A}AR ligand binding pocket by its xanthine moiety. The C6-carbonyl and *N*7 form a key hydrogen bond to N253$^{6.55}$ as previously observed for other A_{2A}AR antagonists and as elaborated in section 3.5.3 (Figure 27a). In contrast to PSB-21007, the hydrogen bond to N253$^{6.55}$ in the PSB-20327 binding pocket is not bridged via a structural water molecule (please refer to section 3.3.2.3 for more details) which likely contributes to its high affinity. PSB-20327 represents a theophylline derivative modified at the *N*1, *N*3 and C8 positions. In fact, the xanthine scaffold of both structures aligns in their crystal structures, and the surrounding water network that is connected to the C2-carbonyl group is virtually identical (Figure 27c). Both xanthines are stabilized by π-π stacking interactions to F168^{ECL2} and show hydrophobic contacts to L249$^{6.51}$. The *N*1-ethyl group of PSB-20327 forms additional hydrophobic contacts to V84$^{3.32}$ and L85$^{3.33}$ whereas the *N*3-cyclopropyl group extends towards helix II and VII with direct contact to I66$^{2.64}$ and I274$^{7.39}$. This contact separates five structural water molecules from the bulk phase (Figure 27c,

bottom, water molecules on the left-hand side). The *N*9 of PSB-20327 is surface-exposed, but interacting structural water molecules could not be resolved.

The extracellular salt bridge between E169^{ECL2} and H264^{ECL3} is disrupted by the C5-phenyl moiety and the sulfonamide of PSB-20327, while it is intact in the Theophylline structure (Figure 27c). The formation of the salt bridge may depend on both the crystallization method and the precipitation conditions, but also on the respective A_{2A}AR antagonist as elaborated in Claff et al.[107] and in the next section. The phenyl moiety of PSB-20327 is stabilized by π-sulfur interactions to M270$^{7.35}$ (distance 4.2 Å) and by hydrophobic contacts to E169^{ECL2} and I252$^{6.54}$. Additionally, one of the sulfonamide oxygen atoms forms a direct hydrogen bond to T256^{ECL3} and a water-mediated hydrogen bond to the backbone of A265^{ECL3}. The piperazine ring forms direct contacts with L267$^{7.32}$ and M270$^{7.35}$ whereas the pyridine moiety extends towards the extracellular surface without obvious specific protein-ligand interactions.

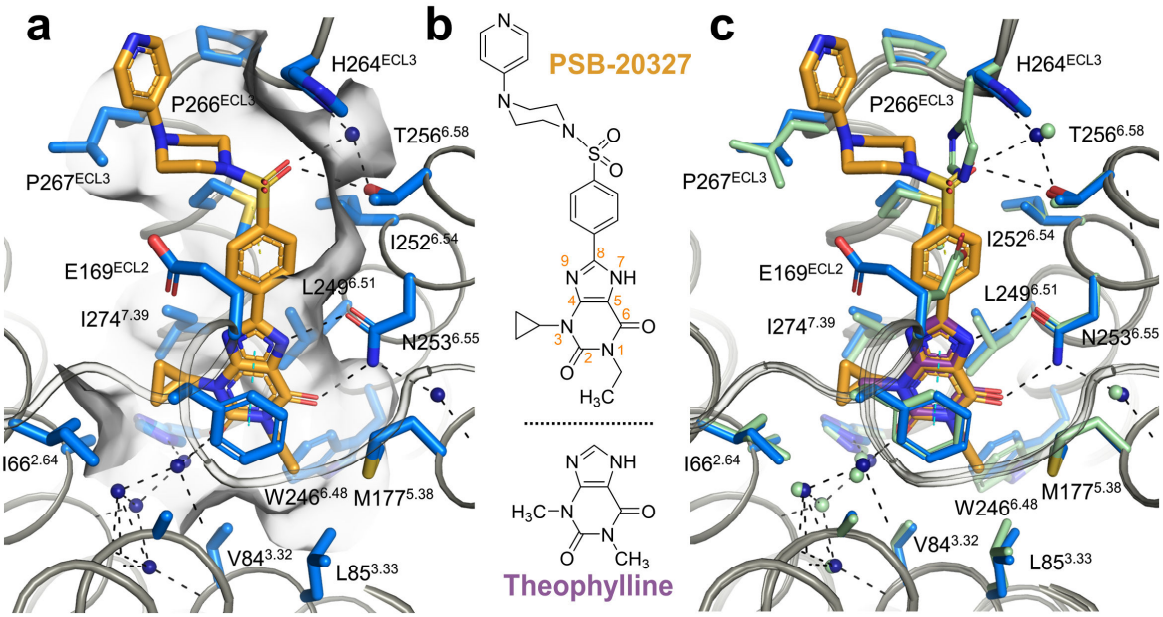

Figure 27. The A_{2A}AR binding pocket of PSB-20327.
a) PSB-20327 binding pose at the A_{2A}AR. The receptor surface is shown in gray. b) Chemical structures and xanthine numbering of PSB-20327 and Theophylline. c) Structural comparison of the binding modes of PSB-20327 and Theophylline (PDB 5MZJ, crystallized with the A_{2A}-StaR2-bRIL construct[135]). Protein figures were created with PyMOL 2.4.1.

3.4.3 The formation and pH dependence of the extracellular salt bridge between E169^{ECL2} and H264^{ECL3}

We have previously compiled an overview of all published A_{2A}AR crystal structures including their E168^{ECL2}-H264^{ECL3} salt bridge conformation (open/closed) and the pH during crystallization (please refer to Table 1 and Table 2 for an overview). In fact, the salt bridge was shown to be in the open conformation for the A_{2A}AR structure obtained with xanthine PSB-36,[135] the former clinical candidate Tozadenant,[134] and the triazine derivatives “4g” and “4e”.[136] However, the majority of A_{2A}AR crystal structures have been obtained with a closed, intact salt bridge.[107] Both ZM241385 and the triazine “4e” are the only A_{2A}AR antagonists that have been crystallized in both open and closed conformation regarding the E169^{ECL2}-H264^{ECL3} salt bridge, depending on the applied crystallization conditions.[107,134] Thus, an acidic pH value (5.0 – 5.2) during A_{2A}AR crystallization favored the closed conformation[120,134] of ZM241385 and “4e” whereas slightly alkaline pH values (8.0 – 8.75) favored the open conformation.[117,136] Additionally, Imaradenant (a derivative of “4e”) also crystallized in the closed conformation at pH 5.3 – 5.4.[207] However, an alkaline pH does not force the open conformation as we showed for the first time with our new A_{2A}-PSB2-bRIL-PSB-21007 structure that was obtained at pH 8.2 with intact E169^{ECL2}-H264^{ECL3} salt bridge (please refer to section 3.3.2).

Here, we solved the A_{2A}-PSB2-bRIL-PSB-20327 structure at pH 7.4, representing the first antagonist-bound A_{2A}AR crystal structure whose crystals grew at physiological pH (pH 7.4). While we were able to co-crystallize A_{2A}-PSB1-bRIL with PSB-20327 at pH 5.0 (Figure 28) and tested multiple crystals for their X-ray diffraction, no high-resolution data could be acquired (diffraction up to 7.5 Å). Only crystals obtained at physiological pH enabled us to solve the crystal structure of the A_{2A}-PSB2-bRIL-PSB-20327 complex (Figure 26d). One possible explanation could be that the (partial) formation of the E169^{ECL2}-H264^{ECL3} salt bridge at acidic pH may allow multiple conformations of PSB-20327 and hence only produced poorly diffracting crystals.

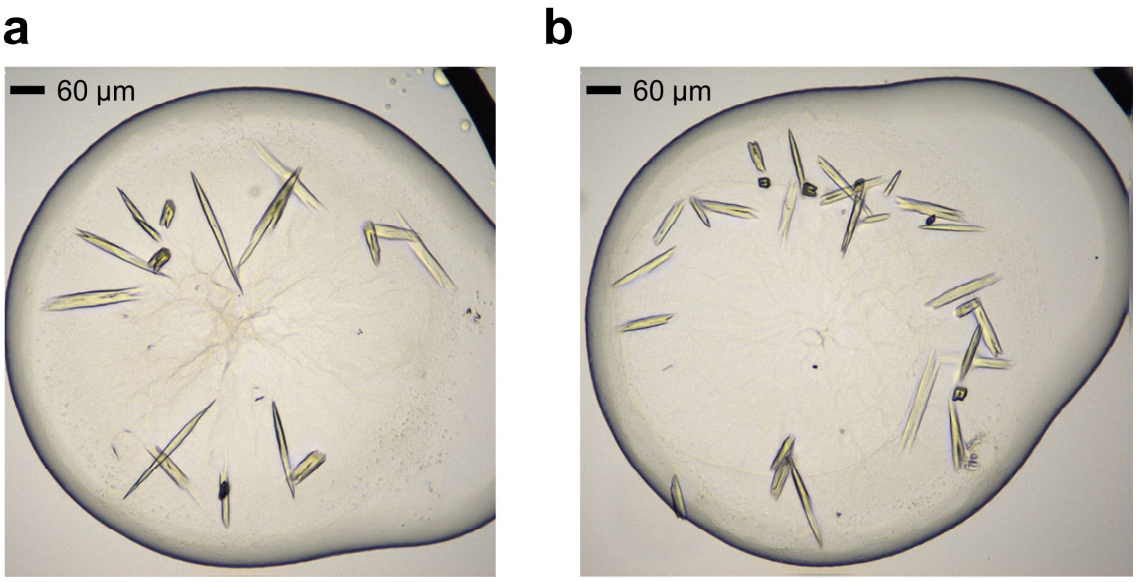

Figure 28. Crystal images of A_{2A}-PSB1-bRIL-PSB-20327 diffracting up to 7.5 Å.
a) Crystallized in 29 % (w/v) PEG400, 150 mM ammonium citrate, 100 mM Na-citrate pH 5.0 and 1.6 % (w/v) 2,5-hexandiol. b) Crystallized in 30 % (w/v) PEG400, 170 mM ammonium citrate, 100 mM sodium citrate pH 5.0 and 1.6 % (w/v) 2,5-hexandiol.

3.4.4 Summary

Here, we obtained the crystal structure of the A_{2A}AR in complex with PSB-20327, a new xanthine-based dual A_{2A}/A_{2B}AR antagonist. This structure represents the first antagonist-bound A_{2A}AR crystal structure whose crystals were obtained at physiological pH values of 7.4. The structure provides valuable insights into the binding mode of this xanthine scaffold at the A_{2A}AR, and into the formation of the extracellular salt bridge between $E169^{ECL2}$ and $H264^{ECL3}$. The new A_{2A}AR structure does not provide additional information on the A_{2B}AR binding mode which still remains to be elucidated. The new structural information can be used to optimize the A_{2A}AR affinity of this xanthine scaffold, that had originally been developed for A_{2B}AR inhibition.

3.5 The Adenosine A_{2A} Receptor Crystal Structure in Complex with the Clinical Candidate Etrumadenant

3.5.1 Pharmacological Characterization of Etrumadenant

Etrumadenant was developed as a novel selective and peripherally restricted dual A_{2A}/A_{2B}AR antagonist that entered the clinical development for the treatment of peripheral cancers.[208–210] Etrumadenant comprises a novel and previously uncharacterized tetracyclic azolopyrimidine scaffold (Figure 29). While the original patent of Arcus Bioscience only reported affinity ranges and no specific values for Etrumadenant,[209] a recent poster showed potencies for all human adenosine receptor subtypes without providing experimental details and statistical variations.[211] The authors reported the following potencies: A_1AR 60 nM, A_{2A}AR 1.4 nM, A_{2B}AR 2.0 nM, and A_3AR 411 nM. Thus, we determined the affinities on the human adenosine receptors and on the crystallization constructs by radioligand binding assays on CHO cell membranes expressing the respective adenosine receptor subtype (Table 4). Our data indicates that Etrumadenant is only 6-fold selective over the A_1AR which stands in contrast to the previously reported 43-fold selectivity in regards to potency. Hence, Etrumadenant does not appear to be a selective dual A_{2A}/A_{2B}AR antagonist since it also exhibits substantial A_1AR affinity.

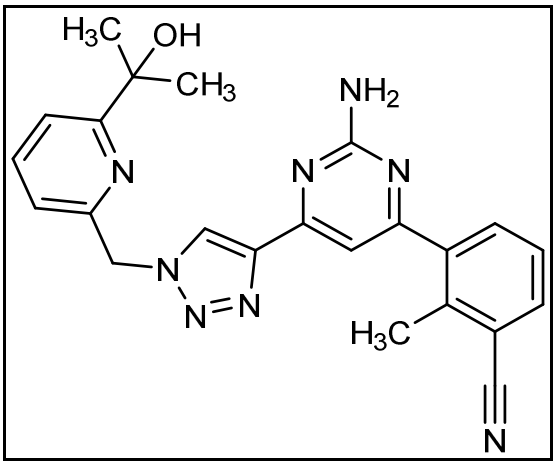

Figure 29. Chemical structure of Etrumadenant.

Table 4. Binding affinities of Etrumadenant to the human adenosine receptors and to the crystallization construct A_{2A}-PSB2-bRIL.[a)]

Target	vs. radioligand	K_i ± SEM (nM)
A_1AR	[^{3}H]CCPA	**7.75** ± 1.28
A_1AR	[^{3}H]DPCPX	**5.74** ± 1.34
A_{2A}AR	[^{3}H]MSX-2	**0.96** ± 0.33
A_{2B}AR	[^{3}H]PSB-603	**3.24** ± 0.50
A_3AR	[^{3}H]PSB-11	**354** ± 120
A_{2A}-PSB2-bRIL	[^{3}H]MSX-2	**0.78**[b)]

[a)] K_i values were determined as means from three independent experiments ± SEM performed on CHO cell membranes expressing the respective human wt adenosine receptor or on Sf9 insect cell membranes for crystallization construct A_{2A}-PSB2-bRIL. [b)] preliminary results (n=1). Radioligand binding experiments were performed by Christin Vielmuth.

3.5.2 Purification and Crystallization of the A_{2A}-PSB2-bRIL-Etrumadenant Complex

The A_{2A}-PSB2-bRIL-Etrumadenant complex was purified and analyzed according to section 1.4. The size-exclusion chromatogram and the SDS-PAGE showed high purity and monodispersity of the purified protein (Figure 30a and c). The T_M of the complex was determined to be 74.1 °C (Figure 30b). Diffraction quality crystals are shown in Figure 30d with an average length of 60 µm. The crystals grew in the following precipitant condition: 30 % (w/v) PEG400, 7 % (w/v) Tacsimate[206] pH 7.0, 100 mM 4-(2-hydroxyethyl)piperazine-1-ethanesulfonic acid (HEPES) pH 7.4, 1.8 % (w/v) 2,5-hexandiol.

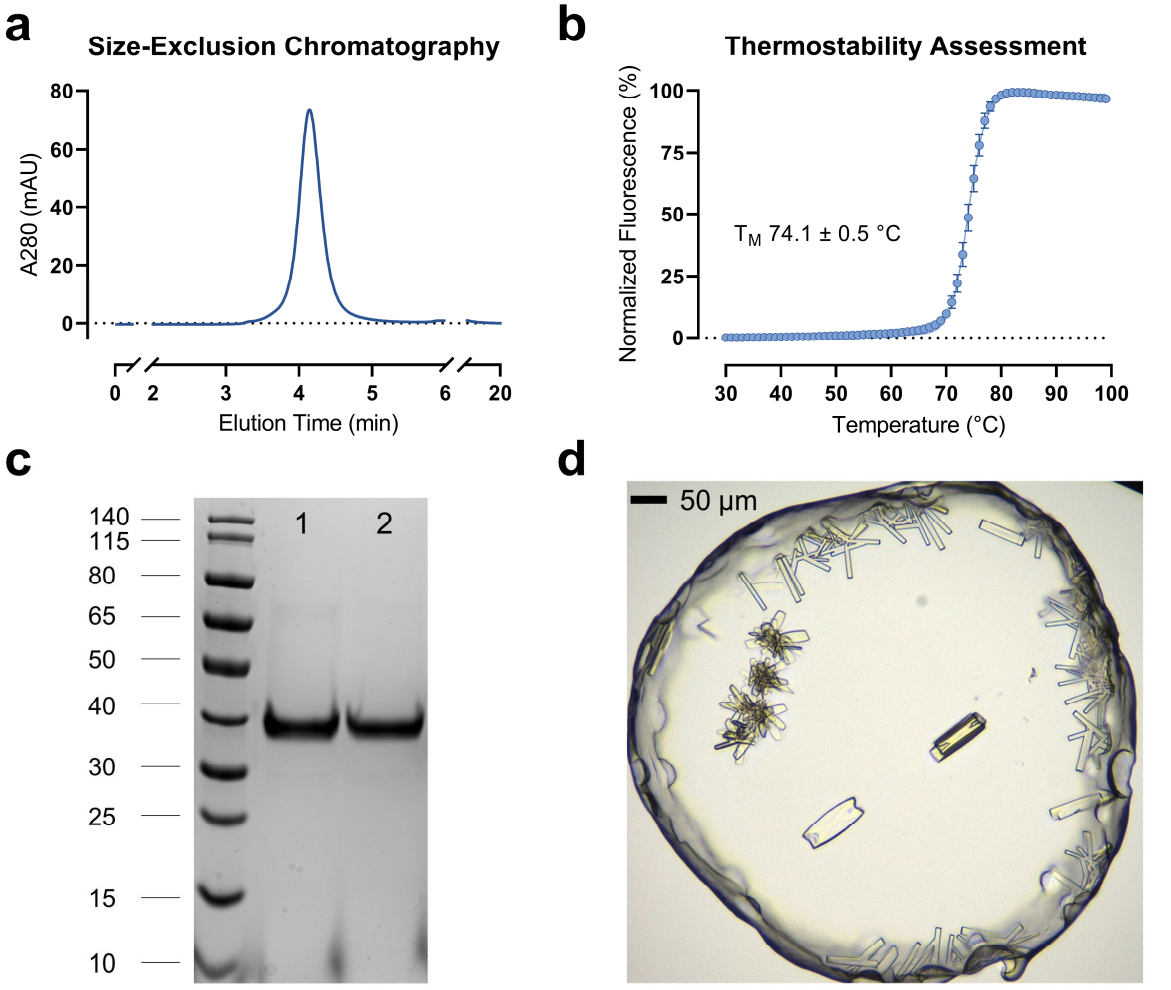

Figure 30. Protein analysis and crystallization of A_{2A}-PSB2-bRIL-Etrumadenant complexes.
a) SEC of the final protein sample used for crystallization (diluted 80-fold, injection volume 30 µL), b) thermostability assessment (in the presence of 25 µM Etrumadenant) and c) SDS-PAGE of the purified A_{2A}-PSB2-bRIL-Etrumadenant complex. The data points in the melting curve and the T_M in panel b are shown as means ± SEM from three different experiments. The SDS-PAGE was loaded with two different samples (1 protein sample before concentration, 2 final protein sample used for crystallization, but ~50-fold diluted with water; equal sample volumes were applied). d) Crystals of A_{2A}-PSB2-bRIL-Etrumadenant in LCP used to obtain high-resolution diffraction data.

3.5.3 The Etrumadenant Binding Pocket

We obtained the first crystal structure of the A_{2A}AR in complex with Etrumadenant at 2.1 Å resolution. Data collection and structure determination were performed by Prof. Norbert Sträter and Dr. Renato Weiße from the University of Leipzig. The novel tetracyclic scaffold of Etrumadenant shows unique interactions to the A_{2A}AR.

Importantly, its nitril group forms a direct hydrogen bond to T88$^{3.36}$ (N-O distance 2.8 Å) representing a novel interaction that has never been observed in A_{2A}AR co-crystal structures with other antagonists (Figure 31). T88$^{3.36}$ goes through significant conformational changes during receptor activation and was shown to be directly involved in agonist binding.[113] Moreover, the mutation of T88$^{3.36}$ to alanine shifts the receptor equilibrium towards the inactive state.[212] Thus, the interaction of Etrumadenant with T88$^{3.36}$ by direct hydrogen bonding represents a novel interaction resulting in the stabilization of the A_{2A}AR in its inactive state. Notably, the A_{2A}-StaR2 construct that is extensively used to solve inactive state A_{2A}AR crystal structures comprises a T88$^{3.36}$A mutation,[117] that would possibly affect the affinity of Etrumadenant.

The phenyl ring of Etrumadenant is stabilized by π-π interactions to H250$^{6.52}$ (T-shaped) and W246$^{6.48}$ (stacked) (Figure 31b). Its 2-methyl group comes in close contact to V84$^{3.32}$, L85$^{3.33}$ and F168^{ECL2} but is also exposed to a water network connecting the ligand to helices II and III (Figure 31b). The aminopyrimidine ring of Etrumadenant forms key anchor interactions by hydrogen bonding to N253$^{6.55}$ and E169^{ECL2} (Figure 31), similar to related moieties of other A_{2A}AR antagonists (refer to blue circles in Figure 32b). The aminopyrimidine ring is additionally stabilized by π-π stacking interactions to F168^{ECL2} (Figure 31a).

The triazole ring of Etrumadenant connects the aminopyrimidine to the pyridine ring and forms water-mediated hydrogen bonding to H278$^{7.43}$ and to the backbone A59$^{2.57}$, I80$^{3.28}$ and A81$^{3.29}$ (Figure 31b). The pyridine ring is located close to the entrance of the orthosteric ligand binding pocket at the extracellular ends of helices I and II with direct contact to Y9$^{1.35}$ and S67$^{2.65}$. The sidechain of Y9$^{1.35}$ has shown to be highly flexible in other A_{2A}AR co-crystal structures[117,213] and adapts the hydrophobic pocket to the size of the ligand (as depicted for a selection of ligands in Figure 32). The relatively large Etrumadenant requires a great sidechain movement of Y9$^{1.35}$. The new conformational space of Y9$^{1.35}$ is occupied by an oleic acid in other A_{2A}AR crystal structures in which the Y9$^{1.35}$ is located closer to the orthosteric binding pocket with involvement in hydrogen bonding to the structural water network (e.g. PDB 4EIY).[120] The hydrophilic head group of the oleate is displaced by the rotation of Y9$^{1.35}$ which is similarly observed in the structures of Imaradenant[207] and Vipadenant.[134] The tertiary alcohol that is attached to the pyridine shows three ambiguous rotamers. We modeled the rotamer conformation

that puts the alcohol in the closest proximity to a nearby water molecule thereby forming an intramolecular water-mediated hydrogen bond to pyrimidine nitrogen *N*3 (Figure 31).

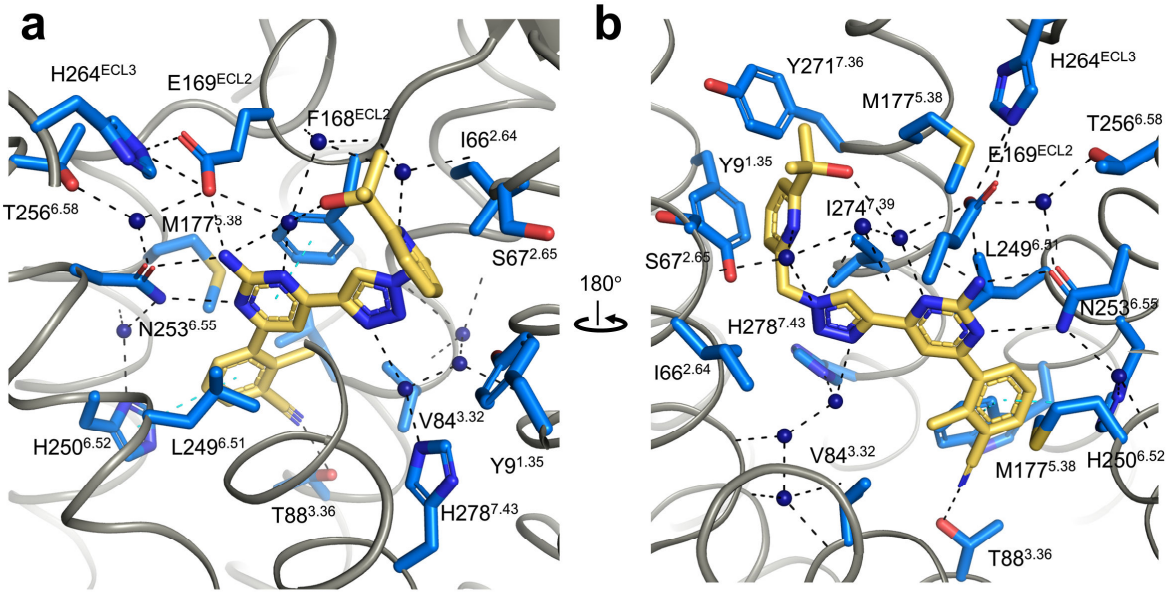

Figure 31. The A_{2A}AR binding pocket of Etrumadenant.
a) Binding pocket of Etrumadenant with residues A265 to M270 clipped for enhanced visualization. b) Binding pocket of Etrumadenant rotated by 180° compared to panel a with parts of the ECL2 and residues L167 and F168 clipped. Black dashed lines represent hydrogen bonds whereas cyan-colored dashed lines show π-π interactions. Protein figures were created with PyMOL 2.4.1.

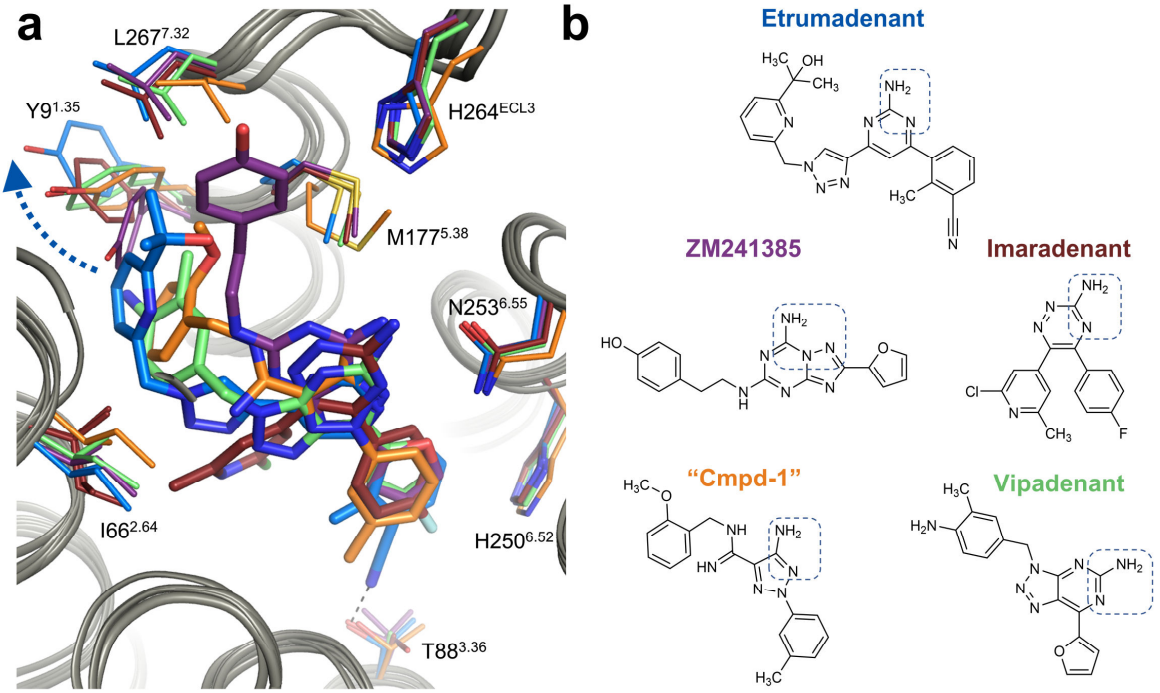

Figure 32. Comparison of the Etrumadenant binding pocket with that of selected A_{2A}AR antagonists reported in previous publications.[120,134,207,213]

a) The binding pose of Etrumadenant (blue) is compared to the binding pockets of ZM241385 (purple, PDB 4EIY), “Cmpd-1” (orange, PDB 5UIG), Vipadenant (green, PDB 5OLH) and Imaradenant (red, PDB 6GT3). The blue-colored dashed arrow represents the conformational movement of $Y271^{7.36}$ in the A_{2A}-PSB2-bRIL-Etrumadenant structure. b) Chemical structures of the depicted antagonists. The dotted blue circles highlight structural similar moieties that form the key hydrogen bonding anchor to $N253^{6.55}$. The protein figure was created with PyMOL 2.4.1.

3.5.4 Summary

The A_{2A}AR crystal structure in complex with Etrumadenant was obtained, a drug that is currently in clinical trials for the immunotherapy of cancer. Etrumadenant bears a novel scaffold and adopts a binding mode that is significantly different from that of other A_{2A}AR antagonists. For example, the binding mode of Etrumadenant revealed a novel hydrogen bonding interaction to $T88^{3.36}$, a residue that has previously been mutated in A_{2A}AR crystallization constructs.[117] Moreover, we observed that Etrumadenant is not selective for the A_{2A} and A_{2B}ARs but also exhibits significant A_1AR affinity, which could, in fact, be counteracting the desired biological effects.

3.6 The Adenosine A_{2A} Receptor Crystal Structure in Complex with the Novel Aminopyrazole Antagonist PSB-21417

3.6.1 Purification and Crystallization of the A_{2A}-PSB1-bRIL-PSB-21417 Complex

The A_{2A}-PSB1-bRIL-PSB-21417 complex was purified and analyzed according to section 1.4. The size-exclusion chromatogram and the SDS-PAGE showed high purity and monodispersity of the purified protein (Figure 33a and c). However, the SDS-PAGE shows smearing as a result of protein glycosylation since the single mutant A_{2A}-PSB1-bRIL was used for the crystallization (please refer to section 3.3.2.1 for more details). Additionally, a minor impurity at around 30 kDa can be observed in Figure 33c. The T_M of the complex was determined to be 72.2 °C (Figure 33b). Diffraction quality crystals are shown in Figure 33d with an average length of 40 µm. The crystals grew in the following precipitant condition: 29 % (w/v) PEG400, 80 mM sodium thiocyanate, 100 mM sodium citrate pH 5.2, 2 % (w/v) 2,5-hexandiol.

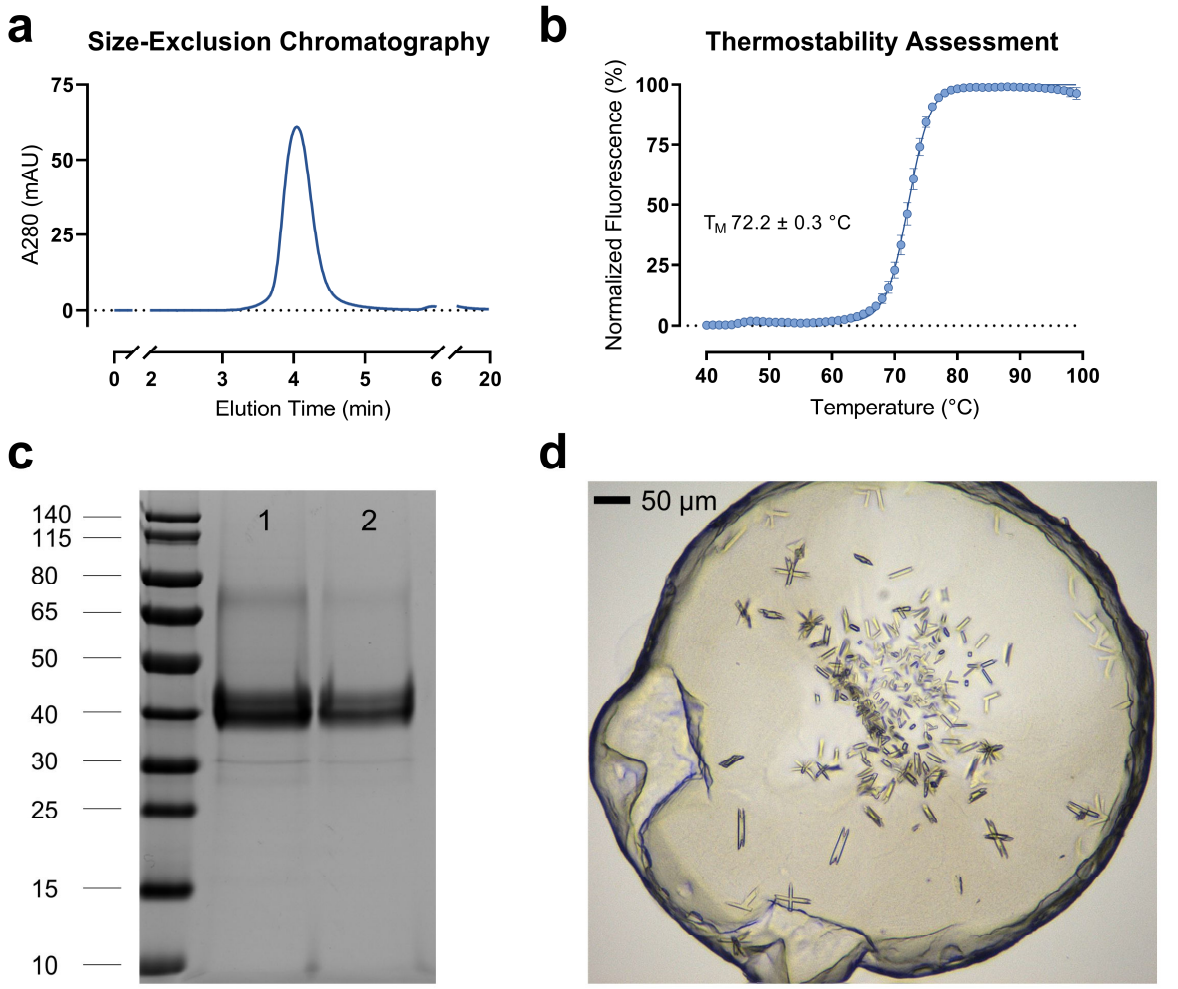

Figure 33. Protein analysis and crystallization of A_{2A}-PSB1-bRIL-PSB-21417.
a) SEC of the final protein sample used for crystallization (diluted 80-fold, injection volume 30 µL), b) thermostability assessment (in the presence of 25 µM PSB-21417) and c) SDS-PAGE of the purified A_{2A}-PSB1-bRIL-PSB-21417 complex. The data points in the melting curve and the T_M in panel b are shown as means ± SEM from three different experiments. The SDS-PAGE was loaded with two different samples (1 protein sample before concentration, 2 final protein sample used for crystallization, but diluted ~50-fold with water; equal sample volumes were applied). d) Crystals of A_{2A}-PSB2-bRIL-PSB-21417 in LCP used to obtain high-resolution diffraction data.

3.6.2 The PSB-21417 Binding Pocket

We obtained the crystal structure of the A_{2A}AR in complex with PSB-21417 at 2.20 Å resolution. Data collection and structure determination were performed by Prof. Norbert Sträter and Dr. Renato Weiße from the University of Leipzig.

PSB-21417 is an A_{2A}AR antagonist with nanomolar affinity (K_i 5.07 nM) that was developed in our group[214] and comprises a 3-aminopyrazole scaffold (Figure 34c). PSB-21417 shows similarity to the previously discovered A_{2A}AR

antagonist “Cmpd-1”, a dual-target drug that additionally blocks the *N*-methyl-D-aspartate receptor subtype 2B (NR2B), but was independently developed.[213] The dual blockade of the A_{2A}AR and NR2B has shown beneficial effects for the treatment of PD.[215] “Cmpd-1” was discovered comprising a novel 4-amino-1,2,3-triazole scaffold that is connected to a methylphenyl in position 2 and to methoxybenzyl in position 5 via an amidine function (refer to Figure 34e). In our compound, the amidine is substituted by an amide moiety that is attached to a 2-chloro-6-fluoro benzyl residue and the methylphenyl is replaced with the larger indazole moiety. Our 3-aminopyrazole core structure corresponds to the *N*1-deaza analog of the “Cmpd-1” scaffold. The pyrazole creates an additional optimization option by derivatization in the C5-position which is not accessible in aminotriazoles. The affinity of PSB-21417 to the A_{2A}AR is two-fold higher than that of “Cmpd-1” (Figure 34d). Moreover, PSB-21417 shows superior A_1AR selectivity (65-fold vs. 14-fold) but has not yet been tested on NR2B.

Here, we solved the A_{2A}AR crystal structure in complex with PSB-21417 at 2.20 Å resolution. A co-crystal structure of “Cmpd-1” with the A_{2A}AR had been previously solved, but only reached 3.50 Å resolution, which had made it impossible to resolve structural water molecules.[213] However, we used the “Cmpd-1” co-crystal structure for comparison with our newly determined structure. While PSB-21417 was generally well-resolved inside the orthosteric ligand binding pocket, the electron density of the halogenated phenyl ring was slightly weaker e.g., suggesting two conformations (with interchanged F,Cl-position). We have modeled the conformation where the 2-chloro substituent faces towards helices II and III as it showed stronger electron density for the chlorine atom and is therefore thought to be predominant.

The 3-aminopyrazole moiety of PSB-21417 forms key hydrogen bonds to $N253^{6.55}$ and to $E169^{ECL2}$ similarly as observed for “Cmpd-1” (Figure 34b). We were able to show that the network extends to $T256^{6.58}$ via one structural water molecule (Figure 34a and b). Moreover, the 3-amino group forms an intramolecular hydrogen bond to the carbonyl of the amide which itself is involved in a water network that connects PSB-21417 to the backbones of $I66^{2.64}$, $F168^{ECL2}$, and $E169^{ECL2}$ (Figure 34a). The pyrazole (and the triazole of “Cmpd-1”) is further stabilized by hydrophobic contacts to $L249^{6.51}$ and by typical π-π stacking interactions although it should be noted that $F168^{ECL2}$ showed a large structural

heterogeneity in the “Cmpd-1” structure.[213] The amide nitrogen is connected to an isolated water network that extends to the sidechain of H278$^{7.43}$ and the backbones of A59$^{2.57}$, I80$^{3.28}$, I81$^{3.29}$, and V84$^{3.32}$ via five structural water molecules. Displacing water molecules from the binding pocket by ligand modification represents an attractive goal in structure-based drug design.[197] Importantly, the amide in PSB-21417 adopts a different conformation than the analogous carboximidamide in “Cmpd-1” which is rotated by approximately 180°. The C5 of PSB-21417’s pyrazole core directly faces towards the water system (Figure 34a and b). As mentioned above, PSB-21417 derivatization in the C5 position is synthetically accessible and may represent optimization potential to further enhance A_{2A}AR affinity and likely selectivity.

The halogenated benzyl moiety occupies a hydrophobic pocket formed by Y9$^{1.35}$, A63$^{2.61}$, I66$^{2.64}$, S67$^{2.65}$, L267$^{7.32}$, M270$^{7.35}$, Y271$^{7.39}$, and I274$^{7.39}$. Although the same amino acids form the pocket to harbor the methoxyphenyl of “Cmpd-1”, both phenyl rings do not align in the same conformation and the pocket architecture is changed in the PSB-21417 structure with many different sidechain rotamers (e.g., please refer to S67$^{2.65}$, M270$^{7.35}$, and Y271$^{7.39}$ of Figure 34b).

The indazole moiety is stabilized by π-π interactions to W246$^{6.48}$ and forms a direct hydrogen bond to T88$^{3.36}$ (N-O distance 3.1 Å) as similarly observed in our new A_{2A}-PSB2-bRIL-Etrumadenant structure. As mentioned in section Figure 31, this is the first time that hydrogen bonding between an A_{2A}AR antagonist and T88$^{3.36}$ could be shown. The indazole core is further stabilized by hydrophobic contacts to V84$^{3.32}$, L85$^{3.33}$, M177$^{5.38}$, and L249$^{6.51}$ while its nitrogen atoms are involved in a water network connecting PSB-21417 to N181$^{5.42}$ and H250$^{6.52}$. This represents another interaction that so far has not been observed for A_{2A}AR antagonists.

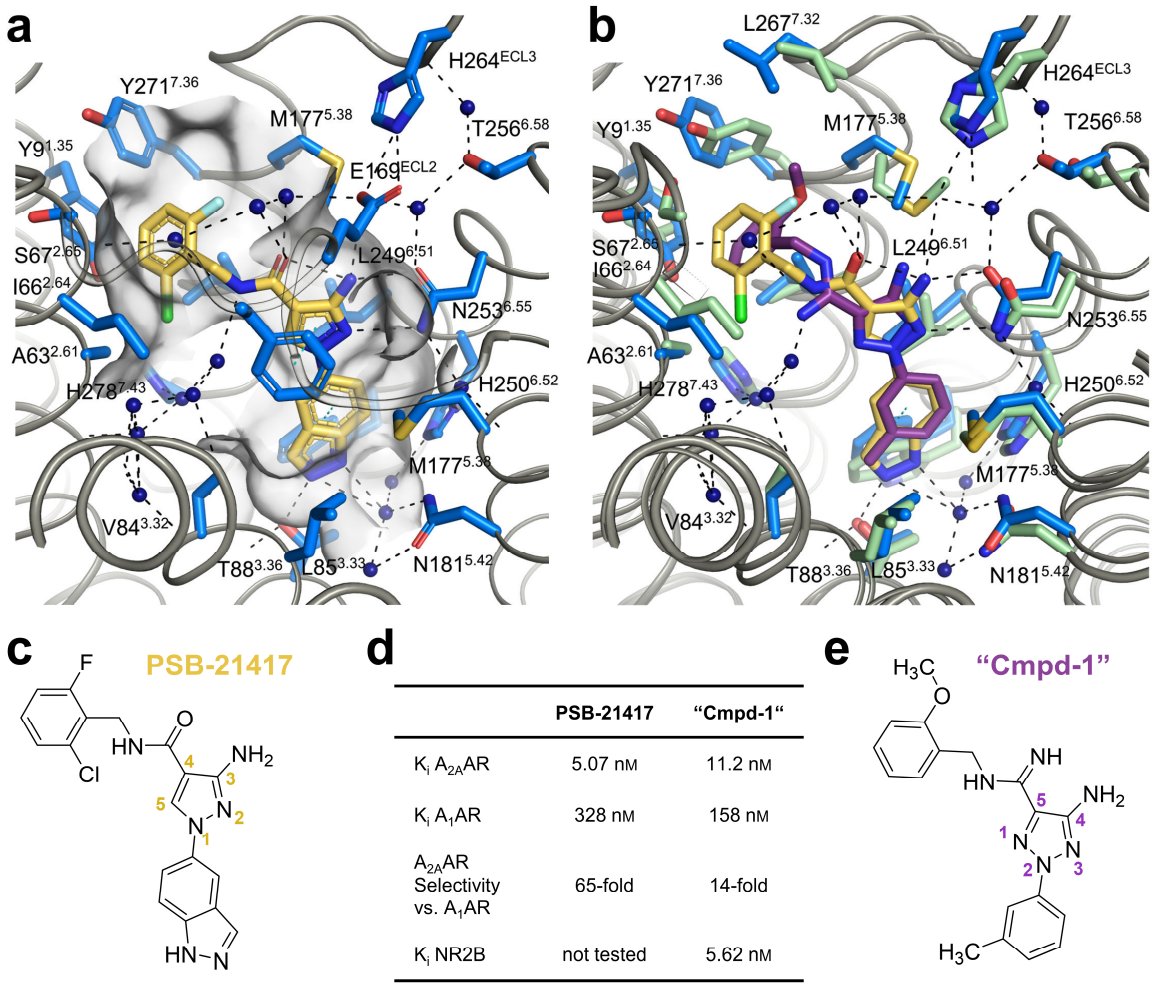

	PSB-21417	"Cmpd-1"
K_i $A_{2A}AR$	5.07 nM	11.2 nM
K_i A_1AR	328 nM	158 nM
$A_{2A}AR$ Selectivity vs. A_1AR	65-fold	14-fold
K_i NR2B	not tested	5.62 nM

Figure 34. The ligand binding pocket of PSB-21417.
a) PSB-21417 binding pose in the orthosteric binding pocket of the $A_{2A}AR$. b) Comparison of the PSB-21417 binding pose to the structurally-related aminotriazole derivative "Cmpd-1"[213] (PDB 5UIG). c) Chemical structure of PSB-21417. d) Binding affinity (K_i) of PSB-21417 and "Cmpd-1" at adenosine receptors or NR2B determined by radioligand binding studies. Radioligand binding experiments for PSB-21417 were performed by Christin Vielmuth. The "Cmpd-1" data was taken from Sun et al.[213] e) Chemical structure of "Cmpd-1". Protein figures were created with PyMOL 2.4.1.

3.6.3 Summary

Here, we elucidated the binding mode of PSB-21417 at the $A_{2A}AR$. PSB-21417 represents a novel aminopyrazole derivative with high affinity towards the $A_{2A}AR$, and was discovered independently from the previously published "Cmpd-1". Both compounds exhibit a binding mode that shows similarities but also significant differences. Importantly, PSB-21417 exhibits a direct hydrogen bond to $T88^{3.36}$ that was simultaneously observed for the first time in our Etrumadenant co-crystal structure.

3.7 Crystallization Attempts of the Adenosine A_{2A} Receptor in Complex with the Approved Drug Istradefylline and Related 8-Ethinylxanthine Derivatives

3.7.1 Purification and Crystallization of the A_{2A}-PSB2-bRIL-Istradefylline Complex

The A_{2A}-PSB2-bRIL-Istradefylline complex was purified and analyzed according to section 1.4. The size-exclusion chromatogram and the SDS-PAGE showed high purity and monodispersity of the purified protein (Figure 36a and c).

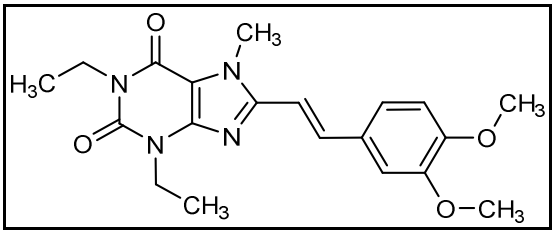

Figure 35. Chemical structure of the approved drug Istradefylline.

The T_M of the complex was determined to be 73.3 °C (Figure 36b). Despite the excellent protein characteristics, only small crystal hits could be obtained (Figure 36d). Importantly, crystal hits were obtained in almost every precipitant condition tested which is unlikely for protein crystals but suggests the crystallization of the compounds itself. Istradefylline shows relatively poor solubility and is photosensitive.[216] The obtained mini-crystals were not further analyzed for their X-ray diffraction.

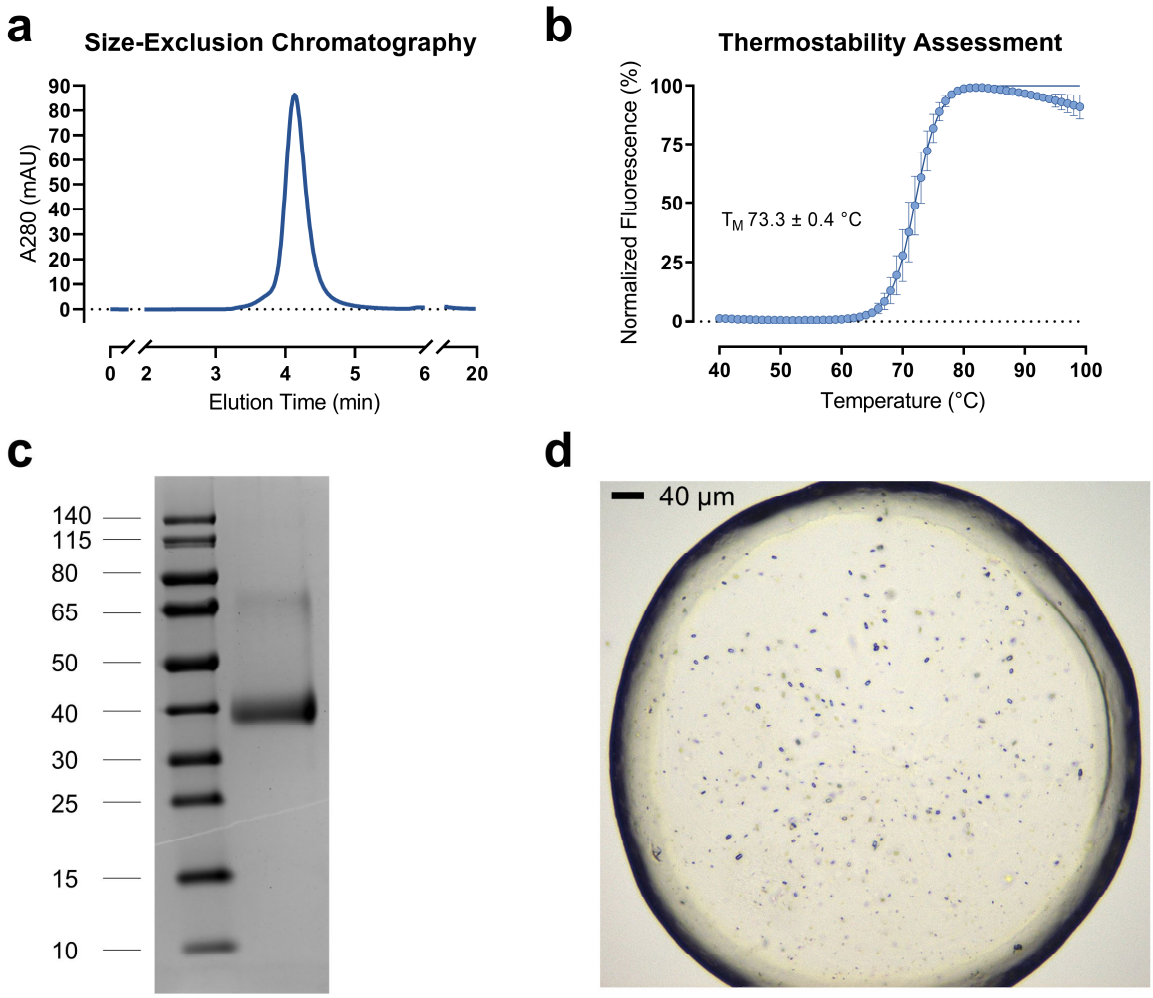

Figure 36. Protein analysis and crystallization of A_{2A}-PSB2-bRIL-Istradefyllin.
a) SEC of the final protein sample used for crystallization (diluted 80-fold, injection volume 30 µL), b) thermostability assessment (in the presence of 15 µM Istradefylline) and c) SDS-PAGE of the purified A_{2A}-PSB2-bRIL-Istradefylline complex. The data points in the melting curve and the T_M in panel b are shown as means ± SEM from four different experiments. The SDS-PAGE was loaded with 10 µL of the protein sample before concentration. d) Crystals of A_{2A}-PSB2-bRIL-Istradefylline or possibly just of Istradefylline in LCP.

3.7.2 Purification and Crystallization of the A_{2A}-PSB1-bRIL-PSB-20002 Complex (first attempt)

The A_{2A}-PSB1-bRIL-PSB-20002 complex was purified and analyzed according to section 1.4. The size-exclusion chromatogram and SDS-PAGE showed high purity and monodispersity of the purified protein (Figure 38a and c).

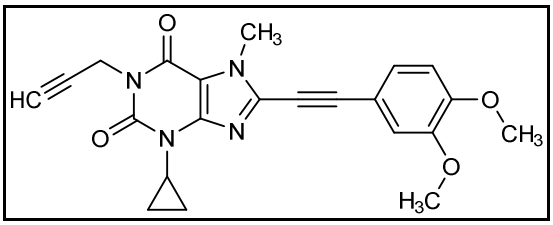

Figure 37. Chemical structure of the xanthine derivative PSB-20002

The T_M of the complex was determined to be 73.1 °C (Figure 38b). Crystal hits are shown in Figure 38d with an average size of 30 µm that grew in the following precipitant condition: 19 % (w/v) PEG400, 100 mM sodium thiocyanate, 100 mM sodium citrate pH 5.2, 2 % (w/v) 2,5-hexandiol. At that time, we did not send the crystals for data collection. However, the crystallization experiment was repeated in an attempt to yield larger and more homogenous crystals.

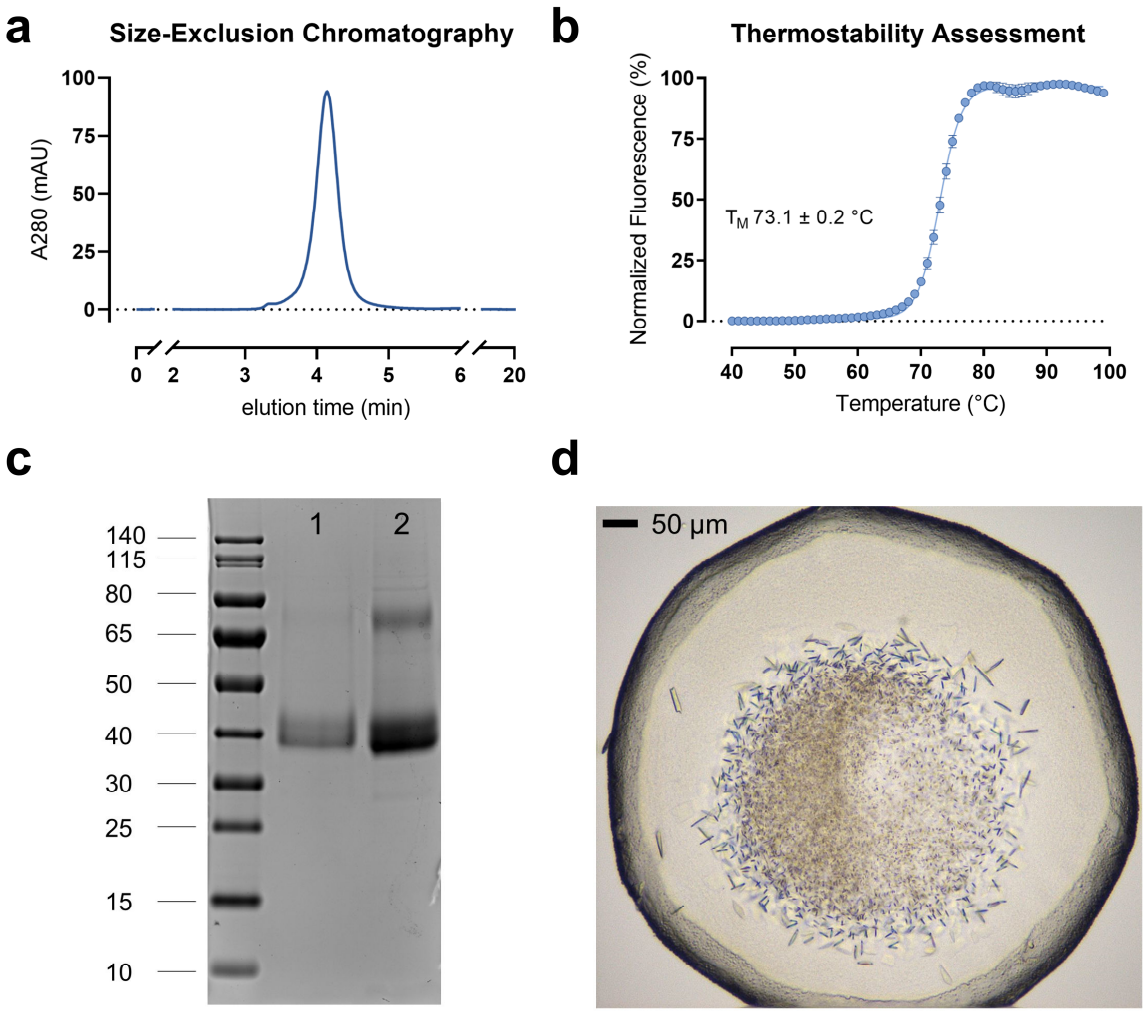

Figure 38. Protein analysis and crystallization of A_{2A}-PSB1-bRIL-PSB-20002 (1st attempt).
a) SEC of the final protein sample used for crystallization (diluted 80-fold, injection volume 30 µL), b) thermostability assessment (in the presence of 5 µM PSB-20002) and c) SDS-PAGE of the purified A_{2A}-PSB1-bRIL-PSB-20002 complex. The data points in the melting curve and the T_M in panel b are shown as means ± SEM from three different experiments. The SDS-PAGE was loaded with two different samples (1 protein sample before concentration, 2 final protein sample used for crystallization, but diluted ~50-fold with water; equal sample volumes were applied). d) Crystals of A_{2A}-PSB1-bRIL-PSB-20002 in LCP.

3.7.3 Purification and Crystallization of the A_{2A}-PSB1-bRIL-PSB-20002 Complex (Second Attempt)

The next crystallization attempt of A_{2A}-PSB1-bRIL-PSB-20002 yielded larger crystals in a similar precipitant condition as before (Figure 39d): 15 % (w/v) PEG400, 50 mM sodium thiocyanate, 100 mM sodium citrate pH 5.2, 2 % (w/v) 2,5-hexandiol. The protein concentration was comparable but slightly lower in the 2nd attempt

compared to the 1st attempt as judged by the size-exclusion chromatogram (Figure 39a). However, the protein was yielded in very high purity (Figure 39c) and the T_M of the complex was determined to be 73.9 °C. Crystals were harvested and analyzed for X-ray diffraction. Although single diffraction spots could be observed up to 3.3 Å resolution during an automatic raster screen of the crystal-containing loops,[217] data from two datasets did not yield sufficient completeness and quality to solve a high-resolution crystal structure.

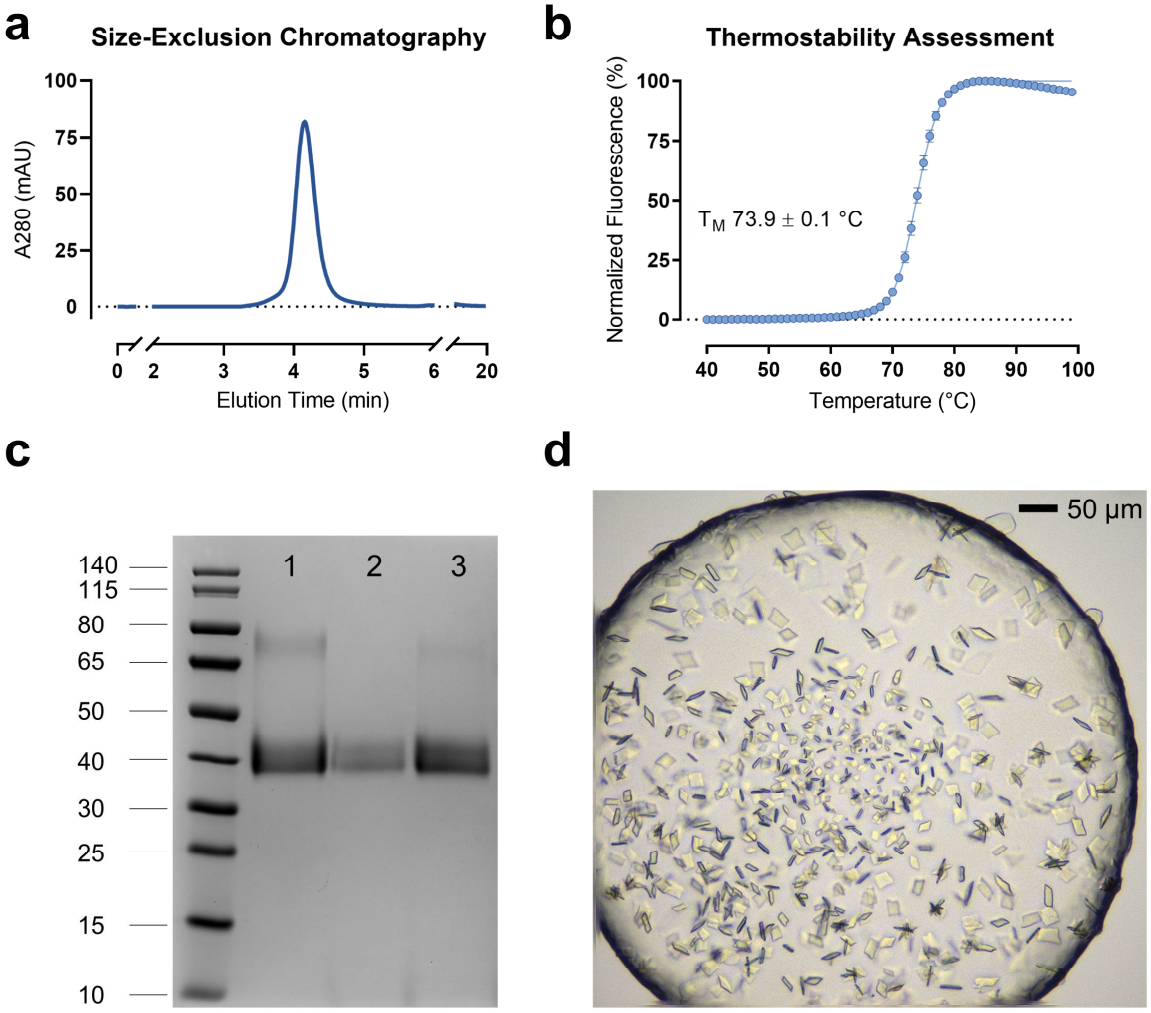

Figure 39. Protein analysis and crystallization of A_{2A}-PSB1-bRIL-PSB-20002 (2nd attempt).
a) SEC of the final protein sample used for crystallization (diluted 80-fold, injection volume 30 µL), b) thermostability assessment (in the presence of 5 µM PSB-20002) and c) SDS-PAGE of the purified A_{2A}-PSB1-bRIL-PSB-20002 complex. The data points in the melting curve and the T_M in panel b are shown as means ± SD from two different experiments. The SDS-PAGE was loaded with three different samples (1 protein sample before concentration, 2 and 3 final protein sample used for crystallization, but diluted ~200-fold (2), or ~100-fold (3) with water; equal sample volumes were applied). d) Crystals of A_{2A}-PSB1-bRIL-PSB-20002 in LCP.

3.7.4 Purification and Crystallization of the A_{2A}-PSB2-bRIL-PSB-21033 Complex

The A_{2A}-PSB2-bRIL-PSB-21033 complex was purified and analyzed according to section 1.4. The size-exclusion chromatogram showed high monodispersity of the purified protein (Figure 41a). However, the proteins were not analyzed by SDS-PAGE in this crystallization experiment.

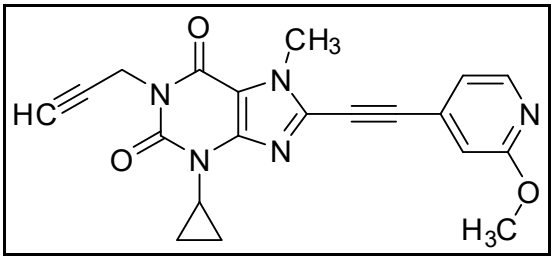

Figure 40. Chemical structure of the xanthine-derivative PSB-21033.

The T_M of the complex was determined to be 73.1 °C (Figure 41b). Despite the excellent protein characteristics, only small crystal hits could be obtained, similarly to the A_{2A}-PSB2-bRIL-Istradefylline complex (Figure 42). Here, mini-crystals with an average size of 8 µm were obtained in 2 % (w/v) PEG400, 7 % (w/v) Tacsimate[206] pH 7.0, 100 mM HEPES-Na pH 7.4, 1.8 % (w/v) 2,5-hexandiol. Moreover, the LCP drop contained a large amount of precipitated protein. The mini-crystals were not further analyzed for their X-ray diffraction.

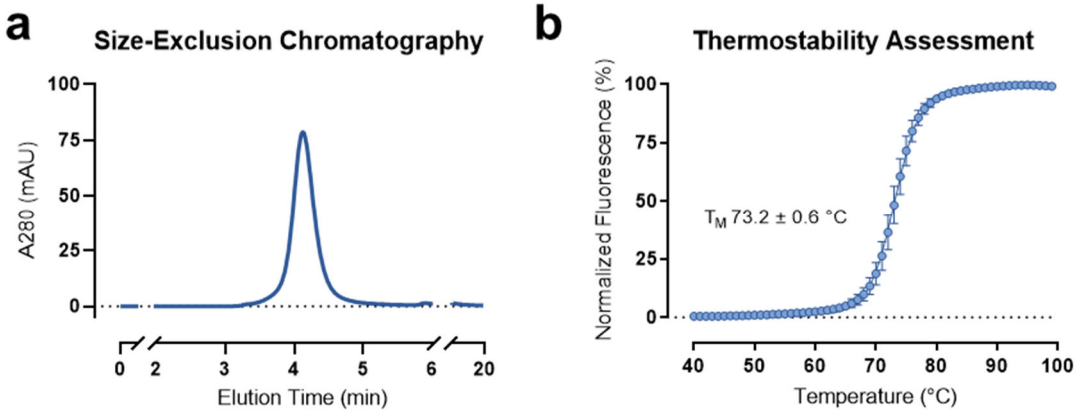

Figure 41. Protein analysis and crystallization of A_{2A}-PSB2-bRIL-PSB-21033.
a) SEC of the final protein sample used for crystallization (diluted 80-fold, injection volume 30 µL), and b) thermostability assessment (in the presence of 10 µM PSB-21033) of the purified A_{2A}-PSB1-bRIL-PSB-21033 complex. The data points in the melting curve and the T_M in panel b are shown as means ± SEM from three different experiments.

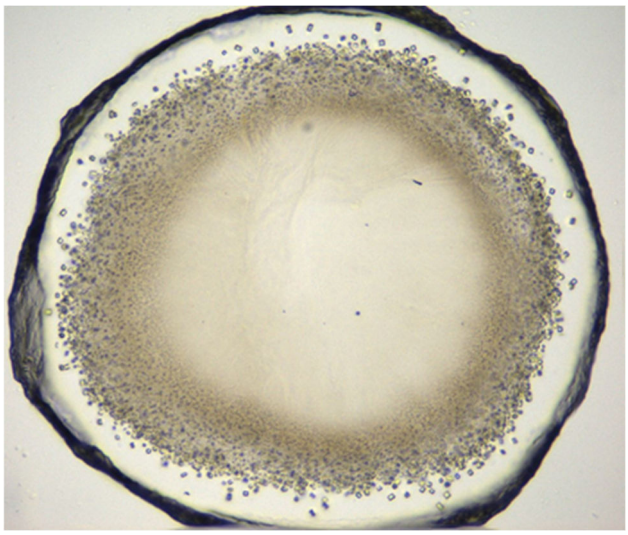

Figure 42. Crystal hits of A_{2A}-PSB2-bRIL-PSB-21033 in LCP.

3.7.5 Summary & Outlook: A_{2A}AR Crystallization in Complex with Xanthine Derivatives

Although highly stable, pure and monodisperse A_{2A}AR complexes together with xanthine derivatives could be produced, their crystallization has not yet yielded well-diffracting crystals. However, we have been able to produce a high-resolution crystal structure of our internal xanthin derivative PSB-20327 (please refer to section 3.4), even though its affinity is lower than that of the other tested ethinylxanthines, PSB-20002 and PSB-21033. The clinical candidate and styrylxanthine Istradefylline only produced mini-crystals, presumably crystals of the antagonist itself. The best success regarding crystallization of these xanthine derivatives so far has been achieved with datasets that showed isolated diffraction spots up to ~3.3 Å resolution by crystals of the A_{2A}-PSB1-bRIL-PSB-20002 complex. However, the quality of these datasets was not sufficient to solve the crystal structure. All of the tested xanthines have in common a rather low water solubility. Hence, they could only be supplemented in relatively low concentrations during protein purification and crystallization which might negatively affect their co-crystallization. Perhaps they additionally have relatively fast off-rates, which, however, remain to be determined. Therefore, xanthine derivatives with higher solubility and/or higher residence time might improve the chances of creating diffraction quality crystals in complex with the A_{2A}AR.

3.8 Crystal Structure of the Adenosine A_{2A} Receptor in Complex with the Potent Partial Agonist LUF5834

A new chemical class of 2-thio-3,5-dicyano-4-aryl-aminopyridine derivatives were initially discovered as unselective adenosine receptor agonists by Bayer in 2001.[218] The authors showed that the derivatives can increase intracellular cAMP concentrations which was consistent with the activation of the A_{2B}AR and less prominent in A_{2A}AR-transfected cells.

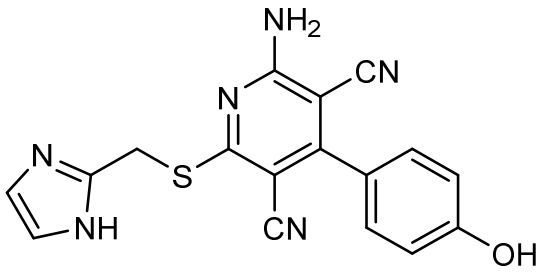

Figure 43. Chemical structure of the partial agonist LUF5834

Three years later, Beukers et al. (re-)synthesized five 2-thio-3,5-dicyano-4-aryl-aminopyridines and analyzed their binding affinity and potencies on all adenosine receptor subtypes.[219] The derivative bearing a *p*-OH-phenyl substituent (Figure 43) was named LUF5834 whereas the respective phenyl derivative was named LUF5833. Within this framework, it was discovered that 2-thio-3,5-dicyano-4-aryl-aminopyridine derivatives were actually partial agonists, hence, their adenosine receptor efficacy was lower than that of full agonists. LUF5833 and LUF5834 showed similar binding to all adenosine receptor subtypes and identical cAMP efficacy at the human A_{2A}AR (55 %).[219] However, LUF5834 was slightly more selective with ~3-fold less affinity to the A_3AR. Subsequently, LUF5834 was extensively characterized[220,221] and now represents an important and commercially available tool compound for the A_{2A}AR and adenosine receptors in general.[222–225]

A comparatively low resolution crystal structure of the A_{2A}-StaR2-bRIL in complex with the partial agonist LUF5833 has already been obtained (3.12 Å) but water molecules, for example, could not be resolved.[108] Additionally, the authors reported that they „[…] also attempted to obtain a receptor crystal structure with LUF5834 but were unsuccessful“.[108] Importantly, the utilized A_{2A}-StaR2-bRIL construct comprises two mutations inside the orthosteric binding pocket (T88$^{3.36}$A and S277$^{7.42}$A).[117] Although it had been shown that both mutations did not affect the binding affinity of LUF5834, S277$^{7.42}$A equalized the efficacy of the partial agonist LUF5834 and the full agonist NECA[220] which might contribute to the fruitless

experiments using the inactive state stabilized A_{2A}-StaR2 construct. Therefore, we aimed to solve the crystal structure of A_{2A}-PSB2-bRIL in complex with LUF5834 and at the same time increase the resolution of the co-crystal structure with this important partial agonist scaffold.

3.8.1 Purification and Crystallization of the A_{2A}-PSB2-bRIL-LUF5834 Complex

The A_{2A}-PSB2-bRIL-LUF5834 complex was purified and analyzed according to section 1.4. The size-exclusion chromatogram showed high monodispersity of the purified protein (Figure 44a). SDS-PAGE analysis was not performed for the A_{2A}-PSB2-bRIL-LUF5834 complex. The T_M of the complex was determined to be 73.1 °C (Figure 44b). Diffraction-quality crystals are shown in Figure 45 with an average size of 30 µm. The crystals grew in the following precipitant condition: 23 % (w/v) PEG400, 90 mM sodium thiocyanate, 100 mM sodium citrate pH 5.2, 2 % (w/v) 2,5-hexandiol. The crystals were used to solve the complex crystal structure at 2.43 Å resolution.

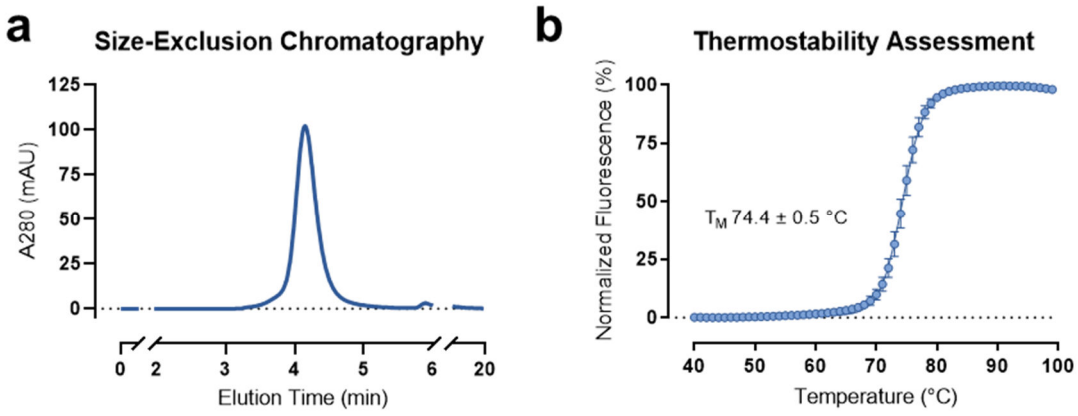

Figure 44. Protein analysis and crystallization of A_{2A}-PSB2-bRIL-LUF5834.
a) SEC of the final protein sample used for crystallization (diluted 80-fold, injection volume 30 µL) and b) thermostability assessment (in the presence of 50 µM LUF5834) of the purified A_{2A}-PSB2-bRIL-LUF5834 complex. The data points in the melting curve and the T_M in panel b are shown as means ± SEM from three different experiments.

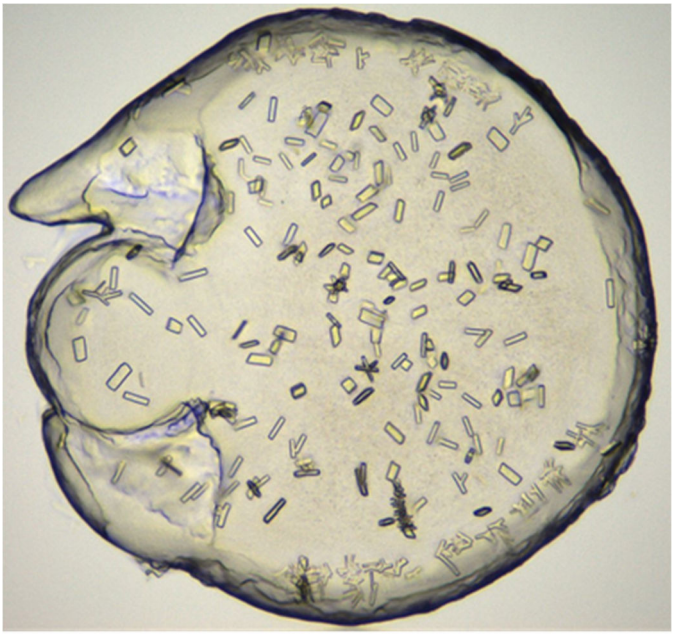

Figure 45. Crystals of A_{2A}-PSB2-bRIL-LUF5834 in LCP used to obtain high-resolution diffraction data.
Crystals grew in LCP with the following precipitant conditions: 23 % (w/v) PEG400, 90 mM sodium thiocyanate, 100 mM sodium citrate pH 5.2, 2 % (w/v) 2,5-hexandiol.

3.8.2 The LUF5834 Binding Pocket

We obtained the crystal structure of the A_{2A}AR in complex with PSB-21417 at 2.43 Å resolution. Data collection and structure determination were performed by Prof. Norbert Sträter and Dr. Renato Weiße from the University of Leipzig.

The partial A_{2A}AR agonist LUF5834 co-crystallized in two alternate binding modes as depicted in Figure 46. The conformation with the phenol of LUF5834 facing towards T88$^{3.36}$ was determined as the predominant binding mode with an occupancy of 0.7. In the alternate conformation, the phenol shows contacts to residues of helices II, III, and VII (A63$^{2.61}$, V84$^{3.32}$, H278$^{7.43}$). Additionally, the phenol forms a direct hydrogen bond to the backbone of A59$^{2.57}$ and A63$^{2.61}$. However, the direct hydrogen bond observed in most of the potent A_{2A}AR ligands (agonists as well as antagonists) to N253$^{6.55}$ is not observed in this alternate binding mode.

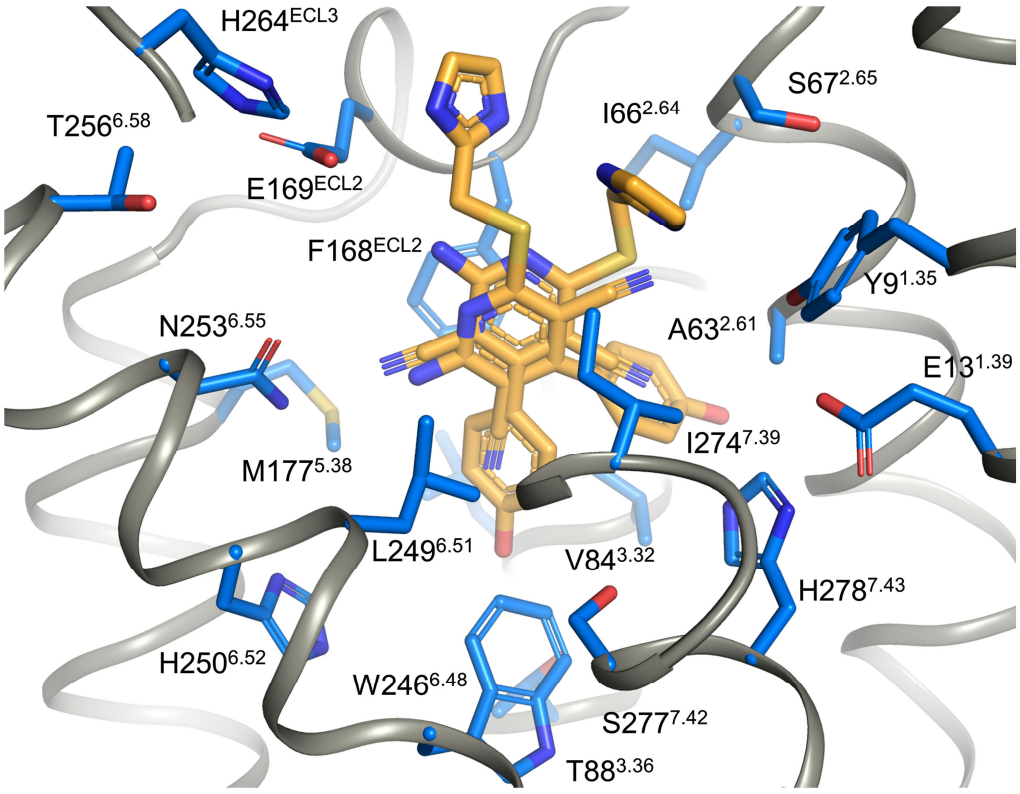

Figure 46. Alternate binding modes of LUF5834 to A_{2A}-PSB2-bRIL.
Two concurrent binding modes for LUF5834 to A_{2A}-PSB2-bRIL could be observed with a predominant binding mode as represented in Figure 47 (occupancy 0.7) and a second binding mode as superposed here. Protein figure was created with PyMOL 2.4.1.

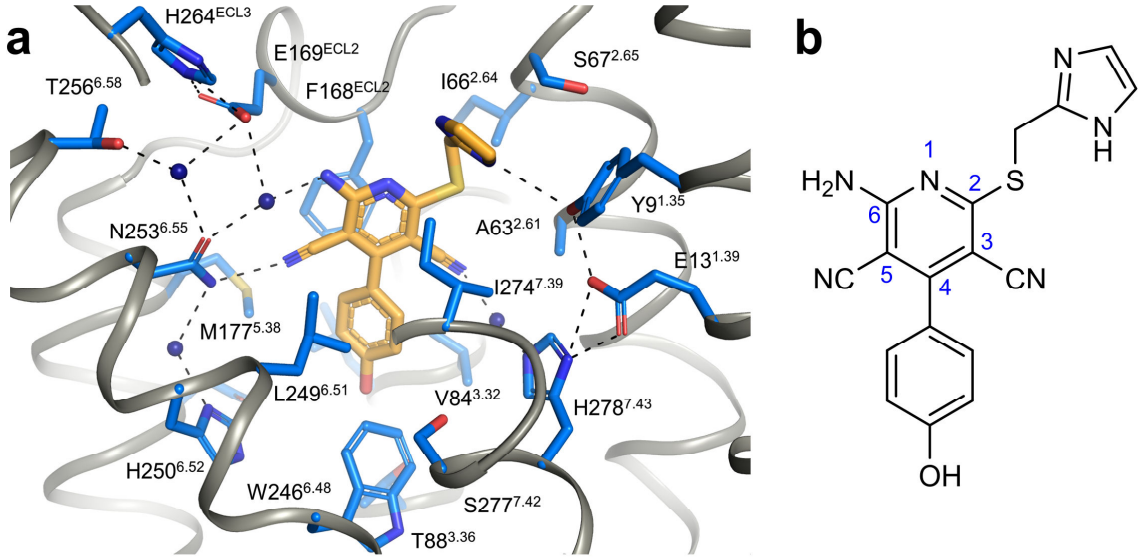

Figure 47. The A_{2A}AR binding pocket of LUF5834.
a) Binding pose of LUF5834 to the A_{2A}AR. Hydrogen bonds are represented with black dashed lines. b) Chemical structure of LUF5834. Protein figures was created with PyMOL 2.4.1.

On the other hand, in the predominant binding mode (Figure 47a), the nitrile in position 5 (for numbering please refer to Figure 47b) forms a direct hydrogen bond to N253$^{6.55}$. The interaction is further supported by a water-mediated hydrogen bond by the 6-amino group of LUF5834. The nitrile in position 3 is connected to H278$^{7.43}$ via one structural water molecule (Figure 47a). A π-π stacking interaction between the pyridine moiety and F168^{ECL2} can be observed, similarly to other previously reported A_{2A}AR structures. The imidazole moiety of LUF5834 is located in a pocket formed by Y9$^{1.35}$, S67$^{2.65}$, L267$^{7.32}$, Y271$^{7.36}$, and I274$^{7.39}$. It forms a direct hydrogen bond to Y9$^{1.35}$ (Figure 47a). The phenol of LUF5834 faces towards the sodium binding pocket and is in close contact to W246$^{6.48}$ of the CxWP motif.[226] This vicinity and the two alternate binding modes led to a minor bending of 2° from planarity of the phenol ring in our refined binding pose. The OH-group of the phenol is located in proximity to T88$^{3.36}$, presumably participating in a weak hydrogen bond (O-O distance 3.9 Å). T88$^{3.36}$ is mutated to alanine in the A_{2A}-StaR2-bRIL construct which may contribute to the fact that co-crystallization trials of LUF5834 with this construct failed previously.[108] T88$^{3.36}$ is also conformationally restricted in the constitutively inactive conformation of our A_{2A}-PSB2-bRIL construct as a result of the introduced S91$^{3.39}$K mutation as previously

elaborated.[107] In fact, T88$^{3.36}$ was modelled in two conformations when A_{2A}-ΔC-bRIL (no point mutations) was used for A_{2A}AR crystallography; these results imply greater flexibility (PDB 4EIY)[120] of T88$^{3.36}$ in the unmutated receptor as compared to the S91$^{3.39}$K mutant. Therefore, LUF5834 may engage T88$^{3.36}$ in a more favorable conformation and perhaps forms a stronger hydrogen bond in the inactive state of the wt A_{2A}AR. Importantly, LUF5834 binds to the S91$^{3.39}$K single mutant A_{2A}-PSB1-bRIL with 11-fold lower affinity compared to the wt A_{2A}AR (K_i 29.8 ± 4.28 nM vs. 336 ± 66.8 nM; ΔpK_i 1.26; p = 0.0126 using the paired two-tailed t-test), determined in three independent radioligand competition binding experiments vs. antagonist radioligand [^{3}H]MSX-2 using *Sf9* insect cell membranes expressing the respective receptor). The conformational restraints towards the inactive state through the S91$^{3.39}$K mutation would provide a plausible explanation for the reduced affinity at the stabilized crystallization construct. However, it is still unclear and has yet to be determined whether the affinity difference originates from the general conformational restriction in the A_{2A}AR inactive state or from the conformational restriction of the T88$^{3.39}$ side chain.

Although with lower affinity, we showed that LUF5834 is indeed able to bind the constitutively inactive state of the A_{2A}AR and revealed its binding pose with our high-resolution crystal structure. However, the structure alone does neither provide a direct structural understanding of partial agonism nor explains the activation mechanism of this partial agonist at the A_{2A}AR. Importantly, the structural mechanism of partial agonism in contrast to full agonism is still not fully understood.[227] In contrast to partial A_{2A}AR agonist LUF5834, we previously showed that the full agonist NECA does not show binding to A_{2A}-PSB1-bRIL (at concentrations up to 3 mM and determined vs. antagonist radioligand [^{3}H]MSX-2) whereas the affinity of antagonists and the radioligand itself was unaffected.[107] Hence, one explanation for the partial agonistic activity of LUF5834 may originate from binding affinity to both inactive and the active states of the A_{2A}AR whereas full A_{2A}AR agonists only exhibit affinity towards the active state. Therefore, the conformational selection of full agonist may be restricted to the active state which thus may result in the greater efficacy that can be observed in contrast to partial agonists.[219] Although partial agonism may not be explained by the same unique mechanism for all GPCRs, this hypothesis is supported by protein NMR experiments

performed on the β_2-adrenergic receptor which revealed that the partial agonists indeed stabilized an equilibrium of both the inactive and active conformations.[228]

Another theory for partial agonism assumes that partial agonists stabilize a conformational state that is different from that of full agonists, and thus, resulting in lower affinity towards the G-protein, ultimately leading to less effective nucleotide exchange. In fact, this hypothesis can also be supported by similar NMR experiments but with different labeling techniques[222] or by allosteric nanobodies.[229]

Interestingly, no information with regards to the binding of LUF5833 to the crystallization construct A_{2A}-StaR2-bRIL had been provided in the respective publication of this co-crystal structure.[108] The binding pose of LUF5833 in that structure is similar to the one that we observed for the dominant binding pose of LUF5834 (Figure 48). However, a crucial difference is observed for the conformation of ECL3 in the LUF5833 co-crystal structure showing a unique position, with H264^{ECL3} pointing towards the surface. This conformation had not been observed in any other A_{2A}AR structure. In addition, the sidechain of E169^{ECL2} is rotated towards the ligand and interacts with the imidazole moiety of LUF5833. In our new structure of the A_{2A}AR in complex with LUF5834, H264^{ECL3} instead forms an ionic lock to E169^{ECL2} as discussed in detail within section 3.4.3 (Figure 48).

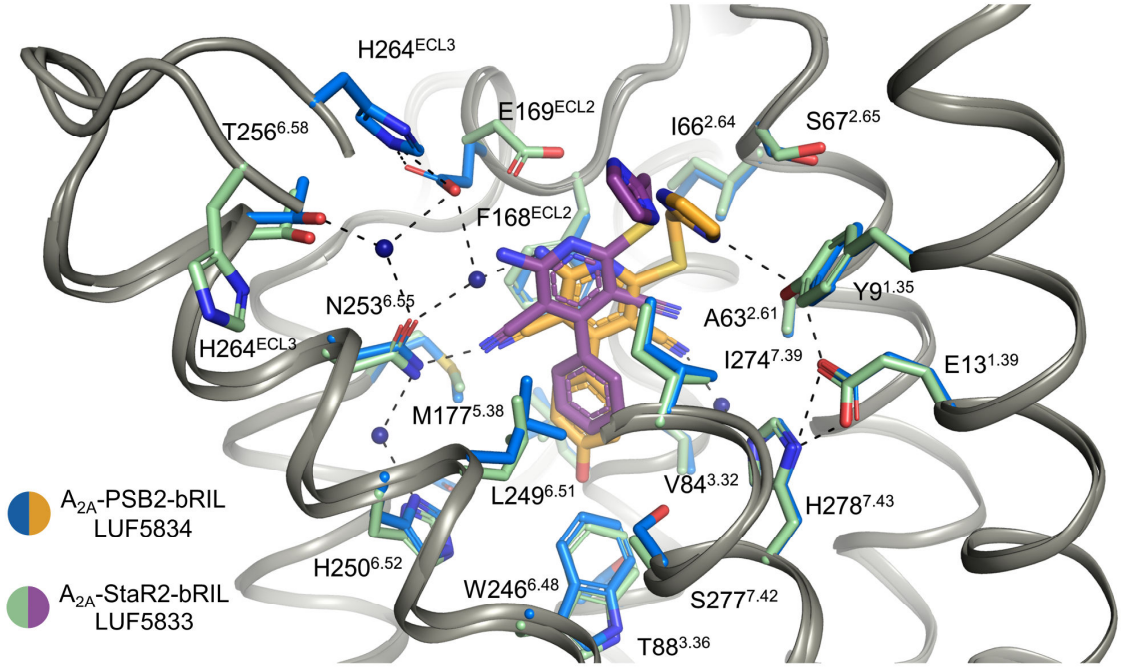

Figure 48. Structural comparison of the binding poses of LUF5834 and LUF5833. A_{2A}-PSB2-bRIL-LUF5834 is represented as blue/orange and A_{2A}-Star2-bRIL-LUF5833 (PDB 7ARO) as green/purple.

3.8.3 Summary

Here, we obtained an inactive state structure of the partial A_{2A}AR agonist LUF5834 in complex with the A_{2A}AR. LUF5834 binds to the constitutively inactive construct A_{2A}-PSB2-bRIL with significantly lower affinity compared to the wt A_{2A}AR, which is consistent with its partial agonistic activity. Thus, the new structure provides valuable new insights into the structural biology of partial agonists.

3.9 Development of Nanobodies Against the Adenosine A_{2A} Receptor by Llama Immunization

3.9.1 Large-Scale Protein Production of A_{2A}-ΔC for Llama Immunization

Similar to human antibodies which consist of a heavy and a light chain, camelids (and llamas in particular) produce heavy chain-only antibodies.[230] While conventional antibodies are significantly larger, nanobodies only consist of the single variable domain of the camelid heavy-chain antibody (VHH).[231] Here, we produced large amounts of purified A_{2A}AR with truncated C-terminus for the immunization of llamas with the aim to identify A_{2A}AR specific nanobodies.

In total, three liter of *Sf9* insect cell culture were expressed in order to produce approximately 1.2 mg purified A_{2A}-ΔC (protein quantified using methods developed by Bradford[232] with BSA for comparison). A_{2A}-ΔC represents the wt A_{2A}AR with its long and flexible C-terminus truncated (please refer to Appendix IV for the protein sequence). The construct is able to bind both antagonists and agonists as shown by increased thermostability (Figure 49b and d). A_{2A}-ΔC can be activated by NECA and recruits G-proteins as previously reported by us.[107] Therefore, A_{2A}-ΔC was chosen to yield nanobodies that could potentially stabilize both the inactive and active state A_{2A}AR. However, the relative conformational flexibility is accompanied by lower stability. Figure 49 shows one out of six characterized batches with high protein purity and monodispersity (please refer to panels c and d).

Six immunization rounds were carried out by the Nanobody Core Facility at the University of Bonn, but unfortunately has not yielded nanobodies against the A_{2A}AR.

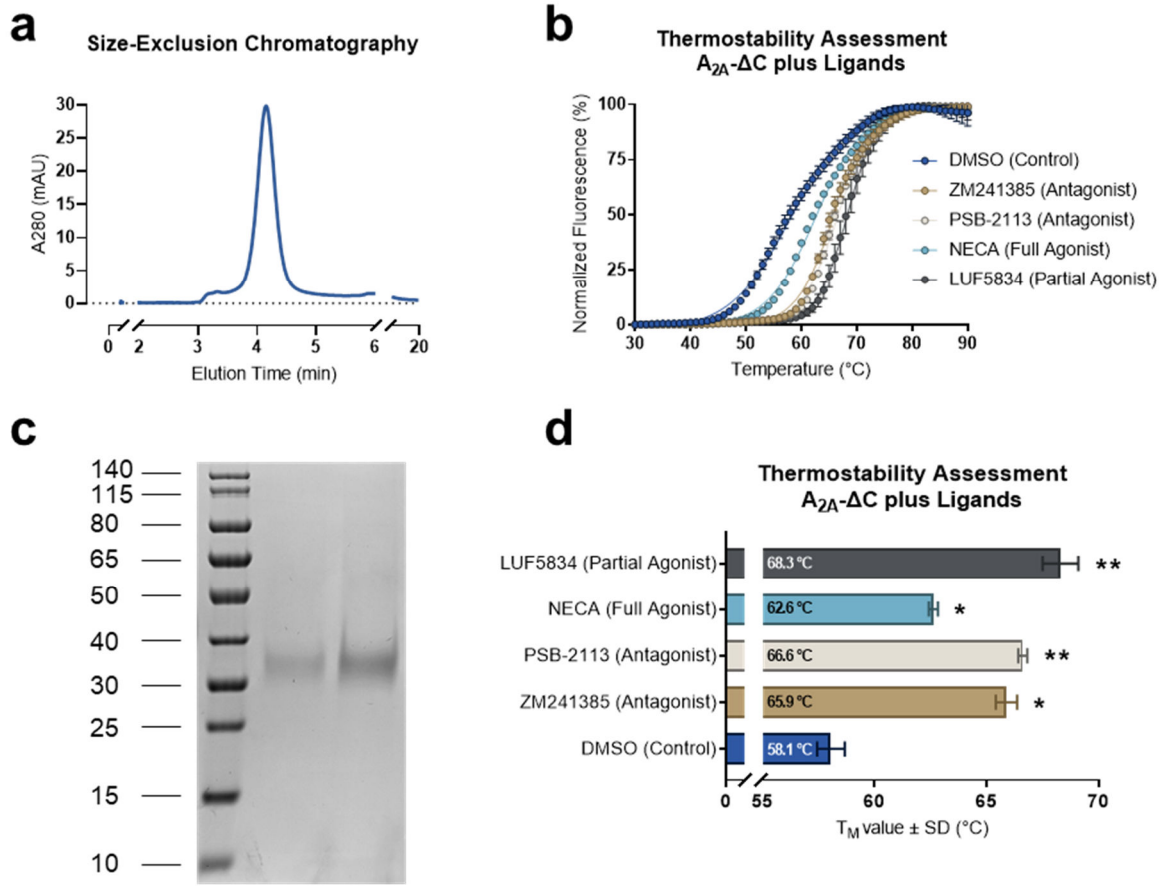

Figure 49. Protein analysis of A_{2A}-ΔC for llama immunization.
a) SEC result of the unconcentrated purified protein (injection volume 30 µL). b) Thermostability assessment of A_{2A}-ΔC and the effect of different A_{2A}AR ligands on thermostability. Data is shown as means ± SD from three independent experiments. c) SDS-PAGE of the purified protein. Left: protein before concentration, right: final concentrated protein used for immunization. Equal sample volumes were applied. d) Column graph representation of T_M values from the thermostability assessment. Data is shown as means ± SD from three independent experiments. Statistical analysis was performed by one-way ANOVA with Dunnett's post-hoc test compared to the dimethyl sulfoxide (DMSO) control (*$p < 0.05$, **$p < 0.01$).

3.9.2 Large-Scale Protein Production of A_{2A}-PSB2-bRIL for Llama Immunization

In order to increase A_{2A}AR stability and solubility, we decided to repeat llama immunization with our highly stable crystallization construct A_{2A}-PSB2-bRIL. Although the construct evolved with superior stability, it represents the constitutively inactive state and thus cannot be activated anymore. Hence, only nanobodies against the inactive state are potentially generated. Moreover, the intracellular fusion partner bRIL enhances solubility but likely represents an additional immunogen for the llama.

Two liters of *Sf9* insect cell culture expressing A_{2A}-PSB2-bRIL were expressed and purified in two batches. The protein was obtained in high purity and monodispersity (Figure 50a and c). The addition of antagonists or of the partial agonist LUF5834 can further increase the stability of the already highly stable A_{2A}-PSB2-bRIL (Figure 50b and d) demonstrating correct protein folding. In total, approximately 1 mg of purified A_{2A}AR was produced and submitted for llama immunization in six additional rounds which is currently ongoing work.

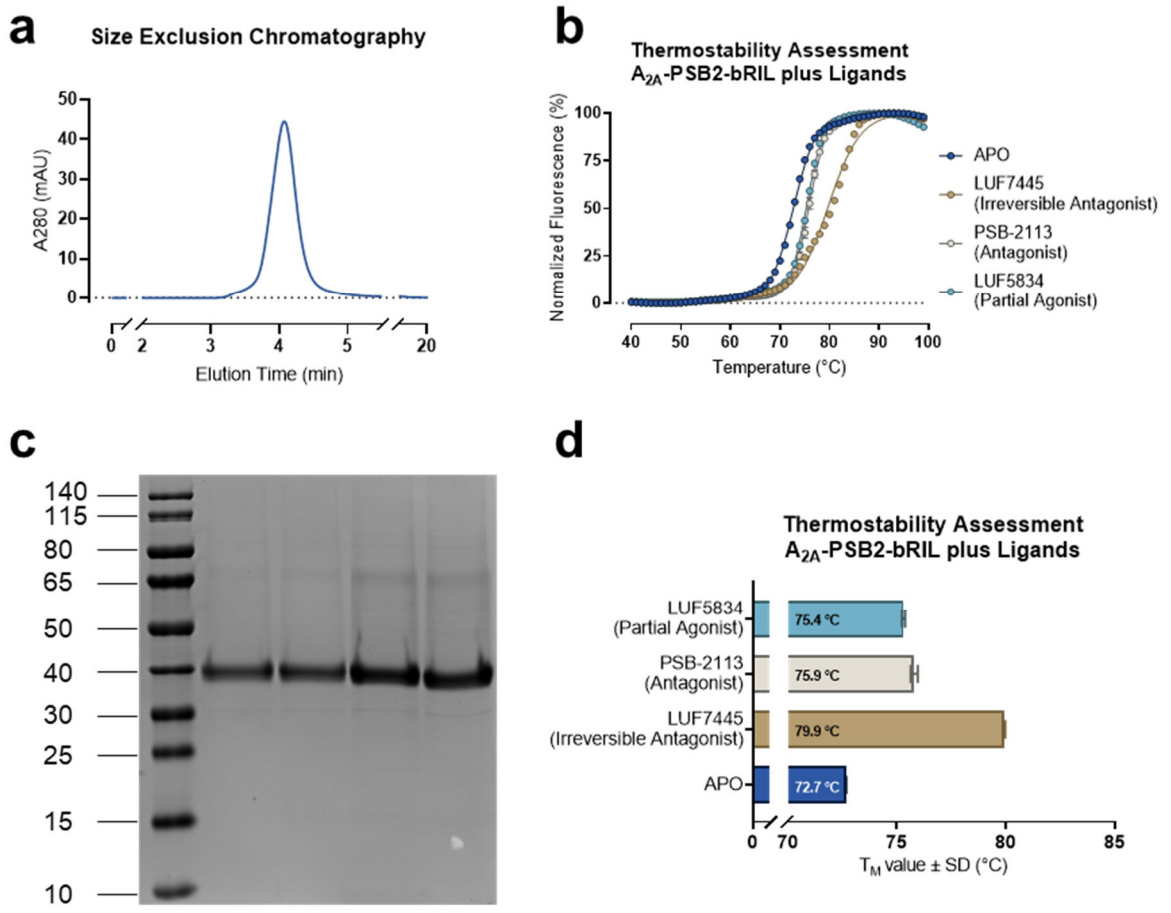

Figure 50. Protein analysis of A_{2A}-PSB2-bRIL for llama immunization.
a) SEC result of the unconcentrated purified protein (injection volume 30 µL). b) Thermostability assessment of A_{2A}-PSB2-bRIL and the effect of different A_{2A}AR ligands on thermostability. Data is shown as means ± SD from two independent experiments. c) SDS-PAGE of the purified protein. Left two bands: 10 µL of protein before concentration, right two bands: 20 µL of protein before concentration. d) Column graph representation of T_M values from the thermostability assessment. Data is shown as means ± SD from two independent experiments.

3.9.3 Summary

Large amounts of purified A_{2A}AR were produced in order to immunize llamas for nanobody production. While a first attempt with A_{2A}AR construct A_{2A}-ΔC failed to produce A_{2A}AR-reactive nanobodies, a second immunization attempt has been started with the more stable construct A_{2A}-PSB2-bRIL. Llama immunization is currently ongoing. If successful, this work could result in the first A_{2A}AR-reactive nanobodies that can potentially be utilized for further pharmacological characterization[233] of the A_{2A}AR or even for therapeutic application.[234]

4 Conclusions

High-resolution protein structures of important drug targets facilitate the structure-based drug discovery and the optimization of novel clinical candidates.[235–237] Due to major structural biology advances in the past two decades, structure-based drug design has substantially progressed and already demonstrated tremendous success.[238–241] However, the structure elucidation of GPCRs is far from being considered routine work and generally requires specialized expertise as well as extensive protein engineering. Within this study, important aims were achieved that have enabled structural biology studies of GPCRs (and other proteins):

1. The effort to solve active state crystal structures of the DOP was continued and resulted in two crystal structures bound to structurally-diverse ligands (one peptide agonist and one small molecule agonist).

2. A structural biology platform for (membrane) proteins was established at the Pharmaceutical Institute of the University of Bonn. This mainly includes the expression (in required quantity), purification, analysis and crystallization of recombinant proteins.

3. The successful implementation of the established research platform was demonstrated by the structure elucidation of seven new GPCR crystal structures of the human adenosine A_{2A} receptor in complex with six structurally diverse antagonists and one partial agonist, that were determined using crystals generated in Bonn (see Table 5).

4. The obtained co-crystal structures were used to comprehensively analyze the ligand binding pocket of the co-crystallized ligands in order to evaluate their affinity determinants and to further increase their A_{2A}AR affinity by subsequent lead optimization.

Herein, the A_{2A}AR was not only used as a showcase to demonstrate the successful establishment of the structural biology platform but also to enhance the structural

understanding of the A_{2A}AR ligand binding pocket. Thus, although several crystal structures of the A_{2A}AR had previously been obtained, a great majority was solved using highly mutated A_{2A}AR constructs (Table 1 and Table 2). We were able to significantly reduce the mutational load and, importantly, avoided any ligand binding pocket mutations. The new construct was designed by introducing a single stabilizing point mutation (S91$^{3.39}$K) into a previously established A_{2A}AR crystallization construct[120] and still displayed superior thermostability compared to previously established constructs. This mutant is suggested to become the new gold standard for the crystallization of the A_{2A}AR in complex with A_{2A}AR antagonists. Our thermostabilization strategy can likely by applied to other GPCRs due to the fact that the thermostabilizing mutation is located inside the conserved sodium binding pocket.

We utilized the new A_{2A}AR crystallization construct to determine six new crystal structures of the A_{2A}AR in complex with A_{2A}AR antagonists (Table 5). Additionally, one new A_{2A}AR co-crystal structure was solved with a partial agonist. The new structures enabled novel insights into previously unknown binding modes, and greatly facilitate future lead optimization. In fact, five of the six A_{2A}AR antagonists were developed in-house and are currently being further optimized using the newly obtained structural information of their binding interactions.

Table 5. Overview of crystal structures solved in this thesis.

GPCR	Construct	Resolution (Å)	PDB ID	Ligand
DOP	bRIL-DOP	2.80	6PT2	KGCHM07
DOP	bRIL-DOP	3.30	6PT3	DPI-287
A_{2A}AR	A_{2A}-PSB1-bRIL	2.25	7XP4	PSB-2113
A_{2A}AR	A_{2A}-PSB1-bRIL	2.60	7YPR	PSB-2115
A_{2A}AR	A_{2A}-PSB2-bRIL	2.65	undisclosed	PSB-21007
A_{2A}AR	A_{2A}-PSB2-bRIL	2.14	undisclosed	PSB-20327
A_{2A}AR	A_{2A}-PSB2-bRIL	2.11	undisclosed	Etrumadenant
A_{2A}AR	A_{2A}-PSB1-bRIL	2.20	undisclosed	PSB-21417
A_{2A}AR	A_{2A}-PSB2-bRIL	2.43	undisclosed	LUF5834

5 Experimental Methods

5.1 Protein Expression, Purification, Crystallization and Structure Elucidation

5.1.1 Expression, Purification and Crystallization of A_{2A}AR Construct A_{2A}-PSB2-bRIL in Complex with PSB-21007

The A_{2A}AR construct A_{2A}-PSB2-bRIL was cloned and expressed in *Sf9* as previously established for A_{2A}-PSB1-bRIL.[107] A_{2A}-PSB2-bRIL differs from A_{2A}-PSB1-bRIL by the addition of one extra point mutation ($N154^{ECL2}A$) in order to remove N-linked glycosylation. Please refer to Appendix III and Appendix IV for full DNA and protein sequences of A_{2A}-PSB1-bRIL and A_{2A}-PSB2-bRIL. For a protein sequence alignment of A_{2A}-PSB2-bRIL with the wt A_{2A}AR refer to Appendix V. *Sf9* insect cells from 900 mL infected cell culture were lysed and washed as previously described using low and high osmotic buffer.[107]

Sf9 insect cell membranes were incubated with 25 µM PSB-21007 (diluted from a 25 mM DMSO stock solution) and 2 mg mL^{-1} iodoacetamide for 60 min. Membranes were then solubilized in an equal volume of solubilization buffer [100 mM HEPES pH 7.5 (4 °C), 1.6 M NaCl, 1.5 % (w/v) dodecyl-β-D-maltopyranoside (DDM) and 0.3 % (w/v) cholesteryl hemisuccinate (CHS)] over 3 h while shaking (end-over-end) at 4 °C. Solubilized proteins were separated from the insoluble material by centrifugation and purified as previously described[107] using 20 column volumes wash buffer I [50 mM HEPES pH 7.5 (4 °C), 800 mM NaCl, 0.5 % (w/v) DDM, 0.1 % (w/v) CHS, 10 % (v/v) glycerol, 20 mM imidazole pH 7.5 (4 °C), 8 mM ATP, 10 mM $MgCl_2$, and 25 µM PSB-21007] and 13 column volumes wash buffer II [50 mM HEPES pH 7.5 (4 °C), 800 mM NaCl, 0.05 % (w/v) DDM, 0.01 % (w/v) CHS, 10 % (v/v) glycerol, 50 mM imidazole pH 7.5 (4 °C), and 25 µM PSB-21007]. The synthesis of PSB-21007 will be published elsewhere. A_{2A}-PSB2-bRIL-PSB-21007 complexes were eluted using elution buffer [25 mM HEPES pH 7.5 (4 °C), 800 mM NaCl, 10 % (v/v) glycerol, 220 mM imidazole, 0.025 % (w/v) DDM, 0.005 % (w/v) CHS, and 12.5 µM PSB-21007] and concentrated to 20 – 30 µL using 100 kDa cut-off Vivaspin concentrators (Sartorius). The protein was immediately used for

crystallization experiments while monodispersity and protein purity were assessed using analytical SEC and SDS-PAGE.

The resulting protein-ligand complex were reconstituted into LCP by mixing of the protein with a molten lipid mixture [90 % (w/v) 1-oleoyl-*rac*-glycerin (Sigma), 10 % (w/v) cholesterol (Sigma)] in a 2 to 3 ratio using the two-syringe method.[173] The automatic crystallization robot Formulatrix NT8 was used to perform crystallization experiments by overlaying 50 nL mesophase with 800 nL precipitant solution on a 96-well glass sandwich plate (Marienfeld). The crystallization plates were sealed and stored at 20 °C and automatically imaged using the crystallization plate imager Formulatrix RockImager 54. Diffraction quality crystals grew in well F06 of the commercially available crystallization screening plate "PEG/Ion400" (Hampton Research, Cat. #HR2-460) with the following composition: 30 % PEG 400, 400 mM $(NH_4)_2HPO_4$ (pH 8.2 at 25 °C). The crystals reached their full size within a week and were directly harvested into liquid nitrogen using 25 – 75 µm micromounts (MiTeGen).

5.1.2 Data Collection of A_{2A}-PSB2-bRIL-PSB-21007 Crystals and Structure Determination

X-ray diffraction data of the A_{2A}-PSB2-bRIL-PSB-21007 crystal were collected on the P11 high-throughput macromolecular crystallography beam line at PETRA III of the German Electron Synchrotron (DESY), Hamburg, Germany. Data were collected until 2.65 Å at 100 K using a microfocused beam (20 x 20 μm^2) of ≈12.0 keV (1.0332 Å) with 1 % transmission at a rate of 100 ms per frame and an oscillation-range of 0.1°. Data processing was performed with XDS, XSCALE and XDSCONV.[242] The structure was determined by molecular replacement with phenix.phaser[243] using the previously solved A_{2A}-PSB1-bRIL-PSB-2113 structure[107] as search model (PDB 7PX4). Then, the model was built with the ligand (PSB-21007) and other components using COOT.[244] Structural refinements were performed using phenix.refine.[245] Data collection and structure determination were performed by Prof. Jörg Labahn and Dr. Udaya K. Tiruttani Subhramanyam.

5.1.3 Expression, Purification and Crystallization of MAO-B in Complex with PSB-21007

All experiments that led to the MAO-B structure including expression and purification were performed by Andrea Gottinger in the research group of Prof. Claudia Binda at the Università di Pavia (Italy). Human MAO-B was recombinantly expressed in *Pichia pastoris* and purified as previously reported.[246] The purified protein sample was concentrated to 50 μM using 30 kDa cut-off Amicon concentrators (Merck Millipore) in a buffer comprising 50 mM potassium phosphate buffer pH 7.5, 0.8 % (w/v) β-octylglucoside, 20 % (w/v) glycerol. The enzyme concentration was determined by measuring the flavin absorbance peak (ε_{456} = 12,000 M^{-1} cm^{-1}) using a NanoDrop ND-100 spectrophotometer (Thermo Scientific).

MAO-B was co-crystallized with PSB-21007 by the sitting-drop vapor diffusion as previously reported.[204] Prior to crystallization, the protein was gel-filtrated in a buffer comprising 25 mM potassium phosphate pH 7.5, 8.5 mM Zwittergent 3-12 using a Superdex200 10-300 Increase column (Cytiva). Crystals were soaked into a mother liquor solution with 18 % (v/v) and flash-cooled in a steam of gaseous nitrogen at 100 K.

5.1.4 Data Collection of MAO-B Crystals and Structure Determination

X-ray diffraction data were collected at the beamline ID30A-1/MASSIF-1 of the European Synchrotron Radiation Facility in Grenoble (France). XDS[242] and the CCP4i suite[247] were used for data processing and scaling. The coordinates of MAO-B in complex with safinamide (PDB 2V5Z) excluding water and inhibitor atoms were used as the initial model for molecular replacement. Model building and refinement were performed using Coot[244] and REFMAC5,[248] respectively. Data collection and structure determination were performed by Prof. Claudia Binda and Andrea Gottinger.

5.1.5 Expression, Purification and Crystallization of A_{2A}AR Construct A_{2A}-PSB2-bRIL in Complex with Etrumadenant and PSB-20327

The expression, purification and crystallization of A_{2A}-PSB2-bRIL in complex with Etrumadenant and PSB-20327 was performed as described for the PSB-21007 complex but with different antagonist concentrations and precipitant conditions. 50 µM Etrumadenant (obtained from MedChemExpress, Cat. #HY-129393) was added before solubilization and Etrumadenant was supplemented to wash buffer I at 50 µM, to wash buffer II at 25 µM and to the elution buffer at 25 µM. For the A_{2A}-PSB2-bRIL-PSB-20327 complex, 4 mM Theophylline was added prior to solubilization and exchanged to PSB-20327 during the subsequent purification. PSB-20327 was synthesized by Dr. Ahmed Temirak.[249] It was supplemented to wash buffer I at 50 µM, to wash buffer II at 25 µM and to the elution buffer at 25 µM. The A_{2A}-PSB2-bRIL-20327 complex crystallized in LCP in well H11 of the commercially available crystallization screening plate “PEG/Ion400” (Hampton Research, Cat. #HR2-460) with the following composition: 30 % (w/v) PEG400, 5 % (w/v) Tacsimate[206] pH 7.0 (pH 7.4 at 25 °C). The A_{2A}-PSB2-bRIL-Etrumadenant complex crystallized in an optimized condition of the abovementioned crystallization screen comprising 30 % (w/v) PEG400, 7 % (w/v) Tacsimate pH 7.0 (Hampton Research Cat. #HR2-755),[206] 100 mM HEPES-Na pH 7.4, 1.8 % (w/v) 2,5-hexandiol (Molecular Dimensions, Cat. #MD2-100-226). Crystals were harvested with micromounts (MiTeGen) similarly to the A_{2A}-PSB2-BRIL-PSB-21007 crystals.

5.1.6 Expression, Purification and Crystallization of A_{2A}AR Construct A_{2A}-PSB1-bRIL in Complex with PSB-21417

The A_{2A}-PSB1-bRIL-PSB-21417 complex was purified and crystallized as previously described with minor changes.[107] In particular, 50 µM PSB-21417 was added before solubilization and PSB-21417 was supplemented to wash buffer I and II as well as to the elution buffer at 25 µM. The A_{2A}-PSB1-bRIL-PSB-21417 complex crystallized in LCP in the following precipitant condition: 29 % (w/v) PEG400, 80 mM sodium thiocyanate, 100 mM sodium citrate pH 5.2, 2 % (w/v) 2,5-hexandiol. Crystals were harvested as described before. PSB-21417 was synthesized by Dr. Tim Harms.[214]

5.1.7 Data Collection of A_{2A}-PSB2-bRIL-Etrumadenant, A_{2A}-PSB2-bRIL-PSB-20327, A_{2A}-PSB1-bRIL-PSB-21417 and A_{2A}-PSB2-bRIL-LUF5834 Crystals and Structure Determination

X-ray diffraction data collection and structure determination was performed by Prof. Dr. Sträter and Dr. Renato Weiße from the University of Leipzig. Data was collected at the P13 and P14 beamlines of the DESY (Hamburg) using an automatic rastering strategy.[217] The structure determination was performed using molecular replacement with previously solved A_{2A}AR structures

5.1.8 Expression, Purification and Crystallization of A_{2A}AR Construct A_{2A}-PSB1-bRIL with PSB-20002

The A_{2A}-PSB1-bRIL-PSB-20002 complex was purified and crystallized as previously described with minor changes.[107] In particular, 10 µM PSB-20002 was added before solubilization and PSB-20002 was supplemented to wash buffer I at 10 µM, to wash buffer II at 10 µM and to the elution buffer at 5 µM. The A_{2A}-PSB1-bRIL-PSB-20002 complex only produced microcrystals in several conditions. The synthesis of PSB-20002 was performed by Angelo Oneto and will be published elsewhere.

5.1.9 Expression, Purification and Crystallization of A_{2A}AR Construct A_{2A}-PSB2-bRIL with Istradefylline, PSB-21033 and LUF5834

The expression, purification and crystallization of A_{2A}-PSB2-bRIL in complex with Istradefylline, PSB-21033 and LUF5834 was performed as described for the PSB-21007 complexes but with different antagonist concentrations. 100 µM Istradefylline was added before solubilization and Istradefylline was supplemented to wash buffer I at 25 µM, to wash buffer II at 25 µM and to the elution buffer at 15 µM. All Istradefylline-containing solutions were strictly protected from light due to its light-sensitivity.[216] 25 µM PSB-21033 was added before solubilization and PSB-21033 was supplemented to wash buffer I at 20 µM, to wash buffer II at 10 µM and to the elution buffer at 10 µM. The synthesis of PSB-21033 was performed by Angelo Oneto and will be published elsewhere. 50 µM LUF5834 (obtained from Tocris, Cat.

#4603) was added before solubilization and LUF5834 was supplemented to wash buffer I and II as well as to the elution buffer at 50 µM. The A_{2A}-PSB2-bRIL-LUF5834 complex crystallized in LCP in the following precipitant condition: 23 % (w/v) PEG400, 90 mM sodium thiocyanate, 100 mM sodium citrate pH 5.2, 2 % (w/v) 2,5-hexandiol whereas A_{2A}-PSB2-bRIL-Istradefylline and A_{2A}-PSB2-bRIL-PSB-21033 only produced microcrystals in several conditions. LUF5834 co-crystals were harvested with micromounts (MiTeGen) similarly to the A_{2A}-PSB2-BRIL-PSB-21007 crystals.

5.2 Protein Analysis

5.2.1 SDS-PAGE Analysis

Proteins were analyzed on homemade 10 % SDS-PAGE gels casted using *bis*-Tris buffer. Protein samples were prepared using NuPAGE loading dye (ThermoFisher, Cat. NP0007) supplemented with a final concentration of 50 mM DTT. Samples were incubated for 30 min at 37 °C prior to SDS-PAGE analysis using 3-(*N*-morpholino)propanesulfonic acid (MOPS) running buffer without the addition of sodium bisulfite. SDS-PAGE gels were stained with Coomassie brilliant blue R-250 and destained using hot water. In order to investigate the effect of Tunicamycin on A_{2A}AR glycosylation, the respective insect cell culture was treated with 1 µg mL^{-1} of Tunicamycin (CaymanChemical, Cat. #11445) during infection. PNGase F (New England Biolabs, Cat. #P0704S) was used to cleave the glycosylation in the purified protein prior to SDS-PAGE analysis using 375 units in a total reaction volume of 22.5 µL followed by incubation at 16 °C for 16 h. The glycosylation SDS-PAGE analysis was performed by Jonathan G. Schlegel.

5.2.2 Size-Exclusion Chromatography Analysis

The SEC analysis was performed on an Agilent 1260 Infinity HPLC using a Sepax Nanofilm SEC-250 column. Proteins were analyzed over a time course of 20 min at 0.5 mL min^{-1} using the following buffer: 25 mM HEPES pH 7.5 (4 °C), 500 mM NaCl, 2 % (w/v) glycerol, 0.05 % (w/v) DDM, 0.01 % (w/v) CHS. Proteins were detected using a UV detector at 280 nm.

5.2.3 Thermostability Assessment

The thermostability of purified GPCRs in detergent micelles was performed as previously described using the fluorescent dye CPM.[107] In the case of sections 3.9.1 and 3.9.2, the tested compounds were added to the purified APO proteins at a concentration of 10 µM (1 % final DMSO concentration).

5.3 Pharmacological Characterization

5.3.1 Radioligand Binding Assays

Radioligand binding assays were performed by Christin Vielmuth on CHO cell membranes or *Sf9* insect cell membranes expressing the human wt ARs or A_{2A}-PSB1-bRIL as previously described.[38,107] [^{3}H]CCPA or [^{3}H]DPCPX were used as radioligands for the A_1AR whereas [^{3}H]MSX-2 was used for the A_{2A}AR, [^{3}H]PSB-603 was used for the A_{2B}AR and [^{3}H]PSB-11 was used for the A_3AR. All assays were performed in 50 mM Tris buffer (pH 7.4 at room temperature). Test substances were incubated at room temperature with the respective membranes and radioligand for 60 min (A_1AR), 30 min (A_{2A}AR), 75 min (A_{2B}AR) and 180 min (A_3AR). The mixture was filtered through GF/B glass fiber filters using a Brandel harvester (Brandel, Gaithersburg, MD, USA). Filters were then washed four times with ice-cold Tris-buffer (50 mM, pH 7.4). Filters containing the A_{2B}AR were washed with the same ice-cold Tris-buffer but with addition of 0.1 % BSA. The remaining radioactivity was quantified after incubation for 9 h with scintillation cocktail (Beckmann Coulter) using a scintillation counter (Tricarb 2700TR).

5.3.2 MAO-B Inhibition Assays

MAO-B inhibitions assays were performed by Dr. Miriam Schlenk and Dr. Meryem Köse as previously described.[250] Briefly, recombinant human MAO-B was obtained from Sigma (Cat. # M7441) and was used at a final concentration of approximately 75 nM for each data point. The assays were carried out at room temperature in a 96-well format using a 50 mM sodium phosphate buffer pH 7.4 in a final volume of 200 µL. All test compounds were incubated for 30 min at room temperature with MAO-B prior to enzymatic measurements. The reaction was started with *p*-tyramine (Alfa Aesar A12220) and detected with Amplex red (Invitrogen A12214) using a microplate fluorescence reader (Polarstar BMG Labtech) at an excitation wavelength of 544 nm and detection wavelength of 590 nm over 45 min. Non-specific MAO-B activity was determined in the presence of 1 µM Selegiline.

5.4 Purification of A_{2A}-ΔC and A_{2A}-PSB2-bRIL for Llama Immunization

The A_{2A}AR constructs were expressed and purified as previously described for crystallization experiments but without the addition of any stabilizing ligand and with only 150 mM NaCl in the elution buffer. Protein quantification was done by Bradford assay with BSA as reference.[232]

6 References

[1] Hauser, A. S.; Attwood, M. M.; Rask-Andersen, M.; Schiöth, H. B.; Gloriam, D. E. Trends in GPCR drug discovery: new agents, targets and indications, *Nat. Rev. Drug Discov.* **2017**, *16* (12), 829–842.

[2] Molday, R. S. Photoreceptor membrane proteins, phototransduction, and retinal degenerative diseases. The Friedenwald Lecture, *Invest. Ophthalmol. Vis. Sci.* **1998**, *39* (13), 2491–2513.

[3] Zarzycka, B.; Zaidi, S. A.; Roth, B. L.; Katritch, V. Harnessing ion-binding sites for GPCR pharmacology, *Pharmacol. Rev.* **2019**, *71* (4), 571–595.

[4] Martin, B.; Maturana, R. L. de; Brenneman, R.; Walent, T.; Mattson, M. P.; Maudsley, S. Class II G protein-coupled receptors and their ligands in neuronal function and protection, *Neuromolecular Med.* **2005**, *7* (1-2), 3–36.

[5] Beaulieu, J.-M.; Espinoza, S.; Gainetdinov, R. R. Dopamine receptors - IUPHAR Review 13, *Br. J. Pharmacol.* **2015**, *172* (1), 1–23.

[6] Cox, B. M.; Christie, M. J.; Devi, L.; Toll, L.; Traynor, J. R. Challenges for opioid receptor nomenclature: IUPHAR Review 9, *Br. J. Pharmacol.* **2015**, *172* (2), 317–323.

[7] Murphy, P. M.; Baggiolini, M.; Charo, I. F.; Hébert, C. A.; Horuk, R.; Matsushima, K.; Miller, L. H.; Oppenheim, J. J.; Power, C. A. International union of pharmacology. XXII. Nomenclature for chemokine receptors, *Pharmacol. Rev.* **2000**, *52* (1), 145–176.

[8] Attwood, T. K.; Findlay, J. B. Fingerprinting G-protein-coupled receptors, *Protein Eng.* **1994**, *7* (2), 195–203.

[9] Foord, S. M.; Bonner, T. I.; Neubig, R. R.; Rosser, E. M.; Pin, J.-P.; Davenport, A. P.; Spedding, M.; Harmar, A. J. International Union of Pharmacology. XLVI. G protein-coupled receptor list, *Pharmacol. Rev.* **2005**, *57* (2), 279–288.

[10] Katritch, V.; Cherezov, V.; Stevens, R. C. Structure-function of the G protein-coupled receptor superfamily, *Annu. Rev. Pharmacol. Toxicol.* **2013**, *53*, 531–556.

[11] Schiöth, H. B.; Fredriksson, R. The GRAFS classification system of G-protein coupled receptors in comparative perspective, *Gen. Comp. Endocrinol.* **2005**, *142* (1-2), 94–101.

[12] Fredriksson, R.; Lagerström, M. C.; Lundin, L.-G.; Schiöth, H. B. The G-protein-coupled receptors in the human genome form five main families. Phylogenetic analysis, paralogon groups, and fingerprints, *Mol. Pharmacol.* **2003**, *63* (6), 1256–1272.

[13] UniProt: the universal protein knowledgebase in 2021, *Nucleic Acids Res.* **2021**, *49* (D1), D480-D489.

[14] Stevens, R. C.; Cherezov, V.; Katritch, V.; Abagyan, R.; Kuhn, P.; Rosen, H.; Wüthrich, K. The GPCR Network: a large-scale collaboration to determine human GPCR structure and function, *Nat. Rev. Drug Discov.* **2013**, *12* (1), 25–34.

[15] Neves, S. R.; Ram, P. T.; Iyengar, R. G protein pathways, *Science* **2002**, *296* (5573), 1636–1639.

[16] Mystek, P.; Rysiewicz, B.; Gregrowicz, J.; Dziedzicka-Wasylewska, M.; Polit, A. Gγ and Gα identity dictate a G-protein heterotrimer plasma membrane targeting, *Cells* **2019**, *8* (10).

[17] Oldham, W. M.; Hamm, H. E. Heterotrimeric G protein activation by G-protein-coupled receptors, *Nat. Rev. Mol. Cell Biol.* **2008**, *9* (1), 60–71.

[18] Smrcka, A. V. G protein βγ subunits: central mediators of G protein-coupled receptor signaling, *Cell. Mol. Life Sci.* **2008**, *65* (14), 2191–2214.

[19] Rajagopal, S.; Shenoy, S. K. GPCR desensitization: Acute and prolonged phases, *Cell. Signal.* **2018**, *41*, 9–16.

[20] Mundell, S. J.; Luo, J.; Benovic, J. L.; Conley, P. B.; Poole, A. W. Distinct clathrin-coated pits sort different G protein-coupled receptor cargo, *Traffic* **2006**, *7* (10), 1420–1431.

[21] Wei, H.; Ahn, S.; Shenoy, S. K.; Karnik, S. S.; Hunyady, L.; Luttrell, L. M.; Lefkowitz, R. J. Independent beta-arrestin 2 and G protein-mediated pathways for angiotensin II activation of extracellular signal-regulated kinases 1 and 2, *Proc. Natl. Acad. Sci. U. S. A.* **2003**, *100* (19), 10782–10787.

[22] Rajagopal, S.; Kim, J.; Ahn, S.; Craig, S.; Lam, C. M.; Gerard, N. P.; Gerard, C.; Lefkowitz, R. J. Beta-arrestin- but not G protein-mediated signaling by the "decoy" receptor CXCR7, *Proc. Natl. Acad. Sci. U. S. A.* **2010**, *107* (2), 628–632.

[23] Shenoy, S. K.; Drake, M. T.; Nelson, C. D.; Houtz, D. A.; Xiao, K.; Madabushi, S.; Reiter, E.; Premont, R. T.; Lichtarge, O.; Lefkowitz, R. J. beta-arrestin-dependent, G protein-independent ERK1/2 activation by the beta2 adrenergic receptor, *J. Biol. Chem.* **2006**, *281* (2), 1261–1273.

[24] Hilger, D.; Masureel, M.; Kobilka, B. K. Structure and dynamics of GPCR signaling complexes, *Nat. Struct. Mol. Biol.* **2018**, *25* (1), 4–12.

[25] Eishingdrelo, H.; Kongsamut, S. Minireview: Targeting GPCR activated ERK pathways for drug discovery, *Curr. Chem. Genom. Transl. Med.* **2013**, *7*, 9–15.

[26] Gurevich, V. V.; Gurevich, E. V. Biased GPCR signaling: Possible mechanisms and inherent limitations, *Pharmacol. Ther.* **2020**, *211*, 107540.

[27] Grundmann, M.; Merten, N.; Malfacini, D.; Inoue, A.; Preis, P.; Simon, K.; Rüttiger, N.; Ziegler, N.; Benkel, T.; Schmitt, N. K.; Ishida, S.; Müller, I.; Reher, R.; Kawakami, K.; Inoue, A.; Rick, U.; Kühl, T.; Imhof, D.; Aoki, J.; König, G. M. et al. Lack of beta-arrestin signaling in the absence of active G proteins, *Nat. Commun.* **2018**, *9* (1), 341.

[28] Gutkind, J. S.; Kostenis, E. Arrestins as rheostats of GPCR signalling, *Nat. Rev. Mol. Cell Biol.* **2018**, *19* (10), 615–616.

[29] Zhao, S.; Wu, B.; Stevens, R. C. Advancing chemokine GPCR structure based drug discovery, *Structure* **2019**, *27* (3), 405–408.

[30] Burnstock, G. Introduction to purinergic signaling, *Methods Mol. Biol.* **2020**, *2041*, 1–15.

[31] Filippo, E. de; Hinz, S.; Pellizzari, V.; Deganutti, G.; El-Tayeb, A.; Navarro, G.; Franco, R.; Moro, S.; Schiedel, A. C.; Müller, C. E. A2A and A2B adenosine receptors: The extracellular loop 2 determines high (A2A) or low affinity (A2B) for adenosine, *Biochem. Pharmacol.* **2020**, *172*, 113718.

[32] Müller, C. E.; Jacobson, K. A. Recent developments in adenosine receptor ligands and their potential as novel drugs, *Biochim. Biophys. Acta* **2011**, *1808* (5), 1290–1308.

[33] Chen, J.-F.; Eltzschig, H. K.; Fredholm, B. B. Adenosine receptors as drug targets-what are the challenges?, *Nature reviews. Drug discovery* **2013**, *12* (4), 265–286.

[34] Fredholm, B. B.; Arslan, G.; Halldner, L.; Kull, B.; Schulte, G.; Wasserman, W. Structure and function of adenosine receptors and their genes, *Naunyn Schmiedebergs. Arch. Pharmacol.* **2000**, *362* (4-5), 364–374.

[35] Jacobson, K. A.; Tosh, D. K.; Jain, S.; Gao, Z.-G. Historical and current adenosine receptor agonists in preclinical and clinical development, *Front. Cell. Neurosci.* **2019**, *13*, 124.

[36] Hauser, R. A.; Hattori, N.; Fernandez, H.; Isaacson, S. H.; Mochizuki, H.; Rascol, O.; Stocchi, F.; Li, J.; Mori, A.; Nakajima, Y.; Ristuccia, R.; LeWitt, P. Efficacy of istradefylline, an adenosine A2A receptor antagonist, as adjunctive therapy to levodopa in Parkinson's Disease: A pooled analysis of 8 phase 2b/3 Trials, *J. Parkinsons. Dis.* **2021**, *11* (4), 1663–1675.

[37] Allard, D.; Turcotte, M.; Stagg, J. Targeting A2 adenosine receptors in cancer, *Immunol. Cell Biol.* **2017**, *95* (4), 333–339.

[38] Alnouri, M. W.; Jepards, S.; Casari, A.; Schiedel, A. C.; Hinz, S.; Müller, C. E. Selectivity is species-dependent: Characterization of standard agonists and antagonists at human, rat, and mouse adenosine receptors, *Purinergic Signal.* **2015**, *11* (3), 389–407.

[39] Dugger, B. N.; Dickson, D. W. Pathology of neurodegenerative diseases, *Cold Spring Harb. Perspect. Biol.* **2017**, *9* (7).

[40] Hou, Y.; Dan, X.; Babbar, M.; Wei, Y.; Hasselbalch, S. G.; Croteau, D. L.; Bohr, V. A. Ageing as a risk factor for neurodegenerative disease, *Nat. Rev. Neurol.* **2019**, *15* (10), 565–581.

[41] Feigin, V. L.; Nichols, E.; Alam, T.; Bannick, M. S.; Beghi, E.; Blake, N.; Culpepper, W. J.; Dorsey, E. R.; Elbaz, A.; Ellenbogen, R. G.; Fisher, J. L.; Fitzmaurice, C.; Giussani, G.; Glennie, L.; James, S. L.; Johnson, C. O.; Kassebaum, N. J.; Logroscino, G.; Marin, B.; Mountjoy-Venning, W. C. et

al. Global, regional, and national burden of neurological disorders, 1990–2016: a systematic analysis for the Global Burden of Disease Study 2016, *Lancet Neurol.* **2019**, *18* (5), 459–480.

[42] Merighi, S.; Borea, P. A.; Varani, K.; Vincenzi, F.; Jacobson, K. A.; Gessi, S. A2A adenosine receptor antagonists in neurodegenerative diseases, *Curr. Med. Chem.* **2021**.

[43] Poewe, W.; Seppi, K.; Tanner, C. M.; Halliday, G. M.; Brundin, P.; Volkmann, J.; Schrag, A.-E.; Lang, A. E. Parkinson Disease, *Nat. Rev. Dis. Primers* **2017**, *3*, 17013.

[44] Schiffmann, S. N.; Fisone, G.; Moresco, R.; Cunha, R. A.; Ferré, S. Adenosine A2A receptors and basal ganglia physiology, *Prog. Neurobiol.* **2007**, *83* (5), 277–292.

[45] Connolly, B. S.; Lang, A. E. Pharmacological treatment of Parkinson disease: a review, *JAMA* **2014**, *311* (16), 1670–1683.

[46] Youdim, M. B. H.; Edmondson, D.; Tipton, K. F. The therapeutic potential of monoamine oxidase inhibitors, *Nat. Rev. Neurosci.* **2006**, *7* (4), 295–309.

[47] Sayre, L. M.; Perry, G.; Smith, M. A. Oxidative stress and neurotoxicity, *Chem. Res. Toxicol.* **2008**, *21* (1), 172–188.

[48] Finberg, J. P. M.; Rabey, J. M. Inhibitors of MAO-A and MAO-B in psychiatry and neurology, *Front. Pharmacol.* **2016**, *7*, 340.

[49] Yoon, B.-E.; Woo, J.; Chun, Y.-E.; Chun, H.; Jo, S.; Bae, J. Y.; An, H.; Min, J. O.; Oh, S.-J.; Han, K.-S.; Kim, H. Y.; Kim, T.; Kim, Y. S.; Bae, Y. C.; Lee, C. J. Glial GABA, synthesized by monoamine oxidase B, mediates tonic inhibition, *J. Physiol.* **2014**, *592* (22), 4951–4968.

[50] Cho, H.-U.; Kim, S.; Sim, J.; Yang, S.; An, H.; Nam, M.-H.; Jang, D.-P.; Lee, C. J. Redefining differential roles of MAO-A in dopamine degradation and MAO-B in tonic GABA synthesis, *Exp. Mol. Med.* **2021**, *53* (7), 1148–1158.

[51] Franco, R.; Navarro, G. Adenosine A2A receptor antagonists in neurodegenerative diseases: huge potential and huge challenges, *Front. Psychiatry* **2018**, *9*, 68.

[52] Villar-Menéndez, I.; Porta, S.; Buira, S. P.; Pereira-Veiga, T.; Díaz-Sánchez, S.; Albasanz, J. L.; Ferrer, I.; Martín, M.; Barrachina, M. Increased striatal

adenosine A2A receptor levels is an early event in Parkinson's disease-related pathology and it is potentially regulated by miR-34b, *Neurobiol. Dis.* **2014**, *69*, 206–214.

[53] Calon, F.; Dridi, M.; Hornykiewicz, O.; Bédard, P. J.; Rajput, A. H.; Di Paolo, T. Increased adenosine A2A receptors in the brain of Parkinson's disease patients with dyskinesias, *Brain* **2004**, *127* (Pt 5), 1075–1084.

[54] Fuxe, K.; Agnati, L. F.; Jacobsen, K.; Hillion, J.; Canals, M.; Torvinen, M.; Tinner-Staines, B.; Staines, W.; Rosin, D.; Terasmaa, A.; Popoli, P.; Leo, G.; Vergoni, V.; Lluis, C.; Ciruela, F.; Franco, R.; Ferré, S. Receptor heteromerization in adenosine A2A receptor signaling: relevance for striatal function and Parkinson's disease, *Neurology* **2003**, *61* (11 Suppl 6), S19-23.

[55] Ferré, S.; Quiroz, C.; Woods, A. S.; Cunha, R.; Popoli, P.; Ciruela, F.; Lluis, C.; Franco, R.; Azdad, K.; Schiffmann, S. N. An update on adenosine A2A-dopamine D2 receptor interactions: implications for the function of G protein-coupled receptors, *Curr. Pharm. Des.* **2008**, *14* (15), 1468–1474.

[56] Falzone, L.; Salomone, S.; Libra, M. Evolution of cancer pharmacological treatments at the turn of the third millennium, *Front. Pharmacol.* **2018**, *9*, 1300.

[57] Pardoll, D. M. The blockade of immune checkpoints in cancer immunotherapy, *Nat. Rev. Cancer* **2012**, *12* (4), 252–264.

[58] Marhelava, K.; Pilch, Z.; Bajor, M.; Graczyk-Jarzynka, A.; Zagozdzon, R. Targeting negative and positive immune checkpoints with monoclonal antibodies in therapy of cancer, *Cancers (Basel)* **2019**, *11* (11).

[59] Leone, R. D.; Lo, Y.-C.; Powell, J. D. A2aR antagonists: Next generation checkpoint blockade for cancer immunotherapy, *Comput. Struct. Biotechnol. J.* **2015**, *13*, 265–272.

[60] Gessi, S.; Varani, K.; Merighi, S.; Ongini, E.; Borea, P. A. A(2A) adenosine receptors in human peripheral blood cells, *Br. J. Pharmacol.* **2000**, *129* (1), 2–11.

[61] Koshiba, M.; Kojima, H.; Huang, S.; Apasov, S.; Sitkovsky, M. V. Memory of extracellular adenosine A2A purinergic receptor-mediated signaling in murine T cells, *J. Biol. Chem.* **1997**, *272* (41), 25881–25889.

[62] Ohta, A.; Sitkovsky, M. Extracellular adenosine-mediated modulation of regulatory T cells, *Front. Immunol.* **2014**, *5*, 304.

[63] Bergamin, L. S.; Braganhol, E.; Zanin, R. F.; Edelweiss, M. I. A.; Battastini, A. M. O. Ectonucleotidases in tumor cells and tumor-associated immune cells: an overview, *J. Biomed. Biotechnol.* **2012**, *2012*, 959848.

[64] Zhang, J.; Yan, W.; Duan, W.; Wüthrich, K.; Cheng, J. Tumor immunotherapy using A2A adenosine receptor antagonists, *Pharmaceuticals* **2020**, *13* (9).

[65] Reddy, A. S.; Zhang, S. Polypharmacology: drug discovery for the future, *Expert Rev. Clin. Pharmacol.* **2013**, *6* (1), 41–47.

[66] Roth, B. L.; Sheffler, D. J.; Kroeze, W. K. Magic shotguns versus magic bullets: selectively non-selective drugs for mood disorders and schizophrenia, *Nat. Rev. Drug Discov.* **2004**, *3* (4), 353–359.

[67] Besnard, J.; Ruda, G. F.; Setola, V.; Abecassis, K.; Rodriguiz, R. M.; Huang, X.-P.; Norval, S.; Sassano, M. F.; Shin, A. I.; Webster, L. A.; Simeons, F. R. C.; Stojanovski, L.; Prat, A.; Seidah, N. G.; Constam, D. B.; Bickerton, G. R.; Read, K. D.; Wetsel, W. C.; Gilbert, I. H.; Roth, B. L. et al. Automated design of ligands to polypharmacological profiles, *Nature* **2012**, *492* (7428), 215–220.

[68] Apsel, B.; Blair, J. A.; Gonzalez, B.; Nazif, T. M.; Feldman, M. E.; Aizenstein, B.; Hoffman, R.; Williams, R. L.; Shokat, K. M.; Knight, Z. A. Targeted polypharmacology: discovery of dual inhibitors of tyrosine and phosphoinositide kinases, *Nat. Chem. Biol.* **2008**, *4* (11), 691–699.

[69] Pisani, L.; Catto, M.; Leonetti, F.; Nicolotti, O.; Stefanachi, A.; Campagna, F.; Carotti, A. Targeting monoamine oxidases with multipotent ligands: an emerging strategy in the search of new drugs against neurodegenerative diseases, *Curr. Med. Chem.* **2011**, *18* (30), 4568–4587.

[70] Steingold, J. M.; Hatfield, S. M. Targeting hypoxia-A2A adenosinergic immunosuppression of antitumor T cells during cancer immunotherapy, *Front. Immunol.* **2020**, *11*, 570041.

[71] Seitz, L.; Jin, L.; Leleti, M.; Ashok, D.; Jeffrey, J.; Rieger, A.; Tiessen, R. G.; Arold, G.; Tan, J. B. L.; Powers, J. P.; Walters, M. J.; Karakunnel, J. Safety, tolerability, and pharmacology of AB928, a novel dual adenosine receptor antagonist, in a randomized, phase 1 study in healthy volunteers, *Invest. New Drugs* **2019**, *37* (4), 711–721.

[72] Palczewski, K.; Kumasaka, T.; Hori, T.; Behnke, C. A.; Motoshima, H.; Fox, B. A.; Le Trong, I.; Teller, D. C.; Okada, T.; Stenkamp, R. E.; Yamamoto, M.; Miyano, M. Crystal structure of rhodopsin: A G protein-coupled receptor, *Science* **2000**, *289* (5480), 739–745.

[73] Rasmussen, S. G. F.; Choi, H.-J.; Rosenbaum, D. M.; Kobilka, T. S.; Thian, F. S.; Edwards, P. C.; Burghammer, M.; Ratnala, V. R. P.; Sanishvili, R.; Fischetti, R. F.; Schertler, G. F. X.; Weis, W. I.; Kobilka, B. K. Crystal structure of the human beta2 adrenergic G-protein-coupled receptor, *Nature* **2007**, *450* (7168), 383–387.

[74] Warne, T.; Serrano-Vega, M. J.; Baker, J. G.; Moukhametzianov, R.; Edwards, P. C.; Henderson, R.; Leslie, A. G. W.; Tate, C. G.; Schertler, G. F. X. Structure of a beta1-adrenergic G-protein-coupled receptor, *Nature* **2008**, *454* (7203), 486–491.

[75] Kobilka, B. The structural basis of G-protein-coupled receptor signaling (Nobel Lecture), *Angew. Chem. Int. Ed.* **2013**, *52* (25), 6380–6388.

[76] Zhao, Q.; Wu, B. Ice breaking in GPCR structural biology, *Acta Pharmacol. Sin.* **2012**, *33* (3), 324–334.

[77] Rosenbusch, J. P. Stability of membrane proteins: relevance for the selection of appropriate methods for high-resolution structure determinations, *J. Struct. Biol.* **2001**, *136* (2), 144–157.

[78] Sarkar, C. A.; Dodevski, I.; Kenig, M.; Dudli, S.; Mohr, A.; Hermans, E.; Plückthun, A. Directed evolution of a G protein-coupled receptor for expression, stability, and binding selectivity, *Proc. Natl. Acad. Sci. U. S. A.* **2008**, *105* (39), 14808–14813.

[79] Dodevski, I.; Plückthun, A. Evolution of three human GPCRs for higher expression and stability, *J. Mol. Biol.* **2011**, *408* (4), 599–615.

[80] Claff, T.; Yu, J.; Blais, V.; Patel, N.; Martin, C.; Wu, L.; Han, G. W.; Holleran, B. J.; van der Poorten, O.; White, K. L.; Hanson, M. A.; Sarret, P.; Gendron, L.; Cherezov, V.; Katritch, V.; Ballet, S.; Liu, Z.-J.; Müller, C. E.; Stevens, R. C. Elucidating the active δ-opioid receptor crystal structure with peptide and small-molecule agonists, *Sci. Adv.* **2019**, *5* (11), eaax9115.

[81] Popov, P.; Peng, Y.; Shen, L.; Stevens, R. C.; Cherezov, V.; Liu, Z.-J.; Katritch, V. Computational design of thermostabilizing point mutations for G protein-coupled receptors, *Elife* **2018**, *7*.

[82] Hino, T.; Arakawa, T.; Iwanari, H.; Yurugi-Kobayashi, T.; Ikeda-Suno, C.; Nakada-Nakura, Y.; Kusano-Arai, O.; Weyand, S.; Shimamura, T.; Nomura, N.; Cameron, A. D.; Kobayashi, T.; Hamakubo, T.; Iwata, S.; Murata, T. G-protein-coupled receptor inactivation by an allosteric inverse-agonist antibody, *Nature* **2012**, *482* (7384), 237–240.

[83] Rasmussen, S. G. F.; Choi, H.-J.; Fung, J. J.; Pardon, E.; Casarosa, P.; Chae, P. S.; Devree, B. T.; Rosenbaum, D. M.; Thian, F. S.; Kobilka, T. S.; Schnapp, A.; Konetzki, I.; Sunahara, R. K.; Gellman, S. H.; Pautsch, A.; Steyaert, J.; Weis, W. I.; Kobilka, B. K. Structure of a nanobody-stabilized active state of the β(2) adrenoceptor, *Nature* **2011**, *469* (7329), 175–180.

[84] Che, T.; English, J.; Krumm, B. E.; Kim, K.; Pardon, E.; Olsen, R. H. J.; Wang, S.; Zhang, S.; Diberto, J. F.; Sciaky, N.; Carroll, F. I.; Steyaert, J.; Wacker, D.; Roth, B. L. Nanobody-enabled monitoring of kappa opioid receptor states, *Nat. Commun.* **2020**, *11* (1), 1145.

[85] Che, T.; Majumdar, S.; Zaidi, S. A.; Ondachi, P.; McCorvy, J. D.; Wang, S.; Mosier, P. D.; Uprety, R.; Vardy, E.; Krumm, B. E.; Han, G. W.; Lee, M.-Y.; Pardon, E.; Steyaert, J.; Huang, X.-P.; Strachan, R. T.; Tribo, A. R.; Pasternak, G. W.; Carroll, F. I.; Stevens, R. C. et al. Structure of the nanobody-stabilized active state of the kappa opioid receptor, *Cell* **2018**, *172* (1-2), 55-67.e15.

[86] Zhang, X.; Stevens, R. C.; Xu, F. The importance of ligands for G protein-coupled receptor stability, *Trends Biochem. Sci.* **2015**, *40* (2), 79–87.

[87] Lee, S.; Ghosh, S.; Jana, S.; Robertson, N.; Tate, C. G.; Vaidehi, N. How do branched detergents stabilize GPCRs in micelles?, *Biochemistry* **2020**, *59* (23), 2125–2134.

[88] Xiang, J.; Chun, E.; Liu, C.; Jing, L.; Al-Sahouri, Z.; Zhu, L.; Liu, W. Successful strategies to determine high-resolution structures of GPCRs, *Trends Pharmacol. Sci.* **2016**, *37* (12), 1055–1069.

[89] Nanev, C. Peculiarities of protein crystal nucleation and growth, *Crystals (Basel)* **2018**, *8* (11), 422.

[90] Chun, E.; Thompson, A. A.; Liu, W.; Roth, C. B.; Griffith, M. T.; Katritch, V.; Kunken, J.; Xu, F.; Cherezov, V.; Hanson, M. A.; Stevens, R. C. Fusion partner toolchest for the stabilization and crystallization of G protein-coupled receptors, *Structure* **2012**, *20* (6), 967–976.

[91] Song, G.; Yang, D.; Wang, Y.; Graaf, C. de; Zhou, Q.; Jiang, S.; Liu, K.; Cai, X.; Dai, A.; Lin, G.; Liu, D.; Wu, F.; Wu, Y.; Zhao, S.; Ye, L.; Han, G. W.; Lau, J.; Wu, B.; Hanson, M. A.; Liu, Z.-J. et al. Human GLP-1 receptor transmembrane domain structure in complex with allosteric modulators, *Nature* **2017**, *546* (7657), 312–315.

[92] Yin, X.; Xu, H.; Hanson, M.; Liu, W. GPCR crystallization using lipidic cubic phase technique, *Curr. Pharm. Biotechnol.* **2014**, *15* (10), 971–979.

[93] Danev, R.; Belousoff, M.; Liang, Y.-L.; Zhang, X.; Eisenstein, F.; Wootten, D.; Sexton, P. M. Routine sub-2.5 Å cryo-EM structure determination of GPCRs, *Nat. Commun.* **2021**, *12* (1), 4333.

[94] Zhang, X.; Johnson, R. M.; Drulyte, I.; Yu, L.; Kotecha, A.; Danev, R.; Wootten, D.; Sexton, P. M.; Belousoff, M. J. Evolving cryo-EM structural approaches for GPCR drug discovery, *Structure* **2021**, *29* (9), 963-974.e6.

[95] García-Nafría, J.; Lee, Y.; Bai, X.; Carpenter, B.; Tate, C. G. Cryo-EM structure of the adenosine A2A receptor coupled to an engineered heterotrimeric G protein, *Elife* **2018**, *7*.

[96] Yin, W.; Li, Z.; Jin, M.; Yin, Y.-L.; Waal, P. W. de; Pal, K.; Yin, Y.; Gao, X.; He, Y.; Gao, J.; Wang, X.; Zhang, Y.; Zhou, H.; Melcher, K.; Jiang, Y.; Cong, Y.; Edward Zhou, X.; Yu, X.; Eric Xu, H. A complex structure of arrestin-2 bound to a G protein-coupled receptor, *Cell Res.* **2019**, *29* (12), 971–983.

[97] Jeong, E.; Kim, Y.; Jeong, J.; Cho, Y. Structure of the class C orphan GPCR GPR158 in complex with RGS7-Gβ5, *Nat. Commun.* **2021**, *12* (1), 6805.

[98] García-Nafría, J.; Tate, C. G. Structure determination of GPCRs: cryo-EM compared with X-ray crystallography, *Biochem. Soc. Trans.* **2021**, *49* (5), 2345–2355.

[99] Zhang, K.; Wu, H.; Hoppe, N.; Manglik, A.; Cheng, Y., *Fusion protein strategies for cryo-EM study of G protein-coupled receptors*, **2021**.

[100] Xu, J.; Chen, G.; Wang, H.; Cao, S.; Heng, J.; Deupi, X.; Du, Y.; Kobilka, B. K., *Calcineurin-fusion facilitates Cryo-EM structure determination of a family A GPCR*, **2022**.

[101] Robertson, M. J.; Papasergi-Scott, M.; He, F.; Seven, A. B.; Meyerowitz, J. G.; Panova, O.; Peroto, M. C.; Che, T.; Skiniotis, G., *Structure determination of inactive-state GPCRs with a universal nanobody*, **2021**.

[102] Sherbiny, F. F.; Schiedel, A. C.; Maass, A.; Müller, C. E. Homology modelling of the human adenosine A2B receptor based on X-ray structures of bovine rhodopsin, the beta2-adrenergic receptor and the human adenosine A2A receptor, *J. Comput. Aided Mol. Des.* **2009**, *23* (11), 807–828.

[103] Jones, K. R.; Choi, U.; Gao, J.-L.; Thompson, R. D.; Rodman, L. E.; Malech, H. L.; Kang, E. M. A novel method for screening adenosine receptor specific agonists for use in adenosine drug development, *Sci. Rep.* **2017**, *7*, 44816.

[104] Seibt, B. F.; Schiedel, A. C.; Thimm, D.; Hinz, S.; Sherbiny, F. F.; Müller, C. E. The second extracellular loop of GPCRs determines subtype-selectivity and controls efficacy as evidenced by loop exchange study at A2 adenosine receptors, *Biochem. Pharmacol.* **2013**, *85* (9), 1317–1329.

[105] Jaakola, V.-P.; Griffith, M. T.; Hanson, M. A.; Cherezov, V.; Chien, E. Y. T.; Lane, J. R.; IJzerman, A. P.; Stevens, R. C. The 2.6 angstrom crystal structure of a human A2A adenosine receptor bound to an antagonist, *Science* **2008**, *322* (5905), 1211–1217.

[106] Berman, H. M.; Westbrook, J.; Feng, Z.; Gilliland, G.; Bhat, T. N.; Weissig, H.; Shindyalov, I. N.; Bourne, P. E. The Protein Data Bank, *Nucleic Acids Res.* **2000**, *28* (1), 235–242.

[107] Claff, T.; Klapschinski, T. A.; Subhramanyam, U. K. T.; Vaaßen, V. J.; Schlegel, J. G.; Vielmuth, C.; Voß, J. H.; Labahn, J.; Müller, C. E. Single stabilizing point mutation enables high-resolution co-crystal Structures of the adenosine A2A receptor with peladenant conjugates, *Angew. Chem. Int. Ed.* **2022**, e202115545.

[108] Amelia, T.; van Veldhoven, J. P. D.; Falsini, M.; Liu, R.; Heitman, L. H.; van Westen, G. J. P.; Segala, E.; Verdon, G.; Cheng, R. K. Y.; Cooke, R. M.; van der Es, D.; IJzerman, A. P. Crystal structure and subsequent ligand design of a nonriboside partial agonist bound to the adenosine A2A receptor, *J. Med. Chem.* **2021**, *64* (7), 3827–3842.

[109] Lebon, G.; Warne, T.; Edwards, P. C.; Bennett, K.; Langmead, C. J.; Leslie, A. G. W.; Tate, C. G. Agonist-bound adenosine A2A receptor structures reveal common features of GPCR activation, *Nature* **2011**, *474* (7352), 521–525.

[110] Xu, F.; Wu, H.; Katritch, V.; Han, G. W.; Jacobson, K. A.; Gao, Z.-G.; Cherezov, V.; Stevens, R. C. Structure of an agonist-bound human A2A adenosine receptor, *Science* **2011**, *332* (6027), 322–327.

[111] Lebon, G.; Edwards, P. C.; Leslie, A. G. W.; Tate, C. G. Molecular determinants of CGS21680 binding to the human adenosine A2A receptor, *Mol. Pharmacol.* **2015**, *87* (6), 907–915.

[112] Carpenter, B.; Nehmé, R.; Warne, T.; Leslie, A. G. W.; Tate, C. G. Structure of the adenosine A(2A) receptor bound to an engineered G protein, *Nature* **2016**, *536* (7614), 104–107.

[113] Carpenter, B.; Lebon, G. Human adenosine A2A receptor: Molecular mechanism of ligand binding and activation, *Front. Pharmacol.* **2017**, *8*, 898.

[114] Dror, R. O.; Arlow, D. H.; Maragakis, P.; Mildorf, T. J.; Pan, A. C.; Xu, H.; Borhani, D. W.; Shaw, D. E. Activation mechanism of the β2-adrenergic receptor, *Proc. Natl. Acad. Sci. U. S. A.* **2011**, *108* (46), 18684–18689.

[115] Hauser, A. S.; Kooistra, A. J.; Munk, C.; Heydenreich, F. M.; Veprintsev, D. B.; Bouvier, M.; Babu, M. M.; Gloriam, D. E. GPCR activation mechanisms across classes and macro/microscales, *Nat. Struct. Mol. Biol.* **2021**, *28* (11), 879–888.

[116] Manglik, A.; Kruse, A. C. Structural basis for G protein-coupled receptor activation, *Biochemistry* **2017**, *56* (42), 5628–5634.

[117] Doré, A. S.; Robertson, N.; Errey, J. C.; Ng, I.; Hollenstein, K.; Tehan, B.; Hurrell, E.; Bennett, K.; Congreve, M.; Magnani, F.; Tate, C. G.; Weir, M.; Marshall, F. H. Structure of the adenosine A(2A) receptor in complex with ZM241385 and the xanthines XAC and caffeine, *Structure* **2011**, *19* (9), 1283–1293.

[118] Langmead, C. J.; Andrews, S. P.; Congreve, M.; Errey, J. C.; Hurrell, E.; Marshall, F. H.; Mason, J. S.; Richardson, C. M.; Robertson, N.; Zhukov, A.; Weir, M. Identification of novel adenosine A(2A) receptor antagonists by virtual screening, *J. Med. Chem.* **2012**, *55* (5), 1904–1909.

[119] Munk, C.; Isberg, V.; Mordalski, S.; Harpsøe, K.; Rataj, K.; Hauser, A. S.; Kolb, P.; Bojarski, A. J.; Vriend, G.; Gloriam, D. E. GPCRdb: the G protein-coupled receptor database - an introduction, *Br. J. Pharmacol.* **2016**, *173* (14), 2195–2207.

[120] Liu, W.; Chun, E.; Thompson, A. A.; Chubukov, P.; Xu, F.; Katritch, V.; Han, G. W.; Roth, C. B.; Heitman, L. H.; IJzerman, A. P.; Cherezov, V.; Stevens, R. C. Structural basis for allosteric regulation of GPCRs by sodium ions, *Science* **2012**, *337* (6091), 232–236.

[121] Melnikov, I.; Polovinkin, V.; Kovalev, K.; Gushchin, I.; Shevtsov, M.; Shevchenko, V.; Mishin, A.; Alekseev, A.; Rodriguez-Valera, F.; Borshchevskiy, V.; Cherezov, V.; Leonard, G. A.; Gordeliy, V.; Popov, A. Fast iodide-SAD phasing for high-throughput membrane protein structure determination, *Sci. Adv.* **2017**, *3* (5), e1602952.

[122] Batyuk, A.; Galli, L.; Ishchenko, A.; Han, G. W.; Gati, C.; Popov, P. A.; Lee, M.-Y.; Stauch, B.; White, T. A.; Barty, A.; Aquila, A.; Hunter, M. S.; Liang, M.; Boutet, S.; Pu, M.; Liu, Z.-J.; Nelson, G.; James, D.; Li, C.; Zhao, Y. et al. Native phasing of x-ray free-electron laser data for a G protein-coupled receptor, *Sci. Adv.* **2016**, *2* (9), e1600292.

[123] Martin-Garcia, J. M.; Conrad, C. E.; Nelson, G.; Stander, N.; Zatsepin, N. A.; Zook, J.; Zhu, L.; Geiger, J.; Chun, E.; Kissick, D.; Hilgart, M. C.; Ogata, C.; Ishchenko, A.; Nagaratnam, N.; Roy-Chowdhury, S.; Coe, J.; Subramanian, G.; Schaffer, A.; James, D.; Ketwala, G. et al. Serial

millisecond crystallography of membrane and soluble protein microcrystals using synchrotron radiation, *IUCrJ* **2017**, *4* (Pt 4), 439–454.

[124] Martin-Garcia, J. M.; Zhu, L.; Mendez, D.; Lee, M.-Y.; Chun, E.; Li, C.; Hu, H.; Subramanian, G.; Kissick, D.; Ogata, C.; Henning, R.; Ishchenko, A.; Dobson, Z.; Zhang, S.; Weierstall, U.; Spence, J. C. H.; Fromme, P.; Zatsepin, N. A.; Fischetti, R. F.; Cherezov, V. et al. High-viscosity injector-based pink-beam serial crystallography of microcrystals at a synchrotron radiation source, *IUCrJ* **2019**, *6* (Pt 3), 412–425.

[125] Broecker, J.; Morizumi, T.; Ou, W.-L.; Klingel, V.; Kuo, A.; Kissick, D. J.; Ishchenko, A.; Lee, M.-Y.; Xu, S.; Makarov, O.; Cherezov, V.; Ogata, C. M.; Ernst, O. P. High-throughput in situ X-ray screening of and data collection from protein crystals at room temperature and under cryogenic conditions, *Nat. Protoc.* **2018**, *13* (2), 260–292.

[126] White, K. L.; Eddy, M. T.; Gao, Z.-G.; Han, G. W.; Lian, T.; Deary, A.; Patel, N.; Jacobson, K. A.; Katritch, V.; Stevens, R. C. Structural connection between activation microswitch and allosteric sodium site in GPCR signaling, *Structure* **2018**, *26* (2), 259-269.e5.

[127] Shimazu, Y.; Tono, K.; Tanaka, T.; Yamanaka, Y.; Nakane, T.; Mori, C.; Terakado Kimura, K.; Fujiwara, T.; Sugahara, M.; Tanaka, R.; Doak, R. B.; Shimamura, T.; Iwata, S.; Nango, E.; Yabashi, M. High-viscosity sample-injection device for serial femtosecond crystallography at atmospheric pressure, *J. Appl. Crystallogr.* **2019**, *52* (Pt 6), 1280–1288.

[128] Ishchenko, A.; Stauch, B.; Han, G. W.; Batyuk, A.; Shiriaeva, A.; Li, C.; Zatsepin, N.; Weierstall, U.; Liu, W.; Nango, E.; Nakane, T.; Tanaka, R.; Tono, K.; Joti, Y.; Iwata, S.; Moraes, I.; Gati, C.; Cherezov, V. Toward G protein-coupled receptor structure-based drug design using X-ray lasers, *IUCrJ* **2019**, *6* (Pt 6), 1106–1119.

[129] Lee, M.-Y.; Geiger, J.; Ishchenko, A.; Han, G. W.; Barty, A.; White, T. A.; Gati, C.; Batyuk, A.; Hunter, M. S.; Aquila, A.; Boutet, S.; Weierstall, U.; Cherezov, V.; Liu, W. Harnessing the power of an X-ray laser for serial crystallography of membrane proteins crystallized in lipidic cubic phase, *IUCrJ* **2020**, *7* (Pt 6), 976–984.

[130] Ihara, K.; Hato, M.; Nakane, T.; Yamashita, K.; Kimura-Someya, T.; Hosaka, T.; Ishizuka-Katsura, Y.; Tanaka, R.; Tanaka, T.; Sugahara, M.; Hirata, K.; Yamamoto, M.; Nureki, O.; Tono, K.; Nango, E.; Iwata, S.; Shirouzu, M. Isoprenoid-chained lipid EROCOC17+4: a new matrix for membrane protein crystallization and a crystal delivery medium in serial femtosecond crystallography, *Sci. Rep.* **2020**, *10* (1), 19305.

[131] Martynowycz, M. W.; Shiriaeva, A.; Ge, X.; Hattne, J.; Nannenga, B. L.; Cherezov, V.; Gonen, T. MicroED structure of the human adenosine receptor determined from a single nanocrystal in LCP, *Proc. Natl. Acad. Sci. U. S. A.* **2021**, *118* (36).

[132] Segala, E.; Guo, D.; Cheng, R. K. Y.; Bortolato, A.; Deflorian, F.; Doré, A. S.; Errey, J. C.; Heitman, L. H.; IJzerman, A. P.; Marshall, F. H.; Cooke, R. M. Controlling the dissociation of ligands from the adenosine A2A receptor through modulation of salt bridge strength, *J. Med. Chem.* **2016**, *59* (13), 6470–6479.

[133] Weinert, T.; Olieric, N.; Cheng, R.; Brünle, S.; James, D.; Ozerov, D.; Gashi, D.; Vera, L.; Marsh, M.; Jaeger, K.; Dworkowski, F.; Panepucci, E.; Basu, S.; Skopintsev, P.; Doré, A. S.; Geng, T.; Cooke, R. M.; Liang, M.; Prota, A. E.; Panneels, V. et al. Serial millisecond crystallography for routine room-temperature structure determination at synchrotrons, *Nat. Commun.* **2017**, *8* (1), 542.

[134] Rucktooa, P.; Cheng, R. K. Y.; Segala, E.; Geng, T.; Errey, J. C.; Brown, G. A.; Cooke, R. M.; Marshall, F. H.; Doré, A. S. Towards high throughput GPCR crystallography: In meso soaking of adenosine A2A receptor crystals, *Sci. Rep.* **2018**, *8* (1), 41.

[135] Cheng, R. K. Y.; Segala, E.; Robertson, N.; Deflorian, F.; Doré, A. S.; Errey, J. C.; Fiez-Vandal, C.; Marshall, F. H.; Cooke, R. M. Structures of human A1 and A2A adenosine receptors with xanthines reveal determinants of selectivity, *Structure* **2017**, *25* (8), 1275-1285.e4.

[136] Congreve, M.; Andrews, S. P.; Doré, A. S.; Hollenstein, K.; Hurrell, E.; Langmead, C. J.; Mason, J. S.; Ng, I. W.; Tehan, B.; Zhukov, A.; Weir, M.; Marshall, F. H. Discovery of 1,2,4-triazine derivatives as adenosine A(2A)

antagonists using structure based drug design, *J. Med. Chem.* **2012**, *55* (5), 1898–1903.

[137] Katritch, V.; Fenalti, G.; Abola, E. E.; Roth, B. L.; Cherezov, V.; Stevens, R. C. Allosteric sodium in class A GPCR signaling, *Trends Biochem. Sci.* **2014**, *39* (5), 233–244.

[138] Hinz, S.; Lacher, S. K.; Seibt, B. F.; Müller, C. E. BAY60-6583 acts as a partial agonist at adenosine A2B receptors, *J. Pharmacol. Exp. Ther.* **2014**, *349* (3), 427–436.

[139] Hori, T.; Okuno, T.; Hirata, K.; Yamashita, K.; Kawano, Y.; Yamamoto, M.; Hato, M.; Nakamura, M.; Shimizu, T.; Yokomizo, T.; Miyano, M.; Yokoyama, S. Na+-mimicking ligands stabilize the inactive state of leukotriene B4 receptor BLT1, *Nat. Chem. Biol.* **2018**, *14* (3), 262–269.

[140] Glukhova, A.; Thal, D. M.; Nguyen, A. T.; Vecchio, E. A.; Jörg, M.; Scammells, P. J.; May, L. T.; Sexton, P. M.; Christopoulos, A. Structure of the adenosine A1 receptor reveals the basis for subtype selectivity, *Cell* **2017**, *168* (5), 867-877.e13.

[141] Barbhaiya, H.; McClain, R.; Ijzerman, A.; Rivkees, S. A. Site-directed mutagenesis of the human A1 adenosine receptor: influences of acidic and hydroxy residues in the first four transmembrane domains on ligand binding, *Mol. Pharmacol.* **1996**, *50* (6), 1635–1642.

[142] Miller-Gallacher, J. L.; Nehmé, R.; Warne, T.; Edwards, P. C.; Schertler, G. F. X.; Leslie, A. G. W.; Tate, C. G. The 2.1 Å resolution structure of cyanopindolol-bound β1-adrenoceptor identifies an intramembrane Na+ ion that stabilises the ligand-free receptor, *PLoS One* **2014**, *9* (3), e92727.

[143] Gao, Z.-G.; IJzerman, A. P. Allosteric modulation of A2A adenosine receptors by amiloride analogues and sodium ions, *Biochem. Pharmacol.* **2000**, *60* (5), 669–676.

[144] Bertarelli, D. C. G.; Diekmann, M.; Hayallah, A. M.; Rüsing, D.; Iqbal, J.; Preiss, B.; Verspohl, E. J.; Müller, C. E. Characterization of human and rodent native and recombinant adenosine A(2B) receptors by radioligand binding studies, *Purinergic signalling* **2006**, *2* (3), 559–571.

[145] Gao, Z.-G.; Melman, N.; Erdmann, A.; Kim, S. G.; Müller, C. E.; IJzerman, A. P.; Jacobson, K. A. Differential allosteric modulation by amiloride analogues of agonist and antagonist binding at A1 and A3 adenosine receptors, *Biochem. Pharmacol.* **2003**, *65* (4), 525–534.

[146] Gao, Z.-G.; Kim, S.-K.; Gross, A. S.; Chen, A.; Blaustein, J. B.; Jacobson, K. A. Identification of essential residues involved in the allosteric modulation of the human A(3) adenosine receptor, *Molecular pharmacology* **2003**, *63* (5), 1021–1031.

[147] Garrity, D. B.; Chang, M. J.; Blissard, G. W. Late promoter selection in the baculovirus gp64 envelope fusion protein gene, *Virology* **1997**, *231* (2), 167–181.

[148] Chambers, A. C.; Aksular, M.; Graves, L. P.; Irons, S. L.; Possee, R. D.; King, L. A. Overview of the baculovirus expression system, *Curr. Protoc. Protein Sci.* **2018**, *91*, 5.4.1-5.4.6.

[149] Audet, M.; Villers, K.; Velasquez, J.; Chu, M.; Hanson, C.; Stevens, R. C. Small-scale approach for precrystallization screening in GPCR X-ray crystallography, *Nat. Protoc.* **2020**, *15* (1), 144–160.

[150] Hopp, T. P.; Prickett, K. S.; Price, V. L.; Libby, R. T.; March, C. J.; Pat Cerretti, D.; Urdal, D. L.; Conlon, P. J. A short polypeptide marker sequence useful for recombinant protein identification and purification, *Biotechnology. (N Y)* **1988**, *6* (10), 1204–1210.

[151] Porath, J.; Carlsson, J.; Olsson, I.; Belfrage, G. Metal chelate affinity chromatography, a new approach to protein fractionation, *Nature* **1975**, *258* (5536), 598–599.

[152] Block, H.; Maertens, B.; Spriestersbach, A.; Brinker, N.; Kubicek, J.; Fabis, R.; Labahn, J.; Schäfer, F. in *Methods in enzymology 0076-6879*, *v. 463* (Eds.: R. R. Burgess, M. P. Deutscher), Elsevier, Amsterdam, **2009**, pp. 439–473.

[153] Kimple, M. E.; Brill, A. L.; Pasker, R. L. Overview of affinity tags for protein purification, *Curr. Protoc. Protein Sci.* **2013**, *73*, 9.9.1-9.9.23.

[154] Sulkowski, E. Purification of proteins by IMAC, *Trends Biotechnol.* **1985**, *3* (1), 1–7.

[155] Lo, A. T. Y.; Hy, T.; Pr, B. Advanced uses of IMAC affinity chromatography, *Austin Chromatogr.* **2016**, *3* (1), 1042.

[156] Cheung, R. C. F.; Wong, J. H.; Ng, T. B. Immobilized metal ion affinity chromatography: a review on its applications, *Appl. Microbiol. Biotechnol.* **2012**, *96* (6), 1411–1420.

[157] Levi, V.; González Flecha, F. Reversible fast-dimerization of bovine serum albumin detected by fluorescence resonance energy transfer, *Biochim. Biophys. Acta Proteins Proteom.* **2002**, *1599* (1-2), 141–148.

[158] Rath, A.; Glibowicka, M.; Nadeau, V. G.; Chen, G.; Deber, C. M. Detergent binding explains anomalous SDS-PAGE migration of membrane proteins, *Proceedings of the National Academy of Sciences of the United States of America* **2009**, *106* (6), 1760–1765.

[159] Grigorian, A. L.; Bustamante, J. J.; Hernandez, P.; Martinez, A. O.; Haro, L. S. Extraordinarily stable disulfide-linked homodimer of human growth hormone, *Protein science : a publication of the Protein Society* **2005**, *14* (4), 902–913.

[160] Shelake, R. M.; Ito, Y.; Masumoto, J.; Morita, E. H.; Hayashi, H. A novel mechanism of "metal gel-shift" by histidine-rich Ni2+-binding Hpn protein from Helicobacter pylori strain SS1, *PloS one* **2017**, *12* (2), e0172182.

[161] Corin, K.; Baaske, P.; Geissler, S.; Wienken, C. J.; Duhr, S.; Braun, D.; Zhang, S. Structure and function analyses of the purified GPCR human vomeronasal type 1 receptor 1, *Scientific reports* **2011**, *1*, 172.

[162] McLane, M. W.; Hatzidimitriou, G.; Yuan, J.; McCann, U.; Ricaurte, G. Heating induces aggregation and decreases detection of serotonin transporter protein on western blots, *Synapse (New York, N.Y.)* **2007**, *61* (10), 875–876.

[163] Nørskov-Lauritsen, L.; Jørgensen, S.; Bräuner-Osborne, H. N-glycosylation and disulfide bonding affects GPRC6A receptor expression, function, and dimerization, *FEBS Letters* **2015**, *589* (5), 588–597.

[164] Nguyen, K. D. Q.; Vigers, M.; Sefah, E.; Seppälä, S.; Hoover, J. P.; Schonenbach, N. S.; Mertz, B.; O'Malley, M. A.; Han, S. Homo-

oligomerization of the human adenosine A2A receptor is driven by the intrinsically disordered C-terminus, *Elife* **2021**, *10*.

[165] Salom, D.; Padayatti, P. S.; Palczewski, K. Crystallization of G protein-coupled receptors, *Methods Cell Biol.* **2013**, *117*, 451–468.

[166] Lindqvist, B.; Storgårds, T. Molecular-sieving properties of starch, *Natl. Womens. Health Rep.* **1955**, *175* (4455), 511–512.

[167] Hong, P.; Koza, S.; Bouvier, E. S. P. Size-exclusion chromatography for the analysis of protein biotherapeutics and their aggregates, *J. Liq. Chromatogr. Relat. Technol.* **2012**, *35* (20), 2923–2950.

[168] Alexandrov, A. I.; Mileni, M.; Chien, E. Y. T.; Hanson, M. A.; Stevens, R. C. Microscale fluorescent thermal stability assay for membrane proteins, *Structure* **2008**, *16* (3), 351–359.

[169] Cherezov, V.; Abola, E.; Stevens, R. C. Recent progress in the structure determination of GPCRs, a membrane protein family with high potential as pharmaceutical targets, *Methods Mol. Biol.* **2010**, *654*, 141–168.

[170] McPherson, A.; Gavira, J. A. Introduction to protein crystallization, *Acta Crystallogr. F Struct. Biol. Commun.* **2014**, *70* (Pt 1), 2–20.

[171] Birch, J.; Axford, D.; Foadi, J.; Meyer, A.; Eckhardt, A.; Thielmann, Y.; Moraes, I. The fine art of integral membrane protein crystallisation, *Methods* **2018**, *147*, 150–162.

[172] Caffrey, M. Crystallizing membrane proteins for structure determination: use of lipidic mesophases, *Annu. Rev. Biophys.* **2009**, *38*, 29–51.

[173] Caffrey, M.; Cherezov, V. Crystallizing membrane proteins using lipidic mesophases, *Nat. Protoc.* **2009**, *4* (5), 706–731.

[174] Landau, E. M.; Rosenbusch, J. P. Lipidic cubic phases: a novel concept for the crystallization of membrane proteins, *Proc. Natl. Acad. Sci. U. S. A.* **1996**, *93* (25), 14532–14535.

[175] Cherezov, V. Lipidic cubic phase technologies for membrane protein structural studies, *Curr. Opin. Struct. Biol.* **2011**, *21* (4), 559–566.

[176] Caffrey, M. Membrane protein crystallization, *J. Struct. Biol.* **2003**, *142* (1), 108–132.

[177] Caffrey, M. On the mechanism of membrane protein crystallization in lipidic mesophases, *Cryst. Growth Des.* **2008**, *8* (12), 4244–4254.

[178] Cherezov, V.; Liu, J.; Griffith, M.; Hanson, M. A.; Stevens, R. C. LCP-FRAP assay for pre-screening membrane proteins for in meso crystallization, *Cryst. Growth Des.* **2008**, *8* (12), 4307–4315.

[179] Caffrey, M. Crystallizing membrane proteins for structure-function studies using lipidic mesophases, *Biochem. Soc. Trans.* **2011**, *39* (3), 725–732.

[180] Boland, C.; Olatunji, S.; Bailey, J.; Howe, N.; Weichert, D.; Fetics, S. K.; Yu, X.; Merino-Gracia, J.; Delsaut, C.; Caffrey, M. Membrane (and soluble) protein stability and binding measurements in the lipid cubic phase using label-free differential scanning fluorimetry, *Anal. Chem.* **2018**, *90* (20), 12152–12160.

[181] Liu, W.; Hanson, M. A.; Stevens, R. C.; Cherezov, V. LCP-Tm: an assay to measure and understand stability of membrane proteins in a membrane environment, *Biophys. J.* **2010**, *98* (8), 1539–1548.

[182] Kors, C. A.; Wallace, E.; Davies, D. R.; Li, L.; Laible, P. D.; Nollert, P. Effects of impurities on membrane-protein crystallization in different systems, *Acta Crystallogr. D Biol. Crystallogr.* **2009**, *65* (Pt 10), 1062–1073.

[183] Ghosh, E.; Kumari, P.; Jaiman, D.; Shukla, A. K. Methodological advances: the unsung heroes of the GPCR structural revolution, *Nat. Rev. Mol. Cell Biol.* **2015**, *16* (2), 69–81.

[184] Ishchenko, A.; Gati, C.; Cherezov, V. Structural biology of G protein-coupled receptors: new opportunities from XFELs and cryoEM, *Curr. Opin. Struct. Biol.* **2018**, *51*, 44–52.

[185] Boom, M.; Niesters, M.; Sarton, E.; Aarts, L.; Smith, T. W.; Dahan, A. Non-analgesic effects of opioids: opioid-induced respiratory depression, *Curr. Pharm. Des.* **2012**, *18* (37), 5994–6004.

[186] Epstein, D. H.; Heilig, M.; Shaham, Y. Science-based actions can help address the opioid crisis, *Trends Pharmacol. Sci.* **2018**, *39* (11), 911–916.

[187] Matthes, H. W.; Maldonado, R.; Simonin, F.; Valverde, O.; Slowe, S.; Kitchen, I.; Befort, K.; Dierich, A.; Le Meur, M.; Dollé, P.; Tzavara, E.; Hanoune, J.; Roques, B. P.; Kieffer, B. L. Loss of morphine-induced

analgesia, reward effect and withdrawal symptoms in mice lacking the mu-opioid-receptor gene, *Nature* **1996**, *383* (6603), 819–823.

[188] Gendron, L.; Mittal, N.; Beaudry, H.; Walwyn, W. Recent advances on the δ opioid receptor: from trafficking to function, *Br. J. Pharmacol.* **2015**, *172* (2), 403–419.

[189] Schütz, M.; Schöppe, J.; Sedlák, E.; Hillenbrand, M.; Nagy-Davidescu, G.; Ehrenmann, J.; Klenk, C.; Egloff, P.; Kummer, L.; Plückthun, A. Directed evolution of G protein-coupled receptors in yeast for higher functional production in eukaryotic expression hosts, *Sci. Rep.* **2016**, *6*, 21508.

[190] Schwyzer, R. ACTH: a short introductory review, *Ann. N. Y. Acad. Sci.* **1977**, *297*, 3–26.

[191] Pepin, M. C.; Yue, S. Y.; Roberts, E.; Wahlestedt, C.; Walker, P. Novel "restoration of function" mutagenesis strategy to identify amino acids of the delta-opioid receptor involved in ligand binding, *J. Biol. Chem.* **1997**, *272* (14), 9260–9267.

[192] Burbiel, J. C.; Ghattas, W.; Küppers, P.; Köse, M.; Lacher, S.; Herzner, A.-M.; Kombu, R. S.; Akkinepally, R. R.; Hockemeyer, J.; Müller, C. E. 2-Amino1,2,4triazolo1,5-cquinazolines and Derived Novel Heterocycles: Syntheses and Structure-Activity Relationships of Potent Adenosine Receptor Antagonists, *ChemMedChem* **2016**, *11* (20), 2272–2286.

[193] Zúñiga-Ramírez, C.; Micheli, F. Preladenant: an adenosine A 2A receptor antagonist for Parkinson's disease, *Future Neurol.* **2013**, *8* (6), 639–648.

[194] Hauser, R. A.; Stocchi, F.; Rascol, O.; Huyck, S. B.; Capece, R.; Ho, T. W.; Sklar, P.; Lines, C.; Michelson, D.; Hewitt, D. Preladenant as an adjunctive therapy with levodopa in Parkinson Disease: Two randomized clinical trials and lessons learned, *JAMA Neurol.* **2015**, *72* (12), 1491–1500.

[195] Kimura, K. T.; Asada, H.; Inoue, A.; Kadji, F. M. N.; Im, D.; Mori, C.; Arakawa, T.; Hirata, K.; Nomura, Y.; Nomura, N.; Aoki, J.; Iwata, S.; Shimamura, T. Structures of the 5-HT2A receptor in complex with the antipsychotics risperidone and zotepine, *Nat. Struct. Mol. Biol.* **2019**, *26* (2), 121–128.

[196] Yasuda, S.; Kajiwara, Y.; Takamuku, Y.; Suzuki, N.; Murata, T.; Kinoshita, M. Identification of thermostabilizing mutations for membrane proteins: rapid method based on statistical thermodynamics, *J. Phys. Chem. B* **2016**, *120* (16), 3833–3843.

[197] Mason, J. S.; Bortolato, A.; Weiss, D. R.; Deflorian, F.; Tehan, B.; Marshall, F. H. High end GPCR design: crafted ligand design and druggability analysis using protein structure, lipophilic hotspots and explicit water networks, *In Silico Pharmacol.* **2013**, *1* (1).

[198] Wang, G.; Jong, R. N. de; van den Bremer, E. T. J.; Parren, P. W. H. I.; Heck, A. J. R. Enhancing accuracy in molecular weight determination of highly heterogeneously glycosylated proteins by native tandem mass spectrometry, *Anal. Chem.* **2017**, *89* (9), 4793–4797.

[199] Duksin, D.; Mahoney, W. C. Relationship of the structure and biological activity of the natural homologues of tunicamycin, *J. Biol. Chem.* **1982**, *257* (6), 3105–3109.

[200] Tarentino, A. L.; Plummer, T. H. in *Methods in Enzymology*, *0076-6879 ; Vol. 230* (Eds.: W. J. Lennarz, G. W. Hart), Elsevier, **1994**, pp. 44–57.

[201] Müller, C. E.; Ferré, S. Blocking striatal adenosine A2A receptors: a new strategy for basal ganglia disorders, *Recent Pat. CNS Drug Discov.* **2007**, *2* (1), 1–21.

[202] Binda, C.; Hubálek, F.; Li, M.; Edmondson, D. E.; Mattevi, A. Crystal structure of human monoamine oxidase B, a drug target enzyme monotopically inserted into the mitochondrial outer membrane, *FEBS Lett.* **2004**, *564* (3), 225–228.

[203] Binda, C.; Hubálek, F.; Li, M.; Herzig, Y.; Sterling, J.; Edmondson, D. E.; Mattevi, A. Crystal structures of monoamine oxidase B in complex with four inhibitors of the N-propargylaminoindan class, *J. Med. Chem.* **2004**, *47* (7), 1767–1774.

[204] Binda, C.; Wang, J.; Pisani, L.; Caccia, C.; Carotti, A.; Salvati, P.; Edmondson, D. E.; Mattevi, A. Structures of human monoamine oxidase B complexes with selective noncovalent inhibitors: safinamide and coumarin analogs, *J. Med. Chem.* **2007**, *50* (23), 5848–5852.

[205] Binda, C.; Newton-Vinson, P.; Hubálek, F.; Edmondson, D. E.; Mattevi, A. Structure of human monoamine oxidase B, a drug target for the treatment of neurological disorders, *Nat. Struct. Biol.* **2002**, *9* (1), 22–26.

[206] McPherson, A.; Cudney, B. Searching for silver bullets: an alternative strategy for crystallizing macromolecules, *J. Struct. Biol.* **2006**, *156* (3), 387–406.

[207] Borodovsky, A.; Barbon, C. M.; Wang, Y.; Ye, M.; Prickett, L.; Chandra, D.; Shaw, J.; Deng, N.; Sachsenmeier, K.; Clarke, J. D.; Linghu, B.; Brown, G. A.; Brown, J.; Congreve, M.; Cheng, R. K.; Dore, A. S.; Hurrell, E.; Shao, W.; Woessner, R.; Reimer, C. et al. Small molecule AZD4635 inhibitor of A2AR signaling rescues immune cell function including CD103+ dendritic cells enhancing anti-tumor immunity, *J. Immunother. Cancer* **2020**, *8* (2).

[208] Walters, M. J.; Tan, J. B.; Becker, A.; Yi, F.; Park, T.; Leleti, M. R.; Rosen, B.; Sharif, E.; Debien, L.; Young, S.; Lim, W. H.; Garrido-Shaqfeh, S.; Jaen, J. C.; Powers, J. P. in *Clinical Research (Excluding Clinical Trials)*, American Association for Cancer Research, **07012017**, p. 4572.

[209] Beatty, J.; Debien, L.; Jeffrey, J.; Leleti, M. R.; Mandal, D.; Miles, D.; Powers, J.; Rosen, B.; Thomas-Tran, R.; Sharif, E. (Arcus Biosciences, Inc.) (WO/2018/136700), **2018**.

[210] Sharif, E. U.; Miles, D. H.; Rosen, B. R.; Jeffrey, J. L.; Debien, L. P. P.; Powers, J. P.; Leleti, M. R. Development of a scalable and practical synthesis of AB928, a dual A 2a /A 2b receptor antagonist, *Org. Process Res. Dev.* **2020**, *24* (7), 1254–1261.

[211] Daniel DiRenzo; Kristen Zhang; Sean Cho; Sachie Marubayashi; Dana Piovesan; Jesus Banuelos; Joanne B.L. Tan; Akshata Udyavar; Jenna Jeffrey; Manmohan R. Leleti; Jay P. Powers; Matthew J. Walters A2bR contributes to adenosine-mediated immunosuppression, which is relieved by the dual A2aR/A2bR antagonist AB928, *Poster P557 at SITC*, **2019**.

[212] Jespers, W.; Heitman, L. H.; IJzerman, A. P.; Sotelo, E.; van Westen, G. J. P.; Åqvist, J.; Gutiérrez-de-Terán, H. Deciphering conformational selectivity in the A2A adenosine G protein-coupled receptor by free energy simulations, *PLoS Comput. Biol.* **2021**, *17* (11), e1009152.

[213] Sun, B.; Bachhawat, P.; Chu, M. L.-H.; Wood, M.; Ceska, T.; Sands, Z. A.; Mercier, J.; Lebon, F.; Kobilka, T. S.; Kobilka, B. K. Crystal structure of the adenosine A2A receptor bound to an antagonist reveals a potential allosteric pocket, *Proc. Natl. Acad. Sci. U. S. A.* **2017**, *114* (8), 2066–2071.

[214] Harms, T. Design, synthesis and optimization of receptor ligands: tools for studying purine-activated and related orphan G protein-coupled receptors, *Doctoral thesis*, University of Bonn, **2022**.

[215] Michel, A.; Downey, P.; Nicolas, J.-M.; Scheller, D. Unprecedented therapeutic potential with a combination of A2A/NR2B receptor antagonists as observed in the 6-OHDA lesioned rat model of Parkinson's disease, *PLoS One* **2014**, *9* (12), e114086.

[216] Hockemeyer, J.; Burbiel, J. C.; Müller, C. E. Multigram-scale syntheses, stability, and photoreactions of A2A adenosine receptor antagonists with 8-styrylxanthine structure: potential drugs for Parkinson's disease, *J. Org. Chem.* **2004**, *69* (10), 3308–3318.

[217] Cherezov, V.; Hanson, M. A.; Griffith, M. T.; Hilgart, M. C.; Sanishvili, R.; Nagarajan, V.; Stepanov, S.; Fischetti, R. F.; Kuhn, P.; Stevens, R. C. Rastering strategy for screening and centring of microcrystal samples of human membrane proteins with a sub-10 microm size X-ray synchrotron beam, *J. R. Soc. Interface* **2009**, *6 Suppl 5*, S587-97.

[218] Rosentreter, U.; Henning, R.; Bauser, M.; Krämer, T.; Vaupel, A.; Hübsch, W.; Dembowsky, K.; Salcher-Schraufstätter, O.; Stasch, J.-P.; Krahn, T.; Perzborn, E. (Bayer AG) (WO01/25210A2), **2001**.

[219] Beukers, M. W.; Chang, L. C. W.; Frijtag Drabbe Künzel, J. K. von; Mulder-Krieger, T.; Spanjersberg, R. F.; Brussee, J.; IJzerman, A. P. New, non-adenosine, high-potency agonists for the human adenosine A2B receptor with an improved selectivity profile compared to the reference agonist N-ethylcarboxamidoadenosine, *J. Med. Chem.* **2004**, *47* (15), 3707–3709.

[220] Lane, J. R.; Klein Herenbrink, C.; van Westen, G. J. P.; Spoorendonk, J. A.; Hoffmann, C.; IJzerman, A. P. A novel nonribose agonist, LUF5834, engages residues that are distinct from those of adenosine-like ligands to activate the adenosine A(2a) receptor, *Mol. Pharmacol.* **2012**, *81* (3), 475–487.

[221] Lane, J. R.; Klaasse, E.; Lin, J.; van Bruchem, J.; Beukers, M. W.; IJzerman, A. P. Characterization of 3HLUF5834: A novel non-ribose high-affinity agonist radioligand for the adenosine A1 receptor, *Biochem. Pharmacol.* **2010**, *80* (8), 1180–1189.

[222] Ye, L.; van Eps, N.; Zimmer, M.; Ernst, O. P.; Prosser, R. S. Activation of the A2A adenosine G-protein-coupled receptor by conformational selection, *Nature* **2016**, *533* (7602), 265–268.

[223] Navarro, G.; Gonzalez, A.; Campanacci, S.; Rivas-Santisteban, R.; Reyes-Resina, I.; Casajuana-Martin, N.; Cordomí, A.; Pardo, L.; Franco, R. Experimental and computational analysis of biased agonism on full-length and a C-terminally truncated adenosine A2A receptor, *Comput. Struct. Biotechnol. J.* **2020**, *18*, 2723–2732.

[224] Eddy, M. T.; Martin, B. T.; Wüthrich, K. A2A adenosine receptor partial agonism related to structural rearrangements in an activation microswitch, *Structure* **2021**, *29* (2), 170-176.e3.

[225] Fernandes, D. D.; Neale, C.; Gomes, G.-N. W.; Li, Y.; Malik, A.; Pandey, A.; Orazietti, A. P.; Wang, X.; Ye, L.; Scott Prosser, R.; Gradinaru, C. C. Ligand modulation of the conformational dynamics of the A2A adenosine receptor revealed by single-molecule fluorescence, *Sci. Rep.* **2021**, *11* (1), 5910.

[226] Nygaard, R.; Frimurer, T. M.; Holst, B.; Rosenkilde, M. M.; Schwartz, T. W. Ligand binding and micro-switches in 7TM receptor structures, *Trends Pharmacol. Sci.* **2009**, *30* (5), 249–259.

[227] Weis, W. I.; Kobilka, B. K. The molecular basis of G protein-coupled receptor activation, *Annu. Rev. Biochem.* **2018**, *87*, 897–919.

[228] Kofuku, Y.; Ueda, T.; Okude, J.; Shiraishi, Y.; Kondo, K.; Maeda, M.; Tsujishita, H.; Shimada, I. Efficacy of the β_2-adrenergic receptor is determined by conformational equilibrium in the transmembrane region, *Nat. Commun.* **2012**, *3*, 1045.

[229] Staus, D. P.; Strachan, R. T.; Manglik, A.; Pani, B.; Kahsai, A. W.; Kim, T. H.; Wingler, L. M.; Ahn, S.; Chatterjee, A.; Masoudi, A.; Kruse, A. C.; Pardon, E.; Steyaert, J.; Weis, W. I.; Prosser, R. S.; Kobilka, B. K.; Costa, T.; Lefkowitz, R. J. Allosteric nanobodies reveal the dynamic range and

diverse mechanisms of G-protein-coupled receptor activation, *Nature* **2016**, *535* (7612), 448–452.

[230] Hamers-Casterman, C.; Atarhouch, T.; Muyldermans, S.; Robinson, G.; Hamers, C.; Songa, E. B.; Bendahman, N.; Hamers, R. Naturally occurring antibodies devoid of light chains, *Nature* **1993**, *363* (6428), 446–448.

[231] Muyldermans, S. Nanobodies: natural single-domain antibodies, *Annu. Rev. Biochem.* **2013**, *82*, 775–797.

[232] Bradford, M. M. A rapid and sensitive method for the quantitation of microgram quantities of protein utilizing the principle of protein-dye binding, *Anal. Biochem.* **1976**, *72* (1-2), 248–254.

[233] Beghein, E.; Gettemans, J. Nanobody technology: A versatile toolkit for microscopic imaging, protein-protein interaction analysis, and protein function exploration, *Front. Immunol.* **2017**, *8*, 771.

[234] Jovčevska, I.; Muyldermans, S. The therapeutic potential of nanobodies, *BioDrugs* **2020**, *34* (1), 11–26.

[235] Batool, M.; Ahmad, B.; Choi, S. A Structure-Based Drug Discovery Paradigm, *Int. J. Mol. Sci.* **2019**, *20* (11).

[236] Wang, T.; Wu, M.-B.; Zhang, R.-H.; Chen, Z.-J.; Hua, C.; Lin, J.-P.; Yang, L.-R. Advances in computational structure-based drug design and application in drug discovery, *Curr. Top. Med. Chem.* **2016**, *16* (9), 901–916.

[237] Acharya, K. R.; Sturrock, E. D.; Riordan, J. F.; Ehlers, M. R. W. Ace revisited: a new target for structure-based drug design, *Nat. Rev. Drug Discov.* **2003**, *2* (11), 891–902.

[238] Congreve, M.; Langmead, C.; Marshall, F. H. The use of GPCR structures in drug design, *Adv. Pharmacol.* **2011**, *62*, 1–36.

[239] Congreve, M.; Dias, J. M.; Marshall, F. H. Structure-based drug design for G protein-coupled receptors, *Prog. Med. Chem.* **2014**, *53*, 1–63.

[240] Congreve, M.; Graaf, C. de; Swain, N. A.; Tate, C. G. Impact of GPCR Structures on Drug Discovery, *Cell* **2020**, *181* (1), 81–91.

[241] Wang, H.; Hetzer, F.; Huang, W.; Qu, Q.; Meyerowitz, J.; Kaindl, J.; Hübner, H.; Skiniotis, G.; Kobilka, B. K.; Gmeiner, P. Structure-based evolution of G

protein-biased μ-opioid receptor agonists, *Angew. Chem. Int. Ed.* **2022**, e202200269.

[242] Kabsch, W. XDS, *Acta Crystallogr. D Biol. Crystallogr.* **2010**, *66* (Pt 2), 125–132.

[243] McCoy, A. J.; Grosse-Kunstleve, R. W.; Adams, P. D.; Winn, M. D.; Storoni, L. C.; Read, R. J. Phaser crystallographic software, *J. Appl. Crystallogr.* **2007**, *40* (Pt 4), 658–674.

[244] Emsley, P.; Cowtan, K. Coot: model-building tools for molecular graphics, *Acta Crystallogr. D Biol. Crystallogr.* **2004**, *60* (Pt 12 Pt 1), 2126–2132.

[245] Liebschner, D.; Afonine, P. V.; Baker, M. L.; Bunkóczi, G.; Chen, V. B.; Croll, T. I.; Hintze, B.; Hung, L. W.; Jain, S.; McCoy, A. J.; Moriarty, N. W.; Oeffner, R. D.; Poon, B. K.; Prisant, M. G.; Read, R. J.; Richardson, J. S.; Richardson, D. C.; Sammito, M. D.; Sobolev, O. V.; Stockwell, D. H. et al. Macromolecular structure determination using X-rays, neutrons and electrons: recent developments in Phenix, *Acta Crystallogr. D Struct. Biol.* **2019**, *75* (Pt 10), 861–877.

[246] Newton-Vinson, P.; Hubalek, F.; Edmondson, D. E. High-level expression of human liver monoamine oxidase B in Pichia pastoris, *Protein Expr. Purif.* **2000**, *20* (2), 334–345.

[247] The CCP4 suite: programs for protein crystallography, *Acta Crystallogr. D Biol. Crystallogr.* **1994**, *50* (Pt 5), 760–763.

[248] Murshudov, G. N.; Skubák, P.; Lebedev, A. A.; Pannu, N. S.; Steiner, R. A.; Nicholls, R. A.; Winn, M. D.; Long, F.; Vagin, A. A. REFMAC5 for the refinement of macromolecular crystal structures, *Acta Crystallogr. D Biol. Crystallogr.* **2011**, *67* (Pt 4), 355–367.

[249] Temirak, A. M. A. Design and synthesis of A2B- and dual-acting A2A/A2B adenosine receptor antagonists, *Doctoral thesis*, University of Bonn, **2020**.

[250] Stössel, A.; Schlenk, M.; Hinz, S.; Küppers, P.; Heer, J.; Gütschow, M.; Müller, C. E. Dual targeting of adenosine A(2A) receptors and monoamine oxidase B by 4H-3,1-benzothiazin-4-ones, *J. Med. Chem.* **2013**, *56* (11), 4580–4596.

[251] Sievers, F.; Wilm, A.; Dineen, D.; Gibson, T. J.; Karplus, K.; Li, W.; Lopez, R.; McWilliam, H.; Remmert, M.; Söding, J.; Thompson, J. D.; Higgins, D. G. Fast, scalable generation of high-quality protein multiple sequence alignments using Clustal Omega, *Mol. Syst. Biol.* **2011**, *7*, 539.

Appendices

Appendix I. Publication I: Elucidating the Active δ-Opioid Receptor Crystal Structure with Peptide and Small-molecule Agonists

Main Text
of
Publication I
in
***Science Advances*[80]**

STRUCTURAL BIOLOGY

Elucidating the active δ-opioid receptor crystal structure with peptide and small-molecule agonists

Tobias Claff[1,2]*, Jing Yu[1,3,4,5]*, Véronique Blais[6], Nilkanth Patel[7], Charlotte Martin[8], Lijie Wu[1], Gye Won Han[7], Brian J. Holleran[6], Olivier Van der Poorten[8], Kate L. White[7], Michael A. Hanson[9], Philippe Sarret[6], Louis Gendron[6], Vadim Cherezov[7], Vsevolod Katritch[7], Steven Ballet[8], Zhi-Jie Liu[1,3], Christa E. Müller[2]†, Raymond C. Stevens[1,7]†

Selective activation of the δ-opioid receptor (DOP) has great potential for the treatment of chronic pain, benefitting from ancillary anxiolytic and antidepressant-like effects. Moreover, DOP agonists show reduced adverse effects as compared to μ-opioid receptor (MOP) agonists that are in the spotlight of the current "opioid crisis." Here, we report the first crystal structures of the DOP in an activated state, in complex with two relevant and structurally diverse agonists: the potent opioid agonist peptide KGCHM07 and the small-molecule agonist DPI-287 at 2.8 and 3.3 Å resolution, respectively. Our study identifies key determinants for agonist recognition, receptor activation, and DOP selectivity, revealing crucial differences between both agonist scaffolds. Our findings provide the first investigation into atomic-scale agonist binding at the DOP, supported by site-directed mutagenesis and pharmacological characterization. These structures will underpin the future structure-based development of DOP agonists for an improved pain treatment with fewer adverse effects.

INTRODUCTION

Global opioid use has reached record levels (*1*), and especially the United States has seen the recent acute opioid epidemic cause drug overdose to become the main cause of accidental deaths (*2*). As a consequence, the development of alternatives to classical opioid painkillers with lower risk of abuse and overdose has become one of the highest priorities in healthcare (*3*).

The opioid receptor family consists of three G protein–coupled receptor (GPCR) subtypes: the μ-, κ-, and δ-opioid receptors (MOP, KOP, and DOP, respectively) (*4*). Both the unrivaled analgesic potency and the well-known adverse effects (e.g., addiction, tolerance, and respiratory depression) of approved opioid drugs are primarily mediated by the MOP (*5*, *6*). However, the other opioid receptors have been extensively investigated as attractive targets for safer treatment of chronic pain (*7*), and the DOP, in particular, has shown additional anxiolytic and antidepressant-like effects (*8*, *9*). This beneficial psychopharmacological profile together with its milder adverse effects put selective DOP agonists at the forefront of the development of superior opioid analgesics.

In 1975, it was discovered that the enkephalin pentapeptides act as the opioid receptors' endogenous ligands (*10*). Subsequently, opioid receptor subtype-selective peptides as well as multifunctional peptides targeting both opioid and non-opioid receptors were prepared and optimized (*11*, *12*). Within a series of compounds designed as dual opioid/neurokinin 1 receptor ligands, the potent peptide agonist KGCHM07 [H-Dmt-D-Arg-Phe-Sar-*N*-Me-3′,5′-$(CF_3)_2$-Bn] was developed (Fig. 1) and showed high affinities to both DOP and MOP (*13*). As an alternative to peptide- and morphine-derived ligands, previously unknown small molecules with piperazine scaffold were discovered as selective DOP agonists by compound library screening (*14*). Further optimization yielded the promising agonist DPI-287 (Fig. 1) that displayed reduced risk of inducing convulsions (*9*), which is a common complication of DOP activation (*15*).

Here, we report two agonist-bound crystal structures of the thermostabilized DOP in an activated state, and in complex with the peptide KGCHM07 at 2.8 Å resolution and the small-molecule DPI-287 at 3.3 Å resolution. These structures provide the first atomic-level insights into DOP activation by two structurally diverse DOP agonists. While the DOP inactive state has been characterized by crystal structures with a small molecule (*16*) and a peptide antagonist (*17*) bound to the orthosteric site, agonist recognition by the DOP has remained elusive, and the structural basis of DOP agonist selectivity is not fully understood. Moreover, both small-molecule agonists that have been cocrystallized with the MOP and KOP are based on morphinan scaffolds (*18*, *19*), limiting our understanding of agonist binding pocket interactions with other small molecules, such as DPI-287. Furthermore, the pharmacological properties of the DOP fusion construct used for crystallization (Fig. 1 and Supplementary Text) were extensively characterized and compared to those of the wild-type (WT) DOP to evaluate potential effects of thermostabilizing mutations on binding and downstream signaling (table S1), which additionally provides the first detailed pharmacological characterization of DPI-287.

[1]iHuman Institute, ShanghaiTech University, Ren Building, 393 Middle Huaxia Rd, Pudong, Shanghai 201210, China. [2]PharmaCenter Bonn, University of Bonn, Pharmaceutical Chemistry I, An der Immenburg 4, D-53121 Bonn, Germany. [3]School of Life Science and Technology, ShanghaiTech University, Shanghai 201210, China. [4]CAS Center for Excellence in Molecular Cell Science, Shanghai Institute of Biochemistry and Cell Biology, Chinese Academy of Sciences, University of Chinese Academy of Sciences, Shanghai 200031, China. [5]University of the Chinese Academy of Sciences, Beijing 100049, China. [6]Department of Pharmacology-Physiology, Faculty of Medicine and Health Sciences, Institut de Pharmacologie de Sherbrooke, Centre de Recherche du CHUS, Université de Sherbrooke, 3001 12e Avenue Nord, Sherbrooke, Quebec J1H 5N4, Canada. [7]Departments of Biological Sciences and Chemistry, Bridge Institute, USC Michelson Center for Convergent Bioscience, University of Southern California, Los Angeles, CA 90089, USA. [8]Research Group of Organic Chemistry, Departments of Chemistry and Bioengineering Sciences, Vrije Universiteit Brussel, Pleinlaan 2, B-1050 Brussels, Belgium. [9]GPCR Consortium, San Marcos, CA 92078, USA.
*These authors contributed equally to this work.
†Corresponding author. Email: christa.mueller@uni-bonn.de (C.E.M.); stevens@shanghaitech.edu.cn (R.C.S.)

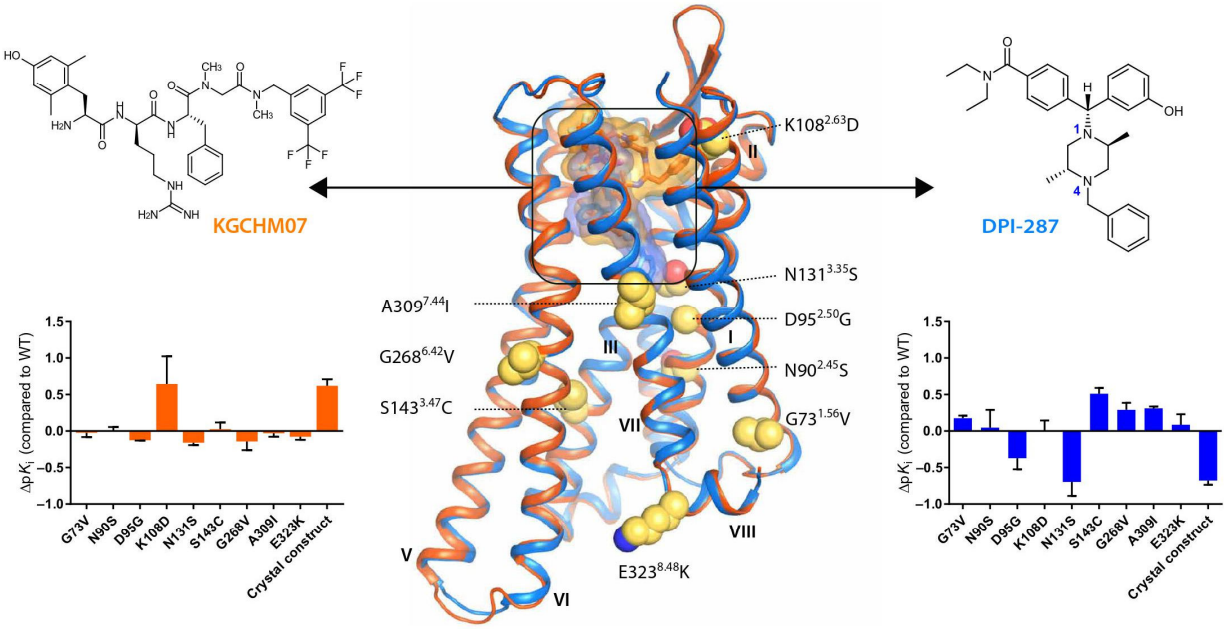

Fig. 1. Thermostabilized DOP construct without the N-terminal fusion protein, with both agonists KGCHM07 and DPI-287, used for crystallization, and effects of the crystal structure construct point mutations on the pK_i values of the agonists. The binding affinities (pK_i) of KGCHM07 (orange) and DPI-287 (blue) on membrane preparations of HEK cells expressing WT or mutant DOP constructs were determined by their ability to inhibit the binding of [^{125}I]-deltorphin I, used as a selective radioligand. Data were analyzed using a nonlinear fitting analysis, and the K_i values were calculated using GraphPad Prism 7.0. K_i values in the competition studies were determined from IC_{50} values using the Cheng-Prusoff equation and are represented as means + SEM of three to six independent experiments, each performed in duplicate. Differences (delta) in pK_i values compared to WT are shown. The statistical significance was determined using a nonparametric one-way analysis of variance (ANOVA), showing that all pK_i differences of crystal construct mutants versus WT were statistically not significant ($P > 0.05$).

RESULTS

Activation-related changes in the DOP

Both agonist-bound structures are in an activated state. Unless otherwise indicated, we will use the higher-resolution BRIL-DOP-KGCHM07 structure for comparison with previously published inactive-state antagonist-bound DOP structures [Protein Data Bank (PDB) 4N6H and 4RWD] (*16*, *17*) and with active-state structures of the MOP (PDB 5C1M and 6DDF) (*18*, *20*) and KOP (PDB 6B73) (*19*). First, the agonist-bound DOP structures display large outward movements of the intracellular parts of helices V (4.5 Å) and VI (9.4 to 11.2 Å), and a 3.9 Å inward movement of helix VII (Fig. 2A), which is a common feature of the active conformational states of GPCRs (*21*). The shift of helix VII at the level of residue N314$^{7.49}$ [superscripts according to the Ballesteros and Weinstein numbering (*22*)] (Fig. 3A), which leads to a collapse of the allosteric sodium-binding pocket in active-state GPCR structures (*23*), is even more pronounced in the determined DOP structures as compared to the active MOP and KOP (Fig. 3B and fig. S1). However, this greater shift of N314$^{7.49}$ in the DOP might be affected by three mutations in the sodium-binding pocket (N90$^{2.45}$S, D95$^{2.50}$G, N131$^{3.35}$S) that were introduced during construct design. The activation-related outward movement of helix VI at the level of residue F270$^{6.44}$ is greater in the agonist-bound DOP than in the MOP and KOP. On the contrary, the very tips of helix VI (at position 6.28 as a reference) are more tilted by 4 to 6 Å in the active-state MOP and KOP (fig. S1), likely due to the bound G protein or nanobody, respectively, pushing helix VI tips further outward (*24*).

The rearrangements in the transmembrane helices are accompanied by several changes in the conserved microswitches that are typical for GPCR activation (*24*, *25*). Included are changes in the so-called P-I-F motif, where P225$^{5.50}$ moves inward by ~1.6 Å, forcing the I136$^{3.40}$ side chain to change its rotamer state and facilitating a major rotation of the bulky side chain of F270$^{6.44}$ (Fig. 2B) toward helix V by as much as ~3.5 Å at the Cγ atoms. For comparison, this movement is only ~2.6 Å in the active-state MOP and KOP structures. The P-I-F motif changes are coupled with rearrangements in the NP$^{7.50}$xxY motif, collapsing the sodium-binding pocket, with a ~3.5 Å inward shift of N314$^{7.49}$. Another residue of the sodium pocket and the NP$^{7.50}$xxY motif, Y318$^{7.53}$, switches its side-chain rotamer to a downward orientation, opening the intracellular entrance to the sodium pocket (Fig. 2C).

The overall conformation of the conserved DR$^{3.50}$Y motif remains largely unaltered between the active-like agonist-bound and the inactive-state DOP structures (Fig. 2C). Notably, the importance of the DRY motif in maintaining the inactive state in most GPCRs is attributable to a strong salt bridge between D$^{3.49}$ and R$^{3.50}$ residues. However, in all inactive-state structures of the DOP and other opioid receptors, this salt bridge is already disrupted, displaying distances of >3.5 Å. Moreover, the differences due to activation in the corresponding MOP and KOP structures manifest only in the side-chain reorientation of R$^{3.50}$ that directly interacts with the G protein (*20*) or nanobody (*18*, *19*), which are lacking in the DOP structures. To assess the activation state more rigorously, we evaluated the two

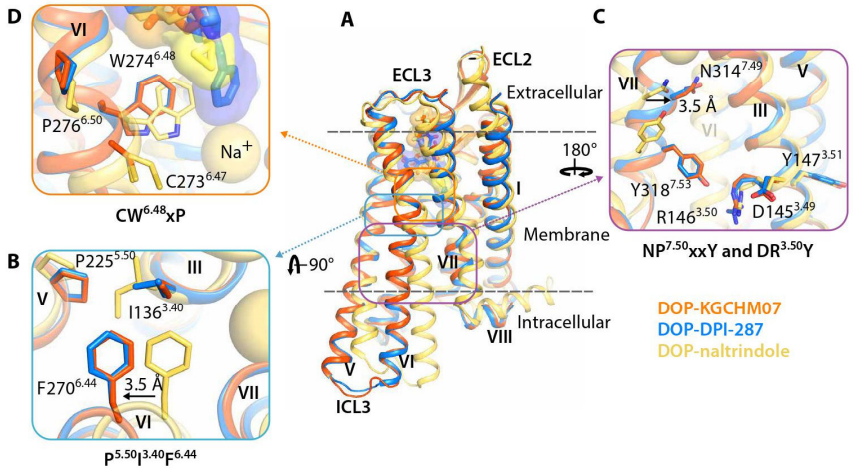

Fig. 2. Activation-related changes in the DOP. Comparison of conserved activation microswitches of the active-like DOP-KGCHM07 (orange) and DOP-DPI-287 (blue) structures with the inactive DOP-naltrindole structure (yellow, PDB 4N6H). Structural superposition of the (**A**) overall architecture, (**B**) PIF motif, (**C**) NPxxY and DRY motifs, and (**D**) CWxP motif.

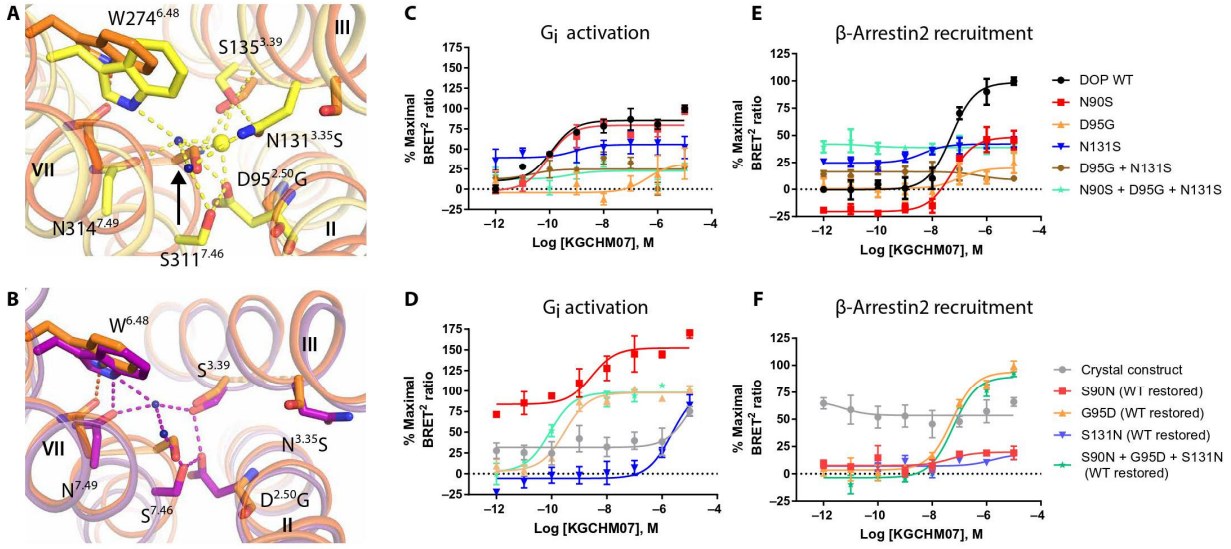

Fig. 3. Effects of sodium-binding mutations on receptor function. Comparison of the collapsed sodium-binding pocket in DOP-KGCHM07 (orange) with (**A**) inactive DOP (yellow, PDB 4N6H) and (**B**) active MOP (purple, PDB 5C1M) with perspective from the extracellular space. Water molecules are shown as blue spheres and the Na^+ ion as a yellow sphere. G_i-mediated cAMP signaling of (**C**) sodium-binding pocket mutants and (**D**) crystal structure construct mutants with sodium-binding pocket mutations restored to WT residues in response to different KGCHM07 concentrations (signals normalized to WT DOP). β-Arrestin2 recruitment of (**E**) sodium-binding pocket mutants and (**F**) crystal structure construct mutants with sodium-binding pocket mutations restored to WT residues in response to different KGCHM07 concentrations (signals normalized to the G95D mutant). Results are expressed as means ± SEM from $n = 4$ (EPAC) or $n = 3$ (β-arrestin2) independent experiments, each performed in triplicate.

new DOP structures along with previously solved opioid receptor structures for their activation-related conformations of microswitches using a GAUGE machine learning–based prediction tool (see Materials and Methods for details). All the microswitches in the new DOP structures, except the DRY motif, were predicted to be in the active-like or fully activated state (table S2).

Sodium pocket mutations allow receptor stabilization and control receptor function

The conserved site involved in binding of the negative allosteric modulator sodium in the DOP (*16*) was found to be collapsed in both agonist-bound DOP structures, similar to other class A GPCR structures determined in active or active-like states (Fig. 3, A and B)

(*18*, *23*). In our case, three mutations in the sodium pocket (N90$^{2.45}$S, D95$^{2.50}$G, N131$^{3.35}$S) apparently facilitated sodium expulsion and the collapse of the pocket, thereby stabilizing the receptor in an active-like state (Supplementary Text). A major decrease in thermostability was seen for agonist-bound DOP constructs lacking any of these mutations, which underlines their critical importance in thermostabilizing the agonist-bound DOP (fig. S2). However, the crystal construct retained high-affinity binding for KGCHM07 (K_i WT, 5.17 ± 1.57 nM; K_i crystal construct, 1.24 ± 0.23 nM), DPI-287 (K_i WT, 0.39 ± 0.12 nM; K_i crystal construct, 1.86 ± 0.23 nM), and [^{125}I]-deltorphin I (K_d WT, 1.11 nM; K_d crystal construct, 4.34 nM), indicating that the authenticity of the agonist-bound DOP binding pocket was not affected by the introduced point mutations (Fig. 1).

It is well established that mutations in the sodium-binding pocket can result in altered signaling properties (*16*), and our crystal structure construct lacked agonist-induced cyclic adenosine monophosphate (cAMP) response and β-arrestin2 recruitment (Fig. 3, C to F, and table S1). Our mutagenesis studies revealed that the DOP WT with the single point mutation D95$^{2.50}$G could be activated neither by KGCHM07 nor by DPI-287, while the agonist binding affinities were virtually unaltered (table S1). This is in contrast to a previously investigated D95$^{2.50}$A mutation that reduced the potency of the DPI-287–related agonist BW373U86 but maintained G protein signaling and β-arrestin recruitment (*16*). The G95$^{2.50}$D mutation in the crystal structure construct (reversing residue 2.50 back to WT) restored both cAMP and β-arrestin2 signaling fully (KGCHM07) or partially (DPI-287) (Fig. 3, C to F; fig. S3; and table S1).

Our mutagenesis experiments showed elevated basal responses in both cAMP and β-arrestin pathways for the single N131$^{3.35}$S and a triple DOP mutant (N90$^{2.45}$S, D95$^{2.50}$G, N131$^{3.35}$S), suggestive of a constitutively active receptor (Fig. 3, C to F, and fig. S3). In addition, when the signaling abilities of the crystal structure construct were evaluated, the baseline signal levels in both pathways were found to be higher than in the G95$^{2.50}$D mutant (used to normalize the crystal construct mutants) (Fig. 3, C to F, and fig. S3). To further assess the constitutive activity of the crystal structure construct, we performed a titration assay in which the amount of receptor construct DNA increased, while the levels of the biosensor (in this case $G_{\alpha i1}$-RLuc2 and $G_{\gamma 1}$-GFP10) remained constant (fig. S3). Increasing amounts of the crystal structure construct produced a decay of the signal, indicative of a ligand-independent dissociation of the G_i protein subunits induced by the receptor. A similar decay of the response signal was observed when the DOP WT construct was stimulated with DPI-287, further supporting that the crystal structure construct is constitutively activating the G_i protein signaling pathway.

A common denominator for opioid receptor activation

The new DOP structures provide atomic-level insights into the key components of molecular recognition for small-molecule and peptide agonists. Most of the opioid receptor ligands share a basic, protonated nitrogen atom forming a salt-bridge interaction to D128$^{3.32}$, which itself is connected to a polar network with potential involvement of Y308$^{7.43}$, T101$^{2.56}$, and Q105$^{2.60}$ linking helices II, III, and VII. In inactive-state DOP structures, this polar network can extend to Y109$^{2.64}$, involving water-mediated interactions. However, in activated structures, the Y109$^{2.64}$ side chain shows a large rotation toward helix I, uncoupling Y109$^{2.64}$ from the polar network, a mechanism that appears to be important for DOP activation. In the case of the DOP-DPI-287 complex, the distance for anchoring interactions between the protonated amine and D128$^{3.32}$ is ~3.0 Å. It is even greater (~3.5 Å) for the peptide KGCHM07, which shows multiple, direct, or potentially water-mediated interactions with D128$^{3.32}$ (Fig. 4, A and C). Another residue of the polar network, Y308$^{7.43}$, forms a direct hydrogen bond to the primary amine of the peptide KGCHM07, while Y308$^{7.43}$ does not interact directly with DPI-287's protonated amine (*N*4). In both structures, Y308$^{7.43}$ positioning is preserved by hydrogen bonds to D128$^{3.32}$, and in DPI-287 by additional π-π stacking interactions with the unsubstituted benzyl moiety (Fig. 4, B and C). At the same time, T101$^{2.56}$ helps in maintaining the polar network in the DOP-DPI-287 complex by forming hydrogen bonds with both Y308$^{7.43}$ and Q105$^{2.60}$, while the T101$^{2.56}$ side chain loses this interaction in the peptide-bound DOP-KGCHM07 complex, which uncouples it from the polar network (Fig. 4, A and C). D128$^{3.32}$ mutations to N or A virtually abolished KGCHM07 activity, while the potency of the small-molecule DPI-287 reduced 10-fold for D128$^{3.32}$N [half maximal effective concentration (EC_{50}), 0.060 nM versus 0.61 nM] and 30-fold for D128$^{3.32}$A (EC_{50}, 0.060 nM versus 1.39 nM) (Fig. 4D). Similarly, previous studies on opioid peptides reported that modifications of the N-terminal amine, including its acetylation or substitution by a methyl group, abolished agonistic activities while retaining low nanomolar affinity (*26*, *27*). However, we were unable to determine the affinity of KGCHM07 and DPI-287 for the D128$^{3.32}$ mutants, because no [^{125}I]-deltorphin I–specific binding could be observed (table S1).

The basic amines of KGCHM07 and DPI-287 are embedded deeper (1.9 and 1.4 Å, respectively) into the binding pocket when compared to the equivalent amines of the DOP antagonists DIPP-NH_2 (Fig. 4E) and naltrindole (Fig. 4F), resulting in the reorientation of the D128$^{3.32}$ side chain and the adjacent polar network. Furthermore, the MOP agonist BU72 (PDB 5C1M) shows the same 1.4 Å amine shift into the binding pocket when compared to a morphinan MOP antagonist (PDB 4DKL). Accordingly, the docking poses of 10 peptide and 7 small-molecule DOP agonists into our new active-like DOP structures (table S3) revealed that all respective amines were located deeper in the binding pocket when compared to DOP antagonists (Fig. 4, E and F, and fig. S4). Hydrophobic contacts with helix V or VII, or both, preclude antagonists such as DIPP-NH_2 and naltrindole to extend as deep into the DOP binding pocket as shown for DOP agonists (Fig. 4F and fig. S4). Therefore, we argue that the polar network around D$^{3.32}$ plays an essential role in agonist-induced activation at the DOP and propose that the positioning of the basic amine (as opposed to antagonists) deeper into the binding pocket is a hallmark of opioid agonist activity for ligands that contain a basic amine interacting with D$^{3.32}$.

Differences between peptide and small-molecule recognition by the DOP

Besides the abovementioned prevalent salt bridge formation, another important anchor of ligand interaction in opioid receptors is the phenol moiety that is conserved in many peptide and small-molecule ligands. Accordingly, the peptide agonist KGCHM07 contains the N-terminal tyrosine derivative 2,6-dimethyl-L-tyrosine (Dmt^1), which was shown to improve binding affinity and activity of peptidic ligands at opioid receptors (*28*). Its position is similar to the one observed for tyrosine in the active structure of MOP in complex with DAMGO [(D-Ala^2,*N*-Me-Phe^4, Gly-ol^5)-enkephalin] (*20*), but Dmt shows additional hydrophobic contacts in the DOP binding pocket. Three water molecules were found in the KGCHM07 binding

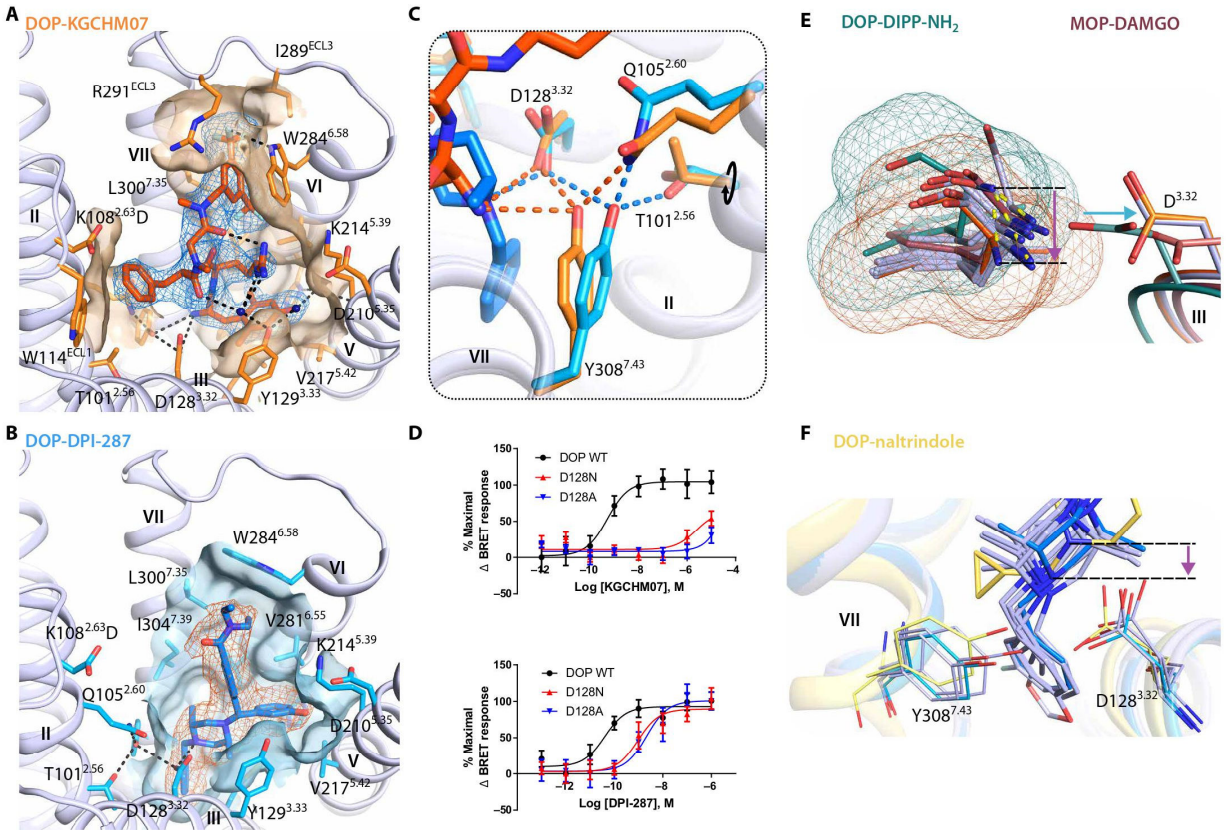

Fig. 4. Polar network around D128$^{3.32}$ and basic amine positioning as potential hallmark for opioid receptor activation. BRIL-DOP-KGCHM07, orange; BRIL-DOP-DPI-287, blue; naltrindole DOP antagonist structure (PDB 4N6H), yellow; DIPP-NH_2 DOP antagonist structure (PDB 4RWD), cyan; DAMGO MOP agonist structure (PDB 6DDF), red. (**A**) Overview of the KGCHM07 peptide binding pocket. The omit F_o-F_c electron density of KGCHM07 is shown in blue mesh (contoured at 3.0 σ). (**B**) Overview of the DPI-287 binding pocket. The omit F_o-F_c electron density of DPI-287 is shown in orange mesh (contoured at 3.0 σ). (**C**) Polar network anchoring the basic amine of DOP agonists. (**D**) G_i-mediated cAMP signaling of D128$^{3.32}$ mutants in response to different DOP agonist concentrations (upper panel, KGCHM07; lower panel, DPI-287). (**E**) Docking poses of DOP agonist peptides (gray) show that all primary amines embedded deeper into the binding pocket (yellow marks), when compared to antagonist DIPP-NH_2 (cyan) as indicated by the purple arrow. Similarly, the MOP-DAMGO complex (dark red) is displaced. The cyan arrow indicates related side movements of D$^{3.32}$. For clarity, only residue one (Phe^1 or Dmt^1) is depicted, and the surfaces of DOP agonist KGCHM07 and DOP antagonist DIPP-NH_2 are shown in orange and green mesh, respectively, to clarify its location in the binding pocket. (**F**) Docking poses of DOP small-molecule agonists (gray) show all substituted basic amines (*N4*) that penetrated deeper into the binding pocket, when compared to the antagonist naltrindole (yellow).

pocket, supported by weak electron densities (fig. S5). These are involved in connecting Dmt^1 to helices III, V, and VI via a polar interaction network with K214$^{5.39}$, H278$^{6.52}$, and Y129$^{3.33}$, which is also effectively connected to D-Arg^2 of KGCHM07 (Fig. 4A). Furthermore, our analysis suggests that the positively charged D-Arg^2 can form a water-mediated salt bridge interaction to D210$^{5.35}$ (fig. S5), supported by a 17-fold reduction in KGCHM07 binding to the D210$^{5.35}$N mutant. Moreover, [^{125}I]-deltorphin I, which was used as the radiotracer in these experiments, contains D-Ala^2 instead of D-Arg^2 and was not affected by D210$^{5.35}$ mutations (table S1). The lower resolution of the DPI-287 structure precluded robust identification of structural water molecules in this case. However, the energy-based prediction of water molecules suggested three tightly bound water molecules at residues H278$^{6.52}$ and Y129$^{3.33}$, linking DPI-287 to helices III, V, and VI as likewise observed in the KGCHM07-bound structure (fig. S5).

Our mutagenesis studies showed a binding decrease to the Y129$^{3.33}$F and Y129$^{3.33}$A mutants by ~7-fold and ~38-fold for KGCHM07 and by about 3-fold and about 5-fold for DPI-287, respectively (table S1). This finding confirms the involvement of Y129$^{3.33}$ in water-mediated polar networks in both structures. Similarly, the EC_{50} in a H278$^{6.52}$A mutant was reduced ~50-fold for KGCHM07 and ~10-fold for DPI-287. In addition, the backbone of K214$^{5.39}$ is also involved in this polar network, and a K214$^{5.39}$A mutant did not alter the potencies of KGCHM07 or DPI-287. However, single mutations of H278$^{6.52}$A and K214$^{5.39}$A abolished [^{125}I]-deltorphin I binding (table S1), indicating distinct binding pocket differences between the diverse agonists.

The Phe^3 side chain of KGCHM07 extends toward helices II and III and extracellular loop 1 (ECL1) and ECL2 and is positioned in a partially hydrophobic pocket formed by Q105$^{2.60}$, W114^{ECL1},

V124$^{3.28}$, L125$^{3.29}$, and C198^{ECL2} (Fig. 4A and fig. S4). In the designed DOP fusion protein, a K108$^{2.63}$D mutation was introduced (Supplementary Text) located at the extracellular entrance of the binding pocket. KGCHM07 binds to the K108$^{2.63}$D mutant with virtually unaltered affinity (table S1), and the docking of the KGCHM07 peptide into a DOP model with the K108$^{2.63}$ residue as in the WT receptor (table S3) suggests that KGCHM07 binds in the same pose as in the crystal structure. The flexible Sar^{4} residue of KGCHM07 adopts an energetically less favorable *cis*-amide bond to Phe^{3}, while all remaining amide bonds are found to be in the *trans*-conformation. This enables the C-terminal bistrifluoromethylated benzyl moiety to address the ECL3 region and extracellular ends of helices VI and VII. A large side-chain rotation of W284$^{6.58}$ by approximately 125°, compared to other DOP structures (Fig. 5, A and B, and fig. S4), opens a hydrophobic pocket consisting of I277$^{6.51}$, F280$^{6.54}$, V281$^{6.55}$, W284$^{6.58}$, I289^{ECL3}, R291^{ECL3}, and L300$^{7.35}$, harboring the benzyl moiety. This moiety is further stabilized by π-π stacking interactions and a hydrogen bond to W284$^{6.58}$ (Fig. 4A).

Structural basis for the selectivity of DOP agonists

The activated conformation of the DOP reveals contraction of the orthosteric binding pocket around the agonists. Helix VI moves into the agonist-binding pocket by 1.6 Å, while helix VII undergoes a 2.5 Å sideways movement (fig. S1). These helix movements close to the binding pocket result in conformational changes in the ECL3 region as compared to antagonist binding pockets. In the inactive state, R291^{ECL3} stabilizes the ECL3 region by forming hydrogen bonds with the carbonyl functions of V287$^{6.61}$ and W284$^{6.58}$ (Fig. 5A) (*16*). In the KGCHM07-bound structure, a large movement (10.0 Å based on the guanidine carbon) of R291^{ECL3} into the binding pocket can be observed, resulting in the disruption of this hydrogen bond network (Fig. 5B). The side chain of R291^{ECL3} is, therefore, more flexible in the agonist-bound DOP, and its electron densities only allowed us to model the full R291^{ECL3} residue in chain A of the BRIL-DOP-KGCHM07 structure, where it forms a lid over the hydrophobic pocket harboring KGCHM07's bistrifluoromethylated benzyl moiety. Although KGCHM07 is not DOP-selective because it also activates MOP (*13*), our BRIL-DOP-KGCHM07 structure reveals that R291^{ECL3} is accessible to the agonist binding pocket and is likely to play a role in the selectivity of DOP-binding peptides, as the MOP has a glutamic acid and the KOP has a histidine in the same position (Fig. 5D).

The small-molecule DPI-287 is ~10-fold selective for DOP over MOP (K_i DOP, 0.39 ± 0.12 nM; K_i MOP, 3.17 ± 0.27 nM). Our docking studies revealed that more selective analogs bind in the same binding pose as DPI-287, as described in the next section (Fig. 6), revealing that the *N*,*N*-diethylbenzamide moiety interacts with the nonconserved extracellular ends of helices VI and VII. The amide forms multiple hydrophobic contacts within a pocket consisting of V281$^{6.55}$, F280$^{6.54}$, W284$^{6.58}$, and L300$^{7.35}$ (Figs. 4B and 5C). Structural comparison with other opioid receptors reveals that the *N*,*N*-diethylbenzamide moiety of DPI-287 and analogs cannot occupy the same receptor space in the MOP and KOP as in the DOP due to steric interactions in positions 6.58 [charged in the case of MOP (K305) and KOP (E297)] and 7.35 (W320 in the MOP and Y312 in the KOP) (Fig. 5, C and D). Therefore, any larger substitution of L300$^{7.35}$ would prevent beneficial hydrophobic contacts due to steric clashes. On the other hand, replacing W284$^{6.58}$ with charged side chains would also make the subpocket less favorable for forming hydrophobic interactions.

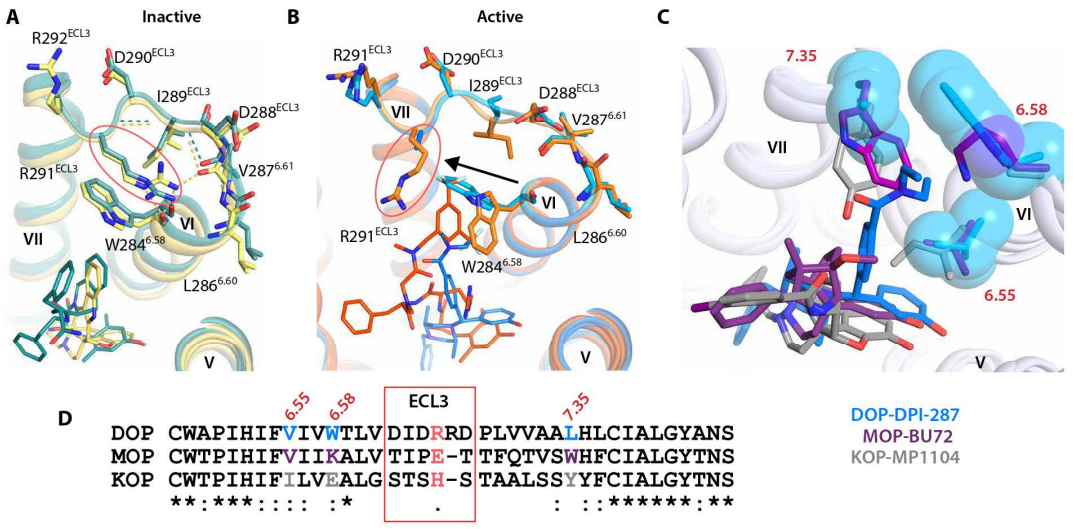

Fig. 5. Activation-related changes in the ECL3 region of the DOP and structural basis for DPI-287 selectivity. Comparison of ECL3 conformations between (**A**) inactive (naltrindole, yellow, PDB 4N6H and DIPP-NH_2, cyan, PDB 4RWD) and (**B**) active DOP binding pockets (DOP-KGCHM07, orange; DOP-DPI-287, blue). (**C**) Alignment of agonist-bound opioid receptor binding pockets. Pocket-forming residues are shown as sticks, with labels indicating Ballesteros-Weinstein nomenclature (*22*) and red numbers pointing to nonconserved residues. Note that the E$^{6.58}$ side chain of the KOP is not resolved in the KOP structure. (**D**) Opioid receptor sequence alignment of the nonconserved ECL3 (light red box) and the region close to the extracellular ends of helices VI and VII. The amino acids of MOP (E312) and KOP (H304) corresponding to DOP's R291 in the ECL3 region are highlighted in light red.

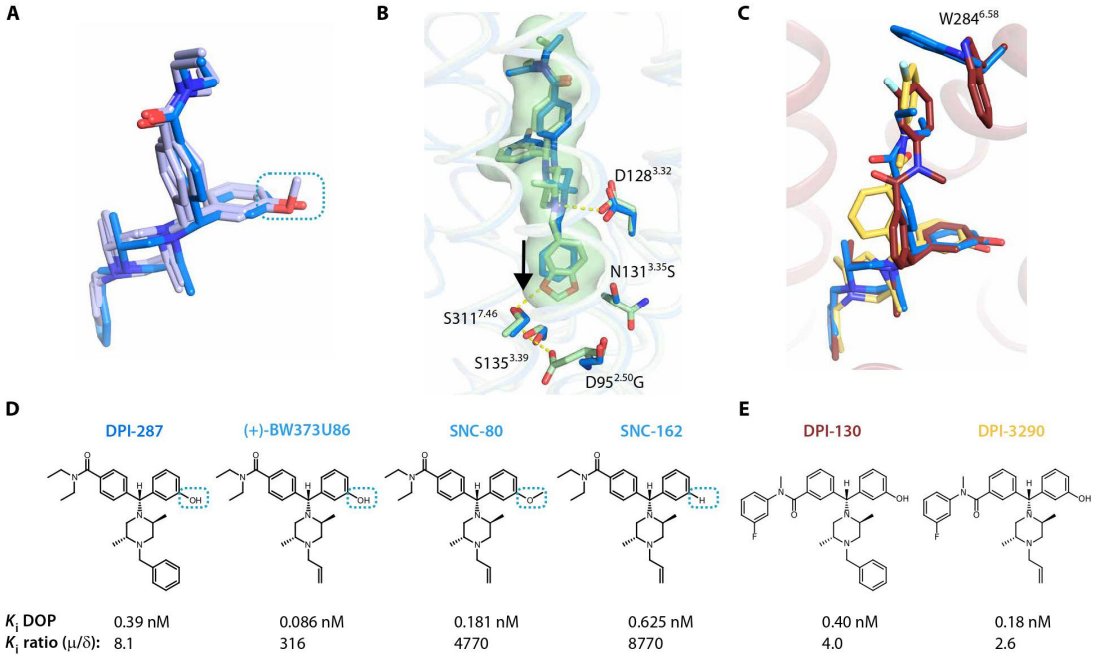

Fig. 6. Docking pose of DPI-287–related DOP agonists. (**A**) Alignment of the docking pose of the selected DPI-287 analogs BW373U86, SNC-80, and SNC-162 (all gray) with DPI-287 (blue). The blue box indicates the moiety with differences between these three docked analogs. (**B**) Docking pose of a DPI-287 analog with *N*-3,4-(methylenedioxy)benzyl substitution (green) and lacking the phenolic hydroxy function into a DOP model derived from the DOP-DPI-287 structure with G95$^{2.50}$D, S131$^{3.35}$N, and D108$^{2.63}$K reversed to WT, superimposed with DPI-287 (blue). The surface of the derivative is shown in green, and the black arrow indicates that the ligand is able to penetrate deeper into the entrance of the former sodium-binding pocket. (**C**) Superposition of the docking poses of DPI-130 (brown) and DPI-3290 (yellow) with DPI-287 suggests that the rotated W284$^{6.58}$ is essential for DOP binding. (**D**) Chemical structures and DOP binding properties (human opioid receptors) of (+)-BW373U86, SNC-80, and SNC-162 (*29*). (**E**) Chemical structures and binding properties (rat opioid receptors) of DPI-130 and DPI-3290 (*32*).

Structure-activity relationship of benzamide DOP agonists

The two new structures of DOP bound to a peptide and small-molecule agonist provide the structural basis for evaluating the key fingerprints that determine DOP selectivity. We performed molecular docking of several small-molecule analogs of DPI-287 at the DOP, MOP, and KOP (table S3). Docking of the selected DPI-287 analogs (+)-BW373U86, SNC-80, and SNC-162 (Fig. 6D) showed that these ligands assume the same orientation as that of DPI-287 with comparable docking scores at the DOP, whereas they exhibited much weaker docking scores at the MOP and KOP. Within this series of compounds, the phenolic hydroxy function of (+)-BW373U86 was either methylated (SNC-80) or removed (SNC-162), which interferes with their ability to form polar interactions. Previous work reported a reduced DOP affinity of these ligands by approximately twofold and approximately sevenfold, respectively, which is in agreement with the decrease of DPI-287 binding to mutants of Y129$^{3.33}$, one residue that interacts with the phenolic function of DPI-287 (table S1). Increased DOP selectivity was observed with phenolic moiety lacking (Fig. 6D) (*29*). However, the DOP docking poses of the respective benzyl moieties of SNC-80 and SNC-162 are overlapping with the phenol ring of DPI-287 in the new crystal structure (Fig. 6A), indicating that the water-mediated phenol interactions are not as important in the DOP as in the MOP.

(+)-BW373U86 differs from the cocrystallized DPI-287 only by its *N*4-allyl moiety but occupies the same position as DPI-287, while the allyl group overlaps with DPI-287's *N*4-benzyl moiety. In contrast, the bulkier *N*4-benzyl group of DPI-287 extends further into the entrance of the sodium-binding pocket. Conformational changes of W274$^{6.48}$ of the CW$^{6.48}$xP motif are essential for opening up the required space for the benzyl moiety (Fig. 2D). Moreover, it has been shown that substitution of the benzyl group with even larger residues like the *N*-3,4-(methylenedioxy)benzyl moiety (Fig. 6B) can be beneficial for DOP affinity (*30*). The docking pose of this analog reveals that it can penetrate further into the entrance of the sodium-binding pocket with only minor adjustment in the pocket-lining side chains, stabilized by a hydrogen bond to S311$^{7.46}$ (Fig. 6B). These findings indicate that the sodium-binding pocket can be targeted by ligand interactions in the DOP, as suggested for other GPCRs (*23*). However, the functional activity of ligands can be affected by further intrusion into the sodium pocket, as recently shown for the leukotriene B_4 receptor in complex with a bitopic ligand protruding deep into the sodium pocket. That ligand no longer activated the receptor but acted as an antagonist with inverse agonistic activity (*31*). The two *N*-(3-fluorophenyl)-*N*-methylbenzamide derivatives DPI-130 and DPI-3290 (*32*) differ from DPI-287 mostly in the bulkier benzamide moiety in the *meta*-position of the phenyl ring (Fig. 6E). Our docking studies show that the rotation of the W284$^{6.58}$ side chain, as observed in the DOP-KGCHM07 complex, can open up space for the 3-fluorophenyl moiety and stabilize it via π-π stacking interactions (Fig. 6C).

The piperazine ring of DPI-287 is represented in the energy-minimized chair conformation with axial methyl groups. Moreover, a conformational energy assessment predicted the axial methyl conformations as more favorable than the equatorial ones (−153.43 kJ/mol versus −109.81 kJ/mol). Methyl groups in the axial position are able to form hydrophobic contacts to Y129$^{3.33}$, M132$^{3.36}$, I304$^{7.39}$, and Y308$^{7.43}$, thereby perfectly occupying the additional binding pocket space. Furthermore, all docked analogs with the same *trans*-dimethyl substitutions showed axial methyl conformations (Figs. 4F and 6, A to C).

DISCUSSION

Here, two new active-like state DOP structures in complex with a peptide and a small-molecule agonist are presented at 2.8 and 3.3 Å resolution, respectively. We characterized both binding pockets and activation states by means of extensive pharmacological experiments and compared their binding poses to previously published opioid receptor structures. This approach allowed the determination of key factors for opioid receptor activation and DOP selectivity of *N*,*N*-diethylbenzamide derivatives, as well as crucial differences between peptide and small-molecule recognition.

Polar networks around the conserved D128$^{3.32}$ with rearrangements in the agonist-bound binding pocket are linked to DOP activation, which complements our understanding of opioid receptor activation. Similar interactions were observed in the active MOP (*18*) and KOP (*19*) structures. Furthermore, we observed that opioid agonists that contain a basic nitrogen interacting with D$^{3.32}$ extend deeper into the binding pocket as compared to structurally similar antagonists. Therefore, we suggest that the positioning of this basic nitrogen in the binding pocket and rearrangements in the polar network around D$^{3.32}$ are common denominators for opioid receptor activation by these ligands. This finding is in line with previous mutagenesis work (*33*). However, certain nonbasic ligands such as salvinorin A that are unable to form salt bridge interactions with D$^{3.32}$ are nonetheless able to activate opioid receptors (*34*), presumably by a unique activation mechanism involving hydrogen bonding to D$^{3.32}$ (*19*).

Moreover, we found substantial changes in the nonconserved ECL3 during activation, which makes R291^{ECL3} available for binding pocket interactions. The ECL3 region has been characterized as important for peptide agonist selectivity (*35*). The involvement of the nonconserved R291^{ECL3} seems reasonable and may represent a cationic counterpart for the carboxylate function of naturally occurring opioid peptides. This finding shows a possible interaction of R291^{ECL3} with the "address" moiety of endogenous peptides, based on the "message-address concept" proposed by Schwyzer in 1977 (*36*).

On the other hand, DOP-selective small molecules address the nonconserved extracellular ends of helices VI and VII with their *N*,*N*-diethylbenzamide moiety, providing a structural basis for DOP selectivity as this region is not similarly accessible in the MOP and KOP due to steric clashes. These findings are in agreement with previous data on DOP selectivity (*37*) and provide rational explanations that represent a substantial advance from our previous understanding. Moreover, the two new DOP structures have shed light on peptide recognition by the DOP. For instance, they revealed a large side-chain rotation of W284$^{6.58}$ in the peptide ligand binding pocket, allowing the peptide agonist KGCHM07 to access a larger subpocket with its C-terminal benzyl moiety. Our molecular docking studies show that the same pocket is probably also accessible for small molecules with bulkier amide substituents.

Together, our findings will be fundamental for DOP-centered, structure-based drug discovery programs in a time where opioid addiction–related deaths are markedly increasing, and safer opioid analgesics are urgently needed.

MATERIALS AND METHODS

Cloning, expression, and purification of the BRIL-DOP fusion protein

The construction of the DOP fusion protein gene was performed in a modified pFastBac1 vector as previously described (*16*). The amino acid residues 339 to 372 were truncated, and residues 1 to 40 were replaced with a thermostabilized apocytochrome b_{562}RIL from *Escherichia coli* (BRIL) containing the point mutations M7W, H102I, and R106L. A total of nine thermostabilizing point mutations were introduced into the DOP (G73$^{1.56}$V, N90$^{2.45}$S, D95$^{2.50}$G, K108$^{2.63}$D, N131$^{3.35}$S, S143$^{3.47}$C, G268$^{6.42}$V, A309$^{7.44}$I, and E323$^{8.48}$K). Eight of these mutations were transferred to the DOP from directed evolution experiments performed on the KOP (*38*). The engineered fusion protein was expressed in *Spodoptera frugiperda* (*Sf*9) insect cells using the Bac-to-Bac Baculovirus Expression System (Invitrogen). Cells were infected at a density of 2 × 10^6 cells ml^{-1} and a multiplicity of infection of 5, and cell pellets were harvested 48 hours after infection for storage at −80°C. Insect cells were lysed by osmotic shock in hypotonic buffer supplemented with EDTA-free complete protease inhibitor cocktail tablets (Roche), and membrane pellets were washed repeatedly as previously described (*16*). Purified membranes were flash-frozen in liquid nitrogen and stored at −80°C after resuspension in a buffer containing 10 mM Hepes (pH 7.5), 10 mM $MgCl_2$, 20 mM KCl, and 30% (v/v) glycerol. Before solubilization, thawed membranes were incubated for 1 hour at 4°C in the presence of iodoacetamide (2 mg ml^{-1}) and either 25 μM DPI-287 (WuXi AppTec, Shanghai, China) or 100 μM KGCHM07 [synthesized as previously described (*13*)]. GPCRs were extracted from Sf9 membranes by solubilization over the course of 3 hours at 4°C in a final buffer composed of 55 mM Hepes (pH 7.5), 500 mM NaCl, 5 mM $MgCl_2$, 10 mM KCl, 15% (v/v) glycerol, 1.0% (w/v) *n*-dodecyl-β-D-maltopyranoside (DDM; Anatrace), 0.2% (w/v) cholesteryl hemisuccinate (CHS; Sigma), and either 12.5 μM DPI-287 or 50 μM KGCHM07. The supernatant was separated from insolubilized material by centrifugation at 60,000*g* for 30 min and incubated with 20 mM imidazole (pH 7.5) and 0.01 ml of TALON immobilized metal affinity chromatography resin beads (Clontech) per milliliter of supernatant overnight at 4°C. The resin was washed with 15 column volumes of wash buffer I [50 mM Hepes (pH 7.5), 600 mM NaCl, 0.1% (w/v) DDM, 0.02% (w/v) CHS, 10% (v/v) glycerol, 10 mM adenosine triphosphate (ATP), 10 mM $MgCl_2$, and either 25 μM DPI-287 or 50 μM KGCHM07] and 10 column volumes of wash buffer II [50 mM Hepes (pH 7.5), 600 mM NaCl, 0.02% (w/v) DDM, 0.004% (w/v) CHS, 10% (v/v) glycerol, 50 mM imidazole, and either 25 μM DPI-287 or 50 μM KGCHM07]. Last, the protein was eluted from the column with three column volumes of elution buffer [50 mM Hepes (pH 7.5), 600 mM NaCl, 0.01% (w/v) DDM, 0.002% (w/v) CHS, 10% (v/v) glycerol, 250 mM imidazole, and either 25 μM DPI-287 or 100 μM KGCHM07], and the protein was concentrated to 20 to 30 mg ml^{-1} using 100-kDa molecular weight cutoff centrifuge concentrators (Vivaspin, GE Healthcare). The resulting protein solution was directly used for crystallization trials, while monodispersity

and protein yield were determined by analytical size exclusion chromatography.

Crystallization

The purified and concentrated DOP construct bound to agonists was reconstituted into lipidic cubic phase by mixing the protein with a molten lipid mixture [10% (w/w) cholesterol and 90% (w/w) monoolein] in a 2:3 ratio using the two-syringe method (*39*). Crystallization trials were performed with an automatic crystallization robot (NT8, Formulatrix) by overlaying 50 nl of mesophase with 0.8 μl of precipitant solution on 96-well glass sandwich plates (NOVA catalog no. NOA90020, Hong Kong). The crystallization plates were stored at 20°C and imaged using an automatic crystal imager (RockImager 1000, Formulatrix). Crystals started to grow overnight and typically reached full size within 10 days of incubation. Diffraction quality crystals (length, 100 to 140 μm) of the BRIL-DOP-DPI-287 complexes were obtained in precipitant solutions composed of 32 to 35% (v/v) PEG-400 (polyethylene glycol, average molecular weight 400), 100 to 110 mM potassium citrate tribasic monohydrate ($C_6H_5K_3O_7{\cdot}H_2O$), and 100 mM MES (pH 6.0), whereas crystals (length, ~70 μm) of the BRIL-DOP-KGCHM07 complexes were obtained in precipitant solutions composed of 27 to 32% (v/v) PEG-400, 100 to 120 mM potassium citrate tribasic monohydrate ($C_6H_5K_3O_7{\cdot}H_2O$), and 100 mM MES (pH 6.0). Crystals were harvested using 50 to 100 μm of MicroMounts (MiTeGen) and flash-frozen in liquid nitrogen.

Data collection and structure determination

X-ray data collection was carried out at the SPring-8 beamline 41XU (Hyogo, Japan) using an x-ray minibeam (x-ray wavelength, 1.0000 Å) with a Pilatus 6M detector for the BRIL-DOP-KGCHM07 crystals (beam size, 11.0 × 9.0 μm^2), whereas an EIGER 16M detector was used for the BRIL-DOP-DPI-287 crystals (beam size, 10.0 × 9.0 μm^2). Automatic rastering and data collection were performed according to previously described strategies (0.1 s of exposure time and 0.1° rotation per frame with a total rotation of 5° to 10°) (*40*). For both the BRIL-DOP-DPI-287 and BRIL-DOP-KGCHM07 complexes, datasets from 23 crystals were integrated, scaled, and merged using XDS/XSCALE (*41*). An initial molecular replacement solution was obtained by PHASER (*42*) in the CCP4 suite, using the receptor portions of the DOP structure (PDB 4N6H), and BRIL from $A_{2A}AR$ (PDB 4EIY) as independent search models. The resulting BRIL-DOP model was refined by manually building in the excessive $2F_o$-F_c density and by repetitive cycling between COOT (*43*) and BUSTER (*44*) until convergence. Ten translation, liberation, and screw-rotation atomic displacement (TLS) groups were used throughout refinement. The elongated electron density tubes near the protein hydrophobic surface were modeled as oleic acids, with the exception of the few that were better fit with monooleins (OLC), the major lipid component used for crystallization. Regarding the BRIL-DOP-DPI-287 complex, 20 μM BMS986187 (Tocris Bioscience) was added as a positive allosteric modulator (PAM) to solve a potential allosteric pocket. However, no additional electron density for the copurified PAM BMS986187 could be observed in the BRIL-DOP-DPI-287 structure, while the overall structures from crystals that were generated with and without copurified PAM were highly similar with a root mean square deviation (RMSD) of 0.372 Å. An unidentified ~2 σ positive $2F_o$-F_c density between DPI-287 and helices II and III was observed in both structures solved from crystals with and without copurified PAM, which was a suspected artifact of crystal condition components. This observation remains unmodeled. The final DOP-DPI-287 complex structure contains DOP receptor residues 41 to 329 (chain A) and 43 to 333 (chain B) with two residues (−1 and 0, chain A) from expression tag, and BRIL residues 1 to 106 (chain A) and 3 to 100 (chain B). The refined DOP-KGCHM07 complex structure contains DOP receptor residues 41 to 329 (chain A) and 41 to 333 (chain B) with two residues (−1 and 0, chain A) from expression tag, and BRIL residues 1 to 106 (chain A) and 2 to 104 (chain B). The C-terminal tail of the B chain in both structures is involved in crystal packing with N-terminal residues of the A chain, which led to disrupted helices VII and VIII in the B chains. The data collection and refinement statistics are shown in table S4.

Molecular modeling of water molecules in the binding pocket

To further evaluate water-mediated interactions in the binding pocket of DOP-KGCHM07 and DOP-DPI-287 structures, we used the energy-based water prediction tool Sample Flood available in ICM-Pro version 3.8.7a (Molsoft) (*45*). Water predictions obtained from this procedure were further evaluated for stability in the given space by performing energy-based conformational minimization and sampling using water molecules and side chains of amino acid residues located within 4 Å of predicted water molecules for at least 100,000 Monte Carlo steps. Water molecules showing consistent conformations were further evaluated by comparison with electron density maps and considered further for docking and ligand interaction analysis.

Molecular docking

Selected opioid small-molecular ligands and peptide structures were obtained from the ChEMBL database (*46*). These ligands were further docked into the DOP-DPI-287 and DOP-KGCHM07 crystal structures using the docking platform available in ICM-Pro version 3.8.7a. The receptor structure complexes were preprocessed for docking to remove nonreceptor fusions. Water molecules inferred from water modeling using Sample Flood procedure implemented in ICM-Pro, and from the electron density data, were maintained in place while preparing receptor potential grid maps for docking. Ligand geometry was preoptimized, and charge assignments were made using Merck Molecular Force Field (MMFF) (*47*). Conformational sampling and optimization in the docking process were performed using the biased probability Monte Carlo (BPMC) method with a sampling thoroughness of 50, beginning with a random seed conformation every time in at least three independent runs. The resulting docking poses were analyzed for their pose and interaction consistencies, and selected results were further analyzed. There were no distance restraints used to bias docking scores.

To revert the thermostabilizing mutations to WT residues in the docking models for a DPI-287 analog, the receptor coordinates from the DOP-DPI-287 complex structure were taken and the mutations around the ligand binding pocket $D95^{2.50}$, $N131^{3.35}$, and $K108^{2.63}$ were restored and the side chains were locally optimized using energy minimization–based refinement protocol in ICM-Pro. To account for the conformational changes, we further performed extensive energy minimization using BPMC protocol in ICM-Pro with at least 1,000,000 steps of conformational sampling and energy refinements. At the beginning of the refinement process, heavy atoms were restrained by soft harmonic tethers to the starting conformation to avoid large structural deviations, and then the tethers were gradually removed for the final refinement by reducing their weights. The refined structure had an RMSD value of 0.19 Å for all

C_α atoms compared to the DOP-DPI-287 complex and was further used for docking of a DPI-287 analog with *N*-3,4-(methylenedioxy) benzyl substitution using the abovementioned docking protocol.

Conformational state assessment with GAUGE

To assess the DOP structures in a rigorous and automated manner, we have developed a machine learning approach using class A GPCR structures available in the Protein Data Bank as a training set. Briefly, we selected a set of class A GPCR structures, in either fully active or inactive confirmations, and calculated distance-based descriptors for microswitches, including $P^{5.50}$-$I^{3.44}$-$F^{6.44}$, $D^{3.49}$-$R^{3.50}$-$Y^{3.51}$, and $N^{7.49}PxxY^{7.53}$ motifs and the conformations of the transmembrane helical domains near the intracellular region. Using this set of features and the annotated set of active and inactive structures as defined in the GPCRdb (*48*) as a training set, we applied a supervised machine learning approach to derive predictive models for each individual microswitch. We used support vector machines implemented in Python v.3.6 Scikit-learn library (*49*) for classification and regression to prepare models, to classify a given conformation as an active or inactive state, and to predict the extent of the activation by using regression models. For the assessment of DOP conformations, we used coordinates from the A chains of DOP-KGCHM07 and DOP-DPI-287. Nonreceptor fusions were removed, and the amino acid residues were mapped to their corresponding GPCRdb numbers (*50*). These structures were further used to calculate the set of corresponding descriptors as described above and used as an input for the prediction models to get the state assessment values (table S2). The method has the following advantages: (i) The scoring function in this tool includes conformational information from diverse class A GPCRs and is therefore less subjective than one representative structure. (ii) The regression models in this approach allow the evaluation of the extent of receptor activation on a scale from −1 (inactive) to 1 (active), derived from an analysis of known structures. (iii) By calculating individual scores at each major switch, one can detect special states that deviate from typical active or inactive states. For example, in the case of new active-state DOP structures, the GAUGE method detected that the DRY switch remains in the inactive state due to a lack of G protein or nanobody interactions with the receptor on the intracellular side.

Thermal shift assay

The protein thermostability of purified DOP constructs was assessed with a thermal shift assay using the thiol-specific fluorochrome *N*-[4-(7-diethylamino-4-methyl-3-coumarinyl)phenyl]maleimide (CPM). Stock solutions of CPM were prepared at 4 mg/ml in dimethyl sulfoxide and diluted 1:40 in buffer [25 mM Hepes (pH 7.5), 500 mM NaCl, 2% glycerol, 0.05% DDM, and 0.01% CHS] before usage. The reaction mixture was prepared in polymerase chain reaction (PCR) tubes of 0.2 ml capacity by mixing 1 μl of the diluted CPM stock solution with approximately 1 μg of purified protein in a total volume of 50 μl using the same buffer. Mixtures were incubated for 5 to 10 min, and protein thermostability was analyzed using a Rotor-Gene Q real-time PCR cycler (Qiagen) with an excitation wavelength of 365 ± 20 nm and a detection wavelength of 460 ± 20 nm (blue channel). The data of all samples were collected over a temperature range from 25° to 95°C with a temperature ramp of 1°C/min, and protein melting temperatures were determined using the Boltzmann sigmoidal fit (least squares) in GraphPad Prism 7.0 (GraphPad Software, San Diego, CA).

Radioligand binding assays

Binding assays were performed using membrane preparations from human embryonic kidney (HEK) 293 cells transiently transfected with 5 μg of DNA of the WT human DOP construct, or one of the various mutants of the full-length DOP or the BRIL-DOP crystal constructs. Cells (2.5×10^6) were transfected with X-tremeGENE HP (Sigma-Aldrich, Oakville, ON, Canada) in a 3:1 ratio using the manufacturer's protocol. Thirty-six hours after transfection, 58-cm^2 petri dishes were frozen at −80°C until use. On the day of the experiment, the cells were submitted to a heat shock by placing the petri dishes at 37°C for 60 s before returning them to ice. The cells were then harvested in 50 mM tris-HCl (pH 7.4) and centrifuged at 3200*g* for 15 min at 4°C. The protein concentration was determined with Bio-Rad DC Protein Assay reagents (Bio-Rad Laboratories, Mississauga, ON, Canada), and the pellet was further diluted in 50 mM tris-HCl (pH 7.4) buffer containing 0.1% bovine serum albumin (BSA) and distributed in 96-well plates. Saturation binding assays with 0.5 to 80 nM isotopically diluted [^{125}I]-deltorphin I were performed to determine the equilibrium dissociation constant (K_d) of each mutant for the radiotracer; 10 μM deltorphin I was used to define nonspecific binding. Determination of the affinity (K_i) of DPI-287 and KGCHM07 for DOP was achieved by competition binding assays with [^{125}I]-deltorphin I. The K_i values of the two compounds for DOP were determined using a membrane concentration of 20 to 40 μg of proteins per well and 1×10^5 counts per minute (cpm) of the radiolabeled ligand (specific activity, ~1700 Ci/mmol). Membranes and the radioligand were incubated for 60 min at room temperature with increasing concentrations of DPI-287 or KGCHM07 (0.1 pM to 10 μM). The reaction was then stopped by rapid vacuum filtration with ice-cold 50 mM tris-HCl (pH 7.4) on 96-well filter plates. Filters were then placed in 5-ml tubes, and the radioactivity was determined using the Wizard2 Automatic Gamma Counter (PerkinElmer, Woodbridge, ON, Canada). Data were analyzed using a nonlinear fitting analysis, and the K_i values were calculated using GraphPad Prism 7.0 (GraphPad Software, San Diego, CA). K_i values are expressed as means ± SEM from three to six independent experiments, each performed in duplicate. The affinity (K_i) of DPI-287 for MOP was achieved by competition binding assays with [^{125}I]DAMGO (specific activity, ~2200 Ci/mmol; K_d = 2 nM) and HEK cells expressing the human Flag-MOP (obtained from M. von Zastrow, University of California, San Francisco, CA). The K_i values in the displacement studies were determined from the half maximal inhibitory concentration (IC_{50}) values using the Cheng-Prusoff equation.

RLuc2-GFP10 BRET2-based biosensor assays

HEK293 cells were maintained in Dulbecco's modified Eagle's medium supplemented with 10% fetal bovine serum, penicillin (100 IU/ml), and streptomycin (100 μg/ml) at 37°C in a humidified 5% CO_2 atmosphere. For RLuc2-EPAC-GFP10 transfection, 500 ng of indicated receptor and 100 ng of RLuc2-EPAC-GFP10 per microgram of total transfected DNA were prepared in 150 mM NaCl. For β-arrestin2-GFP/receptor-RLuc2 transfection, 50 ng of WT and mutant crystallization construct BRIL-DOP or full-length DOP with RLuc2 cloned in the C terminus and 950 ng of β-arrestin2-GFP10 per microgram of total transfected DNA were prepared in 150 mM NaCl. For $G_{\alpha i1}$ biosensor assays, the indicated increasing amount of either DOP WT or BRIL-DOP crystal construct, 40 ng of G_α subunit, 250 ng of $G_{\beta 1}$ subunit, and 250 ng of $G_{\gamma 1}$ subunit per microgram of total transfected DNA were prepared in 150 mM NaCl.

Salmon sperm DNA was used to bring total transfected DNA to 1 μg, and each mixture was incubated for 20 min with 3 μg of polyethylenimine (Polysciences, Warrington, PA) per microgram of total transfected DNA before adding cells (350×10^3 cells/ml). Cells were plated at 35×10^3 cells per well in 96-well, flat-bottom, white opaque tissue culture plates. Forty-eight hours after seeding, cells were gently washed with stimulation buffer (10 mM Hepes, 1 mM $CaCl_2$, 0.5 mM $MgCl_2$, 4.2 mM KCl, 146 mM NaCl, and 5.5 mM glucose), and 80 μl of stimulation buffer was added to each well. Coelenterazine 400A (Gold Biotechnology Inc., St. Louis, MO) was added to a final concentration of 5 μM, 10 min before stimulation. For the EPAC (exchange protein directly activated by cAMP) assay, cells were stimulated with increasing concentrations of indicated ligand containing 3 μM forskolin (to increase cAMP) (Tocris Bioscience, Oakville, ON) for 10 min before signal acquisition. For β-arrestin2 assays, cells were stimulated with increasing concentrations of indicated ligand before signal acquisition. For $G_{\alpha i1}$ assays, cells were either unstimulated or stimulated with 100 nM DPI-287 for 5 min before signal acquisition. $BRET_2$ (bioluminescence resonance energy transfer 2) signals were measured using a TECAN M1000 fluorescence reader (TECAN, Grödig, Austria). RLuc2 and GFP10 emissions were collected in the 400- to 450-nm window (RLuc2) and 500- to 550-nm window (GFP10). The $BRET^2$ signal was calculated as the ratio of light emitted by the acceptor GFP10 over the light emitted by the donor RLuc2. For each assay, data were normalized as percentage of the maximal response for each ligand in the appropriate WT receptor background. All data were analyzed using the nonlinear curve fitting equations in GraphPad Prism 7.0 (GraphPad Software, San Diego, CA) to estimate the pEC_{50} values of the curves for the different pathways. Results are expressed as means ± SEM from $n = 4$ (EPAC) or $n = 3$ (β-arrestin2) independent experiments, each performed in triplicate.

Cell surface expression of the DOP

HEK293 cells (150×10^3) were transfected in suspension with 470 ng of DNA of the WT human DOP construct or one of the various mutants of the full-length DOP or the BRIL-DOP crystal constructs using X-tremeGENE HP 4:1 ratio in 24-well plates precoated with poly-L-lysine. Forty-eight hours after transfection, cells were fixed using a 3.7% formaldehyde/tris-buffered saline (TBS) solution. After 30 min of blocking with 1% BSA/TBS, the cells were incubated for 1 hour with a polyclonal anti-flag antibody (1:1000; Invitrogen, catalog no. 710662) followed by 1-hour incubation with anti-rabbit alkaline phosphatase (1:10,000; Sigma-Aldrich, catalog no. A3687). The level of expression of membrane DOP was detected using alkaline phosphatase substrate (Sigma-Aldrich, catalog no. S0942) in a solution containing 10% diethanolamine and 12.5 μM $MgCl_2$ (pH 9.8). The reaction was stopped by the addition of 0.4 M NaOH before reading absorbance at 405 nm using a TECAN M1000 multimode reader. Results are expressed as means ± SD from $n = 2$ independent experiments, each performed in triplicate.

SUPPLEMENTARY MATERIALS

Supplementary material for this article is available at http://advances.sciencemag.org/cgi/content/full/5/11/eaax9115/DC1

Supplementary Text

Fig. S1. Overall conformational changes of BRIL-DOP-KGCHM07 and BRIL-DOP-DPI-287 compared to other opioid receptor structures.

Fig. S2. The importance of sodium-binding pocket mutations and DOP agonists for protein thermostability.

Fig. S3. Effects of sodium-binding pocket mutations on DOP activation by DOP agonist DPI-287 and enhanced constitutive activity.

Fig. S4. Differences between ligand recognition with different scaffolds by the DOP.

Fig. S5. Water-mediated interactions during DOP activation.

Fig. S6. The crystal lattice of the active-like BRIL-DOP structures is arranged in antiparallel dimers.

Table S1. Pharmacological assessment of crystal structure construct mutants in WT (gray) or crystal structure construct background (blue) and ligand binding pocket mutants (green).

Table S2. Assessment of conformational states with the "GAUGE" tool for the DOP and other opioid receptor structures.

Table S3. Docking results for selected small-molecule and peptide DOP agonists.

Table S4. Data collection and refinement statistics.

View/request a protocol for this paper from *Bio-protocol*.

REFERENCES AND NOTES

1. S. Berterame, J. Erthal, J. Thomas, S. Fellner, B. Vosse, P. Clare, W. Hao, D. T. Johnson, A. Mohar, J. Pavadia, A. K. E. Samak, W. Sipp, V. Sumyai, S. Suryawati, J. Toufiq, R. Yans, R. P. Mattick, Use of and barriers to access to opioid analgesics: A worldwide, regional, and national study. *Lancet* **387**, 1644–1656 (2016).
2. D. H. Epstein, M. Heilig, Y. Shaham, Science-based actions can help address the opioid crisis. *Trends Pharmacol. Sci.* **39**, 911–916 (2018).
3. P.-Y. Law, P. H. Reggio, H. H. Loh, Opioid receptors: Toward separation of analgesic from undesirable effects. *Trends Biochem. Sci.* **38**, 275–282 (2013).
4. B. M. Cox, M. J. Christie, L. Devi, L. Toll, J. R. Traynor, Challenges for opioid receptor nomenclature: IUPHAR Review 9. *Br. J. Pharmacol.* **172**, 317–323 (2015).
5. R. J. Valentino, N. D. Volkow, Untangling the complexity of opioid receptor function. *Neuropsychopharmacology* **43**, 2514–2520 (2018).
6. H. W. Matthes, R. Maldonado, F. Simonin, O. Valverde, S. Slowe, I. Kitchen, K. Befort, A. Dierich, M. Le Meur, P. Dollé, E. Tzavara, J. Hanoune, B. P. Roques, B. L. Kieffer, Loss of morphine-induced analgesia, reward effect and withdrawal symptoms in mice lacking the μ-opioid-receptor gene. *Nature* **383**, 819–823 (1996).
7. L. Gendron, N. Mittal, H. Beaudry, W. Walwyn, Recent advances on the δ opioid receptor: From trafficking to function. *Br. J. Pharmacol.* **172**, 403–419 (2015).
8. L. Gendron, C. M. Cahill, M. von Zastrow, P. W. Schiller, G. Pineyro, Molecular pharmacology of δ-opioid receptors. *Pharmacol. Rev.* **68**, 631–700 (2016).
9. E. M. Jutkiewicz, The antidepressant-like effects of delta-opioid receptor agonists. *Mol. Interv.* **6**, 162–169 (2006).
10. J. Hughes, T. W. Smith, H. W. Kosterlitz, L. A. Fothergill, B. A. Morgan, H. R. Morris, Identification of two related pentapeptides from the brain with potent opiate agonist activity. *Nature* **258**, 577–580 (1975).
11. P. W. Schiller, Opioid peptide-derived analgesics. *AAPS J.* **7**, E560–E565 (2005).
12. J. V. Aldrich, J. P. McLaughlin, Opioid peptides: Potential for drug development. *Drug Discov. Today Technol.* **9**, e23–e31 (2012).
13. K. Guillemyn, P. Kleczkowska, A. Lesniak, J. Dyniewicz, O. Van der Poorten, I. Van den Eynde, A. Keresztes, E. Varga, J. Lai, F. Porreca, N. N. Chung, C. Lemieux, J. Mika, E. Rojewska, W. Makuch, J. Van Duppen, B. Przewlocka, J. Vanden Broeck, A. W. Lipkowski, P. W. Schiller, D. Tourwé, S. Ballet, Synthesis and biological evaluation of compact, conformationally constrained bifunctional opioid agonist–neurokinin-1 antagonist peptidomimetics. *Eur. J. Med. Chem.* **92**, 64–77 (2015).
14. K. J. Chang, G. C. Rigdon, J. L. Howard, R. W. McNutt, A novel, potent and selective nonpeptidic delta opioid receptor agonist BW373U86. *J. Pharmacol. Exp. Ther.* **267**, 852–857 (1993).
15. A. A. Pradhan, K. Befort, C. Nozaki, C. Gavériaux-Ruff, B. L. Kieffer, The delta opioid receptor: An evolving target for the treatment of brain disorders. *Trends Pharmacol. Sci.* **32**, 581–590 (2011).
16. G. Fenalti, P. M. Giguere, V. Katritch, X.-P. Huang, A. A. Thompson, V. Cherezov, B. L. Roth, R. C. Stevens, Molecular control of δ-opioid receptor signalling. *Nature* **506**, 191–196 (2014).
17. G. Fenalti, N. A. Zatsepin, C. Betti, P. Giguere, G. W. Han, A. Ishchenko, W. Liu, K. Guillemyn, H. Zhang, D. James, D. Wang, U. Weierstall, J. C. H. Spence, S. Boutet, M. Messerschmidt, G. J. Williams, C. Gati, O. M. Yefanov, T. A. White, D. Oberthuer, M. Metz, C. H. Yoon, A. Barty, H. N. Chapman, S. Basu, J. Coe, C. E. Conrad, R. Fromme, P. Fromme, D. Tourwé, P. W. Schiller, B. L. Roth, S. Ballet, V. Katritch, R. C. Stevens, V. Cherezov, Structural basis for bifunctional peptide recognition at human δ-opioid receptor. *Nat. Struct. Mol. Biol.* **22**, 265–268 (2015).
18. W. Huang, A. Manglik, A. J. Venkatakrishnan, T. Laeremans, E. N. Feinberg, A. L. Sanborn, H. E. Kato, K. E. Livingston, T. S. Thorsen, R. C. Kling, S. Granier, P. Gmeiner, S. M. Husbands, J. R. Traynor, W. I. Weis, J. Steyaert, R. O. Dror, B. K. Kobilka, Structural insights into μ-opioid receptor activation. *Nature* **524**, 315–321 (2015).

19. T. Che, S. Majumdar, S. A. Zaidi, P. Ondachi, J. D. McCorvy, S. Wang, P. D. Mosier, R. Uprety, E. Vardy, B. E. Krumm, G. W. Han, M.-Y. Lee, E. Pardon, J. Steyaert, X.-P. Huang, R. T. Strachan, A. R. Tribo, G. W. Pasternak, F. I. Carroll, R. C. Stevens, V. Cherezov, V. Katritch, D. Wacker, B. L. Roth, Structure of the nanobody-stabilized active state of the kappa opioid receptor. *Cell* **172**, 55–67.e15 (2018).
20. A. Koehl, H. Hu, S. Maeda, Y. Zhang, Q. Qu, J. M. Paggi, N. R. Latorraca, D. Hilger, R. Dawson, H. Matile, G. F. X. Schertler, S. Granier, W. I. Weis, R. O. Dror, A. Manglik, G. Skiniotis, B. K. Kobilka, Structure of the μ-opioid receptor–G_i protein complex. *Nature* **558**, 547–552 (2018).
21. D. Zhang, Q. Zhao, B. Wu, Structural studies of G protein-coupled receptors. *Mol. Cells* **38**, 836–842 (2015).
22. J. A. Ballesteros, H. Weinstein, Integrated methods for the construction of three-dimensional models and computational probing of structure-function relations in G protein-coupled receptors. *Methods Neurosci.* **25**, 366–428 (1995).
23. V. Katritch, G. Fenalti, E. E. Abola, B. L. Roth, V. Cherezov, R. C. Stevens, Allosteric sodium in class A GPCR signaling. *Trends Biochem. Sci.* **39**, 233–244 (2014).
24. V. Katritch, V. Cherezov, R. C. Stevens, Structure-function of the G protein–coupled receptor superfamily. *Annu. Rev. Pharmacol. Toxicol.* **53**, 531–556 (2013).
25. A. J. Venkatakrishnan, X. Deupi, G. Lebon, C. G. Tate, G. F. Schertler, M. M. Babu, Molecular signatures of G-protein-coupled receptors. *Nature* **494**, 185–194 (2013).
26. A. Ghosh, J. Luo, C. Liu, G. Weltrowska, C. Lemieux, N. N. Chung, Y. Lu, P. W. Schiller, Novel opioid peptide derived antagonists containing (2S)-2-methyl-3-(2,6-dimethyl-4-carbamoylphenyl)propanoic acid (2S)-Mdcp. *J. Med. Chem.* **51**, 5866–5870 (2008).
27. P. W. Schiller, I. Berezowska, T. M.-D. Nguyen, R. Schmidt, C. Lemieux, N. N. Chung, M. L. Falcone-Hindley, W. Yao, J. Liu, S. Iwama, A. B. Smith, R. Hirschmann, Novel ligands lacking a positive charge for the δ- and μ-opioid receptors. *J. Med. Chem.* **43**, 551–559 (2000).
28. D. W. Hansen Jr., A. Stapelfeld, M. A. Savage, M. Reichman, D. L. Hammond, R. C. Haaseth, H. I. Mosberg, Systemic analgesic activity and delta-opioid. selectivity in 2,6-dimethyl-Tyr1,D-Pen2,D-Pen5enkephalin. *J. Med. Chem.* **35**, 684–687 (1992).
29. R. J. Knapp, G. Santoro, I. A. De Leon, K. B. Lee, S. A. Edsall, S. Waite, E. Malatynska, E. Varga, S. N. Calderon, K. C. Rice, R. B. Rothman, F. Porreca, W. R. Roeske, H. I. Yamamura, Structure-activity relationships for SNC80 and related compounds at cloned human delta and mu opioid receptors. *J. Pharmacol. Exp. Ther.* **277**, 1284–1291 (1996).
30. D. R. Barn, A. Bom, J. Cottney, W. L. Caulfield, J. R. Morphy, Synthesis of novel analogues of the delta opioid ligand SNC-80 using $AlCl_3$-promoted aminolysis. *Bioorganic Med. Chem. Lett.* **9**, 1329–1334 (1999).
31. T. Hori, T. Okuno, K. Hirata, K. Yamashita, Y. Kawano, M. Yamamoto, M. Hato, M. Nakamura, T. Shimizu, T. Yokomizo, M. Miyano, S. Yokoyama, Na+-mimicking ligands stabilize the inactive state of leukotriene B_4 receptor BLT1. *Nat. Chem. Biol.* **14**, 262–269 (2018).
32. S.-p. Yi, Q.-h. Kong, Y.-l. Li, C.-l. Pan, J. Yu, B.-q. Cui, Y.-f. Wang, G.-l. Wang, P.-l. Zhou, L.-l. Wang, Z.-h. Gong, R.-b. Su, Y.-h. Shen, G. Yu, K.-J. Chang, The opioid receptor triple agonist DPI-125 produces analgesia with less respiratory depression and reduced abuse liability. *Acta Pharmacol. Sin.* **38**, 977–989 (2017).
33. A. Cavalli, A.-M. Babey, H. H. Loh, Altered adenylyl cyclase responsiveness subsequent to point mutations of Asp 128 in the third transmembrane domain of the δ-opioid receptor. *Neuroscience* **93**, 1025–1031 (1999).
34. B. L. Roth, K. Baner, R. Westkaemper, D. Siebert, K. C. Rice, S. Steinberg, P. Ernsberger, R. B. Rothman, Salvinorin A: A potent naturally occurring nonnitrogenous kappa opioid selective agonist. *Proc. Natl. Acad. Sci. U.S.A.* **99**, 11934–11939 (2002).
35. F. Meng, Y. Ueda, M. T. Hoversten, R. C. Thompson, L. Taylor, S. J. Watson, H. Akil, Mapping the receptor domains critical for the binding selectivity of delta-opioid receptor ligands. *Eur. J. Pharmacol.* **311**, 285–292 (1996).
36. R. Schwyzer, ACTH: A short introductory review. *Ann. N. Y. Acad. Sci.* **297**, 3–26 (1977).
37. C. Marie-Pepin, S. Y. Yue, E. Roberts, C. Wahlestedt, P. Walker, Novel "restoration of function" mutagenesis strategy to identify amino acids of the δ-opioid receptor involved in ligand binding. *J. Biol. Chem.* **272**, 9260–9267 (1997).
38. M. Schütz, J. Schöppe, E. Sedlák, M. Hillenbrand, G. Nagy-Davidescu, J. Ehrenmann, C. Klenk, P. Egloff, L. Kummer, A. Plückthun, Directed evolution of G protein-coupled receptors in yeast for higher functional production in eukaryotic expression hosts. *Sci. Rep.* **6**, 21508 (2016).
39. M. Caffrey, V. Cherezov, Crystallizing membrane proteins using lipidic mesophases. *Nat. Protoc.* **4**, 706–731 (2009).
40. V. Cherezov, M. A. Hanson, M. T. Griffith, M. C. Hilgart, R. Sanishvili, V. Nagarajan, S. Stepanov, R. F. Fischetti, P. Kuhn, R. C. Stevens, Rastering strategy for screening and centring of microcrystal samples of human membrane proteins with a sub-10 microm size X-ray synchrotron beam. *J. R. Soc. Interface* **6 Suppl. 5**, S587–S597 (2009).
41. W. Kabsch, XDS. *Acta Crystallogr. D Biol. Crystallogr.* **66**, 125–132 (2010).
42. A. J. McCoy, R. W. Grosse-Kunstleve, P. D. Adams, M. D. Winn, L. C. Storoni, R. J. Read, Phaser crystallographic software. *J. Appl. Cryst.* **40**, 658–674 (2007).
43. P. Emsley, B. Lohkamp, W. G. Scott, K. Cowtan, Features and development of Coot. *Acta Crystallogr. D Biol. Crystallogr.* **66**, 486–501 (2010).
44. O. S. Smart, T. O. Womack, C. Flensburg, P. Keller, W. Paciorek, A. Sharff, C. Vonrhein, G. Bricogne, Exploiting structure similarity in refinement: Automated NCS and target-structure restraints in BUSTER. *Acta Crystallogr. D Biol. Crystallogr.* **68**, 368–380 (2012).
45. R. Abagyan, M. Totrov, D. Kuznetsov, ICM—A new method for protein modeling and design: Applications to docking and structure prediction from the distorted native conformation. *J. Comput. Chem.* **15**, 488–506 (1994).
46. A. P. Bento, A. Gaulton, A. Hersey, L. J. Bellis, J. Chambers, M. Davies, F. A. Krüger, Y. Light, L. Mak, S. McGlinchey, M. Nowotka, G. Papadatos, R. Santos, J. P. Overington, The ChEMBL bioactivity database: An update. *Nucleic Acids Res.* **42**, D1083–D1090 (2014).
47. T. A. Halgren, Merck molecular force field. I. Basis, form, scope, parameterization, and performance of MMFF94. *J. Comput. Chem.* **17**, 490–519 (1996).
48. G. Pándy-Szekeres, C. Munk, T. M. Tsonkov, S. Mordalski, K. Harpsøe, A. S. Hauser, A. J. Bojarski, D. E. Gloriam, GPCRdb in 2018: Adding GPCR structure models and ligands. *Nucleic Acids Res.* **46**, D440–D446 (2018).
49. F. Pedregosa, G. Varoquaux, A. Gramfort, V. Michel, B. Thirion, O. Grisel, M. Blondel, P. Prettenhofer, R. Weiss, V. Dubourg, J. Vanderplas, A. Passos, D. Cournapeau, M. Brucher, M. Perrot, É. Duchesnay, Scikit-learn: Machine learning in Phyton. *J. Mach. Learn. Res.* **12**, 2825–2830 (2011).
50. V. Isberg, C. de Graaf, A. Bortolato, V. Cherezov, V. Katritch, F. H. Marshall, S. Mordalski, J.-P. Pin, R. C. Stevens, G. Vriend, D. E. Gloriam, Generic GPCR residue numbers – aligning topology maps while minding the gaps. *Trends Pharmacol. Sci.* **36**, 22–31 (2015).

Acknowledgments: The diffraction data were collected at the BL41XU of SPring-8 (JASRI proposals 2017A2708, 2017B2707, 2018A2561, and 2018B2721). We thank T. Hua, Y. Peng, K. Hasegawa, H. Okumura, and H. Murakami for their help with data collection. We thank the Cloning, Cell Expression, Assay, and Protein Purification Core Facilities of the iHuman Institute for their support. R.C.S. acknowledges that the University of Southern California is his primary affiliation. **Funding:** We thank the Shanghai Municipal Government, ShanghaiTech University, and GPCR Consortium for financial support. C.M., O.V.d.P., and S.B. thank the Research Foundation Flanders (FWO Vlaanderen) and the Research Council of the Vrije Universiteit Brussel for financial support. This work was supported by NIH grants R33DA038858 (V.K.) and P01DA035764 (V.K., V.C., and R.C.S.), as well as the Canadian Institute of Health Research (CIHR) (grant numbers MOP-123399 and MOP-136871) awarded to L.G. L.G. is the recipient of a Senior Salary support from the Fonds de Recherche du Québec—Santé. Funding from Shanghai covered the expression, crystallization, data collection, structure solution, and structure analysis research. Funding from the U.S. NIH supported the construct design and structure refinement/analysis. **Author contributions:** T.C., J.Y., V.B., N.P., C.M., L.W., G.W.H., B.J.H., and O.V.d.P. performed the experiments and analyzed the data. K.L.W., M.A.H., P.S., L.G., V.C., V.K., S.B., Z.-J.L., C.E.M., and R.C.S contributed to the study design, planning of the experiments, and interpretation of the data. T.C., J.Y., V.B., N.P., L.G., V.K., S.B., C.E.M., and R.C.S. wrote the manuscript; all other authors contributed to writing and revising the manuscript. **Competing interests:** V.C. is an author and editor at *Science Advances*. M.A.H. and R.C.S. are founders of ShouTi Pharma, a company focused on structure-based drug design for GPCRs. The authors declare that they have no other conflicts of interest. **Data and materials availability:** All data needed to evaluate the conclusions in the paper are present in the paper and/or the Supplementary Materials. Coordinates and structure factors have been deposited in the Protein Data Bank (PDB) under accession codes 6PT2 (BRIL-DOP-KGCHM07) and 6PT3 (BRIL-DOP-DPI-287). Other data are available from the corresponding authors upon reasonable request. Requests for the biosensors (RLuc2-EPAC-GFP10; $G_{\alpha i1}$-RLuc2 and $G_{\gamma 1}$-GFP10) should be submitted to M. Bouvier (michel.bouvier@umontreal.ca).

Submitted 3 May 2019
Accepted 25 September 2019
Published 27 November 2019
10.1126/sciadv.aax9115

Citation: T. Claff, J. Yu, V. Blais, N. Patel, C. Martin, L. Wu, G. W. Han, B. J. Holleran, O. Van der Poorten, K. L. White, M. A. Hanson, P. Sarret, L. Gendron, V. Cherezov, V. Katritch, S. Ballet, Z.-J. Liu, C. E. Müller, R. C. Stevens, Elucidating the active δ-opioid receptor crystal structure with peptide and small-molecule agonists. *Sci. Adv.* **5**, eaax9115 (2019).

Supplementary Materials

of

Publication I

in

***Science Advances*[80]**

Science Advances
AAAS

advances.sciencemag.org/cgi/content/full/5/11/eaax9115/DC1

Supplementary Materials for

Elucidating the active δ-opioid receptor crystal structure with peptide and small-molecule agonists

Tobias Claff, Jing Yu, Véronique Blais, Nilkanth Patel, Charlotte Martin, Lijie Wu, Gye Won Han, Brian J. Holleran, Olivier Van der Poorten, Kate L. White, Michael A. Hanson, Philippe Sarret, Louis Gendron, Vadim Cherezov, Vsevolod Katritch, Steven Ballet, Zhi-Jie Liu, Christa E. Müller*, Raymond C. Stevens*

*Corresponding author. Email: christa.mueller@uni-bonn.de (C.E.M.); stevens@shanghaitech.edu.cn (R.C.S.)

Published 27 November 2019, *Sci. Adv.* **5**, eaax9115 (2019)
DOI: 10.1126/sciadv.aax9115

This PDF file includes:

Supplementary Materials

Supplementary Text

The thermostabilized DOP construct

In order to improve receptor expression and crystallize the DOP in complex with agonists, we introduced eight point mutations ($N90^{2.45}S$, $D95^{2.50}G$, $K108^{2.63}D$, $N131^{3.35}S$, $S143^{3.47}C$, $G268^{6.42}V$, $A309^{7.44}I$ and $E323^{8.48}K$) based on a KOP agonist-stabilized construct, that had been obtained by a directed evolution approach (*38*). We additionally optimized the position of the *N*-terminal fusion partner, and screened for further thermostabilizing point mutations. Forty *N*-terminal amino acids were replaced with a thermostabilized cytochrome b562 (BRIL), and an additional point mutation ($G73^{1.56}V$) was introduced, where $V^{1.56}$ is conserved in the MOP and KOP. In order to further reduce flexibility, thirty-three *C*-terminal amino acids were truncated. The resulting DOP fusion protein proved to be highly stable, and the purified monomeric protein resulted in a prominent increase in thermostability by 23 °C and 27 °C upon binding of the agonists KGCHM07 and DPI-287, respectively (**fig. S2**). Complexes with these agonists were subsequently used to determine the BRIL-DOP-KGCHM07 and BRIL-DOP-DPI-287 crystal structures at 2.8 Å and 3.3 Å resolution, respectively. Except for local ligand-specific variations, the two agonist-bound DOP structures are highly similar with a root-mean-square deviation (RMSD) of 0.44 Å for the backbone Cα atoms of the DOP (see **table S4** for crystallographic statistics). The thermostabilized DOP fusion proteins crystallized as antiparallel dimers (**fig. S6**). Structural analysis and comparisons were undertaken using the A chains in both structures, which have better B-factors than the B chains and lack crystal packing contacts in the transmembrane helices (**table S4** and **fig. S6**).

Supplementary Figures

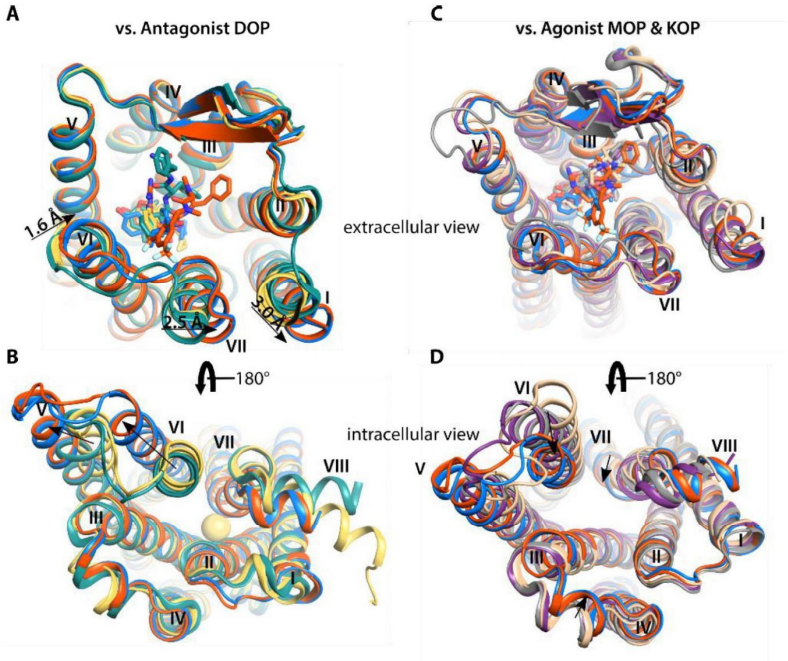

Fig. S1. Overall conformational changes of BRIL-DOP-KGCHM07 and BRIL-DOP-DPI-287 compared to other opioid receptor structures. BRIL-DOP-KGCHM07, orange; BRIL-DOP-DPI-287, blue; DIPP-NH_2 DOP antagonist structure (PDB 4RWD), cyan; naltrindole DOP antagonist structure (PDB 4N6H), yellow; BU72-MOP agonist structure (PDB 5C1M), purple; MP-1104 KOP agonist structure (PDB 6B73), gray; and DAMGO-MOP agonist structure (PDB 6DDF), wheat. (**A**) Top-view and (**B**) intracellular view of agonist-bound DOP structures aligned with inactive opioid receptor structures. (**C**) Top-view and (**D**) intracellular view of agonist-bound DOP structures aligned with active opioid receptor structures.

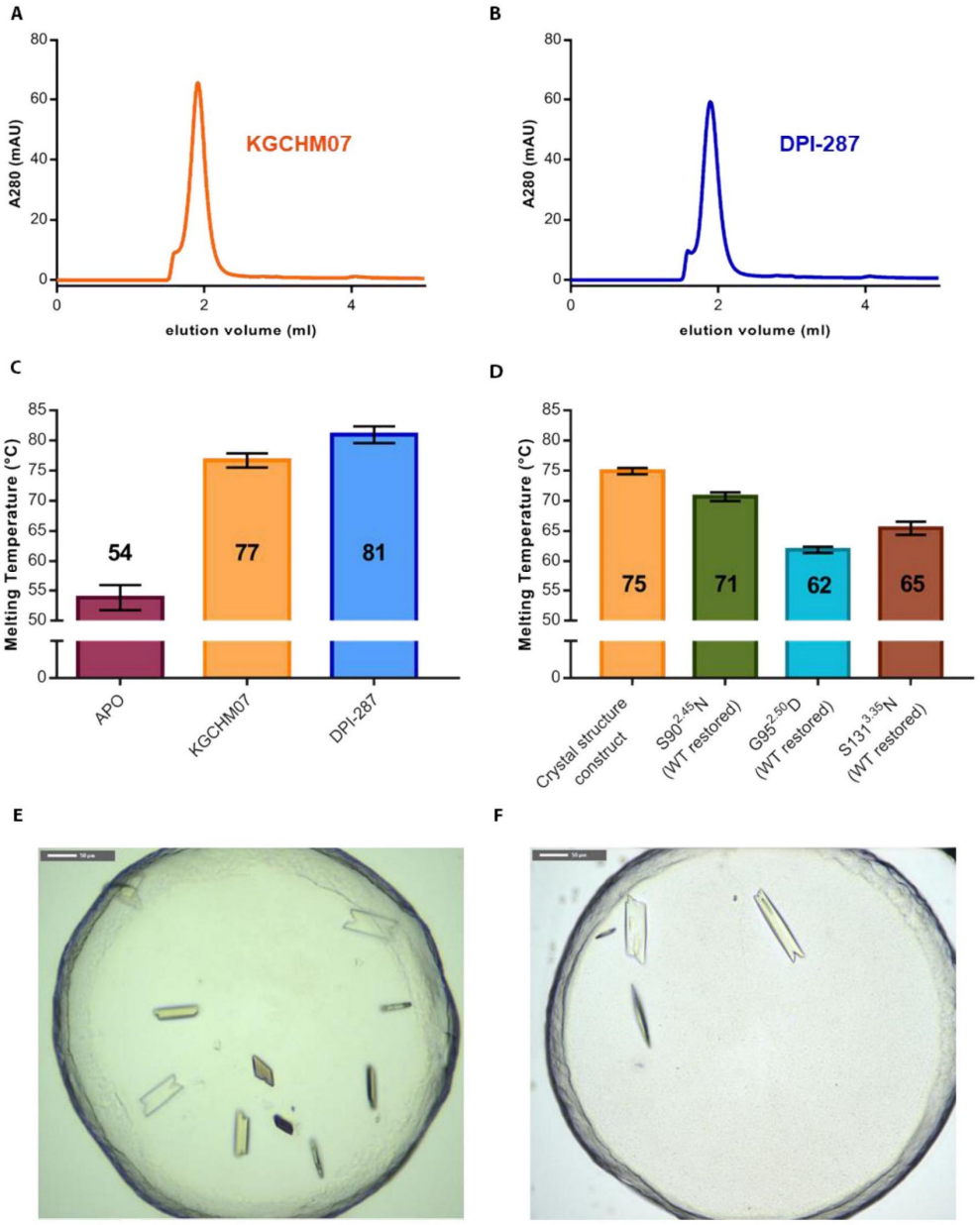

Fig. S2. The importance of sodium-binding pocket mutations and DOP agonists for protein thermostability. Analytical size-exclusion chromatography results for (**A**) typical purified protein preparation of a co-purified KGCHM07 and (**B**) co-purified DPI-287 used for LCP crystallography. (**C**) Changes in thermostability upon binding of different agonists (n=3; means with error bars indicating SEM) (**D**) Impact of sodium-binding pocket mutations on thermostability when restored to its WT-residue in crystal construct background. DOP constructs were co-purified with KGCHM07 (n=5; means with error bars indicating SEM). (**E**) BRIL-DOP-KGCHM07 and (**F**) BRIL-DOP-DPI-287 crystals grown in LCP after 10 days.

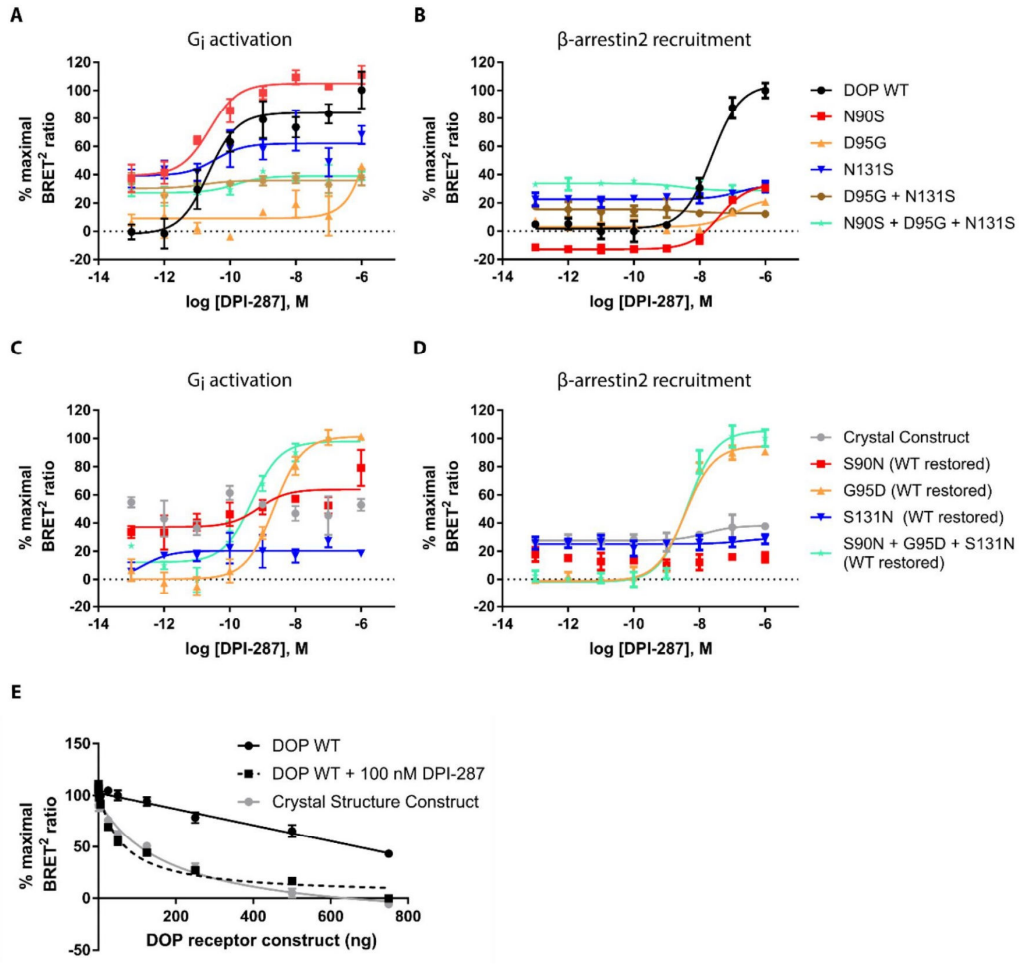

Fig. S3. Effects of sodium-binding pocket mutations on DOP activation by DOP agonist DPI-287 and enhanced constitutive activity. G_i-mediated cAMP signaling of (**A**) sodium binding pocket mutants and (**B**) crystal structure construct mutants with sodium binding pocket mutations restored to WT residues in response to different DPI-287 concentrations. β-arrestin2 recruitment of (**C**) sodium binding pocket mutants and (**D**) crystal structure construct mutants with sodium binding pocket mutations restored to WT residues in response to different DPI-287 concentrations. (**E**) Constitutive activity of crystal structure construct (gray circles) was compared to DOP WT stimulated (black squares) or not (black circles) with 100 nM DPI-287 for 5 min. Increasing amount of receptor DNA was co-transfected with constant amounts of $G_{\alpha i1}$-RLuc2, $G_{\beta 1}$ and $G_{\gamma 1}$-GFP10. Values are means of three separate experiments done in quadruplicate with error bars indicating SEM.

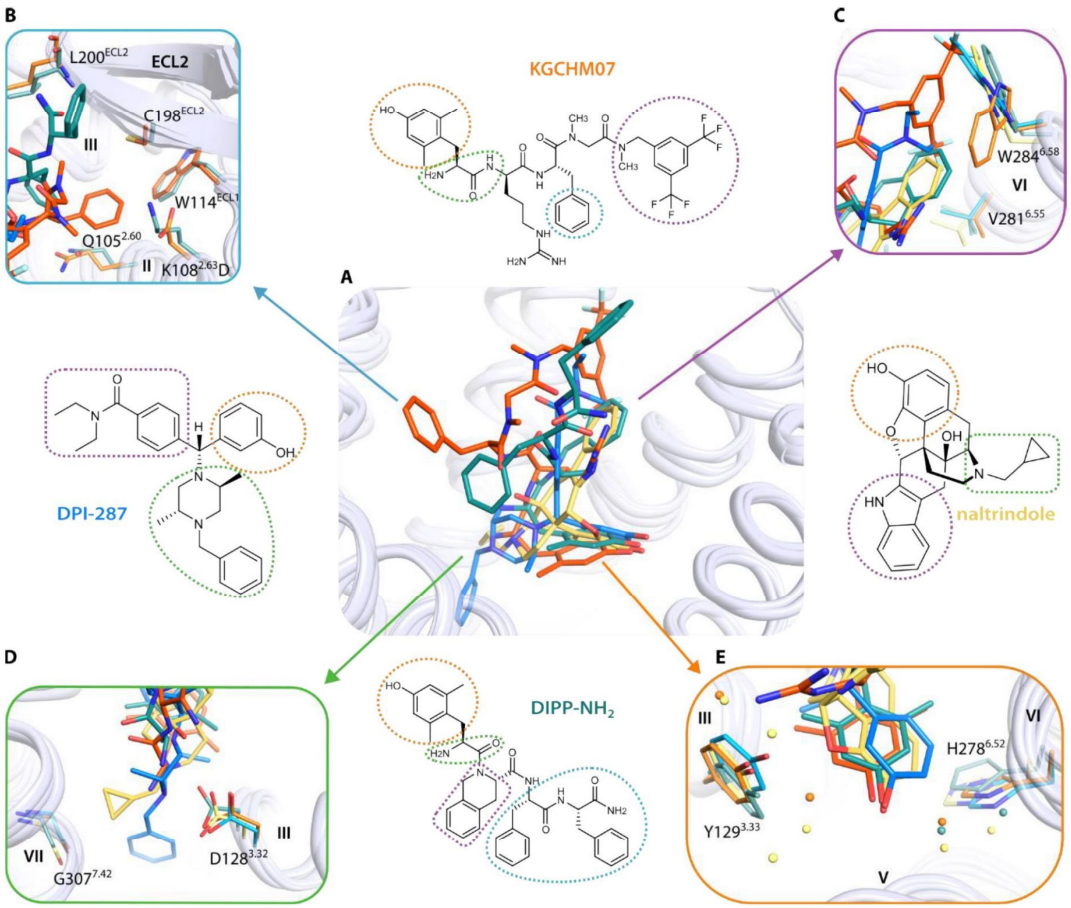

Fig. S4. Differences between ligand recognition with different scaffolds by the DOP. (**A**) Superposition of ligand binding pockets of agonists DOP-KGCHM07 (orange) and DOP-DPI-287 (blue) with antagonists DOP-DIPP-NH_2 (cyan, PDB 4RWD) and DOP-naltrindole (yellow, PDB 4N6H) with their chemical structures. Enlarged segments highlight protein-ligand interaction differences between the diverse scaffolds: (**B**) phenylalanine residues of peptides KGCHM07 and DIPP-NH_2; (**C**) interactions with helix VI; (**D**) interaction of basic primary amines of peptides and the substituted basic amine of small molecules with $D128^{3.32}$; and (**E**) common phenol moieties and comparison of related structural water molecules (represented as spheres).

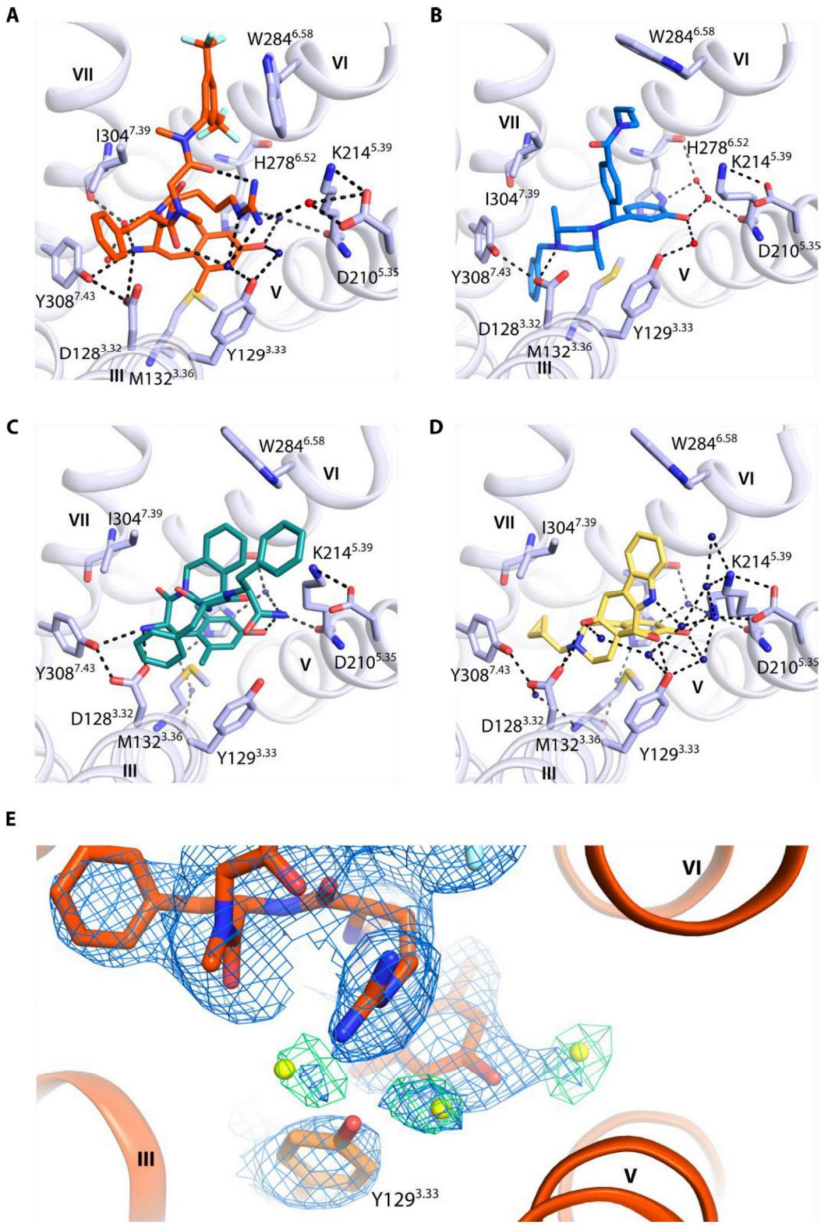

Fig. S5. Water-mediated interactions during DOP activation. Water interactions for the: (**A**) KGCHM07; (**B**) DPI-287; (**C**) DIPP-NH_2 (PDB 4RWD); and (**D**) naltrindole (PDB 4N6H) binding pockets. Structural water molecules are shown as blue spheres while additional highly stable water molecules were predicted for the KGCHM07 and DPI-287 binding pockets and are shown as red spheres. (**E**) Electron density evidence for three structural waters in the DOP-KGCHM07 ligand binding pocket. The $2F_o$-F_c electron density of KGCHM07, three structural waters, and $Y129^{3.33}$ are shown in blue mesh (contoured at 0.7 σ). The omit F_o-F_c density of the three structural waters is shown in green mesh (contoured at 3.0 σ).

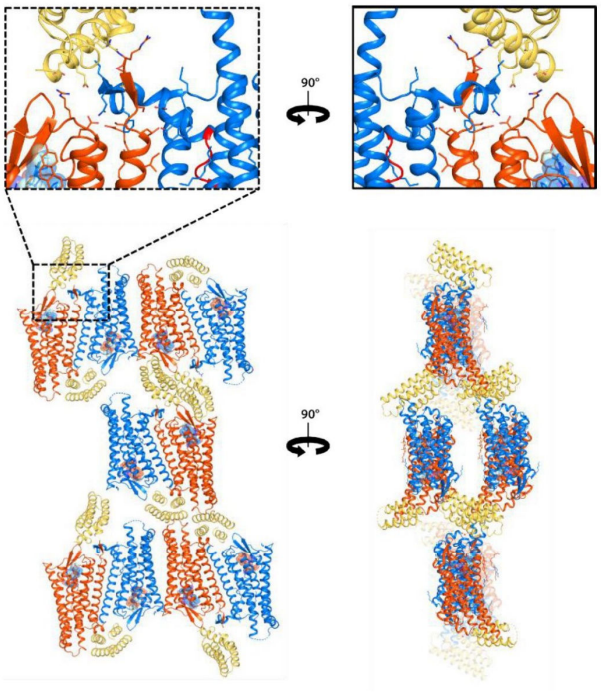

Fig. S6. The crystal lattice of the active-like BRIL-DOP structures is arranged in antiparallel dimers. Chain A, orange; chain B, blue; and BRIL, yellow: Peptide agonist KGCHM07 is shown in stick and ball representation. Enlarged segments highlight the involvement of the *C*-terminal tail of chain B in crystal packing with *N*-terminal residues of chain A, leading to disrupted helices VII (red, loop) and VIII of chain B.

Supplementary Tables

Table S1. Pharmacological assessment of crystal structure construct mutants in WT (gray) or crystal structure construct background (blue) and ligand binding pocket mutants (green).[a]

Mutations	KGCHM07		DPI-287		Binding KGCHM07[b]	Binding DPI-287[b]	Binding radio-tracer[b]	% Cell surface expression ± SD (normalized to WT); n=2
	EC_{50} ± SEM, nM (n)		EC_{50} ± SEM, nM (n)					
	cAMP	β-arrestin2	cAMP	β-arrestin2	K_i ± SEM, nM (n)	K_i ± SEM, nM (n)	K_d, nM	
DOP WT	**0.42 ± 0.18 (8)**	**52.6 ± 10.9 (3)**	**0.060 ± 0.019 (8)**	**7.9 ± 6.2 (3)**	**5.17 ± 1.57 (6)**	**0.39 ± 0.12 (6)**	**1.11**	**100.0 ± 11.0**
$G73^{1.56}V$	0.23 ± 0.08 (4)	54.0 ± 5.8 (3)	0.094 ± 0.052 (4)	28.7 ± 7.2 (3)	5.46 ± 0.69 (4)	0.26 ± 0.02 (4)	0.72	151.9 ± 38.0
$N90^{2.45}S$	1.15 ± 0.91 (4)	45.7 ± 7.4 (3)	0.064 ± 0.033 (4)	20.0 ± 11.9 (3)	5.17 ± 0.62 (4)	0.35 ± 0.15 (3)	1.98	75.4 ± 9.6
$D95^{2.50}G$	NA (4)	NA (3)	NA (4)	NA (3)	6.92 ± 0.06 (3)	0.92 ± 0.27 (3)	0.82	108.3 ± 37.0
$K108^{2.63}D$	0.19 ± 0.07 (4)	26.8 ± 0.8 (3)	0.093 ± 0.026 (4)	17.2 ± 11.8 (3)	1.17 ± 0.68 (3)	0.39 ± 0.11 (4)	3.34	91.8 ± 13.5
$N131^{3.35}S$	CA (4)	CA (3)	CA (4)	CA (3)	7.45 ± 0.56 (3)	1.94 ± 0.69 (3)	3.29	102.4 ± 41.4
$S143^{3.47}C$	0.67 ± 0.10 (4)	69.1 ± 7.2 (3)	0.062 ± 0.027 (4)	20.1 ± 14.2 (3)	4.86 ± 0.91 (4)	0.12 ± 0.02 (4)	0.81	122.3 ± 13.7
$G268^{6.42}V$	1.09 ± 0.23 (4)	61.4 ± 3.5 (3)	0.069 ± 0.034 (4)	16.7 ± 8.8 (3)	7.17 ± 1.73 (4)	0.20 ± 0.04 (4)	1.51	181.8 ± 44.3
$A309^{7.44}I$	0.22 ± 0.10 (4)	53.0 ± 3.4 (3)	0.094 ± 0.024 (4)	17.6 ± 10.7 (3)	5.53 ± 0.59 (4)	0.19 ± 0.01 (4)	1.12	213.9 ± 30.4
$E323^{8.48}K$	0.27 ± 0.10 (4)	38.3 ± 1.1 (3)	0.100 ± 0.060 (4)	25.3 ± 9.8 (3)	6.19 ± 0.56 (4)	0.32 ± 0.09 (3)	1.67	183.8 ± 15.0
$D95^{2.50}G$ + $N131^{3.35}S$	CA (4)	CA (3)	CA (4)	CA (3)	5.02 ± 1.47 (4)	1.14 ± 0.24 (3)	1.69	158.8 ± 31.8
$N90^{2.45}S$ + $D95^{2.50}G$ + $N131^{3.35}S$	CA (4)	CA (3)	CA (4)	CA (3)	5.50 ± 2.70 (4)	1.31 ± 0.48 (4)	1.66	160.9 ± 42.4
Crystal structure construct	**CA (8)**	**CA (3)**	**CA (9)**	**CA (3)**	**1.24 ± 0.23 (4)**	**1.86 ± 0.23 (7)**	**4.34**	**52.2 ± 18.0**
$S90^{2.45}N$ (WT restored)	CA (4)	CA (3)	CA (4)	CA (3)	1.42 ± 0.13 (6)	1.90 ± 0.21 (6)	12.7	39.6 ± 11.7
$G95^{2.50}D$ (WT restored)	0.40 ± 0.11 (4)	35. 3 ± 7.4 (3)	4.44 ± 3.76 (4)	73.9 ± 17.9 (3)	1.08 ± 0.15 (3)	1.39 ± 0.17 (5)	5.88	11.5 ± 2.5
$S131^{3.35}N$ (WT restored)	NA (4)	NA (3)	NA (4)	NA (3)	1.03 ± 0.13 (5)	1.68 ± 0.22 (6)	12.75	36.2 ± 12.2
$S90^{2.45}N$ + $G95^{2.50}D$ + $S131^{3.35}N$ (WT restored)	0.20 ± 0.06 (4)	44.0 ± 6.8 (3)	0.78 ± 0.48 (4)	57.1 ± 43.9 (3)	0.50 ± 0.22 (3)	0.37 ± 0.04 (4)	0.83	21.3 ± 6.0
$D108^{2.63}K$ (WT restored)	CA (4)	ND	CA (4)	ND	3.50 ± 0.32 (3)	1.71 ± 0.25 (4)	2.47	39.7 ± 18.8
$D128^{3.32}N$	>4800 (4)	ND	0.61 ± 0.24 (4)	ND	ND (3)	ND (3)	ND	168.7 ± 9.7
$D128^{3.32}A$	>21000 (4)	ND	1.39 ± 1.19 (4)	ND	ND (3)	ND (3)	ND	79.6 ± 4.1
$Y129^{3.33}F$	3.38 ± 1.81	ND	0.061 ±	ND	34.81 ±	1.04 ± 0.27	3.25	79.9 ± 20.4

	(4)		0.028 (4)		1.60 (4)	(3)		
$Y129^{3.33}A$	CA (4)	ND	CA (4)	ND	193.9 ± 79.8 (4)	1.91 ± 0.06 (3)	> 180	83.2 ± 13.8
$M132^{3.36}A$	7.89 ± 1.88 (4)	ND	0.040 ± 0.016 (4)	ND	147.3 ± 44.1 (4)	1.47 ± 0.08 (3)	9.02	37.3 ± 2.7
$D210^{5.35}N$	1.91 ± 0.70 (6)	ND	0.057 ± 0.022 (4)	ND	90.85 ± 18.33 (3)	1.26 ± 0.19 (4)	2.15	86.5 ± 9.4
$D210^{5.35}A$	2.80 ± 1.06 (4)	ND	0.29 ± 0.12 (4)	ND	27.14 ± 1.01 (3)	1.25 ± 0.28 (3)	1.32	98.3 ± 11.1
$K214^{5.39}A$	0.35 ± 0.15 (4)	ND	0.15 ± 0.03 (4)	ND	ND (3)	ND (3)	ND	90.5 ± 21.0
$V217^{5.42}A$	ND	ND	ND	ND	17.60 ± 1.54 (3)	0.76 ± 0.24 (3)	5.00	40.5 ± 12.0
$W274^{6.48}F$	ND	ND	ND	ND	30.1 ± 4.9 (4)	0.67 ± 0.11 (4)	10.4	24.6 ± 11.2
$W274^{6.48}A$	ND	ND	ND	ND	9.12 ± 3.21 (3)	0.71 ± 0.15 (3)	3.25	26.3 ± 10.1
$I277^{6.51}A$	ND	ND	ND	ND	6.14 ± 1.04 (3)	0.63 ± 0.27 (3)	1.27	120.8 ± 15.4
$H278^{6.52}A$	23.00 ± 4.36 (4)	ND	0.76 ± 0.43 (4)	ND	ND (3)	ND (3)	ND	30.5 ± 9.7
$V281^{6.55}A$	25.94 ± 13.60 (3)	ND	0.25 ± 0.15 (4)	ND	105.7 ± 22.8 (3)	1.50 ± 0.17 (3)	1.10	89.1 ± 11.9
$W284^{6.58}A$	0.69 ± 0.36 (4)	ND	0.073 ± 0.033 (4)	ND	3.31 ± 0.65 (3)	1.12 ± 0.59 (3)	3.33	140.3 ± 22.92
$L300^{7.35}A$	1.50 ± 0.06 (4)	ND	0.034 ± 0.019 (4)	ND	1.21 ± 0.42 (3)	0.58 ± 0.34 (3)	0.93	93.9 ± 11.6
$I304^{7.39}A$	ND	ND	ND	ND	9.48 ± 2.17 (3)	0.57 ± 0.19 (3)	6.34	106.1 ± 10.3
$Y308^{7.43}A$	ND	ND	ND	ND	7.07 ± 0.57 (3)	1.09 ± 0.30 (3)	0.65	114.4 ± 14.8
$Y308^{7.43}F$	ND	ND	ND	ND	13.04 ± 4.26 (3)	0.98 ± 0.12 (3)	4.02	61.8 ± 2.1
MOP WT	ND	ND	ND	ND	ND	3.17 ± 0.27 (3)	2	ND

[a] If not otherwise indicated, all values are represented as means ± SEM with number of replicates indicated in brackets, each performed in triplicate. ND: not determined (in binding assessment, because [^{125}I]-Deltorphin I binding was affected by these mutants); NA: no activity; CA: constitutively active, determined by elevated basal levels, and in the case of the crystal structure construct, confirmed by a DNA titration assay.

[b] K_i values were determined by displacement of [^{125}I]-Deltorphin I (DOP) or [^{125}I]-DAMGO (MOP), as described in the Materials and Methods section. K_d values were determined in single experiments, each performed in duplicate, to check whether the radioligand's affinity remained in the same range in the mutant as compared to the WT receptor, or the crystal structure construct, respectively.

Discussion of K_d values at mutant as compared to the WT receptor

Preliminary saturation assays were performed to estimate K_d values of the employed radioligand for all mutants as compared to the WT receptor, or the crystal structure construct. We could show that the K_d values for all mutants were in the same range as that for the WT receptor, or the crystal structure construct (typically < 3-fold difference). There were only few exceptions, namely $D128^{3.32}N$, $D128^{3.32}A$, $Y129^{3.33}A$, $K214^{5.39}A$, and $H278^{6.52}A$, which showed no high-affinity binding of the radioligand [^{125}I]-Deltorphin I. These residues are located in the ligand binding pocket and therefore important for binding of the radioligand.

Table S2. Assessment of conformational states with the "GAUGE" tool for the DOP and other opioid receptor structures. The assessment shows all activation switches "on", except the DRY motif, which remains in an inactive conformation. Receptor names and corresponding PDB IDs are colored based on their activation state (blue = inactive state; orange = active state), whereas the predicted activation states for the receptor features PIF, DRY, NPxxY and transmembrane helix regions are colored based on the predicted activation state values (blue = inactive state; red = active state). The C_score and R_score show the classification and regression values, respectively, for a given structural feature (1 = active; -1 = inactive).

Receptor	PDB ID	PIF		DRY		NPxxY		Transmembrane helix	
		C_score	R_score	C_score	R_score	C_score	R_score	C_score	R_score
DOP_human (KGCHM07)	**6PT2**	**1**	**0.71**	**-1**	**-1.03**	**1**	**0.35**	**1**	**0.39**
DOP_human (DPI-287)	**6PT3**	**1**	**0.75**	**-1**	**-0.73**	**1**	**0.35**	**1**	**0.38**
DOP_human	4N6H	-1	-1.01	-1	-1.01	-1	-0.94	-1	-0.55
DOP_human	4RWA	-1	-1.05	-1	-0.96	-1	-0.98	-1	-1.01
DOP_human	4RWD	-1	-1.04	-1	-0.97	-1	-0.94	-1	-0.95
DOP_mouse	4EJ4	-1	-0.88	-1	-0.97	-1	-1.07	-1	-0.85
MOP_mouse	5C1M	1	0.73	1	0.9	1	0.91	1	0.9
MOP_mouse	6DDE	1	0.61	1	0.86	1	0.78	1	0.74
MOP_mouse	6DDF	1	0.63	1	0.88	1	0.86	1	0.81
MOP_mouse	4DKL	-1	-1.08	-1	-0.67	-1	-1.08	-1	-0.9
KOP_human	6B73	1	1.04	1	0.73	1	0.88	1	0.86
KOP_human	4DJH	-1	-1.05	-1	-0.94	-1	-1.02	-1	-0.77
NOP_human	4EA3	-1	-0.89	-1	-0.95	-1	-1.12	-1	-1.02
NOP_human	5DHG	-1	-0.9	-1	-0.95	-1	-1.06	-1	-0.98
NOP_human	5DHH	-1	-0.87	-1	-1	-1	-1.05	-1	-1.07

Table S3. Docking results for selected small-molecule and peptide DOP agonists. K_i values are reported from the literature according to the ChEMBL ID's and shown for human opioid receptors, if not indicated otherwise.

ChEMBL ID	**Pub-Chem ID**	**Synonyms** (additional references)	**Chemical Structure**	**K_i human DOP (nM)**	**K_i human MOP (nM)**	**K_i human KOP (nM)**	**Receptor Docking Model (Docking score)**
CHEMBL25230	119029	(+)-BW373U86 SNC-86	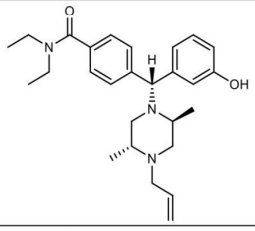	0.32	260	130-3,400	DOP-DPI-287 (-37.56)
CHEMBL13470	123924	SNC-80	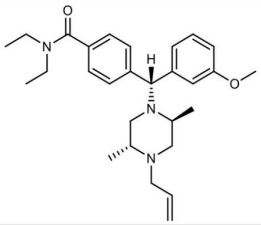	1.2-1.7	352-1,300	3,535-4,169	DOP-DPI-287 (-25.1)
NA	9891642	DPI-221	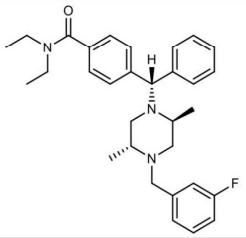	2.0 (rat)	1800 (rat)	2300 (rat)	DOP-DPI-287 (-31.56)
NA	10196358	DPI-130 (*32*)	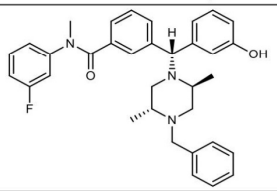	0.4 (rat)	1.58 (rat)	21.8 (rat)	DOP-KGCHM07 (-28.3)
CHEMBL155892	9826770	DPI-3290	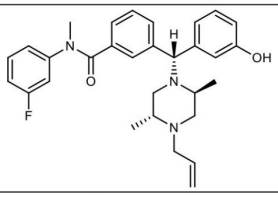	0.18-11.39 (rat)	0.18-7.56 (rat)	0.46 (rat)	DOP-KGCHM07 (-27.7)
CHEMBL153648	6604878	SNC-162	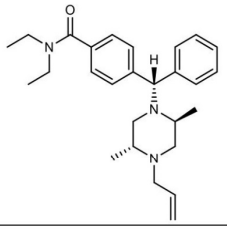	0.5 (rat)	3,000 (rat)	3,000 (guinea)	DOP-DPI-287 (-27.68)

CHEMBL286053	9871102	*N*-3,4-(methylenedioxy) benzyl derivative	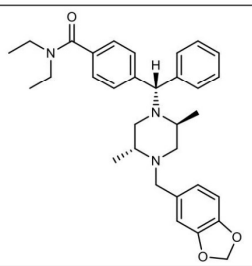	0.54 (IC_{50})	702 (IC_{50}, rat)	ND	DOP-DPI-287[#] (-33.9)
CHEMBL3408735	118731118	KGCHM07	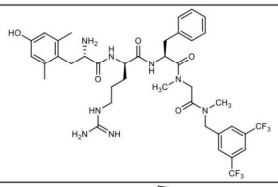	1.7 (rat)	0.62 (rat)	ND	DOP-KGCHM07[*] (-34.12)
CHEMBL1782141	52937467	SBCHM01	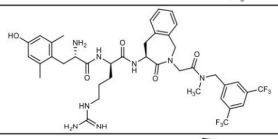	10.4 (rat)	0.42 (rat)	ND	DOP-KGCHM07[*] (-28.23)
CHEMBL1782140	52937468	AN81	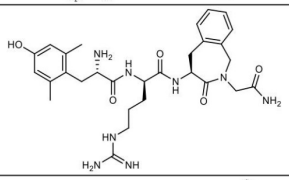	0.6 (rat)	0.15 (rat)	118 (guinea)	DOP-KGCHM07[*] (-24.97)
CHEMBL2151734	56834761	BVD02	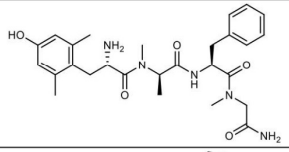	130	60	$>10^6$	DOP-KGCHM07[*] (-32.15)
CHEMBL2151735	54669894	BVD03	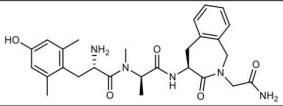	5	14.8	$>10^6$	DOP-KGCHM07[*] (-26.85)
CHEMBL294616	44299404	DPDPE	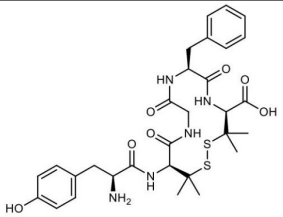	0.5-3.98	>10,000	>10,000	DOP-KGCHM07[*] (-33.59)
CHEMBL159793	44374513	Dmt-DPDPE	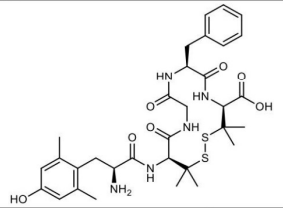	1.8 (rat)	58.3 (rat)	ND	DOP-KGCHM07[*] (-22.15)
CHEMBL442577	109187013	UFP-512	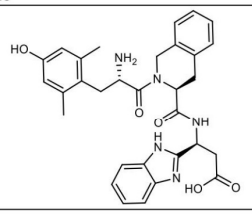	0.44 (rat)	53.9 (rat)	ND	DOP-KGCHM07[*] (-33)

CHEMBL3 17956	1005595 8	Deltorphin I	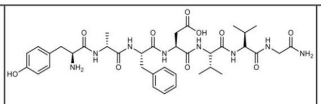	1.73	147-3,930 (rat)	>10,000 (guinea)	DOP-KGCHM07* (-35.32)
CHEMBL3 408519	1187309 33	KGCHM02	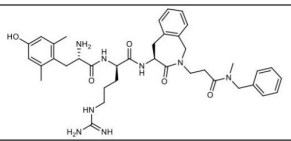	0.28 (rat)	0.08 (rat)	ND	DOP-KGCHM07* (-22.72)
CHEMBL3 408521	1187309 35	KGCHM04	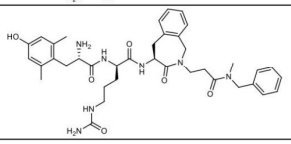	0.48 (rat)	0.28 (rat)	ND	DOP-KGCHM07* (-29.71)

DOP-DPI_water model with $G95^{2.50}D$, $S131^{3.35}N$ and $D108^{2.63}K$ mutations (reversed to WT).
* DOP-KGCHM07_water model with $D108^{2.63}K$ mutation (reversed to WT).
ND: not determined; NA: not applicable

Table S4. Data collection and refinement statistics. Statistics for the highest resolution shell are shown in parentheses.

Data collection				
	BRIL-DOP-KGCHM07 (PDB 6PT2)		**BRIL-DOP-DPI-287 (PDB 6PT3)**	
Number of crystals used	23		23	
Space group	$P2_12_12_1$		$P2_12_12_1$	
Cell parameters a, b, c (Å)	48.96, 140.88, 158.64		49.08, 142.10, 157.49	
Number of reflections processed	166,592		114,938	
Number of unique reflections	26,051		16,342	
Resolution (Å)	49.51-2.80 (2.87-2.80)		49.24-3.30 (3.39-3.30)	
R_{merge} **(%)**	8.5 (80.4)		11.4 (88.9)	
$CC_{1/2}$	99.7 (65.7)		99.9 (55.1)	
Mean I/σ **(I)**	11.9 (1.7)		8.67 (1.1)	
Completeness (%)	93.2 (78.1)		94.5 (84.5)	
Redundancy	6.4 (3.6)		7.0 (2.8)	
Refinement				
Resolution (Å)	2.80		3.30	
Number of reflections (test set)	26,050 (1,269)		16,341 (781)	
R_{work} / R_{free} **(%)**	24.6/28.2		24.5/26.9	
Number of atoms	**Chain A**	**Chain B**	**Chain A**	**Chain B**
DOP	2,234	2,205	2,213	2,233
BRIL	821	457	821	386
Ligand	58	58	36	36
Lipids, PEG and waters	71	68	0	0
Overall B **values (Å^2)**	**Chain A**	**Chain B**	**Chain A**	**Chain B**
DOP	107.0	110.6	123.2	131.0
BRIL	127.8	164.1	137.8	205.6
Ligand	83.9	89.2	109.0	113.0
Lipids, PEG and waters	121.2	115.8	0	0
RMSD				
Bond lengths (Å)	0.010		0.009	
Bond angles (°)	1.05		1.05	
Ramachandran plot statistics				
Favored regions (%)	97.6		95.7	
Allowed regions (%)	2.4		4.3	
Disallowed regions (%)	0		0	

Appendix II. Publication II: Single Stabilizing Point Mutation Enables High-resolution Co-Crystal Structures of the Adenosine A_{2A} Receptor with Preladenant Conjugates

Main Text

of

Publication II

in

***Angewandte Chemie*[107]**

Structural Biology Hot Paper

How to cite:
International Edition: doi.org/10.1002/anie.202115545
German Edition: doi.org/10.1002/ange.202115545

Single Stabilizing Point Mutation Enables High-Resolution Co-Crystal Structures of the Adenosine A_{2A} Receptor with Preladenant Conjugates

*Tobias Claff, Tim A. Klapschinski, Udaya K. Tiruttani Subhramanyam, Victoria J. Vaaßen, Jonathan G. Schlegel, Christin Vielmuth, Jan H. Voß, Jörg Labahn, and Christa E. Müller**

Abstract: The G protein-coupled adenosine A_{2A} receptor (A_{2A}AR) is an important new (potential) drug target in immuno-oncology, and for neurodegenerative diseases. Preladenant and its derivatives belong to the most potent A_{2A}AR antagonists displaying exceptional selectivity. While crystal structures of the human A_{2A}AR have been solved, mostly using the A_{2A}-StaR2 protein that bears 9 point mutations, co-crystallization with Preladenant derivatives has so far been elusive. We developed a new A_{2A}AR construct harboring a single point mutation ($S91^{3.39}K$) which renders it extremely thermostable. This allowed the co-crystallization of two novel Preladenant derivatives, the polyethylene glycol-conjugated (PEGylated) PSB-2113, and the fluorophore-labeled PSB-2115. The obtained crystal structures (2.25 Å and 2.6 Å resolution) provide explanations for the high potency and selectivity of Preladenant derivatives. They represent the first crystal structures of a GPCR in complex with PEG- and fluorophore-conjugated ligands. The applied strategy is predicted to be applicable to further class A GPCRs.

Introduction

The nucleoside adenosine has been recognized as a fundamental signaling molecule of life.[1] It activates a family of G protein-coupled receptors (GPCRs) designated A_1, A_{2A}, A_{2B}, and A_3. The adenosine A_{2A} receptor (A_{2A}AR) subtype plays a pivotal role in a variety of immunological processes. It couples to G_s proteins leading to an increase in intracellular cyclic adenosine monophosphate (cAMP) concentrations.[2] Adenosine represents one of the strongest immunosuppressive agents of the innate immune system, an activity that is mainly mediated by activation of the A_{2A}AR.[3,4] This receptor acts as an immune checkpoint that is exploited by tumor cells to evade the immune system and to promote uncontrolled growth.[5] While extracellular adenosine levels are typically in the nanomolar range, they can dramatically rise in the tumor microenvironment and in inflamed tissues by more than 100-fold reaching micromolar concentrations.[6] Blockade of A_{2A}ARs re-activates the compromised immune cells in the microenvironment of cancer cells thereby allowing, for example, T cell infiltration of tumor tissues.[4] Thus, A_{2A}AR antagonists represent a new, promising class of checkpoint inhibitors for the treatment of cancers and possibly also for the therapy of infections.[7,8]

In the brain, the A_{2A}AR is almost exclusively expressed in the caudate-putamen (striatum) at high levels.[9] Neurodegeneration was found to lead to an upsurge in A_{2A}AR expression.[10] Elevated A_{2A}AR levels are already observed in early-stage patients suffering from Parkinson's Disease (PD)[11] and were found to correlate with the severity of PD.[12]

Preladenant (SCH-420814, see Figure S1) was the first non-xanthine A_{2A}AR antagonist to enter clinical development for the treatment of PD.[13] While the drug was found to be generally safe and well-tolerated, phase III clinical trials failed to provide evidence for its efficacy,[14] possibly due to an imperfect trial design. Nevertheless, Preladenant is one of the most potent A_{2A}AR antagonists with an outstanding selectivity towards the other AR subtypes of several hundred- to more than 1000-fold.[15] The tricyclic Preladenant scaffold has therefore been utilized to develop tool compounds and labeled diagnostics, e.g. positron emission tomography tracers[16] and fluorescence-labeled derivatives.[17]

Although several high-resolution crystal structures of the A_{2A}AR were obtained, no structures in complex with Preladenant or its derivatives have been reported. Thus, the exact binding mode and interactions of this prominent and unique class of A_{2A}AR antagonists are still unknown. In the

[*] T. Claff, Dr. T. A. Klapschinski, V. J. Vaaßen, J. G. Schlegel, C. Vielmuth, J. H. Voß, Prof. Dr. C. E. Müller
Pharmaceutical Institute, Pharmaceutical & Medicinal Chemistry, University of Bonn
An der Immenburg 4, 53121 Bonn (Germany)
E-mail: christa.mueller@uni-bonn.de
Dr. U. K. Tiruttani Subhramanyam, Prof. Dr. J. Labahn
Centre for Structural Systems Biology (CSSB)
Notkestraße 85, 22607 Hamburg (Germany)
Dr. U. K. Tiruttani Subhramanyam, Prof. Dr. J. Labahn
Research Centre Jülich, Institute of Complex Systems (IBI-7)
Wilhelm-Johnen-Straße, 52425 Jülich (Germany)

last decade, advances in A_{2A}AR structural biology were greatly facilitated by a research platform that introduced the stabilized receptor (StaR) A_{2A}-StaR2[18] which had been engineered to achieve enhanced protein stability through multiple point mutations.[19] The A_{2A}-StaR2 has been indispensable to enhance our understanding of A_{2A}AR antagonist binding pockets. According to all protein data bank (PDB) (www.rcsb.org)[20] entries, 18 different A_{2A}AR antagonists have so far been crystallized in complex with the A_{2A}AR (for an overview see Table S1). The vast majority of these ligands (16) was exclusively co-crystallized using the A_{2A}-StaR2 either with or without the intracellular fusion protein bRIL (thermostabilized apocytochrome b_{562}RIL).[19,21] Moreover, a drug design program based on A_{2A}-StaR2 structures enabled the development of the potent A_{2A}AR antagonist Imaradenant (AZD-4635, see Figure S1, K_i A_{2A}AR: 1.7 nM, 37-fold selective versus the A_{2B}AR).[22,23] The A_{2A}-StaR2 construct comprises nine point mutations, two of which, $T88^{3.36}$A and $S277^{7.42}$A, are located inside the orthosteric ligand binding pocket of the A_{2A}AR interfering with agonist binding[24] and, in case of the $S277^{7.42}$A mutation, possibly also with the binding of antagonist scaffolds[25] (superscripts refer to the Ballesteros-Weinstein system[26]). In fact, the recently solved crystal structure of the A_{2A}-StaR2 in complex with the clinical candidate Imaradenant[23] revealed direct ligand contacts to the mutated $A277^{7.42}$.

In an effort to strongly reduce the number of point mutations and, in particular, to avoid mutations located in the orthosteric ligand binding pocket, we developed a new, significantly improved thermostabilized A_{2A}AR mutant harboring only a single point mutation (designated A_{2A}-PSB1-bRIL) and yet endowed with superior stability compared to the A_{2A}-StaR2 mutant. This was inspired by a corresponding mutation in the crystallized serotonin 5-HT_{2A} receptor which appeared to show promise for the A_{2A}AR as well.[27,28]

In parallel, we developed a new series of Preladenant derivatives equipped with polyethylene glycol (PEG) linkers of different length appropriate for connecting reporter molecules, e.g. fluorescent dyes. An optimized PEGylated Preladenant derivative, PSB-2113, was subsequently labeled with a boron-dipyrromethene (BODIPY) fluorophore yielding the fluorescent probe PSB-2115 suitable for specific A_{2A}AR imaging.

Herein, we present the first high-resolution crystal structure of A_{2A}-PSB1-bRIL in complex with the Preladenant conjugates PSB-2113 and PSB-2115 at 2.25 Å and 2.6 Å resolution, respectively. Our results provide insights into the interactions of the potent and highly selective Preladenant scaffold with the orthosteric binding site of the receptor. Moreover, we obtained the first X-ray structures of a GPCR co-crystallized with an antagonist that is conjugated to a PEG linker and a fluorescent dye.

Results and Discussion

As a first step, we synthesized novel conjugated Preladenant derivatives. This was achieved by replacement of the terminal methoxyethyl ether group on the extended phenylpiperazinylethyl residue of Preladenant that is attached to the pyrazole ring of the tricyclic core structure (see Figure 1).

A synthetic strategy to obtain the target compounds was designed as depicted in Figure 1a. The carboxy-functionalized Preladenant derivative **2** was prepared via its protected precursor **1** (details on the synthesis of compounds **1** and **2** are provided in Scheme S1). Carboxylic acid **2** can subsequently be coupled with amines to connect PEG linkers to the pharmacophore via amide formation. To this end, *tert*-butyloxycarbonyl(Boc)-protected PEG linkers of increasing length (4 to 20 ethylene glycol monomer units, **3a–3f**) were attached to compound **1** using (1-[bis(dimethylamino)methylene]-1*H*-1,2,3-triazolo[4,5-*b*]pyridinium-3-oxide hexafluorophosphate (HATU) as a coupling reagent in the presence of diisopropylethylamine (DIPEA) as a base under mild conditions (see Figure 1b). Products **4–9** were obtained in excellent yields (see Figure 1). These were subsequently tested in radioligand competition binding assays to determine A_{2A}AR affinities and selectivities versus the other human AR subtypes (see Table 1). Our aim at this point was to study the consequences of the introduced structural modifications on the Preladenant scaffold, and to find out which linker length would be optimal. While the free carboxylic acid **2**, used as a precursor for the coupling reactions, showed only moderate A_{2A}AR affinity (K_i 200 nM), its Boc-protected ester **1** was ≈100-fold more potent displaying similar affinity as the parent compound Preladenant (Table 1). All investigated Boc-protected PEG derivatives (**4–9**) exhibited higher affinity for the A_{2A}AR than the carboxylate precursor **2**. Increasing PEG linker length resulted in decreased A_{2A}AR affinity. In fact, the highest A_{2A}AR affinity was achieved with the shortest PEG linker comprised of four ethyleneglycol units (compound **4**, PSB-2113, K_i 2.28 nM). Therefore, we selected the PEG-substituted compound **4** for subsequent studies. Deprotection with trifluoroacetic acid in the presence of triisopropylsilane (TIPS) led to carboxylic acid **10** (K_i A_{2A}AR 8.84 nM) in high yield. Subsequent coupling reaction with an aminoalkyl-functionalized BODIPY derivative, prepared as previously described,[29] in the presence of HATU/DIPEA under mild conditions yielded the desired BODIPY-labeled Preladenant derivative **11** (PSB-2115) in excellent yield (see Figure 1c). The final BODIPY-labeled product still showed very high affinity for the A_{2A}AR (K_i 3.47 nM). This is combined with excellent selectivity (>1000-fold) versus the A_{2B}- and A_3AR subtypes, and still around 50-fold selectivity versus the A_1AR (see Table 1). Moreover, PEGylation can be expected to increase water-solubility and modulate pharmacokinetic properties.[30] For example, it will prevent brain penetration and associated side-effects, such as central stimulation which is undesired for peripheral indications, e.g. in immuno-oncology and in the treatment of infections. Moreover, it allows the attachment of targeting moieties,

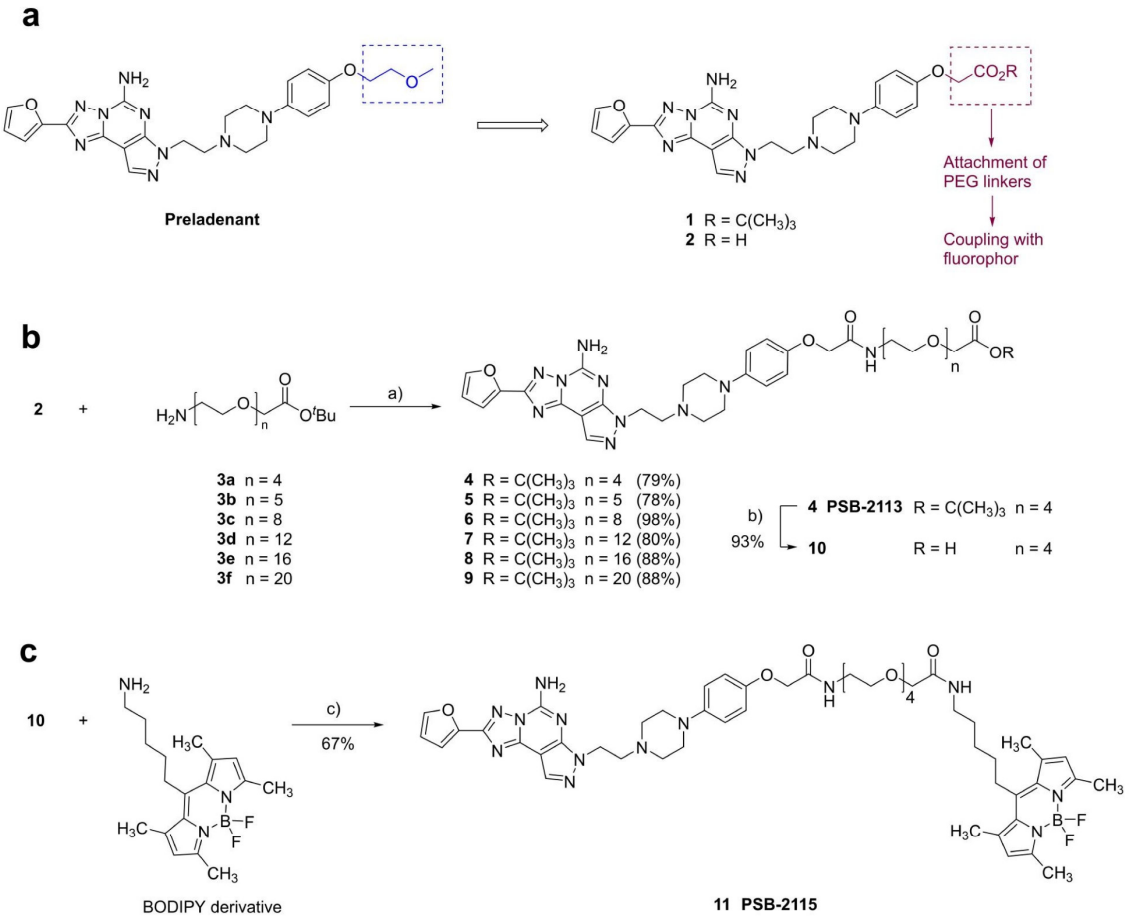

Figure 1. Design and synthesis of conjugated Preladenant derivatives. a) Design and synthetic strategy. b) Synthesis of PEGylated Preladenant derivatives. c) Synthesis of Preladenant derivative labeled with a BODIPY fluorophore attached via an optimized PEG linker. Reaction conditions: a) HATU, DIPEA, CH_2Cl_2, RT, 24 h. b) trifluoroacetic acid, TIPS, CH_2Cl_2, RT, 24 h. c) HATU, DIPEA, CH_2Cl_2, RT, 24 h.

e.g. antibodies, and reporter groups such as fluorophores as in PSB-2115.

With these highly potent and selective Preladenant conjugates in hand we aimed at obtaining co-crystal structures in complex with the human A_{2A}AR to gain insight into their interactions with the receptor protein.

Initially, we attempted to crystallize the human A_{2A}AR in complex with the new Preladenant conjugates using the previously described A_{2A}AR crystallization construct[32] that lacks the long A_{2A}AR *C*-terminal tail and in which the intracellular loop (ICL) 3 is replaced by the soluble fusion protein bRIL (designated A_{2A}-ΔC-bRIL). This construct does not contain any additional stabilizing point mutations. While we accomplished to produce crystals with an average size of 50 µm (Figure S2A), no high-resolution diffraction data could be obtained. Our observation is consistent with previous studies reporting only low-resolution diffraction data or micro-crystal hits deriving from co-crystallization of the same A_{2A}AR protein with the related tricyclic A_{2A}AR antagonists SCH-442416 and SCH-58261[33] (for compound structures see Figure S1). To date, 17 crystal structures of A_{2A}-ΔC-bRIL in complex with the structurally related bicyclic A_{2A}AR antagonist ZM241385 have been obtained. However, the same strategy does not appear to be as straightforward for tricyclic A_{2A}AR antagonists like Preladenant. A plausible explanation could be differences in ligand binding kinetics or inverse agonist efficacies.[34]

More stable A_{2A}AR crystallization constructs have meanwhile become available, the most successful one being the A_{2A}-StaR2 mutant that contains nine point mutations.[19] Rather than utilizing the A_{2A}-StaR2 for crystallization, our objective was to keep the number of mutations at a minimum, and, importantly, to avoid any mutations that may interfere with ligand binding. Inspired by the recently elucidated crystal structure of the serotonin 5-HT_{2A} receptor[27] where the basic amino acid lysine occupies the well-known allosteric sodium binding site,[35] we introduced a single point mutation into the A_{2A}AR construct A_{2A}-ΔC-

Table 1: Affinities of Preladenant derivatives at human adenosine receptor subtypes.[a]

Compound	Human A_1AR Radioligand [^{3}H]CCPA $K_i \pm$ SEM [nM] (or % inhibition ± SEM at 1 μM)	Human A_{2A}AR Radioligand [^{3}H]MSX-2 $K_i \pm$ SEM [nM]	Human A_{2B}AR Radioligand [^{3}H]PSB-603 $K_i \pm$ SEM [nM] (or % inhibition ± SEM at 1 μM)	Human A_3AR Radioligand [^{3}H]PSB-11 $K_i \pm$ SEM [nM] (or % inhibition ± SEM at 1 μM)
ZM241385[b]	**225**	**0.8**	**50**	**>10000**
Preladenant[c]	**295** ± 10	**0.884** ± 0.232	**>1000**	**>1000**
1	**420** ± 36	**1.93** ± 0.75	**>1000** (15 ± 10)	**>1000** (25 ± 2)
2	**>1000** (18 ± 4)	**200** ± 16	**>1000** (2 ± 11)	**>1000** (12 ± 10)
4 (PSB-2113)	**>1000** (38 ± 9)	**2.28** ± 0.41	**>1000** (9 ± 1)	**>1000** (34 ± 4)
5	**>1000** (28 ± 1)	**9.39** ± 1.39	**>1000** (24 ± 1)	**>1000** (8 ± 5)
6	**>1000** (1 ± 6)	**10.3** ± 2.1	**>1000** (0 ± 3)	**>1000** (26 ± 4)
7	**>1000** (23 ± 9)	**8.92** ± 4.05	**>1000** (8 ± 3)	**>1000** (14 ± 5)
8	**>1000** (2 ± 2)	**30.3** ± 7.9	**>1000** (5 ± 2)	**>1000** (2 ± 0)
9	**>1000** (0 ± 12)	**45.5** ± 12.3	**>1000** (−8 ± 2)	**>1000** (2 ± 5)
10	**>1000** (6 ± 5)	**8.84** ± 0.64	**>1000** (17 ± 9)	**>1000** (13 ± 1)
11 (PSB-2115)	**165** ± 20	**3.47** ± 0.23	**>1000** (32 ± 9)	**>1000** (39 ± 6)

[a] K_i values are means from 3 independent experiments shown in bold ± standard error of the mean (SEM). [b] See ref. [31], for structure see Figure S1. [c] See ref. [15].

bRIL at the analogous position to replace the corresponding serine residue S91$^{3.39}$ by lysine (S91$^{3.39}$K). The S91$^{3.39}$K mutation appeared to be in fact beneficial for A_{2A}AR stability.[28] This A_{2A}AR mutant, designated A_{2A}-PSB1-bRIL (PSB, Pharmaceutical Sciences Bonn), led to substantial protein thermostabilization, even in the ligand-free (APO) state, consistent with a melting temperature (T_M) increase by approximately 10 °C compared to A_{2A}-ΔC-bRIL (see Figure 2). In fact, the thermostability of A_{2A}-PSB1-bRIL was significantly higher than the thermostability of the A_{2A}-StaR2-bRIL that was concurrently produced in our laboratory and purified in parallel with the new construct using the same procedure ($\Delta T_M = 3.03$ °C; $p = 0.0025$, two-sided t-test). The resulting new thermostabilized construct, designated A_{2A}-PSB1-bRIL, was expressed in and purified from *Spodoptera frugiperda* (Sf9) insect cells. We succeeded in obtaining A_{2A}-PSB1-bRIL-ligand complexes with high purity (Figure S2B and C) and successfully crystallized them in lipidic cubic phase (LCP) (Figure S2D and E). Importantly, protein crystals of A_{2A}-PSB1-bRIL produced high-resolution diffraction data which enabled the elucidation of two new crystal structures in complex with PSB-2113 and PSB-2115 (see Table S2 for detailed refinement statistics).

The root-mean-square-deviation (RMSD) of all resolved GPCR backbone atoms between A_{2A}-PSB1-bRIL and A_{2A}-ΔC-bRIL (PDB 4EIY) is 0.183 Å (1204 aligned atoms, based on the PSB-2113 complex) indicating that the transmembrane helix geometry is not affected by the newly introduced S91$^{3.39}$K mutation. The respective wild-type (wt) residue in this position (S91$^{3.39}$) is located inside the highly conserved allosteric sodium binding pocket, where it directly coordinates a sodium ion as observed in many inactive state class A GPCRs.[32,35] In the novel mutant, the larger lysine in this position displaces the sodium ion together with three structural water molecules, and fully occupies the former allosteric binding pocket without disrupting the overall helix geometry of the A_{2A}AR (Figure 2a, b and c). In fact, the protonated amino group of K91$^{3.39}$ mimics the positively charged sodium ion, thereby stabilizing the same inactive receptor conformation. Precisely, K91$^{3.39}$ forms a salt bridge to D52$^{2.50}$, a direct hydrogen bond interaction to N280$^{7.45}$ and water-mediated hydrogen bonds to S281$^{7.46}$ and W246$^{6.48}$ (Figure 2c). Thus, the long K91$^{3.39}$ sidechain sterically prevents the activation-induced collapse of the former sodium binding pocket[24] and restricts the "rotamer toggle switch",[36] including amino acids T88$^{3.36}$, F242$^{6.44}$ and W246$^{6.48}$, in the inactive conformation (Figure 2c).

Radioligand binding experiments were performed with Sf9 insect cell membranes expressing A_{2A}-PSB1-bRIL using the A_{2A}-selective antagonist radioligand [^{3}H]MSX-2.[37] For comparison, various other A_{2A}AR constructs were additionally investigated. For the wt A_{2A}AR, radioligand binding experiments were further performed on membranes from Chinese hamster ovary (CHO–S) suspension cells. The affinity of the Preladenant conjugate PSB-2113 to the wt A_{2A}AR was virtually identical regardless of the cell line, CHO–S cells or Sf9 insect cells, in which the receptor was expressed (K_i 2.28 nM vs. 6.30 nM). Moreover, the new,

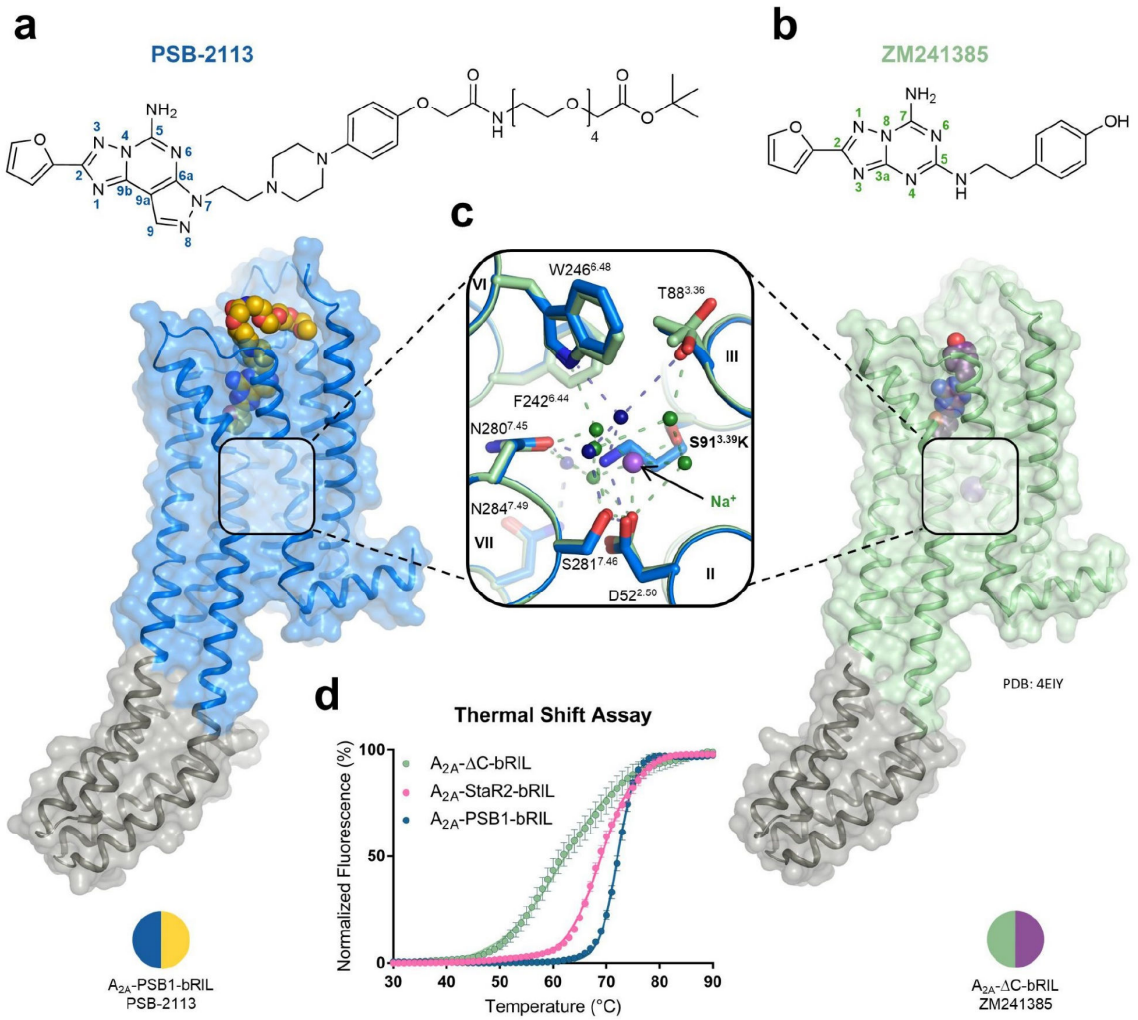

Figure 2. Architecture of the single-mutated thermostabilized A_{2A}AR. Overview of the crystal structures and A_{2A}AR antagonists of a) A_{2A}-PSB1-bRIL-PSB-2113 compared to b) A_{2A}-ΔC-bRIL-ZM241385. c) Sodium binding pocket comparison between A_{2A}-ΔC-bRIL and A_{2A}-PSB1-bRIL highlighting the introduced S91$^{3.39}$K mutation. d) Thermostability assessment of different A_{2A}AR crystallization constructs without the presence of A_{2A}AR ligands. Error bars indicate the SEM.

PEGylated A_{2A}AR antagonist PSB-2113 as well as the standard xanthine antagonist MSX-2 (for structure see Figure S1) were binding to the non-mutated A_{2A}-ΔC-bRIL and A_{2A}-ΔC with the same affinities as to the wt A_{2A}AR (Figure 3 and Table S3). This demonstrates that A_{2A}AR antagonist binding was neither altered by introduction of the bRIL fusion protein nor by truncation of the C-terminus. The binding affinity of MSX-2 to the S91$^{3.39}$K-mutated A_{2A}-PSB1-bRIL receptor was also unaltered as compared to the wt A_{2A}AR, while the affinity of PSB-2113 was slightly (≈3-fold) lower at the mutant than at the wt A_{2A}AR, but still in the low nanomolar range (19.6 nM vs. 6.30 nM; $p = 0.0801$; paired t-test) (Figure 3 and Table S3). The S91$^{3.39}$K mutation stabilizes the same inactive state as sodium ions. Since high sodium concentrations do not alter the affinity of A_{2A}AR antagonists,[32] we cannot expect an affinity increase towards A_{2A}-PSB1-bRIL either.[32] On the other hand, it has been shown that Preladenant and other antagonists bind to active state-stabilized A_{2A}AR constructs with significantly lower affinity.[24]

Moreover, we observed that the agonist 5′-*N*-ethyl-carboxamidoadenosine (NECA) could still bind to the truncated but non-mutated A_{2A}AR constructs regardless of the presence of the fusion partner in the ICL3 (A_{2A}-ΔC and A_{2A}-ΔC-bRIL) with similar affinity as to the wt A_{2A}AR (Figure 3). However, no agonist binding to A_{2A}-PSB1-bRIL could be detected ($pK_i < 4.0$) as exemplarily shown for NECA versus [^{3}H]MSX-2 (Figure 3 and Table S3). A rationale for the observed abolished agonist binding to A_{2A}-PSB1-bRIL may be provided by the fact that the S91$^{3.39}$K mutation

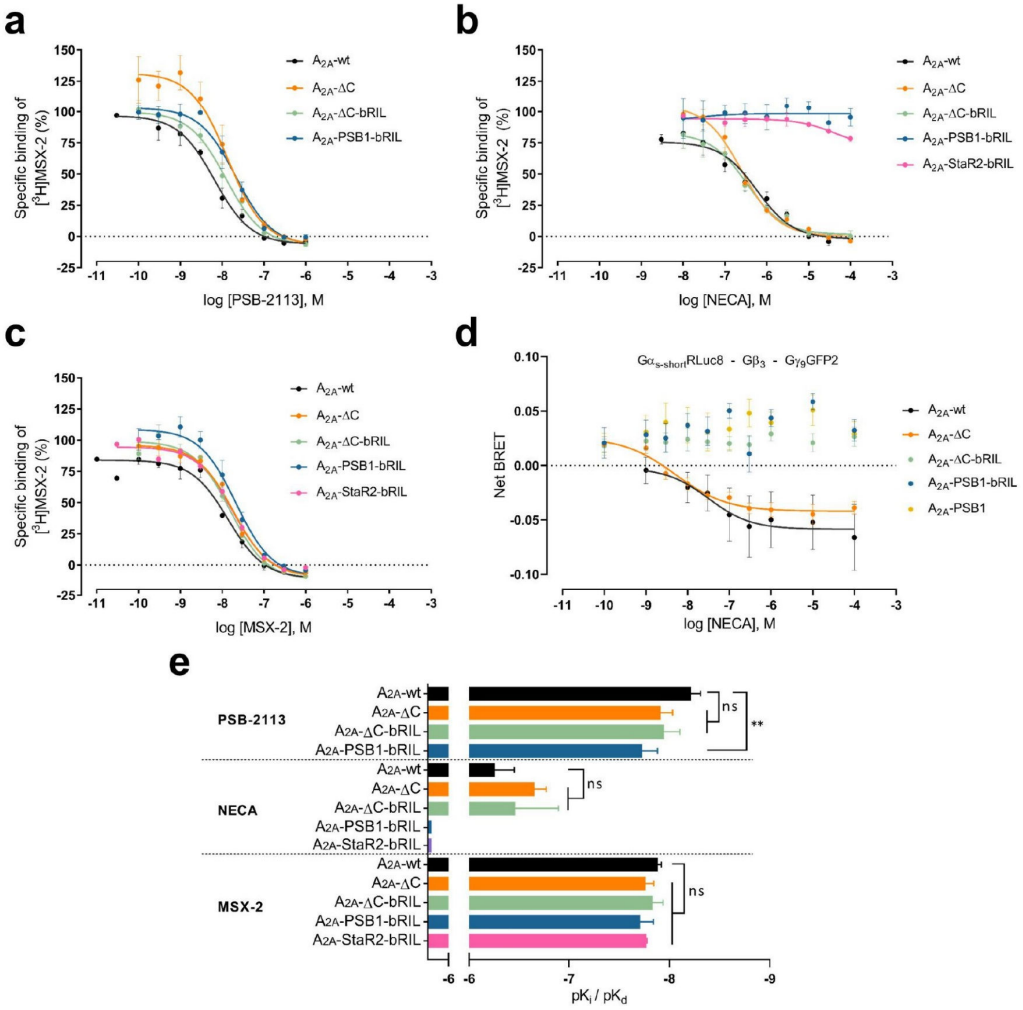

Figure 3. Pharmacological characterization of A_{2A}AR constructs. Results of competitive radioligand binding experiments on Sf9 insect cell membranes with a) PSB-2113, b) NECA and c) MSX-2 using [^{3}H]MSX-2 as radioligand. Error bars indicate SEM. d) TRUPATH assay results using HEK293 cells expressing $G\alpha_{s\text{-short}}$Rluc8, $G\beta_3$, $G\gamma_9$GFP2 and the respective A_{2A}AR construct with error bars indicating SEM. e) Comparison of pK_i and pK_d values calculated from radioligand binding experiments with error bars indicating the standard deviation (SD). The statistical evaluation was performed using the one-way-ANOVA with Dunnett's post-hoc test.

restrains key activation switches in the inactive conformation. This prevents movements of W246$^{6.48}$, H250$^{6.52}$ and helix III that are required to accommodate the ribose moiety of A_{2A}AR agonists (adenosine and its derivatives) in the ligand binding pocket.[38] In our hands, NECA binding to the A_{2A}-StaR2-bRIL was equally abolished.

Next, we utilized the biosensor platform TRUPATH[39] to test the effect of the S91$^{3.39}$K mutation on $G\alpha_s$ activation. For this purpose, we stimulated the truncated A_{2A}AR constructs with or without bRIL applying the agonist NECA. A_{2A}-ΔC-bRIL served as a negative control since the fusion partner in the ICL3 sterically blocks the G protein binding site. In support of our findings from radioligand binding experiments, the results showed that the S91$^{3.39}$K mutated A_{2A}AR was not able to activate $G\alpha_s$ proteins in HEK293 cells. On the other hand, $G\alpha_s$ activation was unaffected in the *C*-terminal truncated A_{2A}AR construct when compared to the wt A_{2A}AR (Figure 3d and Table S3).

The core scaffold of Preladenant and its derivatives PSB-2113 and PSB-2115 exhibits certain similarities but also significant differences to the structurally well-investigated A_{2A}AR antagonist ZM241385 (for structures see Figure S1).[32,40] Both antagonists contain an aromatic ring system that is connected to a 2-furanyl moiety. However, while ZM241385 carries a bicyclic aromatic system, Preladenant possesses an additional five-membered ring that likely contributes to its high selectivity compared to ZM241385. Despite the sterically more demanding tricyclic

core, the Preladenant derivative PSB-2113 binds to the $A_{2A}AR$ in the same orientation as ZM241385 and shows similar direct ligand interactions to helices V, VI, VII and extracellular loop (ECL) 2 (Figure 4a and b).

This includes a key hydrogen bond network to $N253^{6.55}$ and $E169^{ECL2}$ by the furan oxygen atom and the 5-amino group of the heterocyclic core. In addition, the tricyclic aromatic system is stabilized by π–π stacking to $F168^{ECL2}$ and by hydrophobic contacts to $L249^{6.51}$ and $I274^{7.39}$ (Figure 4a). PSB-2113 is connected to helices I, II, III, and VII via water-mediated hydrogen bonds, similarly as observed for ZM241385.[32] However, the tricyclic core of PSB-2113 extends further towards helix II which leads to the displacement of one of the structural water molecules from the

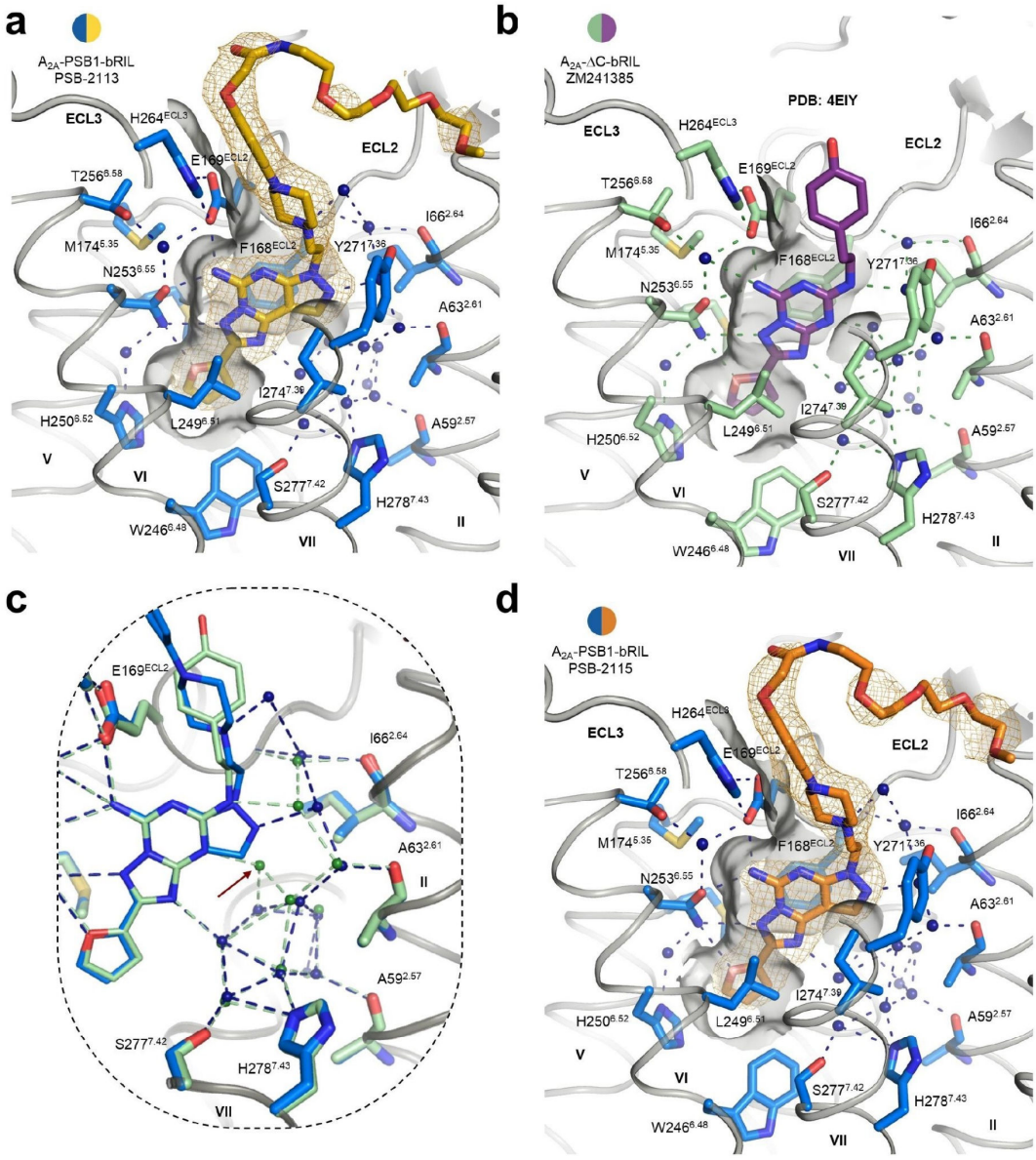

Figure 4. Comparison of ligand binding pockets. a) Ligand binding pocket of A_{2A}-PSB1-bRIL-PSB-2113. The $2F_o-F_c$ electron density of PSB-2113 is shown in yellow mesh (contoured at 1.0 σ). b) Ligand binding pocket of A_{2A}-ΔC-bRIL-ZM241385. Coordinates were extracted from PDB entry 4EIY. c) Comparison of the water networks in A_{2A}-PSB1-bRIL-PSB-2113 (blue) and A_{2A}-ΔC-bRIL-ZM241385 (green). The red arrow points to the structural water molecule that is displaced from the ligand binding pocket by the tricyclic core scaffold. d) Ligand binding pocket of A_{2A}-PSB1-bRIL-PSB-2115. The $2F_o-F_c$ electron density of PSB-2115 is shown in orange mesh (contoured at 1.0 σ).

ligand binding pocket (Figure 4c). The water molecules in this particular water network were previously termed "unhappy waters"[41] as they would prefer to be in the bulk solvent but cannot leave a vacuum behind. Hence, the displacement of the water molecule by PSB-2113 from the ligand binding pocket would be expected to be energetically favorable and is likely one of the reasons for the compound's high affinity. Moreover, while the number of nitrogen atoms is identical in the core scaffold of PSB-2113 and ZM241385, their altered position (compare *N*7 and N8 in PSB-2113 with *N*4 and N^5 in ZM241385, Figure 2a and b) results in a different pattern of hydrogen bond donors and acceptors. Specifically, PSB-2113 does neither possess a hydrogen bond acceptor in position 9a nor a hydrogen bond donor in the *N*7-position due to the additional five-membered ring. This leads to small positional movements of water molecules within the hydrogen bonding network (Figure 4c) but does not interfere with the overall system that connects the ligand to the backbone of helices II and III and the sidechains of $E13^{1.39}$, $Y271^{7.36}$, $S277^{7.42}$, and $H278^{7.43}$ (Figure 4a and c). The phenylpiperazinylethyl moiety that is attached to the N7 in PSB-2113 extends towards the extracellular surface of the $A_{2A}AR$, stabilized by π–π stacking to $H264^{ECL3}$ (Figure 4a). A similar binding mode was previously determined for the $A_{2A}AR$ antagonist 12x that also features a phenylpiperazinylethyl extension but is derived from ZM241385 (Figure S3).[21] $H264^{ECL3}$ itself forms an ionic lock with $E169^{ECL2}$ that has frequently been observed in both active and inactive state $A_{2A}AR$ structures.[42] Structures of the $A_{2A}AR$ lacking the ionic lock have also been obtained but appear to be dependent on either crystallization conditions[19] or the co-crystallized ligand (Table S1).[43] No unambiguous electron density evidence could be observed for the PEG linker that clearly sticks out of the binding pocket (Figure 4a). This indicates that the PEG-chain located at the receptor surface is highly flexible, which is a desired characteristic for the intended purpose to attach variable reporter molecules to the terminus of the linker.

Next, we solved the crystal structure of the $A_{2A}AR$ in complex with the new fluorescence-labeled $A_{2A}AR$ antagonist PSB-2115. This ligand differs from PSB-2113 by the attached BODIPY fluorophore (Figure S1). The binding pocket that accommodates the Preladenant scaffold is virtually identical in both structures (Figure 4a and d), proving that the attached fluorophore does not interfere with $A_{2A}AR$ binding. In analogy to PSB-2113, no electron density could be observed neither for the flexible PEG linker, nor for the BODIPY fluorophore, and no specific interactions of the $A_{2A}AR$ with the linker or fluorophore could be detected. Analytical size-exclusion chromatography confirmed the presence of the fluorophore in the A_{2A}-PSB1-bRIL-PSB-2115 complex (Figure 5). A signal could be observed for the latter complex at the absorption maximum of the respective BODIPY derivative (495 nm, for the fluorescence spectrum see Figure S4), whereas the analogous PSB-2113 complex that is lacking the fluorophore was only detectable at a lower, protein-specific wavelength (280 nm).

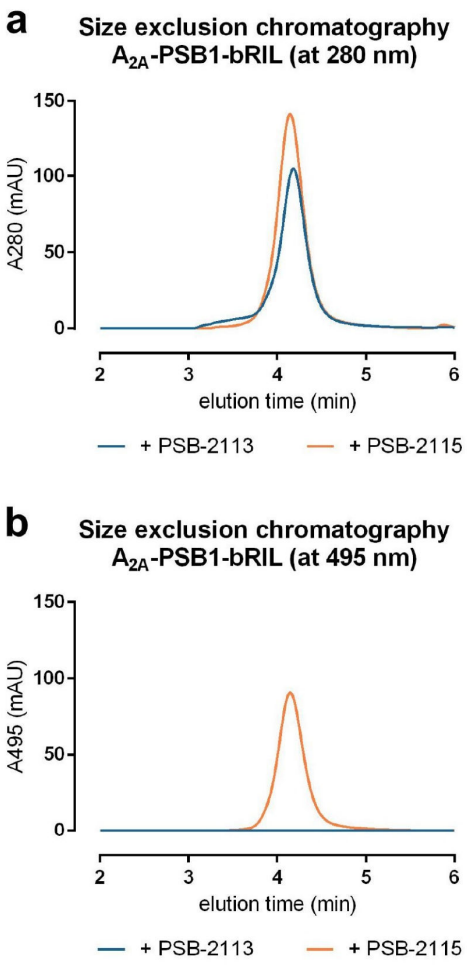

Figure 5. Size-exclusion chromatography analysis. The complexes of $A_{2A}AR$ antagonists PSB-2113 and PSB-2115 together with A_{2A}-PSB1-bRIL were analyzed by size-exclusion chromatography using two different detection wavelengths (a) 280 nm and b) 495 nm).

In contrast to the tricyclic Preladenant and its new conjugates, which show high selectivity for the $A_{2A}AR$, the previously co-crystallized bicyclic antagonist ZM241385 is only weakly selective, binding additionally to the $A_{2B}AR$ with high affinity.[44] The new crystal structures suggest that the tricyclic core and the resulting conformational restriction of the substituent at the *N*7-position of Preladenant represent important determinants for $A_{2A}AR$ selectivity. To date, no $A_{2B}AR$ structures have yet been solved. However, homology modeling approaches have proposed structural features of the $A_{2B}AR$ and its orthosteric ligand binding site.[45] The extracellular amino-terminus and loops differ significantly between the A_{2A}- and the $A_{2B}AR$ whereas the amino acids in the orthosteric ligand binding pocket of both receptor subtypes are nearly identical with only one single amino acid difference ($L249^{6.51}$ in the $A_{2A}AR$ and $V250^{6.51}$ in the $A_{2B}AR$). The leucine residue in position $249^{6.51}$ of the

A_{2A}AR exhibits direct hydrophobic contacts to the tricyclic Preladenant structure as observed in our newly determined structures (Figure 4a). Moreover, an L249$^{6.51}$V mutation in the A_{2A}AR has been shown to lower the binding affinity of ZM241385.[46] Hence, its exchange to valine in the A_{2B}AR may contribute to the observed high A_{2A}AR selectivity of Preladenant and its derivatives. Moreover, the additional pyrazole ring in Preladenant determines the direction of the elongated *N*7-substituent, whose conformation is thereby restricted, i.e. the exit vector is sterically fixed (see Figure 6). In contrast, the phenylethyl residue attached to the analogous N^5 (the amino group attached to C5) in the non-selective bicyclic antagonist ZM241385 is much more flexible and therefore able to adopt different conformations, e.g. conformation **A**, similar to Preladenant (Figure 6) or conformation **B**, in which the phenyethyl residues points into a completely different direction. Conformation **A** of the N^5-substituent in ZM241385 is consistent with the predominant A_{2A}AR binding mode[32] and with the fixed conformation in Preladenant. However, a structure of the A_{2A}-StaR2 in complex with ZM241385,[19] crystallized by vapor-diffusion in alkaline conditions, showed that the A_{2A}AR can also harbor binding mode **B**, and is thus able to accommodate both conformations. On the other hand, previous molecular docking experiments suggested binding mode **B** for ZM241385 in the A_{2B}AR binding pocket[45] and we propose that binding mode **A** would lead to a sterical clash with A_{2B}AR residues at the extracellular terminus of its helix VII (e.g. K269$^{7.32}$). The fact that Preladenant analogs substituted at *N*8 rather than *N*7, can, in contrast, display high A_{2B}AR affinity,[47] further supports our hypothesis. Shifting of the large residue in Preladenant from the *N*7- to the *N*8-position will allow it to adopt a conformation that can now interact with both the A_{2B}- and the A_{2A}AR binding pocket.

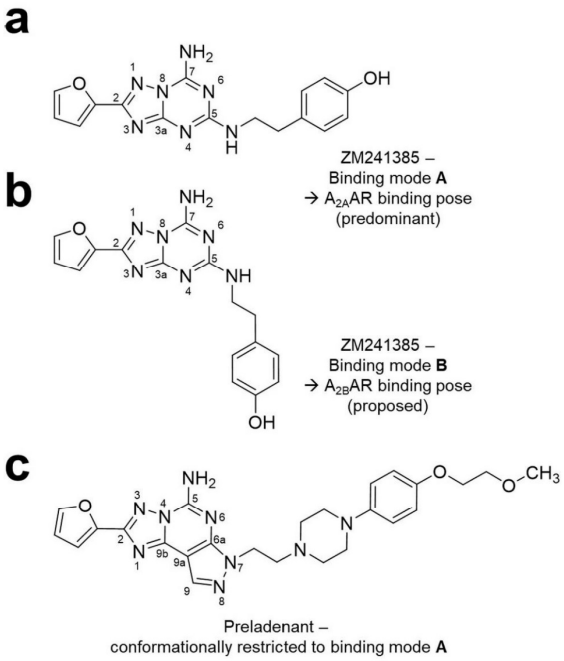

Figure 6. a) Binding pose **A** of ZM241385 to the A_{2A}AR as seen in PDB ID 4EIY. b) Proposed binding pose **B** of ZM241385 in the A_{2B}AR.[45] c) Binding mode of the Preladenant scaffold as observed in the new A_{2A}AR structures.

Conclusion

The A_{2A}AR has become an important drug target.[7,8,22] In particular, A_{2A}AR antagonists are being developed for the treatment of neurodegenerative diseases and for cancer therapy due to their immunostimulatory and anti-proliferative effects. Extensive efforts have been invested in studying the A_{2A}AR's structure in complex with various ligands.[19,21,24,32] Nevertheless, a co-crystal structure of one of the most potent (K_i < 1 nM) and selective (≈3 orders of magnitude) A_{2A}AR antagonists, Preladenant, has not been accessible to date. We have now been able to solve A_{2A}AR crystal structures in complex with two Preladenant derivatives, PSB-2113 and PSB-2115. This has been possible due to the design and construction of the novel thermostabilized A_{2A}AR mutant A_{2A}-PSB1-bRIL, which harbors only a single, but crucial point mutation in the transmembrane domain. Although we achieved a marked decrease in the number of mutated amino acid residues (with only a single exchange) compared to the previously optimized A_{2A}AR crystallization construct (with nine mutations),[19] the stability of the novel construct is even greater than that of any other A_{2A}AR mutant reported to date. Thus, the A_{2A}-PSB1-bRIL receptor construct is proposed to become the new gold standard for the determination of A_{2A}AR structures in its inactive state, which will be most helpful for the development of novel A_{2A}AR blockers. The A_{2A}AR is being used as a test case for class A GPCRs in general, and we predict that our strategy for GPCR stabilization should be useful for many other GPCRs that are modulated in the same way by sodium ions as the A_{2A}AR. The newly developed PEGylated and fluorescence-labeled Preladenant derivatives represent prototypes of valuable and versatile pharmacological tools for studying this (patho)physiologically important receptor and drug target. Their high-resolution X-ray structures will guide the way to improved A_{2A}AR antagonists which have great potential as novel drugs for diseases with urgent medical need, such as neurodegeneration and cancer.

Acknowledgements

C.E.M. is grateful for funding by the Deutsche Forschungsgemeinschaft in the field of purinergic signaling (SFB1328) and GPCR signal transduction (FOR2372). T.C., T.K., J.H.V., J.G.S., V.J.V., and C.E.M. acknowledge support by the German Federal Ministry of Research and Technology (BMBF) for the Bonn Graduate School of Drug Sciences (BIGS DrugS). J.G.S. and J.H.V. were supported by the DFG (FOR2372). T.K. received a PhD scholarship by the Fonds der Chemischen Industrie (FCI). We thank Dr. Bryan

Roth, University of North Carolina School of Medicine, Chapel Hill, NC, USA, for sharing the TRUPATH Biosensor Platform. Open Access funding enabled and organized by Projekt DEAL.

Conflict of Interest

The authors declare no conflict of interest.

Data Availability Statement

The data that support the findings of this study are available in the supplementary material of this article. Coordinates and structure factors have been deposited in the Protein Data Bank (PDB) under accession codes 7PX4 (A_{2A}-PSB1-bRIL-PSB-2113) and 7PYR (A_{2A}-PSB1-bRIL-PSB-2115).

Keywords: Adenosine A_{2A} Receptor · Cancer · G Protein-Coupled Receptor (GPCR) · Preladenant Conjugates · Protein Structures

[1] a) G. Burnstock, *Nat. Rev. Drug Discovery* **2008**, *7*, 575–590; b) B. Fredholm, A. Verkhratsky, *Acta Physiol.* **2010**, *199*, 91–92.
[2] a) P. A. Borea, S. Gessi, S. Merighi, F. Vincenzi, K. Varani, *Physiol. Rev.* **2018**, *98*, 1591–1625; b) C. E. Müller, K. A. Jacobson, *Biochim. Biophys. Acta Biomembr.* **2011**, *1808*, 1290–1308.
[3] J. Kjaergaard, S. Hatfield, G. Jones, A. Ohta, M. Sitkovsky, *J. Immunol.* **2018**, *201*, 782–791.
[4] A. Ohta, E. Gorelik, S. J. Prasad, F. Ronchese, D. Lukashev, M. K. K. Wong, X. Huang, S. Caldwell, K. Liu, P. Smith, et al, *Proc. Natl. Acad. Sci. USA* **2006**, *103*, 13132–13137.
[5] a) A. Young, D. Mittal, K. Stannard, M. Yong, M. W. Teng, B. Allard, J. Stagg, M. J. Smyth, *Oncoimmunology* **2014**, *3*, e958952; b) S. M. Hatfield, M. Sitkovsky, *Curr. Opin. Pharmacol.* **2016**, *29*, 90–96.
[6] B. B. Fredholm, A. P. IJzerman, K. A. Jacobson, J. Linden, C. E. Müller, *Pharmacol. Rev.* **2011**, *63*, 1–34.
[7] A. Hammami, D. Allard, B. Allard, J. Stagg, *Semin. Immunol.* **2019**, *42*, 101304.
[8] D. Allard, M. Turcotte, J. Stagg, *Immunol. Cell Biol.* **2017**, *95*, 333–339.
[9] S. N. Schiffmann, G. Fisone, R. Moresco, R. A. Cunha, S. Ferré, *Prog. Neurobiol.* **2007**, *83*, 277–292.
[10] C. Laurent, S. Burnouf, B. Ferry, V. L. Batalha, J. E. Coelho, Y. Baqi, E. Malik, E. Marciniak, E. Mariciniak, S. Parrot, et al, *Mol. Psychiatry* **2016**, *21*, 149.
[11] I. Villar-Menéndez, S. Porta, S. P. Buira, T. Pereira-Veiga, S. Díaz-Sánchez, J. L. Albasanz, I. Ferrer, M. Martín, M. Barrachina, *Neurobiol. Dis.* **2014**, *69*, 206–214.
[12] F. Calon, M. Dridi, O. Hornykiewicz, P. J. Bédard, A. H. Rajput, T. Di Paolo, *Brain* **2004**, *127*, 1075–1084.
[13] C. Zúñiga-Ramírez, F. Micheli, *Future Neurol.* **2013**, *8*, 639–648.
[14] R. A. Hauser, F. Stocchi, O. Rascol, S. B. Huyck, R. Capece, T. W. Ho, P. Sklar, C. Lines, D. Michelson, D. Hewitt, *JAMA Neurol.* **2015**, *72*, 1491–1500.
[15] J. C. Burbiel, W. Ghattas, P. Küppers, M. Köse, S. Lacher, A.-M. Herzner, R. S. Kombu, R. R. Akkinepally, J. Hockemeyer, C. E. Müller, *ChemMedChem* **2016**, *11*, 2272–2286.
[16] S. Khanapur, A. van Waarde, K. Ishiwata, K. L. Leenders, R. A. J. O. Dierckx, P. H. Elsinga, *Curr. Med. Chem.* **2014**, *21*, 312–328.
[17] X. Yang, L. H. Heitman, A. P. IJzerman, D. van der Es, *Purinergic Signal.* **2021**, *17*, 85–108.
[18] N. Robertson, A. Jazayeri, J. Errey, A. Baig, E. Hurrell, A. Zhukov, C. J. Langmead, M. Weir, F. H. Marshall, *Neuropharmacology* **2011**, *60*, 36–44.
[19] A. S. Doré, N. Robertson, J. C. Errey, I. Ng, K. Hollenstein, B. Tehan, E. Hurrell, K. Bennett, M. Congreve, F. Magnani, et al, *Structure* **2011**, *19*, 1283–1293.
[20] H. M. Berman, J. Westbrook, Z. Feng, G. Gilliland, T. N. Bhat, H. Weissig, I. N. Shindyalov, P. E. Bourne, *Nucleic Acids Res.* **2000**, *28*, 235–242.
[21] E. Segala, D. Guo, R. K. Y. Cheng, A. Bortolato, F. Deflorian, A. S. Doré, J. C. Errey, L. H. Heitman, A. P. IJzerman, F. H. Marshall, et al, *J. Med. Chem.* **2016**, *59*, 6470–6479.
[22] M. Congreve, G. A. Brown, A. Borodovsky, M. L. Lamb, *Expert Opin. Drug Discovery* **2018**, *13*, 997–1003.
[23] A. Borodovsky, C. M. Barbon, Y. Wang, M. Ye, L. Prickett, D. Chandra, J. Shaw, N. Deng, K. Sachsenmeier, J. D. Clarke, et al, *J. Immunother. Cancer* **2020**, *8*, e000417.
[24] G. Lebon, T. Warne, P. C. Edwards, K. Bennett, C. J. Langmead, A. G. W. Leslie, C. G. Tate, *Nature* **2011**, *474*, 521–525.
[25] C. J. Langmead, S. P. Andrews, M. Congreve, J. C. Errey, E. Hurrell, F. H. Marshall, J. S. Mason, C. M. Richardson, N. Robertson, A. Zhukov, M. Weir, *J. Med. Chem.* **2012**, *55*, 1904–1909.
[26] J. A. Ballesteros, H. Weinstein in *Methods in Neurosciences* (Ed.: S. C. Sealfon), Elsevier, Amsterdam, **1995**, pp. 366–428.
[27] K. T. Kimura, H. Asada, A. Inoue, F. M. N. Kadji, D. Im, C. Mori, T. Arakawa, K. Hirata, Y. Nomura, N. Nomura, et al, *Nat. Struct. Mol. Biol.* **2019**, *26*, 121–128.
[28] S. Yasuda, Y. Kajiwara, Y. Takamuku, N. Suzuki, T. Murata, M. Kinoshita, *J. Phys. Chem.* **2016**, *120*, 3833–3843.
[29] F. Heisig, S. Gollos, S. J. Freudenthal, A. El-Tayeb, J. Iqbal, C. E. Müller, *J. Fluoresc.* **2014**, *24*, 213–230.
[30] V. Hoguet, M. Lasalle, M. Maingot, G. Dequirez, R. Boulahjar, F. Leroux, C. Piveteau, A. Herledan, A. Biela, J. Dumont, et al, *J. Med. Chem.* **2021**, *64*, 1593–1610.
[31] C. E. Müller, S. Ferré, *Recent Pat. CNS Drug Discovery* **2007**, *2*, 1–21.
[32] W. Liu, E. Chun, A. A. Thompson, P. Chubukov, F. Xu, V. Katritch, G. W. Han, C. B. Roth, L. H. Heitman, A. P. IJzerman, V. Cherezov, R. C. Stevens, *Science* **2012**, *337*, 232–236.
[33] X. Zhang, R. C. Stevens, F. Xu, *Trends Biochem. Sci.* **2015**, *40*, 79–87.
[34] K. A. Bennett, B. Tehan, G. Lebon, C. G. Tate, M. Weir, F. H. Marshall, C. J. Langmead, *Mol. Pharmacol.* **2013**, *83*, 949–958.
[35] K. L. White, M. T. Eddy, Z.-G. Gao, G. W. Han, T. Lian, A. Deary, N. Patel, K. A. Jacobson, V. Katritch, R. C. Stevens, *Structure* **2018**, *26*, 259-269.e5.
[36] X. Pang, M. Yang, K. Han, *Proteins Struct. Funct. Bioinf.* **2013**, *81*, 1399–1410.
[37] C. E. Müller, J. Maurinsh, R. Sauer, *Eur. J. Pharm. Sci.* **2000**, *10*, 259–265.
[38] F. Xu, H. Wu, V. Katritch, G. W. Han, K. A. Jacobson, Z.-G. Gao, V. Cherezov, R. C. Stevens, *Science* **2011**, *332*, 322–327.
[39] R. H. J. Olsen, J. F. DiBerto, J. G. English, A. M. Glaudin, B. E. Krumm, S. T. Slocum, T. Che, A. C. Gavin, J. D. McCorvy, B. L. Roth, R.T. Strachan, *Nat. Chem. Biol.* **2020**, *16*, 841–849.

[40] V.-P. Jaakola, M. T. Griffith, M. A. Hanson, V. Cherezov, E. Y. T. Chien, J. R. Lane, A. P. IJzerman, R. C. Stevens, *Science* **2008**, *322*, 1211–1217.
[41] J. S. Mason, A. Bortolato, D. R. Weiss, F. Deflorian, B. Tehan, F. H. Marshall, *In Silico Pharmacol.* **2013**, *1*, 23.
[42] B. Carpenter, G. Lebon, *Front. Pharmacol.* **2017**, *8*, 898.
[43] P. Rucktooa, R. K. Y. Cheng, E. Segala, T. Geng, J. C. Errey, G. A. Brown, R. M. Cooke, F. H. Marshall, A. S. Doré, *Sci. Rep.* **2018**, *8*, 41.
[44] C. Carbajales, J. Azuaje, A. Oliveira, M. I. Loza, J. Brea, M. I. Cadavid, C. F. Masaguer, X. García-Mera, H. Gutiérrez-de-Terán, E. Sotelo, *J. Med. Chem.* **2017**, *60*, 3372–3382.
[45] F. F. Sherbiny, A. C. Schiedel, A. Maass, C. E. Müller, *J. Comput.-Aided Mol. Des.* **2009**, *23*, 807–828.
[46] X. Wang, W. Jespers, R. Prieto-Díaz, M. Majellaro, A. P. IJzerman, G. J. P. van Westen, E. Sotelo, L. H. Heitman, H. Gutiérrez-de-Terán, *Sci. Rep.* **2021**, *11*, 14171.
[47] P. G. Baraldi, B. Cacciari, R. Romagnoli, K.-N. Klotz, G. Spalluto, K. Varani, S. Gessi, S. Merighi, P. A. Borea, *Drug Dev. Res.* **2001**, *53*, 225–235.

Manuscript received: November 15, 2021
Accepted manuscript online: February 17, 2022
Version of record online: ■■, ■■

Supplementary Materials

of

Publication II

in

***Angewandte Chemie*[107]**

Angewandte Chemie
Eine Zeitschrift der Gesellschaft Deutscher Chemiker

Supporting Information

Single Stabilizing Point Mutation Enables High-Resolution Co-Crystal Structures of the Adenosine A_{2A} Receptor with Preladenant Conjugates

*T. Claff, T. A. Klapschinski, U. K. Tiruttani Subhramanyam, V. J. Vaaßen, J. G. Schlegel, C. Vielmuth, J. H. Voß, J. Labahn, C. E. Müller**

Author Contributions

T.C. Investigation:Lead; Methodology:Lead; Validation:Lead; Writing – original draft:Lead
T.K. Investigation:Lead; Writing – review & editing:Supporting
U.S. Formal analysis:Lead; Investigation:Equal; Validation:Equal; Writing – review & editing:Supporting
J.S. Investigation:Supporting; Methodology:Supporting; Writing – review & editing:Supporting
C.V. Investigation:Supporting; Writing – review & editing:Supporting
J.V. Investigation:Equal; Methodology:Equal; Writing – review & editing:Supporting
J.L. Data curation:Equal; Formal analysis:Equal; Supervision:Equal; Writing – original draft:Supporting; Writing – review & editing:Supporting
C.M. Conceptualization:Lead; Supervision:Lead; Writing – original draft:Equal

SUPPORTING INFORMATION

Table of Contents

SUPPORTING INFORMATION

1. Experimental Procedures

1.1 Synthesis of Preladenant derivatives

General

Chemicals were purchased from Merck (Darmstadt, Germany), ABCR (Karlsruhe, Germany), or TCI (Eschborn, Germany); dried solvents were purchased from Acros Organics (Fisher Scientific GmbH, Schwerte, Germany). Solvents were of HPLC quality. Thin-layer chromatography (TLC) was performed on silica gel plates F_{254} (0,25 mm) or on reverse phase silica gel plates 60 RP-18 F_{254} (Merck). Compounds were detected under UV light (254 nm, 366 nm) or by spraying the plates with a basic $KMnO_4$ solution (1.5 g of $KMnO_4$, 10 g of K_2CO_3, and 1.25 ml of 10% aq. NaOH solution in 200 ml of water), or a ninhydrin solution (1.5 g of ninhydrin dissolved in 100 mL of butanol containing 3.0 ml of acetic acid). Reaction controls were performed by measuring the molecular masses of the products on an Advion Expression L mass spectrometer with a TLC interface, following atomic pressure chemical ionization (APCI) or electrospray ionization (ESI). Column chromatography was performed using glass columns filled with silica gel 60 (35-70 µm), or using the automated flash chromatography system Combiflash Rf 200 (Teledyne ISCO, Nebraska, USA). The final compounds were purified by reversed phase HPLC (Knauer, Berlin, Germany), on a C18ec column, 250 x 20 mm, Nucleodur 100-5. Analytical LCMS spectra were obtained on an API2000 mass spectrometer with an ESI source (ABSciex, Darmstadt, Germany) coupled with an Agilent HPLC HP1100 system (column: EC50/2 Nucleodur C18 Gravity 3 µm, Macherey-Nagel, Düren, Germany) at 25 °C. The following eluents were used: water containing 2 mM ammonium acetate (A) and methanol containing 2 mM ammonium acetate (B). A gradient was used starting from 90% A, reaching 100% B within 10 min. The column was flushed for additional 10 min with B. The flow rate was 0.3 ml/min. The samples were dissolved in B or in acetonitrile at a concentration of 1 mg/ml, and 8 µl of the solution were injected. The total ion current (TIC) was measured for the relevant masses, routinely from 150-800 m/z. UV absorption was measured from 190-900 nm using a diode array detector (DAD), and purity was determined at 220-400 nm.

High resolution mass spectra were obtained by HPLC-QToF-MS spectroscopy on a Bruker micrOTOF-Q mass spectrometer connected to a Dionex Ultimate 3000 HPLC system (column: EC50/2 Nucleodur C18 Gravity 3 µm, Macherey-Nagel, Düren, Germany). Conditions were the same as described above.

UV spectra were determined from 300 to 800 nm on a Varian/Cary 50 Bio instrument (Agilent Technologies, USA). Fluorescence spectra were recorded on a Flx-Monaco spektrofluorometer (Monaco, Monaco) using a xenon lamp. The band width was 5 nm for excitation and emission, and the emission was recorded from 300 to 800 nm. The excitation wavelenth was selected according to the absorption maxima. Stock solutions were prepared in DMSO (10 mM or 0.1 mM), and 1 µl of stock solution was added to a cuvette containing 990 µl of solvent (H_2O, CH_2Cl_2 or MeOH) and 9 µl of DMSO. The final DMSO concentration ways 1%, and the final compound concentration was 10 µM for UV spectra determination, and 0.1 µM for fluorescence spectra.

^1H and ^{13}C NMR spectra were measured in $CDCl_3$ or DMSO-d_6 on a Bruker Ascend 600 MHz spectrometer at 600.18 MHz (^1H) and 150.93 MHz (^{13}C). Chemical shifts (δ) are given in ppm, and were related to the solvent signals ($CDCl_3$, 7.26 ppm for ^1H NMR spectra, 77.16 ppm for ^{13}C NMR spectra; DMSO-d_6, 2.50 ppm for ^1H NMR spectra, 39.52 ppm for ^{13}C NMR spectra). Multiplicities are designated as follows: s, singlet; d, doublet; q, quartet; p, pentet; sext, sextet; m, multiplet; b, broad. Coupling constants (J) are in Hertz (Hz). Melting points were determined on a Büchi 545 melting point apparatus and are uncorrected. The syntheses of the functionalized Preladenant derivatives **1** and **2** and of the amino-substituted PEG linkers **3a-3f** are described in **Scheme S1**.

***tert*-Butyl 1-(4-(4-(2-(5-amino-2-(furan-2-yl)-7*H*-pyrazolo[4,3-*e*][1,2,4]triazolo[1,5-*c*]pyrimidin-7-yl)ethyl)piperazin-1-yl)phenoxy)-2-oxo-6,9,12,15-tetraoxa-3-azaheptadecan-17-oate (4, PSB-2113)**

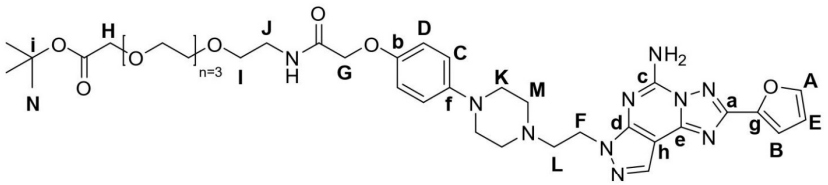

Compound **2** (20 mg, 0.04 mmol, 1.0 eq.) is dissolved in dichloromethane (500 µl) and HATU (17.9 mg, 0.07 mmol, 1.2 eq.) is added. In a separate vial, compound **3a** (13.5 mg, 0.044 mmol, 1.1 eq.) is dissolved in dichloromethane (500 µl) and diisopropylethylamine (10.3 mg, 0.08 mmol, 2.0 eq.) is added. After 5 min of pre-activation of the carboxylic acid **2**, the solution of the amine **3a** is added, and the mixture is stirred for 24 h at room temperature (RT). Then, the solvent is removed *in vacuo*, and the product is purified by HPLC, applying a gradient within 15 min from 70% aq. methanol to 100% methanol, yielding 25.1mg (0.032 mmol, 79%) of **4**.

^1H NMR (600 MHz, DMSO-d_6) δ [ppm]: 8.16 (s, 1H, NCH), 8.05 (bs, 2H, NH_2), 7.95 (t, $^3J_{H,H}$ = 5.73 Hz, 1H, NH), 7.94–7.93 (m, 1H, A), 7.22 (dd, $^3J_{H,H}$ = 3.32 Hz, $^3J_{H,H}$ = 0.85 Hz 1H, B), 6.88–6.80 (m, 4H, C, D), 6.73 (dd, $^3J_{H,H}$ = 1.77 Hz, $^3J_{H,H}$ = 3.41 Hz, 1H, E), 4.42 (t, $^3J_{H,H}$ = 6.79 Hz 2H, F), 4.36 (s, 2H, G), 3.96 (s, 2H, H), 3.56–3.54 (m, 2H, CH_2), 3.52–3.48 (m, 10H, 5 x CH_2), 3.44 (t, $^3J_{H,H}$ = 5.96 Hz, I), 3.30–3.25 (m, 2H, J), 2.98–2.93 (m, 4H, K), 2.83 (t, $^3J_{H,H}$ = 6.81 Hz, 2H, L), 2.61–2.58 (m, 4H, M), 1.40 (s, 9H, N). **^{13}C NMR** (126 MHz, DMSO-d_6) δ [ppm]: 169.3 (C_q, C_{ester}), 168.0 (C_q, C_{amide}), 155.4 (C_q, a), 151.2 (C_q, b), 148.7 (C_q, c), 148.6 (C_q, d), 146.2 (C_q, e), 146.0 (C_q, f), 145.5 (C_q, g), 145.1 (CH, A), 131.4 (CH, NCH), 117.1 (2 x CH, C, D), 115.3 (2 x CH, C, D), 112.3 (CH, B), 112.1 (CH, B), 95.7 (C_q, h), 80.6 (C_q, i), 69.9 (CH_2), 69.8 (CH_2), 69.7 (2 x CH_2), 69.7 (CH_2), 69.5 (CH_2), 68.8 (CH_2), 68.1 (CH_2), 67.6 (CH_2), 56.5 (CH_2,

L), 52.6 (2 x CH_2, M), 49.4 (2 x CH_2, K), 44.4 (CH_2, F), 38.2 (CH_2, J), 27.7 (3 x CH_3, N). **Mp**. 115.9–117.6 °C. **HRMS** (ESI-QTOF) calculated for $C_{38}H_{52}N_{10}O_9$ [M+H]$^+$: 793.3991; found: 793.3850. **Purity**: 99%.

***tert*-Butyl 1-(4-(4-(2-(5-amino-2-(furan-2-yl)-7*H*-pyrazolo[4,3-*e*][1,2,4]triazolo[1,5-*c*]pyrimidin-7-yl)ethyl)piperazin-1-yl)phenoxy)-2-oxo-6,9,12,15,18-pentaoxa-3-azaicosan-20-oate (5)**

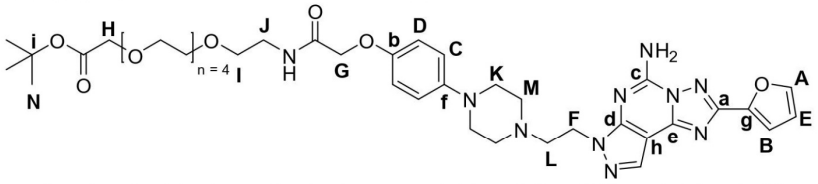

The reaction is performed as described for the synthesis of compound **4** from 2.8 mg (5.5 µmol, 1.0 eq.) of **2** and HATU (2.5 mg, 6.6 µmol, 1.2 eq.) dissolved in 500 µl of dichloromethane, and 2.1 mg (6.1 µmol, 1.1 eq.) of **3b**, in the presence of 2.0 µl (11.0 µmol, 2.0 eq.) of diisopropylethylamine. The product was purified by HPLC as described for compound **4**. Yield: 3.6 mg (4.3 µmol, 78%) of product **5**.

^{1}H NMR (600 MHz, DMSO-d_6) δ [ppm]: 8.16 (s, 1H, NCH), 8.05 (bs, 2H, NH_2), 7.95 (t, $^3J_{H,H}$ = 5.75 Hz, 1H, NH), 7.94–7.93 (m, 1H, A), 7.22 (d, $^3J_{H,H}$ = 3.32 Hz, 1H, B), 6.87–6.84 (m, 2H, C), 6.84–6.81 (m, 2H, D), 6.73 (dd, $^3J_{H,H}$ = 1.71 Hz, $^3J_{H,H}$ = 3.45 Hz, 1H, E), 4.42 (t, $^3J_{H,H}$ = 6.83 Hz, 2H, F), 4.36 (s, 2H, G), 3.97 (s, 2H, H), 3.58–3.47 (m, 16H, PEG), 3.44 (t, $^3J_{H,H}$ = 5.96Hz, I), 3.30–3.26 (m, 2H, J), 2.99–2.92 (m, 4H, K), 2.83 (t, $^3J_{H,H}$ = 6.85 Hz, 2H, L), 2.62–2.57 (m, 4H, M), 1.41 (s, 9H, N). **^{13}C NMR** (151 MHz, DMSO-d_6) δ [ppm]: 169.3 (C_q, C_{Ester}), 168.0 (C_q, C_{amide}), 155.4 (C_q, a), 151.2 (C_q, b), 148.7 (C_q, c), 148.6 (C_q, d), 146.2 (C_q, e), 146.0 (C_q, f), 145.5 (C_q, g), 145.1 (CH, A), 131.4 (CH, NCH), 117.0 (2 x CH, C, D), 115.3 (2 x CH, C, D), 112.2 (CH, B), 112.1 (CH, E), 95.6 (C_q, h), 80.6 (C_q, i), 69.8 (CH_2, PEG), 69.8 (CH_2, PEG), 69.8 (CH_2, PEG), 69.7 (CH_2, PEG), 69.7 (CH_2, PEG), 69.7 (CH_2, PEG), 69.7 (CH_2, PEG), 69.5 (CH_2, PEG), 68.8 (CH_2, I), 68.1 (CH_2, H), 67.6 (CH_2, G), 56.5 (CH_2, L), 52.6 (2 x CH_2, M), 49.4 (2 x CH_2, K), 44.4 (CH_2, F), 38.2 (CH_2, J), 27.7 (3 x CH_3, N). **Mp.** 295 – 300 °C (decomposition). **LCMS**: positive [*m*/*z*] = 837.5 ([M+H]$^+$). **HRMS** (ESI-QTOF) calculated for $C_{40}H_{56}N_{10}O_{10}$ [M+Na]$^+$: 859.4073; found: 859.4074. **Purity**: 96%.

***tert*-Butyl 1-(4-(4-(2-(5-amino-2-(furan-2-yl)-7*H*-pyrazolo[4,3-*e*][1,2,4]triazolo[1,5-*c*]pyrimidin-7-yl)ethyl)piperazin-1-yl)phenoxy)-2-oxo-6,9,12,15,18,21,24,27-octaoxa-3-azanonacosan-29-oate (6)**

The reaction is performed as described for the synthesis of compound **4** from 20 mg (0.04 mmol, 1.0 eq.) of **2** and HATU (17.9 mg, 0.07 mmol, 1.2 eq.) dissolved in 500 µl of dichloromethane, and 21.3 mg (0.044 mol, 1.1 eq.) of **3c**, in the presence of 10.3 mg (0.08 mmol, 2.0 eq.) of diisopropylethylamine. The product is purified by HPLC as described for compound **4**. Yield: 37.9 mg (0.039 mmol, 98%) of product **6**.

^{1}H NMR (600 MHz, DMSO-d_6) δ [ppm]: 8.16 (s, 1H, NCH), 8.05 (bs, 2H, NH_2), 7.95 (t, $^3J_{H,H}$ = 5.75 Hz, 1H, NH), 7.94–7.93 (m, 1H, A), 7.22 (d, $^3J_{H,H}$ = 3.30 Hz, 1H, B), 6.87–6.81 (m, 4H, C+D), 6.73 (dd, $^3J_{H,H}$ = 1.74 Hz, $^3J_{H,H}$ = 3.39 Hz, 1H, E), 4.42 (t, $^3J_{H,H}$ = 6.81 Hz, 2H, F), 4.36 (s, 2H, G), 3.97 (s, 2H, H), 3.57–3.54 (m, 2H, CH_2), 3.53–3.51 (m, 2H, CH_2), 3.51–3.47 (m, 24H, 12 x CH_2), 3.44 (t, $^3J_{H,H}$ = 5.96 Hz, I), 3.28 (q, $^3J_{H,H}$ = 5.92 Hz, 2H, J), 2.99–2.93 (m, 4H, K), 2.83 (t, $^3J_{H,H}$ = 6.80 Hz, 2H, L), 2.62–2.57 (m, 4H, M), 1.41 (s, 9H, N). **^{13}C NMR** (151 MHz, DMSO-d_6) δ [ppm]: 169.3 (C_q, C_{ester}), 168.0 (C_q, C_{amide}), 155.3 (C_q, a), 151.2 (C_q, b), 148.7 (C_q, c), 148.6 (C_q, d), 146.2 (C_q, e), 146.0 (C_q, f), 145.5 (C_q, g), 145.1 (CH, A), 131.4 (CH, NCH), 117.0 (2 x CH, C, D), 115.3 (2 x CH, C, D), 112.2 (CH, B), 112.1 (CH, E), 95.6 (C_q, h), 80.6 (C_q, i), 69.8 (CH_2, PEG), 69.8 (9 x CH_2, PEG), 69.7 (2 x CH_2, PEG), 69.7 (CH_2, PEG), 69.5 (CH_2, PEG), 68.8 (CH_2, I), 68.1 (CH_2, H), 67.6 (CH_2, G), 56.5 (CH_2, L), 52.6 (2 x CH_2, M), 49.3 (2 x CH_2, K), 44.4 (CH_2, F), 38.2 (CH_2, J), 27.7 (3 x CH_3, N). Mp: could not be determined due to hygroscopic nature of the compound. **HRMS** (ESI-QTOF) calculated for $C_{46}H_{69}N_{10}O_{13}$ [M+H]$^+$: 969.5040; found: 969.5027. **Purity**: 98%.

***tert*-Butyl 1-(4-(4-(2-(5-amino-2-(furan-2-yl)-7*H*-pyrazolo[4,3-*e*][1,2,4]triazolo[1,5-*c*]pyrimidin-7-yl)ethyl)piperazin-1-yl)phenoxy)-2-oxo-6,9,12,15,18,21,24,27,30,33,36,39-dodecaoxa-3-azahentetracontan-41-oate (7)**

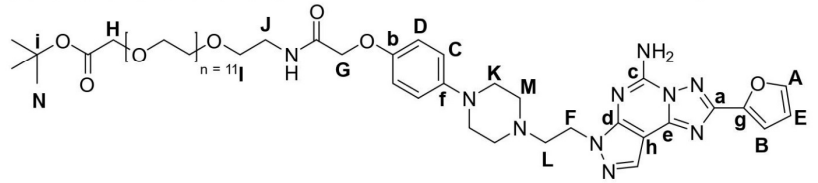

The reaction is performed as described for the synthesis of compound **4** from 20 mg (0.04 mmol, 1.0 eq.) of **2** and HATU (17.9 mg, 0.07 mmol, 1.2 eq.) dissolved in 500 µl of dichloromethane, and 29.0 mg (0.044 mol, 1.1 eq.) of **3d**, in the presence of 10.3 mg (0.08 mmol, 2.0 eq.) of diisopropylethylamine. The product is purified by HPLC as described for compound **4**. Yield: 36.6 mg (0.032 mmol, 80%) of product **7**.

^{1}H NMR (600 MHz, DMSO-d_6) δ [ppm]: 8.16 (s, 1H, NCH), 8.05 (bs, 2H, NH_2), 7.95 (t, $^3J_{H,H}$ = 5.73 Hz, 1H, NH), 7.94–7.93 (m, 1H, A), 7.22 (d, $^3J_{H,H}$ = 3.35 Hz, 1H, B), 6.87–6.81 (m, 4H, C+D), 6.73 (dd, $^3J_{H,H}$ = 1.73 Hz, $^3J_{H,H}$ = 3.51 Hz, 1H, E), 4.42 (t, $^3J_{H,H}$ = 6.78 Hz, 2H, F), 4.36 (s, 2H, G), 3.97 (s, 2H, H), 3.58–3.54 (m, 2H, CH_2), 3.53–3.51 (m, 2H, CH_2), 3.51–3.47 (m, 40H, 20 x CH_2), 3.44 (t, $^3J_{H,H}$ = 5.96 Hz, I), 3.28 (q, $^3J_{H,H}$ = 5.87 Hz, 2H, J), 2.99–2.93 (m, 4H, K), 2.83 (t, $^3J_{H,H}$ = 6.80 Hz, 2H, L), 2.61–2.57 (m, 4H, M), 1.41 (s, 9H, N). **^{13}C NMR** (151 MHz, DMSO-d_6) δ [ppm]: 169.4 (C_q, C_{Ester}), 168.0 (C_q, C_{amide}), 155.4 (C_q, a), 151.2 (C_q, b), 148.7 (C_q, c), 148.6 (C_q, d), 146.2 (C_q, e), 146.0 (C_q, f), 145.5 (C_q, g), 145.1 (CH, A), 131.4 (CH, NCH), 117.0 (2 x CH, C, D), 115.3 (2 x CH, C, D), 112.3 (CH, B), 112.1 (CH, E), 95.7 (C_q, h), 80.6 (C_q, i), 69.9 (CH_2, PEG), 69.8 (17 x CH_2, PEG), 69.7 (CH_2, PEG), 69.7 (CH_2, PEG), 69.7 (CH_2, PEG), 69.5 (CH_2, PEG), 68.8 (CH_2, I), 68.1 (CH_2, H), 67.6 (CH_2, G), 56.5 (CH_2, L), 52.6 (2 x CH_2, M), 49.4 (2 x CH_2, K), 44.4 (CH_2, F), 38.2 (CH_2, J), 27.7 (3x CH_3, N). Mp could not be determined due to the hygroscopic nature of the compound. **HRMS** (ESI-QTOF) calculated for $C_{54}H_{84}N_{10}O_{17}$ $[M+H]^+$: 1145.6089; found: 1145.6064. **Purity**: 98%.

***tert*-Butyl 1-(4-(4-(2-(5-amino-2-(furan-2-yl)-7*H*-pyrazolo[4,3-*e*][1,2,4]triazolo[1,5-*c*]pyrimidin-7-yl)ethyl)piperazin-1-yl)phenoxy)-2-oxo-6,9,12,15,18,21,24,27,30,33,36,39,42,45,48,51-hexadecaoxa-3-azatripentacontan-53-oate (8)**

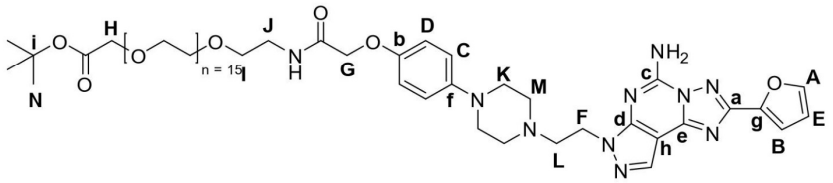

The reaction is performed as described for the synthesis of compound **4** from 20 mg (0.04 mmol, 1.0 eq.) of **2** and HATU (17.9 mg, 0.07 mmol, 1.2 eq.) dissolved in 500 µl of dichloromethane, and 36.8 mg (0.044 mol, 1.1 eq.) of **3e**, in the presence of 10.3 mg (0.08 mmol, 2.0 eq.) of diisopropylethylamine. The product is purified by HPLC as described for compound **4**. Yield: 46.4 mg (0.035 mmol, 88%) of product **8**.

^{1}H NMR (600 MHz, DMSO-d_6) δ [ppm]: 8.16 (s, 1H, NCH), 8.05 (bs, 2H, NH_2), 7.95 (t, $^3J_{H,H}$ = 5.71 Hz, 1H, NH), 7.94–7.93 (m, 1H, A), 7.22 (d, $^3J_{H,H}$ = 3.36 Hz, 1H, B), 6.87–6.81 (m, 4H, C+D), 6.73 (dd, $^3J_{H,H}$ = 1.75 Hz, $^3J_{H,H}$ = 3.40 Hz, 1H, E), 4.42 (t, $^3J_{H,H}$ = 6.81 Hz, 2H, F), 4.36 (s, 2H, G), 3.97 (s, 2H, H), 3.58–3.55 (m, 2H, CH_2), 3.54–3.51 (m, 2H, CH_2), 3.52–3.48 (m, 56H, 28 x CH_2), 3.44 (t, $^3J_{H,H}$ = 5.96 Hz, I), 3.28 (q, $^3J_{H,H}$ = 5.86 Hz, 2H, J), 2.99–2.93 (m, 4H, K), 2.83 (t, $^3J_{H,H}$ = 6.81 Hz, 2H, L), 2.63–2.57 (m, 4H, M), 1.41 (s, 9H, N). **^{13}C NMR** (151 MHz, DMSO-d_6) δ [ppm]: 169.3 (C_q, C_{Ester}), 168.0 (C_q, C_{Amid}), 155.4 (C_q, a), 151.2 (C_q, b), 148.7 (C_q, c), 148.6 (C_q, d), 146.2 (C_q, e), 146.0 (C_q, f), 145.5 (C_q, g), 145.1 (CH, A), 131.4 (CH, NCH), 117.0 (2 x CH, C, D), 115.3 (2 x CH, C, D), 112.2 (CH, B), 112.1 (CH, E), 95.6 (C_q, h), 80.6 (C_q, i), 69.8 (CH_2, PEG), 69.8 (25 x CH_2, PEG), 69.7 (CH_2, PEG), 69.7 (CH_2, PEG), 69.7 (CH_2, PEG), 69.5 (CH_2, PEG), 68.8 (CH_2, I), 68.1 (CH_2, H), 67.6 (CH_2, G), 56.5 (CH_2, L), 52.6 (2x CH_2, M), 49.3 (2x CH_2, K), 44.4 (CH_2, F), 38.2 (CH_2, J), 27.7 (3x CH_3, N). Mp could not be determined due to the hygroscopic nature of the compound. **HRMS** (ESI-QTOF) calculated for $C_{62}H_{100}N_{10}O_{21}$ $[M+H]^+$: 1321.7086; found: 1321.7137. **Purity**: 98%.

***tert*-Butyl 1-(4-(4-(2-(5-amino-2-(furan-2-yl)-7*H*-pyrazolo[4,3-*e*][1,2,4]triazolo[1,5-*c*]pyrimidin-7-yl)ethyl)piperazin-1-yl)phenoxy)-2-oxo-6,9,12,15,18,21,24,27,30,33,36,39,42,45,48,51,54,57,60,63-icosaoxa-3-azapentahexacontan-65-oate (9)**

The reaction is performed as described for the synthesis of compound **4** from 20 mg (0.04 mmol, 1.0 eq.) of **2** and HATU (17.9 mg, 0.07 mmol, 1.2 eq.) dissolved in 500 µl of dichloromethane, and 44.5 mg (0.044 mol, 1.1 eq.) of **3f**, in the presence of 10.3 mg (0.08 mmol, 2.0 eq.) of diisopropylethylamine. The product is purified by HPLC as described for compound **4**. Yield: 52.7 mg (0.035 mmol, 88%) of product **9**.

^{1}H NMR (600 MHz, DMSO-d_6) δ [ppm]: 8.16 (s, 1H, NCH), 8.05 (bs, 2H, NH_2), 7.95 (t, $^3J_{H,H}$ = 5.82 Hz, 1H, NH), 7.93 (dd, $^3J_{H,H}$ = 1.78 Hz, $^3J_{H,H}$ = 0.77 Hz, 1H, A), 7.22 (dd, $^3J_{H,H}$ = 3.43 Hz, $^3J_{H,H}$ = 0.77 Hz, 1H, B), 6.87–6.81 (m, 4H, C+D), 6.73 (dd, $^3J_{H,H}$ = 1.76 Hz, $^3J_{H,H}$ = 3.41 Hz, 1H, E), 4.42 (t, $^3J_{H,H}$ = 6.81 Hz, 2H, F), 4.36 (s, 2H, G), 3.97 (s, 2H, H), 3.58–3.55 (m, 2H, CH_2), 3.54–3.51 (m, 2H, CH_2), 3.51–3.48 (m, 72H, 28 x CH_2), 3.44 (t, $^3J_{H,H}$ = 5.96 Hz, I), 3.28 (q, $^3J_{H,H}$ = 5.88 Hz, 2H, J), 2.98–2.94 (m, 4H, K), 2.83 (t, $^3J_{H,H}$ = 6.79 Hz, 2H, L), 2.61–2.57 (m, 4H, M), 1.42 (s, 9H, N). **^{13}C NMR** (151 MHz, DMSO-d_6) δ [ppm]: 169.3 (C_q, C_{Ester}), 168.0 (C_q, C_{Amid}), 155.4 (C_q, a), 151.2 (C_q, b), 148.7 (C_q, c), 148.6 (C_q, d), 146.2 (C_q, e), 146.0 (C_q, f), 145.5 (C_q, g), 145.1 (CH, A), 131.4 (CH, NCH), 117.0 (2 x CH, C, D), 115.3 (2 x CH, C, D), 112.2 (CH, B), 112.1 (CH, E), 95.6 (C_q, h), 80.6 (C_q, i), 69.8 (CH_2, PEG), 69.8 (33 x CH_2, PEG), 69.7 (CH_2, PEG), 69.7 (CH_2, PEG), 69.7 (CH_2, PEG), 69.5 (CH_2, PEG), 68.8 (CH_2, I), 68.1 (CH_2, H), 67.6 (CH_2, G), 56.5 (CH_2, L), 52.6 (2 x CH_2,

M), 49.3 (2 x CH_2, K), 44.4 (CH_2, F), 38.2 (CH_2, J), 27.7 (3x CH_3, N). Mp could not be determined due to the hygroscopic nature of the compound. **HRMS** (ESI-QTOF) calculated fro $C_{70}H_{116}N_{10}O_{25}$ [M+H]$^+$: 1497.8139; found: 1497.8186. **Purity**: 96%.

1-(4-(4-(2-(5-Amino-2-(furan-2-yl)-7*H*-pyrazolo[4,3-*e*][1,2,4]triazolo[1,5-*c*]pyrimidin-7-yl)ethyl)piperazin-1-yl)phenoxy)-2-oxo-6,9,12,15-tetraoxa-3-azaheptadecan-17-carboxylic acid (10)

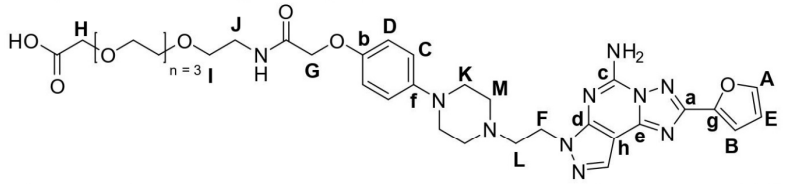

Compound **4** (8.7 mg, 0.01 mmol, 1.0 eq.) is dissolved in a mixture of trifluoroacetic acid/dichloromethane (6:4), and 25 µl of TIPS are added. The mixture is stirred for 2h at RT. Then, the solvent is removed *in vacuo*, 200 µl of acetonitrile and a few drops of trifluoroacetic acid are added until fully dissolved, and the product is purified by HPLC, applying a gradient from 50% aq. acetonitrile reaching 100% acetonitrile within 15 min, then eluting for 5 more min yielding 6.9 mg (0.0093 mmol, 93%) of carboxylic acid derivative **10**.
^{1}H NMR (600 MHz, DMSO-d_6) δ [ppm]: 8.64 (t, $^3J_{H,H}$ = 5.85 Hz, NH), 8.16 (s, 1H, NCH), 8.08 (bs, 2H, NH_2), 7.95–7.91 (m, 1H, A), 7.22 (d, $^3J_{H,H}$ = 3.37 Hz, 1H, B), 6.84–6.82 (m, 4H, C, D), 6.73 (dd, $^3J_{H,H}$ = 1.77 Hz, $^3J_{H,H}$ = 3.43 Hz, 1H, E), 4.42 (s, 2H, G), 4.42 (t, $^3J_{H,H}$ = 6.72 Hz 2H, F), 3.55 (s, 2H, H), 3.53–3.49 (m, 12H, 6 x CH_2), 3.47 (t, $^3J_{H,H}$ = 5.61 Hz, I), 3.31–3.26 (m, 2H, J), 2.98–2.93 (m, 4H, K), 2.83 (t, $^3J_{H,H}$ = 6.81 Hz, 2H, L), 2.62–2.57 (m, 4H, M). **^{13}C NMR** (151 MHz, DMSO-d_6) δ [ppm]: 171.8 (C_q, C_{acid}), 168.0 C_q, C_{amide}), 155.3 (C_q, a), 151.2 (C_q, b), 148.7 (C_q, c), 148.6 (C_q, d), 146.2 (C_q, e), 145.9 (C_q, f), 145.5 (C_q, g), 145.1 (CH, A), 131.4 (CH, NCH), 117.0 (2 x CH, C, D), 115.3 (2 x CH, C, D), 112.2 (CH, B), 112.1 (CH, E), 95.6 (C_q, h), 69.7 (2 x CH_2), 69.7 (CH_2), 69.6 (CH_2), 69.5 (2 x CH_2), 68.8 (CH_2), 68.4 (CH_2), 67.5 (CH_2, G), 56.5 (CH_2, L), 52.6 (2 x CH_2, M), 49.3 (2 x CH_2, K), 44.4 (CH_2, F), 38.2 (CH_2, J). **Mp**: 183.2–183.3 °C**. HRMS** (ESI-QTOF) calculated for $C_{34}H_{45}N_{10}O_9$ [M+H]$^+$: 737.3365; found: 737.3360. **Purity**: 99%.

14-(2-(4-(4-(2-(5-Amino-2-(furan-2-yl)-7*H*-pyrazolo[4,3-*e*][1,2,4]triazolo[1,5-*c*]pyrimidin-7-yl)ethyl)piperazin-1-yl)phenoxy)acetamido)-*N*-(5-(5,5-difluoro-1,3,7,9-tetramethyl-5*H*-4*l*4,5*l*4-dipyrrolo[1,2-*c*:2',1'-*f*][1,3,2]diazaborinin-10-yl)pentyl)-3,6,9,12-tetraoxatetradecanamide (11, PSB-2115)

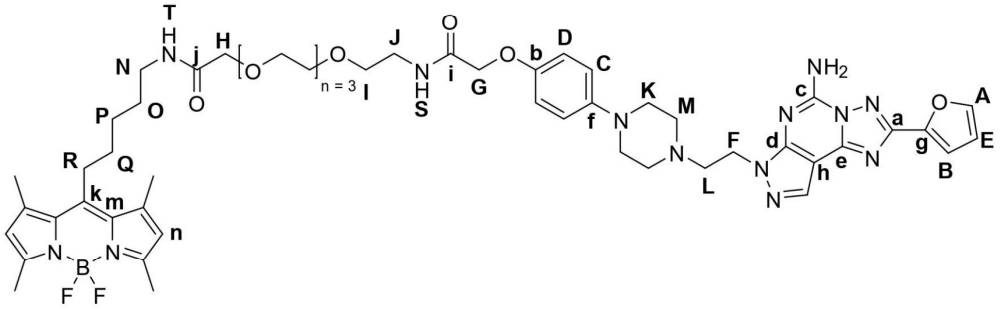

Carboxylic acid derivative **10** (7.4 mg, 0.01 mmol, 1.0 eq.) is dissolved in 0.2 ml of dichloromethane, and HATU (4.6 mg, 0.012 mmol, 1.2 eq.) is added. In a separate vial, the aminopentyl-substituted BODIPY derivative (8-(5-aminopentyl)-4,4-difluoro-1,3,5,7-tetramethyl-4-bora-3a,4a-diaza-*s*-indacene, 5 mg, 0.015 mmol, 1.1 eq.), synthesized as previously described[1], was dissolved in 0.2 ml of dichloromethane, and diisopropylethylamine (2.6 mg, 0.02 mmol, 2.0 eq.) was added. After 5 min of pre-activation of carboxylic acid **10**, the solution of the amino-substituted BODIPY derivative is added, and the mixture is stirred at RT for 12h. The product is purified by
^{1}H NMR (600 MHz, DMSO-d_6) δ [ppm]: 8.16 (s, 1H, NCH), 8.05 (bs, 2H, NH_2), 7.94 (t, $^3J_{H,H}$ = 4.59 Hz, 1H, S), 7.95–7.91 (m, 1H, A), 7.64 (t, $^3J_{H,H}$ = 5.76 Hz, 1H, T), 7.22 (d, $^3J_{H,H}$ = 3.31 Hz, 1H, B), 6.87–6.80 (m, 4H, C, D), 6.72 (dd, $^3J_{H,H}$ = 1.80 Hz, $^3J_{H,H}$ = 3.43 Hz, 1H, E), 6.21 (s, 2H, n), 4.41 (t, $^3J_{H,H}$ = 6.72 Hz, 2H, F), 4.35 (s, 2H, G), 3.85 (s, 2H, H), 3.57–3.45 (m, 12H, 6 x CH_2), 3.42 (t, $^3J_{H,H}$ = 6.01 Hz, I), 3.27 (dt, $^3J_{H,H}$ = 6.01 Hz, $^3J_{H,H}$ = 6.01 Hz, 2H, J), 3.12 (dt, $^3J_{H,H}$ = 6.58 Hz, $^3J_{H,H}$ = 6.58 Hz, 2H, N), 2.98–2.93 (m, 4H, K), 2.94–2.89 (m, 2H, R), 2.86–2.80 (m, 2H, L), 2.62–2.56 (m, 4H, M), 2.39 (s, 6H, 2 x CH_3), 2.39 (s, 6H, 2 x CH_3), 1.59–1.52 (m, 2H, Q), 1.52–1.47 (m, 2H, O) 1.47–1.41 (m, 2H, P). **^{13}C NMR** (151 MHz, DMSO-d_6) δ [ppm]: 169.1 (C_q, j), 168.0 (C_q, i), 155.4 (C_q, a), 153.0 (2 x C_q, C_{BODIPY}), 151.2 (C_q, b), 148.7 (C_q, e), 148.6 (C_q, d), 146.7 (C_q, k), 146.3 (C_q, c), 146.0 (C_q, f), 145.5 (C_q, g), 145.1 (CH, A), 140.8 (2 x C_q, C_{BODIPY}), 131.4 (CH, NCH), 130.7 (2 x C_q, m), 121.7 (2 x CH, n), 117.1 (2 x CH, C, D), 115.3 (2 x CH, C, D), 112.3 (CH, B), 112.1 (CH, E), 95.7 (C_q, h), 70.2 (CH_2), 70.0 (CH_2, H), 69.8 (CH_2), 69.7 (CH_2), 69.5 (CH_2), 68.8 (CH_2, I), 67.6 (CH_2, G), 56.5 (CH_2, L), 52.6 (2 x CH_2, M), 49.3 (2 x CH_2, K), 44.4 (CH_2, F), 38.2 (CH_2, J), 37.8 (CH_2, N), 31.1 (CH_2, Q), 28.8 (CH_2, O), 27.8 (CH_2, R), 27.0 (CH_2, P), 15.8 (2 x CH_3), 14.1 (2 x CH_3). Mp: 171 °C (decomposition). **HRMS** (ESI-QTOF) calculated for $C_{52}H_{68}BF_2N_{13}O_8$ [M+H]$^+$: 1052.5456; found: 1052.5324. Purity: 95%. Absorption/emission: 498 nm / 508 nm.

1.2 Expression of A_{2A}AR constructs in Sf9 insect cells

Sf9 insect cells (Expression Systems) were cultured in ESF921 cell culture medium (Expression Systems) at 27 °C and were frequently tested negative for mycoplasma contamination (PCR-test, in-house). A_{2A}AR constructs were expressed utilizing a baculoviral expression system (Bac-to-Bac, ThermoFisher). For this purpose, the DNA sequence encoding for the wt A_{2A}AR and the A_{2A}-ΔC construct (comprising A_{2A}AR residues 2-316) was cloned into a modified pFastBac1 vector (ThermoFisher) that has its original polyhedrin promoter substituted with a GP64 promoter (GP64-pFastBac1).[2] The overall expression cassette is identical to previously described A_{2A}AR crystallization constructs[3] including an *N*-terminal auto-cleavable influenza hemagglutinin (HA) signal sequence[4] followed by a FLAG-tag and a *C*-terminal deca-histidine tag. The *C*-terminal histidine tag is not present in the wt A_{2A}AR plasmid. For A_{2A}-ΔC-bRIL, the third intracellular loop (residues 209-218) of A_{2A}-ΔC was substituted with a thermostabilized apocytochrome bRIL.[5] The S91$^{3.39}$K point mutation was introduced using site-directed mutagenesis to create A_{2A}-PSB1-bRIL and A_{2A}-PSB1. The DNA sequence encoding for the A_{2A}-StaR2-bRIL[6] comprising nine point mutations (A54$^{2.42}$L, T88$^{3.36}$A, R107$^{3.55}$A, K122$^{4.43}$A, N154^{ECL2}A, L202$^{5.63}$A, L235$^{6.37}$A, V239$^{6.41}$A, S277$^{7.42}$A) was gene-synthesized by BioCat and subcloned into the same GP64-pFastBac1 vector.
The final plasmids were transfected into Sf9 insect cells at a cell density of 1.0 mio cells per ml as previously described [7] to generate the initial P0 virus. 400 µl of the P0 viral solutions were used to infect 40 ml of Sf9 insect cells at a density of 2.0-3.0 mio cells per ml following incubation at 27 °C for 48 h at 140 revolutions per minute. Both, the P1 virus and cells expressing the different A_{2A}AR constructs were harvested by centrifugation. Proteins purified from these cells were used to assess protein stability. For upscaling, 6 ml of P1 viruses were used to infect 900 ml of Sf9 insect cells at a density of 2.0-3.0 mio cells per ml following incubation at 27 °C for 48 h at 140 revolutions per minute. Cells were harvested by centrifugation, washed with phosphate-buffered saline (PBS) and stored at -80 °C for further use.

1.3 Protein purification for crystallization experiments

Protein purification for crystallization experiments was performed according to previously described procedures.[3] Sf9 insect cells from 900 ml infected cell culture were lyzed by osmotic shock in low osmotic buffer [10 mM HEPES pH 7.5, 10 mM $MgCl_2$, 20 mM KCl and EDTA-free cOmplete protease inhibitor cocktail (Roche)] using a dounce homogenizer and washed repeatedly using a high osmotic buffer that is identical to the low osmotic buffer but with the addition of 1 M NaCl. Membranes were finally resuspended in 50 ml resuspension buffer [10 mM HEPES pH 7.5, 10 mM $MgCl_2$, 20 mM KCl, 30% (v/v) glycerol] and stored at -80 °C for further use. Purified membranes corresponding to a volume of 25 ml were incubated with 4 mM theophylline and 2 mg per ml iodoacetamide for 60 min. The A_{2A}AR was then solubilized using an equal volume of solubilization buffer I [100 mM HEPES pH 7.5, 1.6 M NaCl, 1.0 % (w/v) dodecyl-β-d-maltopyranoside (DDM) and 0.2% (w/v) cholesteryl hemisuccinate (CHS)] over 3 h while shaking (end-over-end) at 4 °C. Solubilized proteins were separated from insoluble material by centrifugation at 48,000 g. The supernatant was supplemented with 20 mM imidazole (aqueous solution pH 7.5) and 500 µl of a pre-washed cobalt-based immobilized metal affinity chromatography (IMAC) medium (TALON Superflow, cytiva) following overnight incubation at 4 °C. In order to remove protein impurities and to exchange the low affinity A_{2A}AR antagonist theophylline for PSB-2113 or PSB-2115, the IMAC medium was washed with 30 column volumes (CVs) of wash buffer I [50 mM HEPES pH 7.5, 800 mM NaCl, 0.5 % (w/v) DDM, 0.1% (w/v) CHS, 10% (v/v) glycerol, 20 mM imidazole pH 7.5, 8 mM adenosine triphosphate (ATP), 10 mM $MgCl_2$, and 50 µM PSB-2113 or 50 µM PSB-2115] and 20 CVs of wash buffer II [50 mM HEPES pH 7.5, 800 mM NaCl, 0.05 % (w/v) DDM, 0.01% (w/v) CHS, 10% (v/v) glycerol, 50 mM imidazole pH 7.5, and 50 µM PSB-2113 or 50 µM PSB-2115]. A_{2A}-PSB1-bRIL-PSB-2113 and A_{2A}-PSB1-bRIL-PSB-2115 complexes were eluted from the column using 4 CVs elution buffer [25 mM HEPES pH 7.5, 800 mM NaCl, 10% (v/v) glycerol, 220 mM imidazole, 0.025 % (w/v) DDM, 0.005% (w/v) CHS, and 25 µM PSB-2113 or 25 µM PSB-2115]. The purified receptor complex was concentrated to volume of 20-30 µl using 100 kDa cut-off Vivaspin concentrators (Sartorius). The protein was immediately used for crystallization experiments while protein purity, monodispersity and thermostability were assessed using analytical size-exclusion chromatography, sodium dodecyl sulfate polyacrylamide gel electrophoresis (SDS-PAGE) and a thermal shift assay, respectively.

1.4 Protein purification for stability screening

A_{2A}ARs from 40 ml of Sf9 insect cell culture were purified accordingly but with minor modifications. Cells were lyzed by osmotic shock in low osmotic buffer and washed once with high osmotic buffer. Purified membranes were resuspended in 3 ml resuspension buffer and stored at -80 °C until further use. Prior to solubilization, membranes were incubated with 2 mg per ml iodoacetamide for 30 min at 4 °C. No ligand was added during purification so that the A_{2A}ARs were obtained in their APO state. Solubilization was performed using an equal volume of solubilization buffer II [100 mM HEPES pH 7.5, 1.6 M NaCl, 2.0 % (w/v) DDM and 0.4% (w/v) CHS] over the time course of 3 h while shaking (end-over-end) at 4 °C. Solubilized proteins were obtained by centrifugation at 14,000 g. The supernatant was supplemented with 20 mM imidazole pH 7.5 and 12.5 µl cobalt-based IMAC medium (TALON Superflow, cytiva) following overnight incubation at 4 °C. The IMAC medium was washed with 60 CVs of ligand-free wash buffer I (without the addition of ATP and $MgCl_2$) and 40 CVs of ligand-free wash buffer II. Finally, the proteins were eluted using 10 CVs of ligand-free elution buffer without further protein concentration. The protein was used directly for analytical size-exclusion chromatography, SDS-PAGE and thermal shift assays.

1.5 Thermal shift assay

The thermostability of different A_{2A}AR protein preparations was determined as previously described[8] using the thiol-specific fluorescent dye *N*-[4-(7-diethylamino-4-methyl-3-coumarinyl)phenyl]maleimide (CPM). Briefly, CPM (final concentration 2 µg per ml) was incubated for 10 min with an appropriate amount of protein in a buffer consisting of 25 mM HEPES pH 7.5, 500 mM NaCl, 2% (v/v) glycerol, 0.05% (w/v), 0.01% (w/v) CHS and the tested A_{2A}AR ligand (ligand stock solutions were prepared at a concentration of 1 mM in DMSO) or control. The protein thermostability was assessed on a Rotor-Gene Q real-time PCR cycler (Qiagen) using the excitation wavelength of 365 ± 20 nm and the detection wavelength of 460 ± 20 nm. Data was collected over a temperature range of 30 °C to 90 °C with a ramp of 1 °C per min and a fluorescence gain of 1. The T_M values were calculated from the turning point of the non-linear regression (Boltzmann sigmoidal fit) in GraphPad Prism 7.0 after subtraction of a respective buffer control value. Thermostability data was obtained from at least three independent measurements.

1.6 Crystallization

The purified and concentrated A_{2A}-PSB1-bRIL-PSB-2113 and A_{2A}-PSB1-bRIL-PSB-2115 complexes were reconstituted into LCP by mixing the protein with a molten lipid mixture [90% (w/v) 1-oleoyl-*rac*-glycerin (Sigma), 10 % (w/v) cholesterol (Sigma)] in a 2 to 3 ratio using the two-syringe method.[9] An automatic crystallization robot (Formulatrix NT8) was used to perform crystallization experiments by overlaying 50 nl mesophase with 0.8 nl precipitant solution on 96-well glass sandwich plates (Marienfeld). The crystallization plates were stored at 20 °C and automatically imaged using a crystallization plate imager (Formulatrix RockImager 54). Diffraction quality crystals grew under the following precipitant condition: 24% (v/v) PEG-400 (polyethylene glycol 400, average molecular weight 400, Hampton Research), 10-30 mM sodium thiocyanate (Hampton Research), 100 mM sodium citrate pH 5.2 (Hampton Research), and 2% (v/v) 2,5-hexanediol (Molecular Dimensions). Crystals were harvested using 50-100 µm Micromounts (MiTeGen) and were directly flash-frozen in liquid nitrogen without further cryoprotection.

1.7 Data collection and structure determination

X-ray diffraction data were collected on the P11-high-throughput-MX beam line at PETRA III, Hamburg, Germany. Data were collected at 100 K using a microfocused beam (20 × 20 µm^2) of ~12.0 keV (1.0332 Å) with 1 % transmission at a rate of 100 ms per frame and an oscillation-range of 0.1°. Data were collected until 1.8 Å and 2.5 Å for the A_{2A}-PSB1-bRIL-PSB-2113 and A_{2A}-PSB1-bRIL-PSB-2115 crystals, respectively. XDS, XSCALE and XDSCONV[10] were used for data processing (see **Table S2** for details). The PSB-2113 structure was determined by phenix.phaser [11] using the previously solved A_{2A}-ΔC-bRIL structure[3] as a model (PDB 4EIY) (translation function Z score (TFZ) - 67.0 and log-likelihood gain (LLG) - 9667.819). The PSB-2115 structure was determined similarly (TFZ - 61.2 and LLG - 6257.201), but instead using the A_{2A}-PSB1-bRIL-PSB-2113 coordinates as the search model. Each model went through phenix.autobuild[12] once, which included density modification, iterative-model building and refinement. Then, each model was built with respective ligands (PSB-2113 and PSB-2115) and other components like cholesterol hemisuccinate, monoolein and PEG using COOT.[13] The newly determined protein structures were consistent with the published PDB 4EIY structure, the RMSD being 0.28 Å. For the ligands, well-defined electron densities were observed within the orthosteric binding site, while no significant electron density was observed for the fluorophores and the connecting flexible PEG linker. The refined structures of the PSB-2113 and PSB-2115 complexes showed good agreement with the obtained data (R_{work} / R_{free} ratios of 0.190 / 0.235 and 0.187 / 0.245 (2.6 Å), respectively). Detailed refinement statistics are reported in **Table S2**.

1.8 Radioligand binding assays

Radioligand binding assays were performed on Sf9 insect cell and CHO-S cell membranes. Sf9 membrane preparations were obtained from 40 ml of baculovirus infected Sf9 insect cells using a dounce homogenizer with one step low osmotic buffer and one step high osmotic buffer as described above, but resuspended in the following resuspension buffer: 10 mM HEPES pH 7.5, 10 mM $MgCl_2$, 20 mM KCl. CHO-S cells were disrupted in a buffer consisting of 50 mM tris(hydroxymethyl)aminomethane (Tris) pH 7.4 and 2 mM EDTA using an Ultra-Turrax homogenizer and cell membranes were resuspended in a 50 mM Tris pH 7.4 buffer. Total protein concentrations were determined using a Bradford assay[14] with bovine serum albumin (BSA) as a reference, and 15 µg of protein per well was used in the radioligand binding experiments. Competition binding experiments to determine the affinity (K_i) of A_{2A}AR ligands were performed using the A_{2A}AR-selective antagonist radioligand [^{3}H]MSX-2 (specific activity 85 Ci per mmol, final concentration 1 nM)[15] in a buffer consisting of 50 mM Tris buffer pH 7.4 (supplemented with 2 U per ml adenosine desaminase). Nonspecific binding was determined in the presence of 10 µM CGS15943, and total binding was determined in the presence of DMSO. The assays were incubated for 30 min at RT followed by filtration through GF/B glass fiber filters (Whatman) using a 48-well harvester (Brandel). Filters were pre-incubated for 30 to 60 min in a solution of 0.3 % (w/v) polyethylenimine to reduce nonspecific binding. After harvesting, filters were washed with ice-cold Tris buffer (50 mM Tris, pH 7.4), transferred into scintillation vials, and incubated with 2.5 ml of scintillation cocktail (ProSafe FC plus) for 6 h. Subsequently, the radioactivity was determined on a liquid scintillation counter (Tricarb 2810TR, Perkin Elmer, efficiency of 53%). At least three independent experiments were performed. Homologous competition with unlabeled MSX-2 was

performed to determine the equilibrium dissociation constant (K_d) of each A_{2A}AR construct. K_i values of A_{2A}AR antagonists and agonists were calculated using the Cheng-Prusoff equation (GraphPad Prism 7.0).

1.9 TRUPATH assay

Human embryonic kidney 293 (HEK293) cells were cultured at 37° C and 5% CO_2 in Dulbecco's modified eagle's medium (DMEM) supplemented with 10% (v/v) fetal bovine serum (FBS), 100 U penicillin per ml, and 100 µg streptomycin per ml. Repeated in-house PCR tests confirmed the cells to be free of mycoplasma contamination.

The TRUPATH bioluminescence resonance energy transfer (BRET) assay was conducted with minor variations to the originally published protocol.[16] TRUPATH biosensors were a gift from Bryan Roth (Addgene kit #1000000163). On the first day, HEK293 cells were detached from the flask with trypsin and seeded into 6-well plates at a density of 10^6 cells per well in 2 ml DMEM. After 2 h, the cells were transiently transfected with the biosensors and the GPCR of interest. For this purpose, the A_{2A}AR constructs with or without bRIL fusion protein were PCR-amplified without *N*-terminal HA- and *C*-terminal His-tags and subcloned into pcDNA3.1(+) using BamHI and EcoRI. For each well, 3 µl lipofectamine 2000 (ThermoFisher) per µg DNA were mixed with OptiMEM medium (ThermoFisher) to a volume of 250 µl per well and then incubated for 10 min at RT. Then, the lipofectamine solution was mixed with an equal volume of OptiMEM-DNA mixture (100 ng of each pcDNA5/FRT/To-$G\alpha_{s\text{-}short}$-RLuc8, pcDNA3.1-$G\beta_3$, pcDNA3.1-$G\gamma_9$-GFP2, and pcDNA3.1-FLAG-GPCR) and incubated for 30 min at RT. The mixture was added to the cells following overnight incubation. The next day, the cells were detached from the 6-well plate by pipetting and were seeded into a white-bottom 96-well plate (Greiner BioOne) at a density of 30,000 cells per well. After 24 h, the cells were washed with assay buffer (Hank's balanced salt solution (ThermoFisher) plus 20 mM HEPES pH 7.4). Then, 60 µl of assay buffer supplemented with 1000 U per ml of adenosine desaminase (Roche) and 10 µl of luciferase substrate (50 µM coelenterazine 400a (Biomol) in assay buffer) was added to the cells and incubated for another 5 min. Agonist solution (30 µl, 1% final DMSO concentration) was added and the BRET measurement was started in a Mithras LB940 plate reader after 5 min (RLuc8 emission at 395 nm, GFP2 emission at 510 nm). The BRET2 ratio was calculated by division of the GFP2 signal by the RLuc8 signal. Data analysis was performed by means of GraphPad PRISM 8.0. netBRET values were calculated by subtraction of buffer control BRET2 ratio from the BRET2 ratio of each data point. Concentration-response curves were then fitted by a sigmoidal dose-response curve with variable slope (four parameters) to yield EC_{50} and E_{max} values. Data was obtained in at least three independent experiments performed in duplicate.

1.10 Synthesis of carboxy-functionalized Preladenant analog 2

The synthesis of the precursor **2** is depicted in **Scheme S1** below.

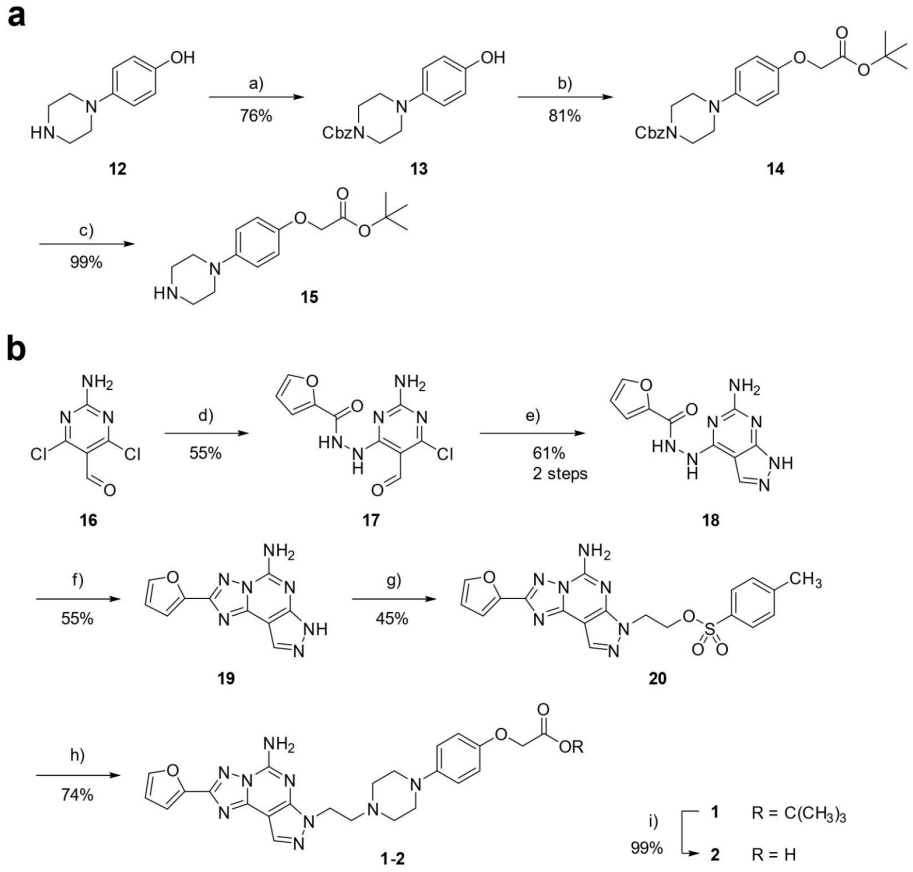

Scheme S1. a Synthesis of the piperazine adduct **15**. **b** Synthesis of the carboxy-functionalized Preladenant derivative **2**.
Reaction conditions: a) CbzCl, MeOH, RT, 12h. b) *tert*-butyl bromoacetate, K_2CO_3, acetone, RT, 12 h. c) 10% Pd/C, H_2, MeOH, RT, 2h. d) 2-Furoic acid hydrazide, NEt_3, DMSO, 120 °C, 18 h. e) N_2H_4, CH_3CN, 70 °C, 1h. f) BSA, HMDS, 120 °C, 3h. g) Ethylene glycol ditosylate, NaH, DMF, RT, 4h. h) **4**, DMF, 80 °C, 20h. i) trifluoroacetic acid, CH_2Cl_2, RT, 1h.

1.10.1 Synthesis of the side-chain (a)

Benzyl 4-(4-hydroxyphenyl)piperazine-1-carboxylate (13)

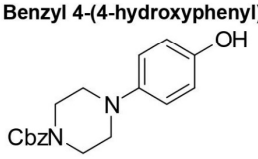

4-(Piperazin-1-yl)phenol (**12**, 500 mg, 2.8 mmol, 1.0 eq.) is dissolved in 2.8 ml of methanol, and benzyl chloroformate (402 µl, 2.8 mmol, 1.0 eq.) is added dropwise. The reaction mixture is stirred for 12h at RT. Then, the solvent is removed *in vacuo*, and the residue is dissolved in 50 ml of a saturated aq. $NaHCO_3$ solution. After extraction with ethyl acetate (3 x 50 ml) the united organic phases are dried over $MgSO_4$, and the solvent is subsequently removed *in vacuo*. The product is purified by column chromatography on silica gel with dichloromethane/methanol (95:5) yielding 661 mg (2.1 mmol) of **13** (yield: 76 %).
^{1}H NMR (500 MHz, DMSO-d_6) δ [ppm]: 8.85 (s, 1H, OH), 7.42–7.28 (m, 5H, H_{Cbz}), 6.85–6.75 (m, 2H, $H_{arom.}$), 6.70–6.61 (m, 2H, $H_{arom.}$), 5.10 (s, 2H, H_{Cbz}), 3.59–3.45 (m, 4H, $H_{Piperazin}$), 2.94–2.89 (m, 4H, $H_{Piperazin}$). **^{13}C NMR** (126 MHz, DMSO-d_6) δ [ppm] = 154.4 (C_q, CO), 151.4 (C_q, COH), 144.0 (C_q, NC), 136.9 (C_q, C_{Cbz}), 128.4 (2x CH, C_{Cbz}), 127.8 (C_q, C_{Cbz}), 127.5 (2x CH, C_{Cbz}), 118.5 (C_q, $C_{arom.}$), 115.5 (C_q, $C_{arom.}$), 66.2 (CH_2, C_{Cbz}), 50.2 (2x CH_2, $C_{Piperazin}$), 43.6 (2x CH_2, $C_{Piperazin}$). **LC-MS**: 313.2 ([M+H]$^+$). **Purity**: 95%.

Benzyl 4-(4-(2-(*tert*-butoxy)-2-oxoethoxy)phenyl)piperazine-1-carboxylate (14)

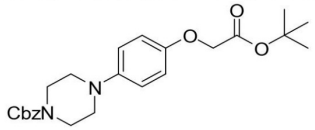

Compound **13** (100 mg, 0.32 mmol, 1.0 eq.) is dissolved in acetone (500 µl), and K_2CO_3 (49 mg, 0.35 mmol, 1.1 eq.) und *tert*-butyl bromoacetate (62 mg, 0.32 mmol, 1.0 eq.) are added under an atmosphere of argon. After a reaction time of 12 h at RT, the solvent is removed *in vacuo*, and the residue is dissolved in 5 ml of water, and subsequently extracted with ethyl acetate (3 x 20 ml). The united organic phases are dried over $MgSO_4$, and the solvent is subsequently removed *in vacuo*. The product is purified by column chromatography on silica gel with dichloromethane/methanol (97:3) yielding 110 mg (2.6 mmol) of **14** (yield: 81 %).
^{1}H NMR (500 MHz, DMSO-d_6) δ [ppm]: 7.40–7.30 (m, 5H, H_{Cbz}), 6.93–6.87 (m, 2H, $H_{arom.}$), 6.84–6.76 (m, 2H, $H_{arom.}$), 5.10 (s, 2H, H_{Cbz}), 4.54 (s, 2H, CH_2), 3.58–3.48 (m, 4H, $H_{Piperazin}$), 3.02–2.95 (m, 4H, $H_{Piperazin}$), 1.42 (s, 9H, 3x CH_3). **^{13}C NMR** (126 MHz, DMSO-d_6) δ [ppm] = 168.1 (C_q, $CO_{t\text{-Butylester}}$), 154.4 (C_q, CO_{Cbz}), 151.7 (C_q, C_{Ether}), 145.6 (C_q, CN), 136.8 (C_q, C_{Cbz}), 128.4 (2x CH, C_{Cbz}), 127.8 (C_q, C_{Cbz}), 127.5 (2x CH, C_{Cbz}), 117.8 (C_q, $C_{arom.}$), 115.0 (C_q, $C_{arom.}$), 81.2 (C_q, $C(CH_3)_3$), 66.2 (CH_2, C_{Cbz}), 65.5 (CH_2), 49.6 (2x CH_2, $C_{Piperazin}$), 43.4 (2x CH_2, $C_{Piperazin}$), 27.7 (3x CH_3). **LC-MS**: 427.2 ([M+H]$^+$). **Purity**: 98%.

***tert*-Butyl 2-(4-(piperazin-1-yl)phenoxy)acetate (15)**

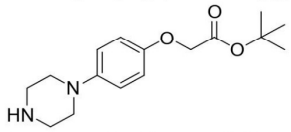

Compound **14** (100 mg, 0.23 mmol, 1.0 eq.) is dissolved in methanol (1 ml). Under an atmosphere of argon (using an argon-filled ballon), 10% Pd/C (10 mg) is added. Then, the argon atmosphere is replaced by an atmosphere of hydrogen gas (H_2) again using a balloon (a T-connector is used for switching between the two gas-containing balloons), and the solution is stirred for 2h at RT. The solution is filtered over Celite®, and the solvent is removed *in vacuo*. The product is obtained in 99% yield (67 mg, 0.23 mmol).
^{1}H NMR (600 MHz, DMSO-d_6) δ [ppm]: 6.88–6.82 (m, 2H, $H_{arom.}$), 6.80–6.75 (m, 2H, $H_{arom.}$), 4.53 (s, 2H), 2.95–2.91 (m, 4H, $H_{piperazine}$), 2.86–2.81 (m, 4H, $H_{piperazine}$), 1.42 (s, 9H, 3 x CH_3). **^{13}C NMR** (151 MHz, DMSO-d_6) δ [ppm] = 168.2 (C_q, $CO_{t\text{-Butylester}}$), 151.1 (C_q, C_{Ether}), 146.4 (C_q, CN), 117.1 (C_q, $C_{arom.}$), 115.0 (C_q, $C_{arom.}$), 81.2 (C_q, $C(CH_3)_3$), 65.5 (CH_2), 50.3 (2x CH_2, $C_{piperazine}$), 45.5 (2 x CH_2, $C_{piperazine}$), 27.7 (3 x CH_3). **LC-MS**: 293.0 ([M+H]$^+$). **Purity**: 97%.

1.10.2 Synthesis of the tricyclic Preladenant core (19) and attachment of the side chain yielding the functionalized Preladenant derivative 2 (b)

(*E*/*Z*)-*N*'-(6-Chloro-5-formyl-2-imino-2,3-dihydropyrimidin-4(1*H*)-ylidene)furan-2-carbohydrazide (17)[17]

2-Amino-4,6-dichloropyrimidine-5-carbaldehyde (**16**, 1,0 g, 5.2 mmol, 1 eq.) is dissolved in 40 ml of THF, and furane-2-carbonic acid hydrazide (730 mg, 5.72 mmol, 1.1 eq.) and triethylamine (526 mg, 5.2 mmol, 1 eq.) are added under an atmosphere of argon. After 2 h of heating under reflux, the solvent is removed *in vacuo*, and water is added (20 ml). The aqueous solution is extracted with EtOAc (5 x 20 ml), and the united organic phases are dried over $MgSO_4$. After filtration, the solvent is removed *in vacuo*. The remaining solid is recrystallized from methanol/diethyl ether (8:1) yielding 811 mg (2.9 mmol, 55%) of **17** (lit. yield: 82% [17]).
^{1}H NMR (500 MHz, DMSO-d_6) δ [ppm]: 10.64 (s, 1H), 10.38 (s, 1H), 9.97 (s, 1H, $H_{aldehyde}$), 7.92–7.90 (m, 1H, H_{furane}), 7.88 (s, 1H), 7.85 (s, 1H), 7.25 (d, $^3J_{H,H}$ = 3.54 Hz, 1H, H_{furane}), 6.67 (dd, $^3J_{H,H}$ = 1.76 Hz, $^3J_{H,H}$ = 3.48 Hz, 1H, H_{furane}). **^{13}C NMR** (126 MHz, DMSO-d_6) δ [ppm] = 187.5 (CH, $C_{aldehyde}$), 165.0 (Cq), 163.0 (Cq), 162.5 (Cq), 156.5 (Cq), 146.0 (Cq), 145.7 (CH, C_{furane}), 114.9 (CH, C_{furane}), 111.9 (CH, C_{furane}), 100.8 (Cq). **LC-MS**: positive [*m*/*z*] = 282.1 ([M+H]$^+$). **Purity**: 98%.

***N*'-(6-Amino-1*H*-pyrazolo[3,4-*d*]pyrimidin-4-yl)furane-2-carbohydrazide (18)**

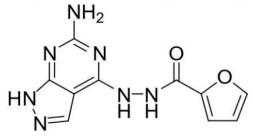

Compound **17** (0.5 g, 1.7 mmol, 1.0 eq.) is dissolved in 25 ml of acetonitrile, heated to 70 °C, and hydrazine (80% aqueous solution, 323 mg, 5.1 mmol, 3.0 eq.) is added. After 1 h of heating under reflux, the resulting solid is filtered off and washed with acetonitrile (ca. 25 ml) yielding 250 mg (0.96 mmol, 57%) of **18** (lit. yield: 83%[17]).
^{1}H NMR/^{13}C NMR in 2M-DCl/DMSO-d_6: signals for 3 tautomers are observed which cannot be unambigously assigned. **LC-MS**: positive [*m*/*z*] = 260.2 ([M+H]$^+$). **Purity**: 99%.

5-Amino-2-(furan-2-yl)-7*H*-pyrazolo[4,3-*e*][1,2,4]triazolo[1,5-*c*]pyrimidine (19)

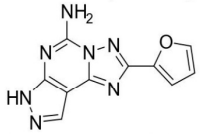

Compound **18** (200 mg, 0.77 mmol, 1 eq.), *N*,*O*-bis(trimethylsilyl)acetamide (1.08 g, 5.3 mmol, 6.8 eq.) and hexamethyldisilazane (2.85 g, 17.7 mmol, 23 eq.) are heated under an atmosphere of argon at 120 °C for 3h. The residue is suspended in hot water and filtered. The residue is recrystallized from 80% aqueous acetic acid yielding 94 mg (0.4 mmol, 51 % yield) of **19** (lit. yield 67% [17]).
^{1}H NMR (600 MHz, DMSO-d_6) δ [ppm]: 13.37 (bs, 1H, NH), 8.14 (bs, 1H, NCH), 7.94–7.93 (m, 1H, H_{Furan}), 7.92 (bs, 2H, NH_2) 7.22 (d, $^3J_{H,H}$ = 3.31 Hz, 1H, H_{Furan}), 6.73 (dd, $^3J_{H,H}$ = 1.73, $^3J_{H,H}$ = 3.38 Hz, 1H, H_{Furan}). **^{13}C NMR** (151 MHz, DMSO-d_6) δ [ppm] =155.2 (C_q), 150.2 (C_q), 148.7 (C_q), 146.2 (C_q), 145.6 (CH, C_{furane}), 145.0 (CH, C_{furane}), 132.4 (CH, NCH), 112.1 (CH, C_{furane}), 112.1 (CH, C_{furane}), 95.4 (C_q). **LC-MS**: positive [*m*/*z*] = 242.1 ([M+H]$^+$). **Purity**: 99%.

2-(5-Amino-2-(furan-2-yl)-7*H*-pyrazolo[4,3-*e*][1,2,4]triazolo[1,5-*c*]pyrimidin-7-yl)ethyl 4-methylbenzenesulfonate (20)[18]

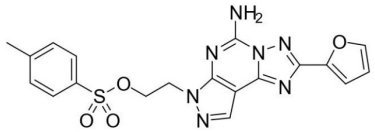

Compound **19** (50 mg, 0.21 mmol, 1.0 eq.) is dissolved in DMF (252 µl) under an atmosphere of argon, and NaH (10 mg, 0.25 mmol, 1.2 eq.), followed by ethylene di(*p*-toluenesulfonate) (95,5 mg, 0.25 mmol, 1.2 eq.), and the mixture is stirred for 4h at RT. The solvent is removed *in vacuo*, and the remaining solid is purified by flash chromatography on silica gel, applying a gradient from 99% dichloromethane/1% methanol to 95% dichloromethane/5% methanol within 20 min, yielding 42 mg (0.1 mmol, 45% yield) of **20**.
^{1}H NMR (600 MHz, DMSO-d_6) δ [ppm]: 8.11–8.00 (bs, 2H, NH_2), 8.04 (s, 1H, NCH), 7.97–7.94 (m, 1H, H_{furane}), 7.43–7.38 (m, 2H, $H_{arom.}$), 7.25 (d, $^3J_{H,H}$ = 3.36 Hz, 1H, H_{furane}), 7.11–7.07 (m, 2H, $H_{arom.}$), 6.74 (dd, $^3J_{H,H}$ = 1.77 Hz, $^3J_{H,H}$ = 3.38 Hz, 1H, H_{furane}), 4.55–4.52 (m, 2H, OCH_2), 4.51–4.47 (m, 2H, NCH_2), 2.13 (s, 3H, CH_3). **^{13}C NMR** (151 MHz, DMSO-d_6) δ [ppm] = 155.4 (C_q), 148.6 (C_q), 148.5 (C_q), 146.2 (C_q), 145.5 (C_q, C_{Furan}), 145.2 (CH, C_{furane}), 144.5 (C_q, C_{tosyl}), 131.7 (CH, NCH), 131.7 (C_q, C_{tosyl}), 129.4 (2 x CH_2, $C_{arom.}$), 127.1 (2 x CH_2, $C_{arom.}$), 112.3 (CH, C_{furane}), 112.1 (CH, C_{furane}), 95.9 (C_q), 68.1 (CH_2, OCH_2), 46.0 (CH_2, NCH_2), 20.8 (CH_3, C_{methyl}). **LC-MS**: positive [*m*/*z*] = 440.2 ([M+H]$^+$). **Purity**: 98%.

***tert*-Butyl 2-(4-(4-(2-(5-amino-2-furan-2-yl)-7*H*-pyrazolo[4,3-*e*][1,2,4]triazolo[1,5-*c*]pyrimidin-7-yl)ethyl)piperazin)-1-yl)phenoxy)acetate (1)**

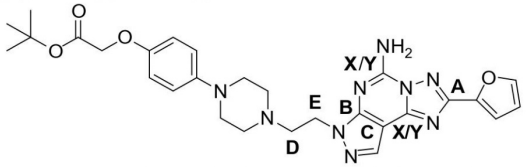

Compound **20** (39 mg, 0.09 mol, 1.0 eq.) is dissolved in DMF (504 µl) under an atmosphere of argon, and *tert*-butyl 2-(4-piperazin-1-yl)phenoxy)acetate (52 mg, 0.18 mmol, 2.0 eq.) is added. After 20h of stirring at 80 °C the solvent is removed *in vacuo*, and the product is purified by flash chromatography as described for compound 20 (the same gradient is run, however within 25 min). Yielding 24 mg (0.04 mmol) of **1** (yield: 48 %).
^{1}H NMR (600 MHz, DMSO-d_6) δ [ppm: 8.16 (s, 1H, NCH), 8.05 (bs, 2H, NH_2), 7.96–7.90 (m, 1H, H_{furane}), 7.22 (d, $^3J_{H,H}$ = 3.39 Hz, 1H, H_{furane}), 6.87–6.82 (m, 2H, 2x $CH_{arom.}$), 6.80–6.74 (m, 2H, 2 x $CH_{arom.}$), 6.73 (dd, $^3J_{H,H}$ = 1.76 Hz, $^3J_{H,H}$ = 3.34 Hz, 1H, H_{furane}), 4.52 (s, 2H, CO_2CH_2), 4.42 (t, $^3J_{H,H}$ = 6.89 Hz, 2H, NCH_2), 3.02–2.90 (m, 4H, 2x $CH_{2xpiperazine}$), 2.83 (t, $^3J_{H,H}$ = 6.94 Hz, 2H, $N_{piperazine}CH_2$), 2.65–2.54 (m, 4H, 2x $CH_{2xpiperazine}$), 1.41 (s, 9H, 3 x CH_3). **^{13}C NMR** (151 MHz, DMSO-d_6) δ [ppm] = 168.1 (C_q, $CO_{t\text{-}Butylester}$), 155.3 (C_q, A), 151.2 (C_q, C_{ether}), 148.7 (C_q, X/Y), 148.6 (C_q, B), 146.2 (C_q, X/Y), 145.8 (C_q, $CN_{piperazine}$), 145.5 (C_q, C_{furane}), 145.1 (CH, C_{furane}), 131.4 (CH, NCH), 117.0 (C_q, $C_{arom.}$), 115.0 (C_q, $C_{arom.}$), 112.2 (CH, C_{furane}), 112.1 (CH, C_{furane}), 95.6 (C_q, C), 81.1 (C_q, $C(CH_3)_3$), 65.5 (CH_2, CO_2CH_2), 56.5 (CH_2, D), 52.6 (2x CH_2, $C_{piperazine}$), 49.3 (2 x CH_2, $C_{piperazine}$), 44.4 (CH_2, E), 27.7 (3 x CH_3). Mp. 192.9–196.8 °C. **LC-MS**: positive [*m*/*z*] = 560.1 ([M+H]$^+$). **HRMS** (ESI-QTOF) calculated for $C_{28}H_{33}N_9O_4$ [M+H]$^+$: 560.2728; found: 560.2725. **Purity**: 97%.

2-(4-(4-(2-(5-Amino-2-(furan-2-yl)-7*H*-pyrazolo[4,3-*e*][1,2,4]triazolo[1,5-*c*]pyrimidin-7-yl)ethyl)piperazin-1-yl)phenoxy)acetic acid (2)

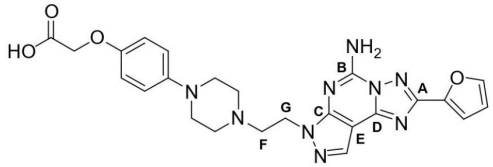

Compound **1** (21 mg, 0.038 mmol, 1.0 eq.) is dissolved in a round bottom flask in 10 ml of dichloromethane, and trifluoroacetic acid (1.2 ml) is added dropwise upon cooling with ice. Then, the ice bath is removed, and 2 drops of water are added. After stirring for 24h at RT, the solvent is removed *in vacuo*, and the residue is purifed by HPLC, applying a gradient of 50% aq. acetonitrile to 100% acetonitrile within 15 min, followed by elution for 5 min with 100% acetonitrile, yielding 19 mg (0.038 mmol) of **2** (yield: 100%).
^{1}H NMR (600 MHz, DMSO-d_6) δ [ppm]: 8.16 (s, 1H, NCH), 8.05 (bs, 2H, NH_2), 7.93 (d, $^3J_{H,H}$ = 1.6 Hz, 1H, H_{furane}), 7.22 (d, $^3J_{H,H}$ = 3.37 Hz, 1H, H_{furane}), 6.88–6.81 (m, 2H, 2 x $CH_{arom.}$), 6.79–6.75 (m, 2H, 2 x $CH_{arom.}$), 6.73 (dd, $^3J_{H,H}$ = 1.76 Hz, $^3J_{H,H}$ = 3.37 Hz, 1H, H_{furane}), 4.52 (s, 2H, CO_2CH_2), 4.42 (t, $^3J_{H,H}$ = 6.85 Hz, 2H, NCH_2), 2.99–2.92 (m, 4H, 2 x $CH_{2\ x\ piperazine}$), 2.84 (t, $^3J_{H,H}$ = 6.85 Hz, 2H, $N_{üiperazine}CH_2$), 2.64–2.57 (m, 4H, 2 x $CH_{2\ x\ piperazine}$). **^{13}C NMR** (151 MHz, DMSO-d_6) δ [ppm] = 170.5 (C_q, COOH), 155.4 (C_q, A), 153.0 (C_q, C_{ether}), 148.7 (C_q, B), 148.6 (C_q, C), 146.3 (C_q, D), 145.5 (C_q, $CN_{piperazine}$), 145.5 (C_q, C_{furane}), 145.1 (CH, C_{furane}), 131.4 (CH, NCH), 117.2 (C_q, $C_{arom.}$), 114.8 (C_q, $C_{arom.}$), 112.3 (CH, C_{furane}), 112.2 (CH, C_{furane}), 95.7 (C_q, E), 68.3 (CH_2, CO_2CH_2), 56.6 (CH_2, F), 52.8 (2x CH_2, $C_{piperazine}$), 49.9 (2 x CH_2, $C_{piperazine}$), 44.4 (CH_2, G). **Mp** >300 °C. **LC-MS**: positive [*m*/*z*] = 504.2 ([M+H]$^+$). **HRMS** (ESI-QTOF) calculated for $C_{24}H_{25}N_9O_4$ [M-H]$^-$: 502.1950; found: 502.1943. **Purity**: 98%.

1.10.3 Synthesis of amino-substituted PEG derivatives 3a-3f

The following azido-functionalized PEG esters used as starting materials were synthesized as previously described[19,20] and reduced using Method A or Method B, respectively, to yield the desired amino-functionalized PEG derivatives.

1.10.3.1 Method A

The appropriate ester (1.0 eq.) is dissolved in dichloromethane (1 ml per 100 mg of ester) under an atmosphere of argon (using a ballon), and 10% Pd/C (10 mg per 100 mg of ester) is added. The argon atmosphere is exchanged for hydrogen gas (H_2) using a balloon, and the mixture is stirred for 8h at RT. Then, the solution is filtered through Celite®, and the solvent is subsequently removed *in vacuo*. The product is purified by column chromatography on silica gel using 7N ammonia solution in methanol/dichloromethane as eluent; for details see below.

***tert*-Butyl 14-amino-3,6,9,12-tetraoxatetradecanoate (3a)**

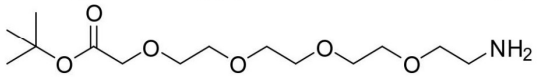

tert-Butyl 14-azido-3,6,9,12-tetraoxatetradecanoate (400 mg, 1.2mmol, 1.0 eq.); 7N NH_3 in methanol/dichloromethane (5:95); yield: 240 mg (0.78 mmol, 71%).
^{1}H-NMR (600 MHz, DMSO-d_6) δ [ppm]: 3.98 (s, 2H, CO_2CH_2), 3.58–3.55 (m, 2H, CH_2), 3.55–3.47 (m, 12H, 6 x CH_2), 3.36–3.33 (t, $^3J_{H,H}$ = 5.85 Hz, 2H, CH_2), 2.63 (t, $^3J_{H,H}$ = 5.83 Hz, 2H, NH_2), 1.42 (s, 9H, 3 x CH_3). **^{13}C-NMR** (151 MHz, DMSO-d_6) δ [ppm] = 169.4 (C_q, $C_{carbonyl}$), 80.7 (C_q, $C(CH_3)_3$), 73.0 (CH_2), 69.9 (CH_2), 69.8 (CH_2), 69.8 (CH_2), 69.8 (CH_2), 69.7 (CH_2), 69.6 (CH_2), 68.1 (CH_2), 41.3 (CH_2), 27.8 (3 x CH_3, $C(CH_3)_3$). **LC-MS**: positive [*m*/*z*] = 308.1 ([M+H]$^+$). **Purity** (determined by NMR): 95%.

***tert*-Butyl 17-amino-3,6,9,12,15-pentaoxaheptadecanoate (3b)**

tert-Butyl 17-azido-3,6,9,12,15-pentaoxaheptadecanoate (100 mg, 0.26 mmol, 1.0 eq.). The compound was used without further purification.
^{1}H-NMR (500 MHz, DMSO-d_6) δ [ppm]: 3.98 (s, 2H, $COOCH_2$), 3.58–3.48 (m, 18H, 9 x CH_2), 3.37–3.33 (m, 2H, CH_2), 2.64 (t, $^3J_{H,H}$ = 5.82 Hz, NH_2) 1.42 (s, 9H, 3x CH_3). **^{13}C-NMR** (151 MHz, DMSO-d_6) δ [ppm]: 169.3 (C_q, CO), 80.6 (C_q, $C_{t\text{-}butyl}$), 73.0 (CH_2, CO_2CH_2O), 69.8 (CH_2), 69.8 (CH_2), 69.8 (CH_2), 69.8 (CH_2), 69.8 (CH_2), 69.7 (CH_2), 69.7 (CH_2), 69.6 (CH_2), 68.1 (CH_2) 41.3 (CH_2, NH_2CH_2), 27.8 (CH_3, 3 x CH_3). **LC-MS**: positive [*m*/*z*] = 351.8 ([M+H]$^+$). Purity determined by NMR: >90%.

***tert*-Butyl 26-amino-3,6,9,12,15,18,21,24-octaoxahexacosanoate (3c)**

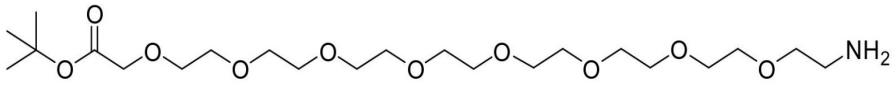

tert-Butyl 26-azido-3,6,9,12,15,18,21,24-octaoxahexacosanoate (170 mg, 0.33 mmol, 1.0 eq.; 7N NH_3 in methanol/dichloromethane (5:95); yield: 90.8 mg, 0.19 mmol, 57%.
^{1}H-NMR (600 MHz, DMSO-d_6) δ [ppm]: 3.98 (s, 2H, CO_2CH_2), 3.59–3.54 (m, 2H, CH_2), 3.55–3.46 (m, 28H, 14 x CH_2), 3.35 (t, $^3J_{H,H}$ = 5.81 Hz, 2H, CH_2), 2.64 (t, $^3J_{H,H}$ = 5.79 Hz, 2H, NH_2), 1.42 (s, 9H, 3 x CH_3). **^{13}C-NMR** (151 MHz, DMSO-d_6) δ [ppm]: 169.3 (C_q, $C_{carbonyl}$), 80.6 (C_q, $C(CH_3)_3$), 73.0 (CH_2), 69.8 (CH_2), 69.8 (CH_2), 69.8 (9 x CH_2), 69.7 (CH_2), 69.7 (CH_2), 69.6 (CH_2), 68.1 (CH_2), 41.3 (CH_2), 27.7 (3 x CH_3, $C(CH_3)_3$). **HRMS** (ESI-QTOF) calculated for $C_{22}H_{45}NO_{10}$ $[M+H]^+$: 484.3116; found: 484.3106. **Purity** determined by NMR: 95%.

1.10.3.2 Method B[20]

The appropriate ester (1.0 eq.) is dissolved in tetrahydrofurane (0.04 M) under an atmosphere of argon, and triphenylphosphane (2.0 eq.) is added. After stirring the solution for 24 h at RT, water (5.0 eq.) is added, and the mixture is stirred for additional 3 h. Then, the solvent is removed *in vacuo*, and the product is purified by column chromatography on silica gel using 7N NH_3 in methanol/dichloromethane as eluent. For details see below.

***tert*-Butyl 38-amino-3,6,9,12,15,18,21,24,27,30,33,36-dodecaoxaoctatriacontanoate (3d)**

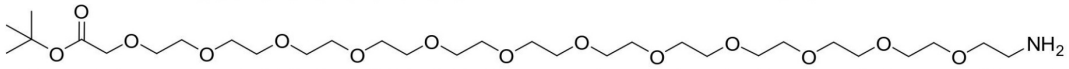

tert-Butyl 38-azido-3,6,9,12,15,18,21,24,27,30,33,36-dodecaoxaoctatriacontanoate (313 mg, 0.19 mmol, 1.0 eq.); 7N NH_3 in methanol/dichloromethane (7:93); yield: 109.1 mg, 0.17 mmol, 87%.
^{1}H-NMR (600 MHz, DMSO-d_6) δ [ppm]: 3.97 (s, 2H, CO_2CH_2), 3.58–3.55 (m, 2H, CH_2), 3.54–3.48 (m, 44H, 22 x CH_2), 3.35 (t, $^3J_{H,H}$ = 5.80 Hz, 2H, CH_2), 2.64 (t, $^3J_{H,H}$ = 5.77 Hz, 2H, NH_2), 1.42 (s, 9H, 3 x CH_3). **^{13}C-NMR** (151 MHz, DMSO-d_6) δ [ppm]: 169.4 (C_q, $C_{carbonyl}$), 80.7 (C_q, $C(CH_3)_3$), 72.9 (CH_2), 69.9 (CH_2), 69.8 (2 x CH_2), 69.8 (16 x CH_2), 69.8 (CH_2), 69.7 (CH_2), 69.6 (CH_2), 68.1 (CH_2), 41.3 (CH_2), 27.8 (3 x CH_3, $C(CH_3)_3$). **HRMS** (ESI-QTOF) calculated for $C_{30}H_{61}NO_{14}$ $[M+H]^+$: 660,4165; found: 660,4129. **Purity** determined by NMR: 93%.

***tert*-Butyl 50-amino-3,6,9,12,15,18,21,24,27,30,33,36,39,42,45,48-hexadecaoxapentacontanoate (3e)**

tert-Butyl 50-azido-3,6,9,12,15,18,21,24,27,30,33,36,39,42,45,48-hexadecaoxapentacontanoate (89.1 mg, 0.103 mmol, 1.0 eq.); 7N NH_3 in methanol/dichloromethane (10:90); yield: 77.7 mg, 0.093 mmol, 90%.
^{1}H-NMR (600 MHz, DMSO-d_6) δ [ppm]: 3.98 (s, 2H, CH_2), 3.58–3.55 (m, 2H, CH_2), 3.54–3.48 (m, 60H, 30 x CH_2), 3.36 (t, $^3J_{H,H}$ = 5.80 Hz, 2H, CH_2), 2.65 (t, $^3J_{H,H}$ = 5.77 Hz, 2H, NH_2), 1.42 (s, 9H, 3 x CH_3). **^{13}C-NMR** (151 MHz, DMSO-d_6) δ [ppm]: 169.3 (C_q, $C_{carbonyl}$), 80.6 (C_q, $C(CH_3)_3$), 72.9 (CH_2), 69.8 (CH_2), 69.8 (26 x CH_2), 69.7 (CH_2), 69.7 (CH_2), 69.6 (CH_2), 68.1 (CH_2), 41.3 (CH_2), 27.7 (3 x CH_3, $C(CH_3)_3$). **HRMS** (ESI-QTOF) calculated for $C_{38}H_{77}NO_{18}$ $[M+H]^+$: 836.5213; found: 836.5193. **Purity** determined by NMR: 95%.

***tert*-Butyl 62-amino-3,6,9,12,15,18,21,24,27,30,33,36,39,42,45,48,51,54,57,60-icosaoxadohexacontanoate (3f)**

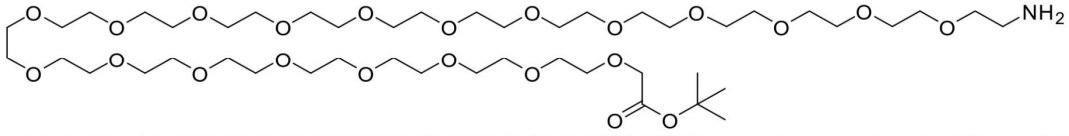

tert-Butyl 62-azido-3,6,9,12,15,18,21,24,27,30,33,36,39,42,45,48,51,54,57,60-icosaoxadohexacontanoate (200 mg, 0.19 mmol, 1.0 eq.); 7N NH_3 in methanol/dichloromethane (8:92); yield: 140.2 mg, 0.14 mmol, 71%.
^{1}H-NMR (600 MHz, DMSO-d_6) δ [ppm]: 3.98 (s, 2H, CH_2), 3.58–3.55 (m, 2H, CH_2), 3.55–3.48 (m, 76H, 38 x CH_2), 3.36 (t, $^3J_{H,H}$ = 5.79 Hz, 2H, CH_2), 2.65 (t, $^3J_{H,H}$ = 5.79 Hz, 2H, NH_2), 1.42 (s, 9H, 3 x CH_3). **^{13}C-NMR** (151 MHz, DMSO-d_6) δ [ppm]: 169.3 (C_q, $C_{carbonyl}$), 80.6 (C_q, $C(CH_3)_3$), 72.9 (CH_2), 69.8 (CH_2), 69.8 (2 x CH_2), 69.8 (32 x CH_2), 69.7 (CH_2), 69.7 (CH_2), 69.6 (CH_2), 68.1 (CH_2), 41.3 (CH_2), 27.7 (3 x CH_3, $C(CH_3)_3$). **HRMS** (ESI-QTOF) calculated for $C_{46}H_{93}NO_{22}$ $[M+H]^+$: 1012.6262; found: 1012.6239. **Purity** determined by NMR: 93%.

2. Supplementary Figures

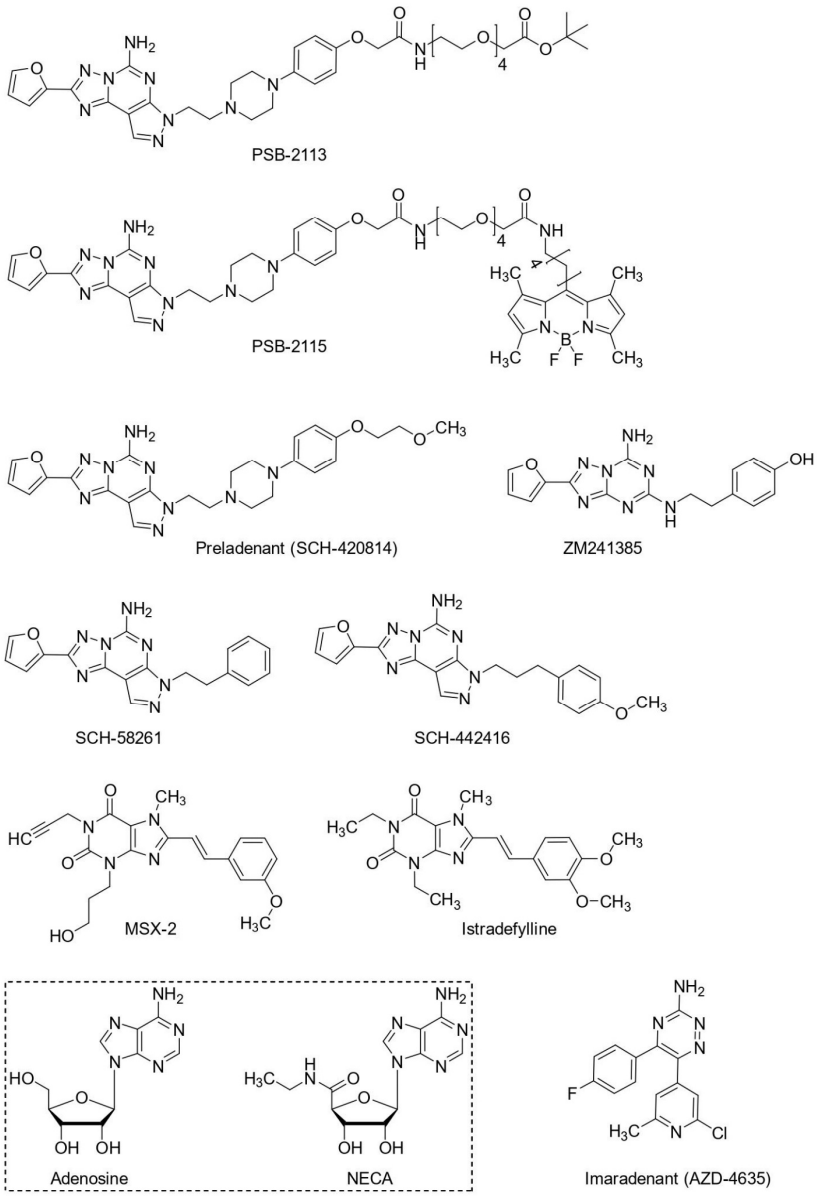

Figure S1. Chemical structures of discussed A_{2A}AR antagonists and agonists. The two agonists adenosine and NECA are highlighted by a dashed rectangle.

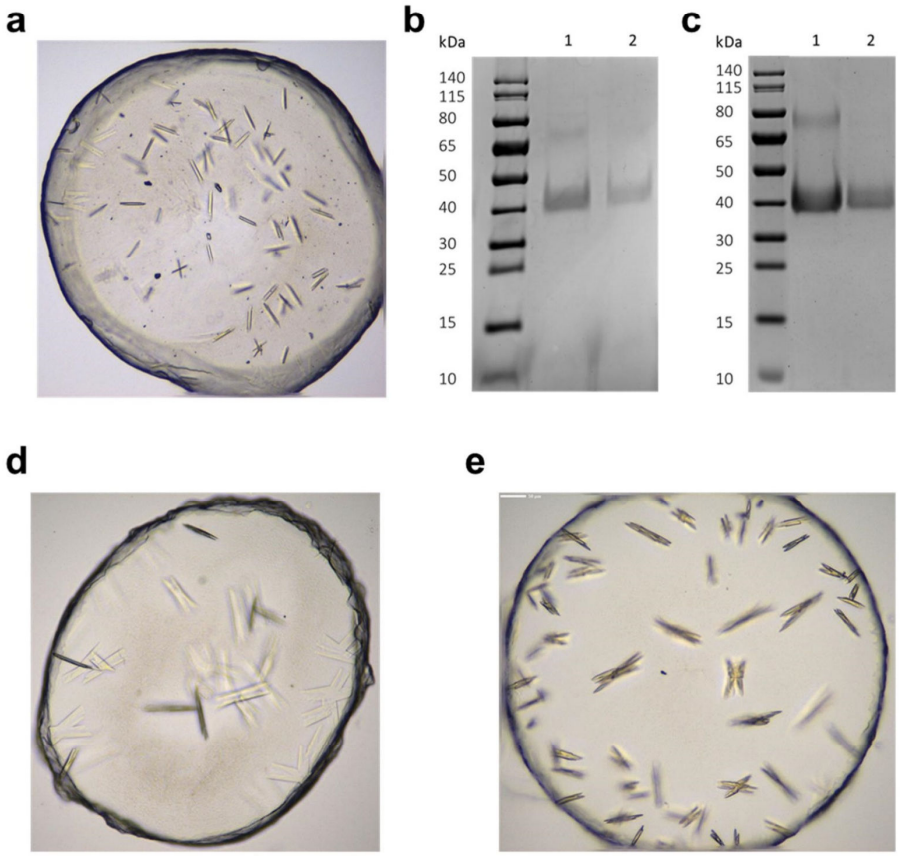

Figure S2. Crystallization and SDS-PAGE results. **a** Non-diffracting crystals of A_{2A}-ΔC-bRIL purified in complex with PSB-2113. **b** SDS-PAGE results of the unconcentrated A_{2A}-PSB1-bRIL-PSB-2113 complex, either (1) undiluted or (2) diluted with water in a 1 to 4 ratio. **c** SDS-PAGE results of the unconcentrated A_{2A}-PSB1-bRIL-PSB-2115 complex, either (1) undiluted or (2) diluted with water in a 1 to 4 ratio. **d** Crystals of the A_{2A}-PSB1-bRIL-PSB-2113 complex in LCP. **e** Crystals of the A_{2A}-PSB1-bRIL-PSB-2115 complex in LCP.

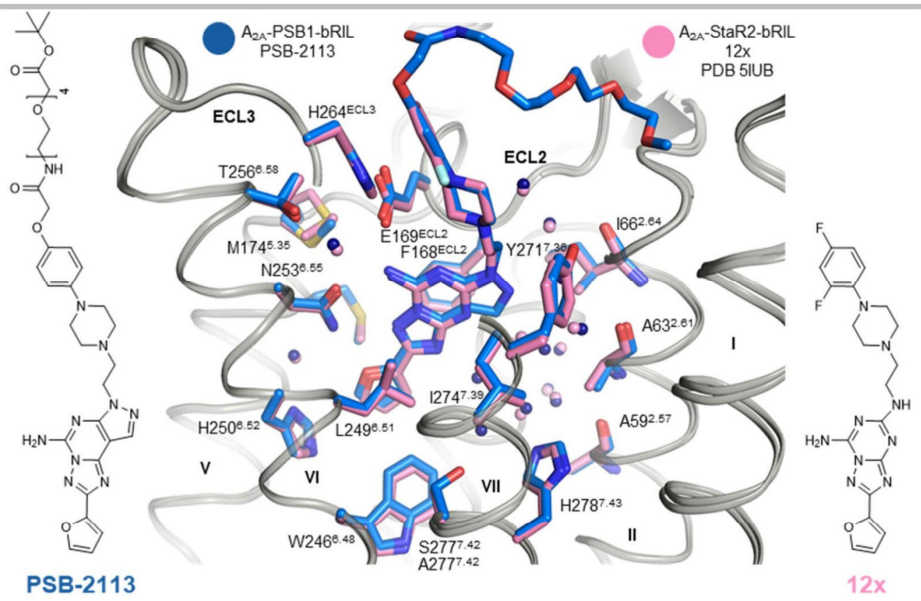

Figure S3. Binding pocket comparison of the new A_{2A}-PSB1-bRII-PSB-2113 structure (blue) with the structure of A_{2A}-StaR2-bRIL in complex with A_{2A}AR antagonist **12x** (pink, PDB 5UIB).[6] 12x comprises a comparable phenylpiperazinylethyl extension as PSB-2113 and forms similar π-π interactions to $H264^{ECL3}$.

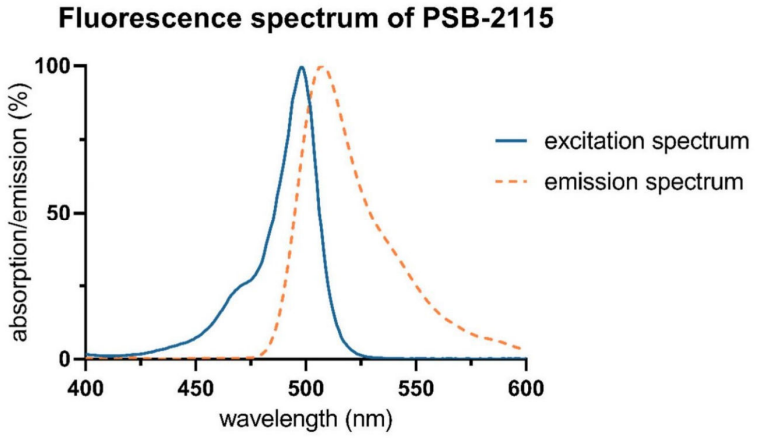

Figure S4. Fluorescence spectrum of BODIPY-conjugated preladenant derivative PSB-2115.

3. Supplementary Tables

Table S1. Complete list of all published A_{2A}AR crystal structures in complex with A_{2A}AR antagonists in the Protein Data Bank as of January 2022.

PDB Identifier	Ligand	A_{2A}AR construct	Resolution (Å)	H264-E169 ionic lock	pH during crystallization	Reference
3EML	ZM241385	A_{2A}-ΔC-T4L	2.60	intact	5.5 – 6.5	[21]
4EIY 5JTB 6WQA 5K2A 5VRA 6LPJ 5K2B 6AQF 6LPK 5K2C 6MH8 6LPL 5K2D 6JZH 7RM5 5UVI 6PS7	ZM241385	A_{2A}-ΔC-bRIL (+ N154Q in 6AQF)	1.80 – 4.20	intact	4.8 – 5.0	[3,22]
3PWH	ZM241385	A_{2A}-StaR2	3.30	open	8.0 – 8.75	[23]
3VGA 3VG9	ZM241385	A_{2A}-ΔC + N154Q	2.70 – 3.10	intact/open	6.5	[24]
5IU4 5NM4 6S0L 5NLX 5OLG 6S0Q 5NM2	ZM241385	A_{2A}-StaR2-bRIL	1.72 – 2.14	intact	5.0 – 5.4	[6,25,26]
3REY	Xanthine amine congener (XAC)	A_{2A}-StaR2	3.31	open	8.0 – 8.75	[23]
3RFM	Caffeine	A_{2A}-StaR2	3.60	open	8.0 – 8.75	[23]
5MZP	Caffeine	A_{2A}-StaR2-bRIL	2.10	intact	5.0	[27]
3UZA	4g	A_{2A}-StaR2	3.27	open	8.0 – 8.75	[28]
3UZC	4e	A_{2A}-StaR2	3.34	open	8.0 – 8.75	[28]
5OLZ	4e	A_{2A}-StaR2-bRIL	1.90	intact	5.3 – 5.4	[26]
5OM1	4e	A_{2A}-StaR2-bRIL	2.10	intact	5.3 – 5.4	[26]
5OM4	4e	A_{2A}-StaR2-bRIL	2.00	intact	5.3 – 5.4	[26]
5IU7	12c	A_{2A}-StaR2-bRIL	1.90	intact	5.3 – 5.4	[6]
5IU8	12f	A_{2A}-StaR2-bRIL	2.00	intact	5.5	[6]
5IUA	12b	A_{2A}-StaR2-bRIL	2.20	intact	5.3 – 5.4	[6]
5IUB	12x	A_{2A}-StaR2-bRIL	2.10	intact	5.5	[6]
5MZJ	Theophylline	A_{2A}-StaR2-bRIL	2.00	intact	5.1	[27]
5N2R	PSB-36	A_{2A}-StaR2-bRIL	2.80	open	5.1	[27]
5OLH	Vipadenant	A_{2A}-StaR2-bRIL	2.60	intact	5.3 – 5.4	[26]
5OLO	Tozadenant	A_{2A}-StaR2-bRIL	3.10	open	5.3 – 5.4	[26]
5OLV	LUAA47070	A_{2A}-StaR2-bRIL	2.00	intact	5.3 – 5.4	[26]
5UIG	Cmpd-1	A_{2A}-ΔC-bRIL (modified N- and C- terminus	3.50	intact	6.5	[29]
6GT3	Imaradenant	A_{2A}-StaR2-bRIL	2.00	intact	5.3 – 5.4	[30]
6ZDR	Chromone 4d	A_{2A}-StaR2-bRIL	1.92	intact	4.7 – 5.4	[31]
6ZDV	Chromone 5d	A_{2A}-StaR2-bRIL	2.13	intact	4.7 – 5.4	[31]

Table S2. Data collection and refinement statistics. Statistics for the highest resolution shell are shown in parentheses.

	Data collection	
	A_{2A}-PSB1-bRIL-PSB-2113 (PDB 7PX4)	**A_{2A}-PSB1-bRIL-PSB-2115 (PDB 7PYR)**
Number of crystals used	1	1
Space group	*C 2 2 2_1*	*C 2 2 2_1*
Cell parameters a, b, c (Å)	39.6, 180.262, 139.483	39.31, 180.11, 140.4
Number of reflections processed	158,598 (15,265)	103,499 (10,564)
Number of unique reflections	24,297 (2,375)	15,875 (1,545)
Resolution (Å)	41.32 – 2.25 (2.33 – 2.25)	45.03 - 2.6 (2.69 – 2.6)
R_{merge} (%)	21.30 (134.5)	19.53 (133.8)
$CC_{1/2}$	0.995 (0.574)	0.995 (0.585)
Mean *I/σ (I)*	7.69 (1.36)	9.26 (2.42)
Completeness (%)	99.70 (98.02)	97.92 (94.70)
Redundancy	6.5 (6.4)	6.5 (6.8)
	Refinement	
Resolution (Å)	2.25	2.6
Number of reflections (test set)	24,282 (2,372)	15,569 (1,464)
R_{work} / R_{free} (%)	19.55 / 23.94 (29.50 / 37.11)	19.15 / 25.04 (23.36 / 28.84)
	Number of atoms	
A_{2A}AR	2,308	2,312
bRIL	696	693
Ligand	50	50
Lipids, PEG and waters	759	721
	Overall *B* values (Å^2)	
A_{2A}AR	35.60	40.16
bRIL	70.17	82.48
Ligand	44.00	49.45
Lipids, PEG and waters	55.48	61.59
	RMSD	
Bond lengths (Å)	0.002	0.003
Bond angles (°)	0.42	0.49
	Ramachandran plot statistics	
Favored regions (%)	98.45	98.70
Allowed regions (%)	1.55	1.30
Disallowed regions (%)	0	0

Table S3. Affinities determined in radioligand binding assays and potencies determined in the TRUPATH G protein activation assay.[a]

A_{2A}AR construct	MSX-2	PSB-2113	NECA	NECA
	vs. [^{3}H]MSX-2 K_d ± SEM (nM)	vs. [^{3}H]MSX-2 K_i ± SEM (nM)	vs. [^{3}H]MSX-2 K_i ± SEM (nM)	$G\alpha_{s\text{-short}}$RLuc8-$G\beta_3$-$G\gamma_9$GFP2 EC_{50} ± SEM (nM)
A_{2A} wt	**13.3** ± 0.756	**6.30** ± 0.792	**603** ± 141	**58.6** ± 28.6
A_{2A}-ΔC	**17.7** ± 2.02	**12.7** ± 3.30	**230** ± 39.8	**6.86** ± 3.50
A_{2A}-ΔC-bRIL	**15.1** ± 2.09	**12.0** ± 2.31	**494** ± 296	**no activation**
A_{2A}-PSB1-bRIL	**20.4** ± 3.54	**19.6** ± 3.60	**no binding**	**no activation**
A_{2A}-PSB1	N.D.	N.D.	N.D.	**no activation**
A_{2A}-StaR2-bRIL	**17.1** ± 0.240	N.D.	**no binding**	N.D.

[a] K_d and K_i values are means ± SEM from three independent experiments. EC_{50} values are means ± SEM from four to five independent experiments. N.D. not determined.

4. References

[1] F. Heisig, S. Gollos, S. J. Freudenthal, A. El-Tayeb, J. Iqbal, C. E. Müller, *J. Fluoresc.* **2014**, *24*, 213–230.
[2] D. B. Garrity, M. J. Chang, G. W. Blissard, *Virology* **1997**, *231*, 167–181.
[3] W. Liu, E. Chun, A. A. Thompson, P. Chubukov, F. Xu, V. Katritch, G. W. Han, C. B. Roth, L. H. Heitman, A. P. IJzerman et al., *Science* **2012**, *337*, 232–236.
[4] X. M. Guan, T. S. Kobilka, B. K. Kobilka, *J. Biol. Chem.* **1992**, *267*, 21995–21998.
[5] E. Chun, A. A. Thompson, W. Liu, C. B. Roth, M. T. Griffith, V. Katritch, J. Kunken, F. Xu, V. Cherezov, M. A. Hanson et al., *Structure* **2012**, *20*, 967–976.
[6] E. Segala, D. Guo, R. K. Y. Cheng, A. Bortolato, F. Deflorian, A. S. Doré, J. C. Errey, L. H. Heitman, A. P. IJzerman, F. H. Marshall et al., *J. Med. Chem.* **2016**, *59*, 6470–6479.
[7] M. Audet, K. Villers, J. Velasquez, M. Chu, C. Hanson, R. C. Stevens, *Nat. Protoc.* **2020**, *15*, 144–160.
[8] T. Claff, J. Yu, V. Blais, N. Patel, C. Martin, L. Wu, G. W. Han, B. J. Holleran, O. van der Poorten, K. L. White et al., *Sci. Adv.* **2019**, *5*, eaax9115.
[9] M. Caffrey, V. Cherezov, *Nat. Protoc.* **2009**, *4*, 706–731.
[10] W. Kabsch, *Acta Crystallogr. D Biol. Crystallogr.* **2010**, *66*, 125–132.
[11] A. J. McCoy, R. W. Grosse-Kunstleve, P. D. Adams, M. D. Winn, L. C. Storoni, R. J. Read, *J. Appl. Crystallogr.* **2007**, *40*, 658–674.
[12] T. C. Terwilliger, R. W. Grosse-Kunstleve, P. V. Afonine, N. W. Moriarty, P. H. Zwart, L. W. Hung, R. J. Read, P. D. Adams, *Acta Crystallogr. D Biol. Crystallogr.* **2008**, *64*, 61–69.
[13] P. Emsley, B. Lohkamp, W. G. Scott, K. Cowtan, *Acta Crystallogr. D Biol. Crystallogr.* **2010**, *66*, 486–501.
[14] M. M. Bradford, *Anal. Biochem.* **1976**, *72*, 248–254.
[15] C. E. Müller, R. Sauer, Y. Maurinsh, R. Huertas, F. Flle, K.-N. Klotz, J. Nagel, W. Hauber, *Drug Dev. Res.* **1998**, *45*, 190–197.
[16] R. H. J. Olsen, J. F. DiBerto, J. G. English, A. M. Glaudin, B. E. Krumm, S. T. Slocum, T. Che, A. C. Gavin, J. D. McCorvy, B. L. Roth et al., *Nat. Chem. Biol.* **2020**, *16*, 841–849.
[17] P. Baraldi, *Bioorg. Med. Chem.* **2003**, *11*, 4161–4169.
[18] B. R. Neustadt, N. A. Lindo, W. J. Greenlee, D. Tulshian, L. S. Silverman, Y. Xia, C. D. Boyle, S. Chackala-Mannil, *International Patent* **2001**, *WO 01/92264 A1*.
[19] H. Zhang, X. Li, Q. Shi, Y. Li, G. Xia, L. Chen, Z. Yang, Z.-X. Jiang, *Angew. Chem. Int. Ed.* **2015**, *127*, 3834–3838.
[20] Z. Wan, Y. Li, S. Bo, M. Gao, X. Wang, K. Zeng, X. Tao, X. Li, Z. Yang, Z.-X. Jiang, *Org. Biomol. Chem.* **2016**, *14*, 7912–7919.
[21] V.-P. Jaakola, M. T. Griffith, M. A. Hanson, V. Cherezov, E. Y. T. Chien, J. R. Lane, A. P. IJzerman, R. C. Stevens, *Science* **2008**, *322*, 1211–1217.
[22] a) M. W. Martynowycz, A. Shiriaeva, X. Ge, J. Hattne, B. L. Nannenga, V. Cherezov, T. Gonen, *PNAS* **2021**, *118*; b) K. Ihara, M. Hato, T. Nakane, K. Yamashita, T. Kimura-Someya, T. Hosaka, Y. Ishizuka-Katsura, R. Tanaka, T. Tanaka, M. Sugahara et al., *Sci. Rep.* **2020**, *10*, 19305; c) M.-Y. Lee, J. Geiger, A. Ishchenko, G. W. Han, A. Barty, T. A. White, C. Gati, A. Batyuk, M. S. Hunter, A. Aquila et al., *IUCrJ* **2020**, *7*, 976–984; d) A. Ishchenko, B. Stauch, G. W. Han, A. Batyuk, A. Shiriaeva, C. Li, N. Zatsepin, U. Weierstall, W. Liu, E. Nango et al., *IUCrJ* **2019**, *6*, 1106–1119; e) Y. Shimazu, K. Tono, T. Tanaka, Y. Yamanaka, T. Nakane, C. Mori, K. Terakado Kimura, T. Fujiwara, M. Sugahara, R. Tanaka et al., *J. Appl. Crystallogr.* **2019**, *52*, 1280–1288; f) J. M. Martin-Garcia, L. Zhu, D. Mendez, M.-Y. Lee, E. Chun, C. Li, H. Hu, G. Subramanian, D. Kissick, C. Ogata et al., *IUCrJ* **2019**, *6*, 412–425; g) K. L. White, M. T. Eddy, Z.-G. Gao, G. W. Han, T. Lian, A. Deary, N. Patel, K. A. Jacobson, V. Katritch, R. C. Stevens, *Structure* **2018**, *26*, 259-269.e5; h) J. Broecker, T. Morizumi, W.-L. Ou, V. Klingel, A. Kuo, D. J. Kissick, A. Ishchenko, M.-Y. Lee, S. Xu, O. Makarov et al., *Nat. Protoc.* **2018**, *13*, 260–292; i) I. Melnikov, V. Polovinkin, K. Kovalev, I. Gushchin, M. Shevtsov, V. Shevchenko, A. Mishin, A. Alekseev, F. Rodriguez-Valera, V. Borshchevskiy et al., *Sci. Adv.* **2017**, *3*, e1602952; j) J.

M. Martin-Garcia, C. E. Conrad, G. Nelson, N. Stander, N. A. Zatsepin, J. Zook, L. Zhu, J. Geiger, E. Chun, D. Kissick et al., *IUCrJ* **2017**, *4*, 439–454; k) A. Batyuk, L. Galli, A. Ishchenko, G. W. Han, C. Gati, P. A. Popov, M.-Y. Lee, B. Stauch, T. A. White, A. Barty et al., *Sci. Adv.* **2016**, *2*, e1600292.

[23] A. S. Doré, N. Robertson, J. C. Errey, I. Ng, K. Hollenstein, B. Tehan, E. Hurrell, K. Bennett, M. Congreve, F. Magnani et al., *Structure* **2011**, *19*, 1283–1293.

[24] T. Hino, T. Arakawa, H. Iwanari, T. Yurugi-Kobayashi, C. Ikeda-Suno, Y. Nakada-Nakura, O. Kusano-Arai, S. Weyand, T. Shimamura, N. Nomura et al., *Nature* **2012**, *482*, 237–240.

[25] T. Weinert, N. Olieric, R. Cheng, S. Brünle, D. James, D. Ozerov, D. Gashi, L. Vera, M. Marsh, K. Jaeger et al., *Nat. Commun.* **2017**, *8*, 542.

[26] P. Rucktooa, R. K. Y. Cheng, E. Segala, T. Geng, J. C. Errey, G. A. Brown, R. M. Cooke, F. H. Marshall, A. S. Doré, *Sci. Rep.* **2018**, *8*, 41.

[27] R. K. Y. Cheng, E. Segala, N. Robertson, F. Deflorian, A. S. Doré, J. C. Errey, C. Fiez-Vandal, F. H. Marshall, R. M. Cooke, *Structure* **2017**, *25*, 1275-1285.e4.

[28] M. Congreve, S. P. Andrews, A. S. Doré, K. Hollenstein, E. Hurrell, C. J. Langmead, J. S. Mason, I. W. Ng, B. Tehan, A. Zhukov et al., *J. Med. Chem.* **2012**, *55*, 1898–1903.

[29] B. Sun, P. Bachhawat, M. L.-H. Chu, M. Wood, T. Ceska, Z. A. Sands, J. Mercier, F. Lebon, T. S. Kobilka, B. K. Kobilka, *PNAS* **2017**, *114*, 2066–2071.

[30] A. Borodovsky, C. M. Barbon, Y. Wang, M. Ye, L. Prickett, D. Chandra, J. Shaw, N. Deng, K. Sachsenmeier, J. D. Clarke et al., *J. ImmunoTher. Cancer* **2020**, *8*, e000417.

[31] W. Jespers, G. Verdon, J. Azuaje, M. Majellaro, H. Keränen, X. García-Mera, M. Congreve, F. Deflorian, C. de Graaf, A. Zhukov et al., *Angew. Chem. Int. Ed.* **2020**, *59*, 16536–16543.

5. Author Contributions

T.C. designed and performed expression, purification and crystallization experiments and analyzed the data; T.A.K. designed, synthesized and analyzed preladenant derivatives; U.K.T.S. collected and analyzed X-ray diffraction data and solved the crystal structures; V.J.V. and J.G.S. helped with protein expression, purification, crystallization experiments and data analysis; C.V. performed radioligand binding experiments; J.H.V. performed TRUPATH experiments; J.L. supervised X-ray data collection and structural refinement; C.E.M. initiated the project, acquired funding and supervised the project. T.C. and C.E.M. wrote the manuscript with contributions from all co-authors.

6. ^{1}H and ^{13}C NMR Spectra

^{1}H-NMR *tert*-Butyl-2-(4-(4-(2-(5-amino-2-furan-2-yl)-7H-pyrazolo[4,3-*e*][1,2,4]triazolo[1,5-*c*]pyrimidin-7-yl)ethyl)piperazin)-1-yl)phenoxy)acetat in DMSO-d_6

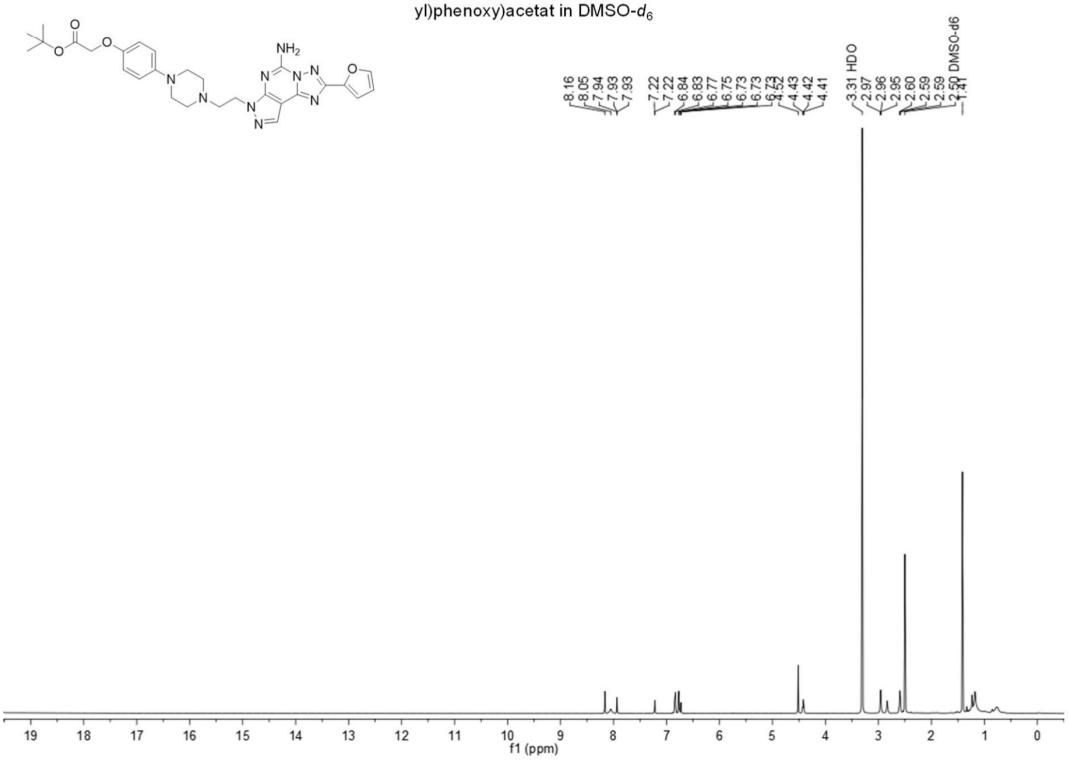

^{13}C-NMR *tert*-Butyl-2-(4-(4-(2-(5-amino-2-furan-2-yl)-7H-pyrazolo[4,3-*e*][1,2,4]triazolo[1,5-*c*]pyrimidin-7-yl)ethyl)piperazin)-1-yl)phenoxy)acetat in DMSO-d_6

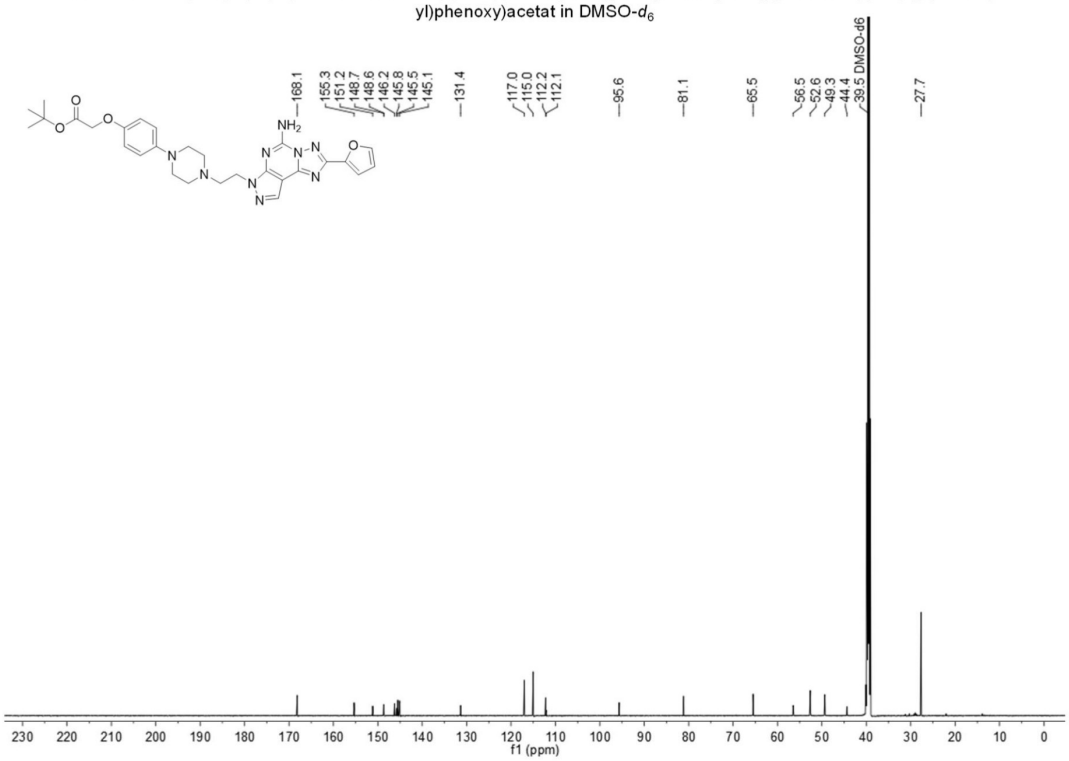

^{1}H-NMR 2-(4-(4-(2-(5-Amino-2-(furan-2-yl)-7*H*-pyrazolo[4,3-*e*][1,2,4]triazolo[1,5-*c*]pyrimidin-7-yl)ethyl)piperazin-1-yl)phenoxy)essigsäure in DMSO-d_6

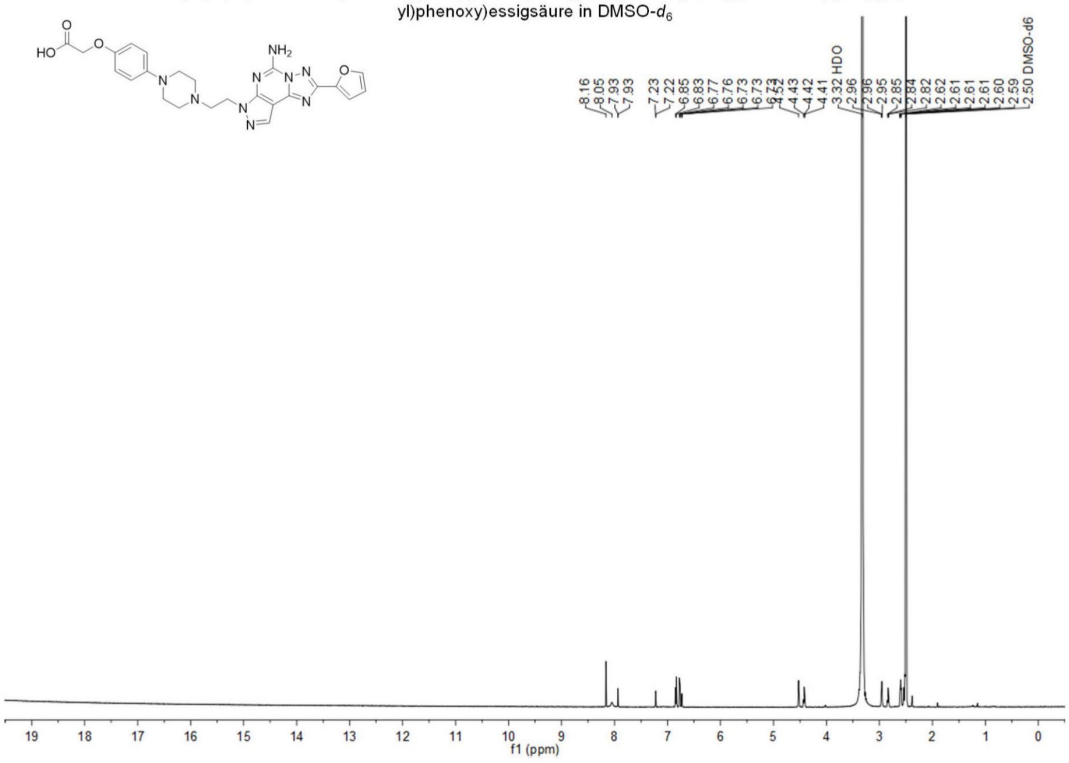

^{13}C-NMR 2-(4-(4-(2-(5-Amino-2-(furan-2-yl)-7*H*-pyrazolo[4,3-*e*][1,2,4]triazolo[1,5-*c*]pyrimidin-7-yl)ethyl)piperazin-1-yl)phenoxy)essigsäure in DMSO-d_6

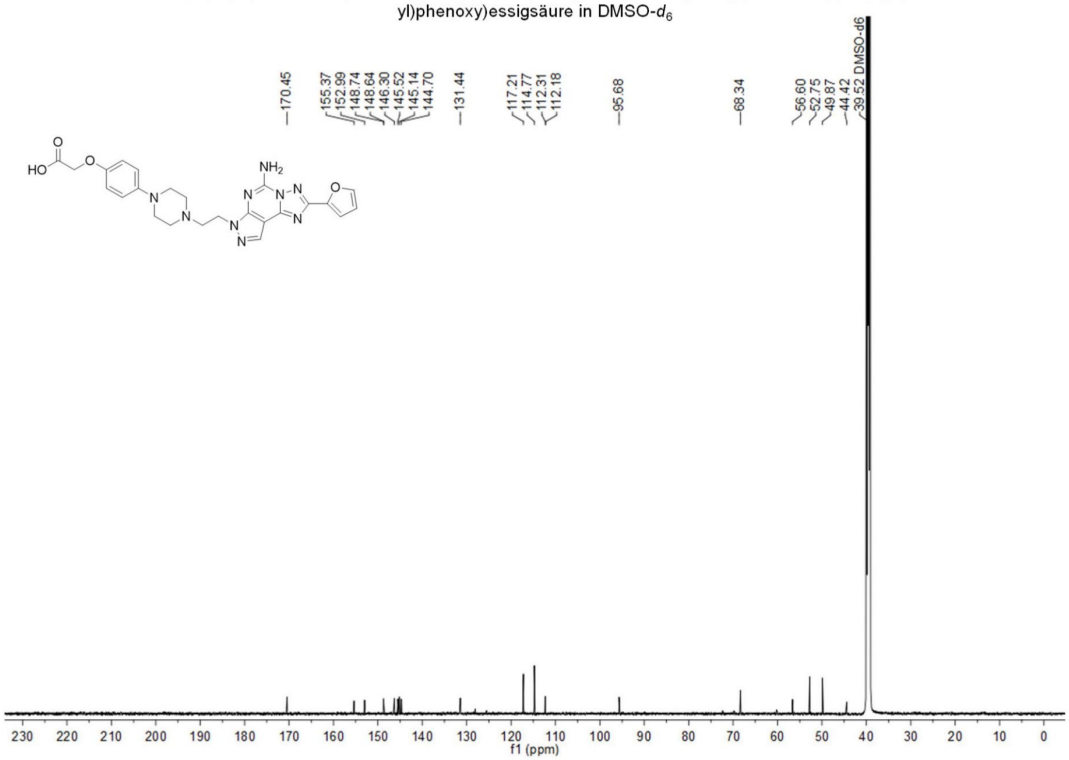

^{1}H-NMR *tert*-Butyl-1-(4-(4-(2-(5-amino-2-(furan-2-yl)-7*H*-pyrazolo[4,3-*e*][1,2,4]triazolo[1,5-*c*]pyrimidin-7-yl)ethyl)piperazin-1-yl)phenoxy)-2-oxo-6,9,12,15-tetraoxa-3-azaheptadecan-17-oat in DMSO-d_6

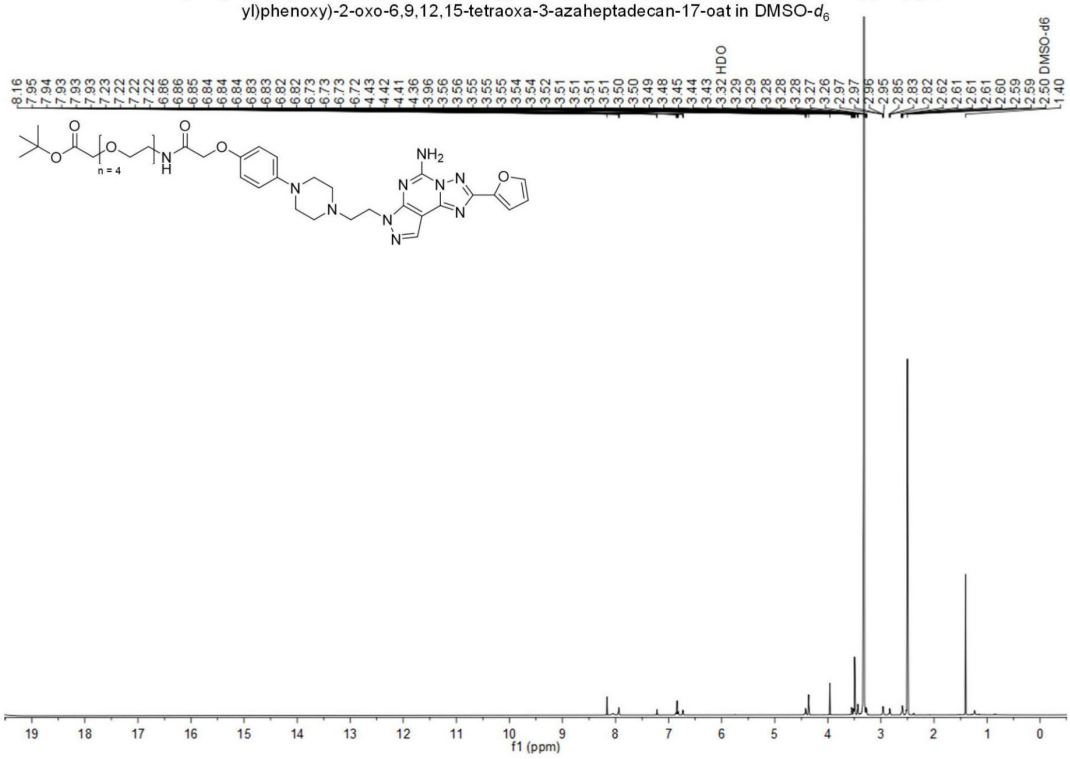

^{13}C-NMR *tert*-Butyl-1-(4-(4-(2-(5-amino-2-(furan-2-yl)-7*H*-pyrazolo[4,3-*e*][1,2,4]triazolo[1,5-*c*]pyrimidin-7-yl)ethyl)piperazin-1-yl)phenoxy)-2-oxo-6,9,12,15-tetraoxa-3-azaheptadecan-17-oat in DMSO-d_6

^{1}H-NMR *tert*-Butyl-1-(4-(4-(2-(5-amino-2-(furan-2-yl)-7*H*-pyrazolo[4,3-*e*][1,2,4]triazolo[1,5-*c*]pyrimidin-7-yl)ethyl)piperazin-1-yl)phenoxy)-2-oxo-6,9,12,15,18-pentaoxa-3-azaicosan-20-oat in DMSO-d_6

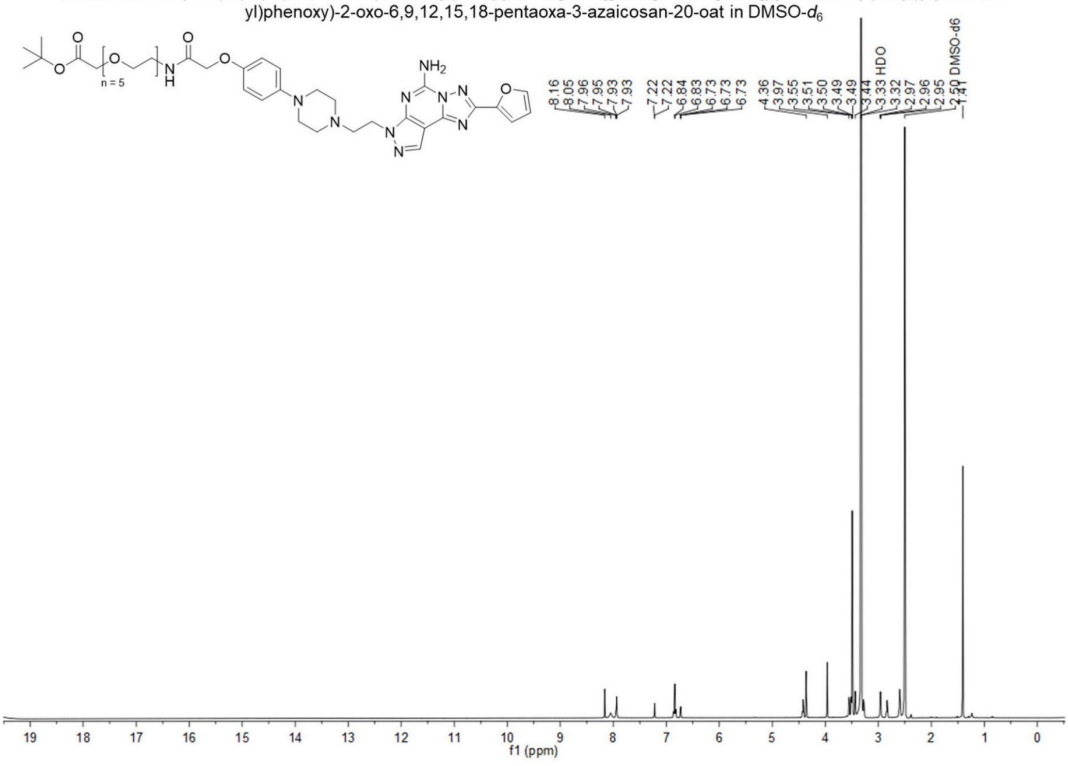

^{13}C-NMR *tert*-Butyl-1-(4-(4-(2-(5-amino-2-(furan-2-yl)-7*H*-pyrazolo[4,3-*e*][1,2,4]triazolo[1,5-*c*]pyrimidin-7-yl)ethyl)piperazin-1-yl)phenoxy)-2-oxo-6,9,12,15,18-pentaoxa-3-azaicosan-20-oat in DMSO-d_6

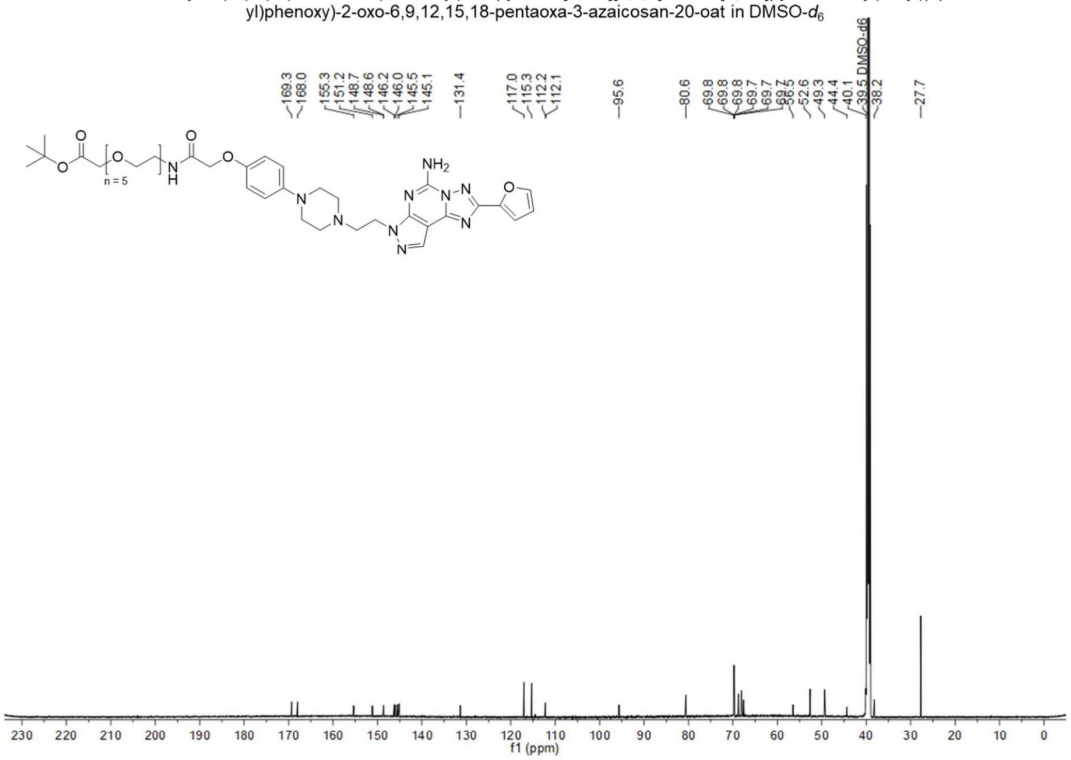

^{1}H-NMR *tert*-Butyl 1-(4-(4-(2-(5-amino-2-(furan-2-yl)-7*H*-pyrazolo[4,3-*e*][1,2,4]triazolo[1,5-*c*]pyrimidin-7-yl)ethyl)piperazin-1-yl)phenoxy)-2-oxo-6,9,12,15,18,21,24,27-octaoxa-3-azanonacosan-29-oat in DMSO-d_6

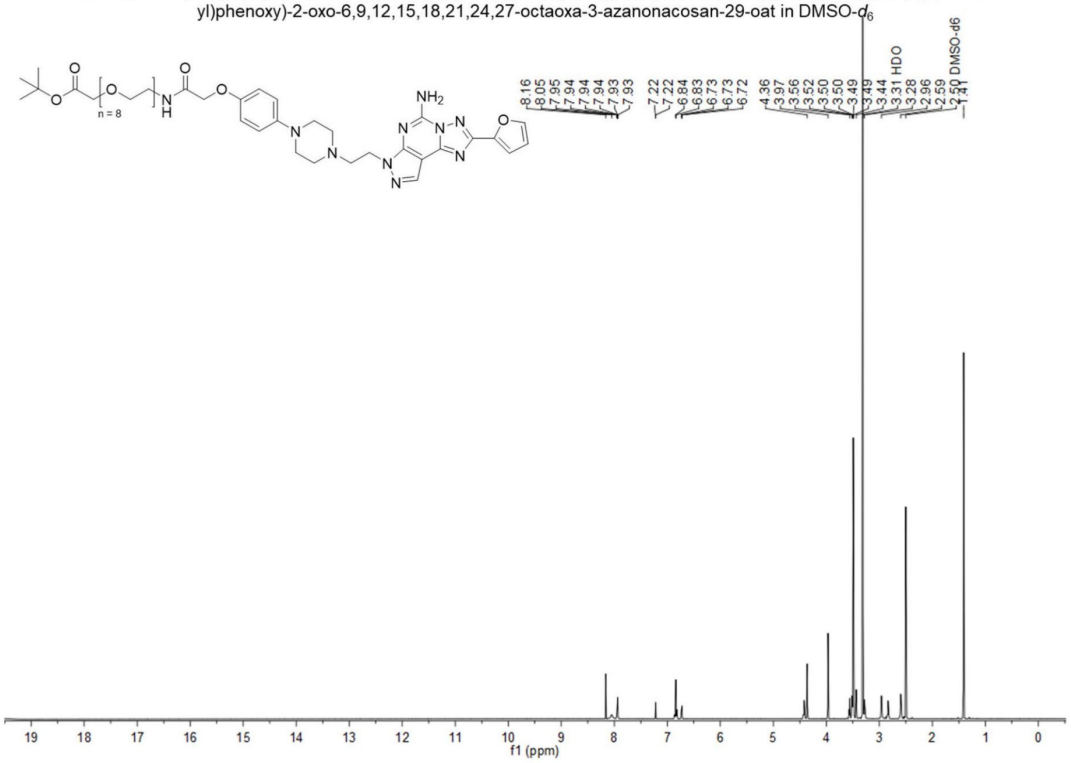

^{13}C-NMR *tert*-Butyl 1-(4-(4-(2-(5-amino-2-(furan-2-yl)-7*H*-pyrazolo[4,3-*e*][1,2,4]triazolo[1,5-*c*]pyrimidin-7-yl)ethyl)piperazin-1-yl)phenoxy)-2-oxo-6,9,12,15,18,21,24,27-octaoxa-3-azanonacosan-29-oat in DMSO-d_6

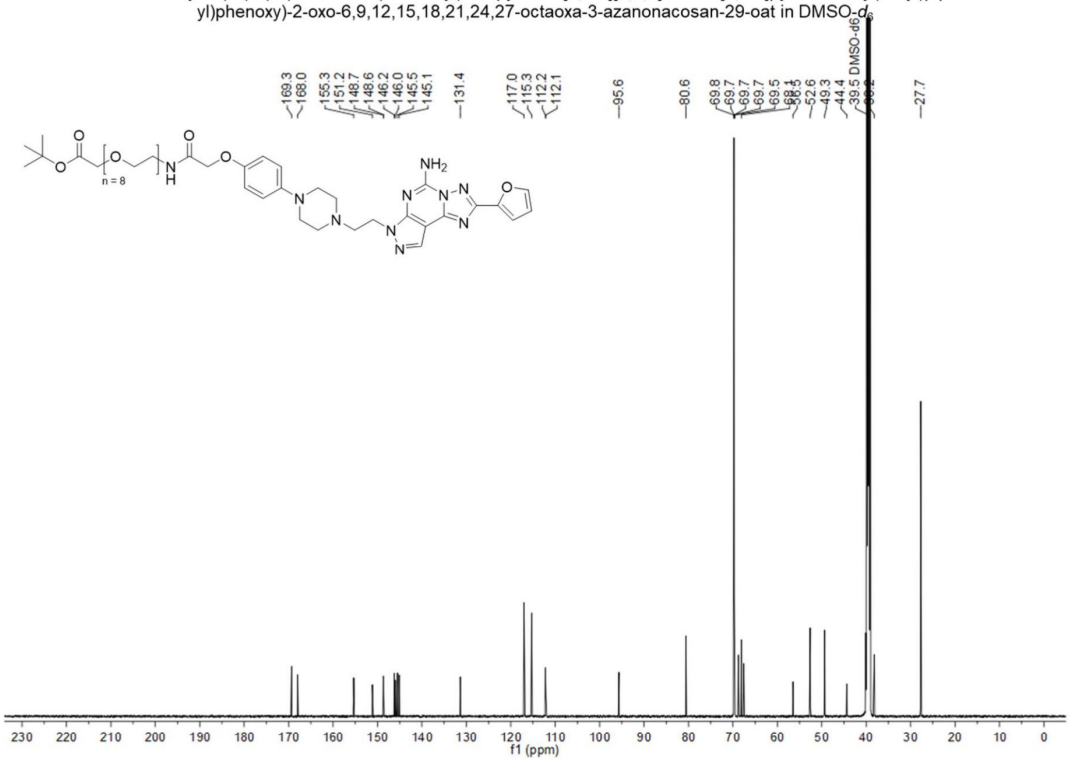

^{1}H-NMR *tert*-Butyl 1-(4-(4-(2-(5-amino-2-(furan-2-yl)-7*H*-pyrazolo[4,3-*e*][1,2,4]triazolo[1,5-*c*]pyrimidin-7-yl)ethyl)piperazin-1-yl)phenoxy)-2-oxo-6,9,12,15,18,21,24,27,30,33,36,39-dodecaoxa-3-azahentetracontan-41-oat in DMSO-d_6

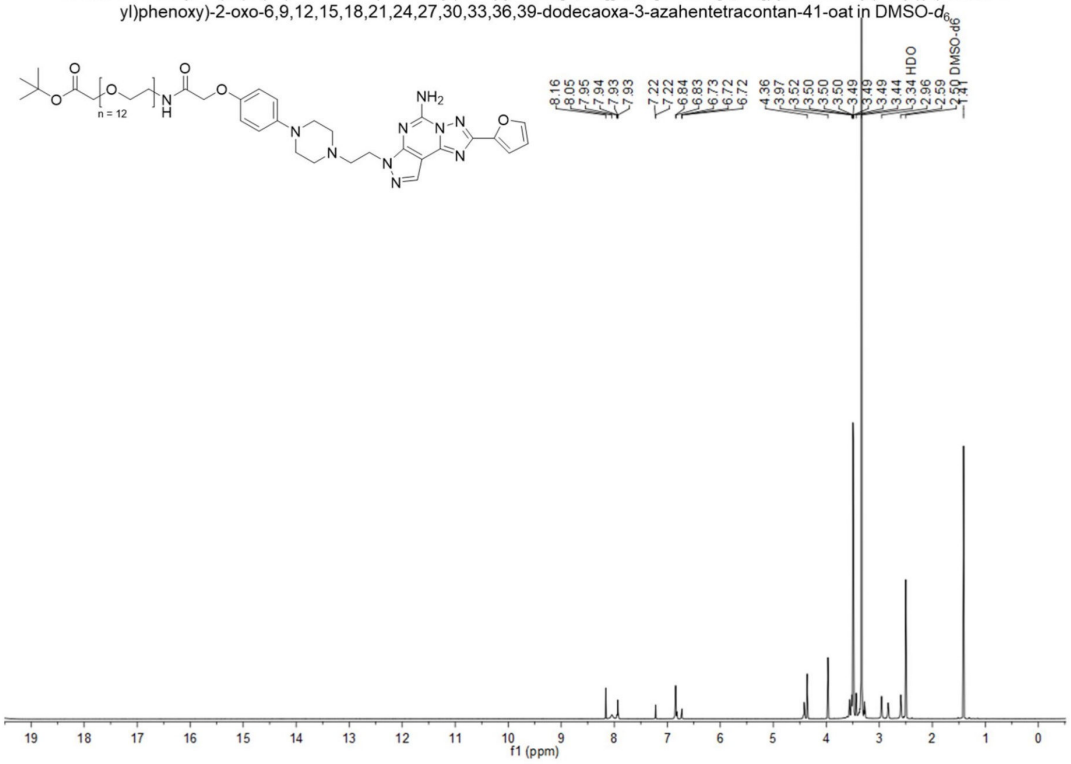

^{13}C-NMR *tert*-Butyl 1-(4-(4-(2-(5-amino-2-(furan-2-yl)-7*H*-pyrazolo[4,3-*e*][1,2,4]triazolo[1,5-*c*]pyrimidin-7-yl)ethyl)piperazin-1-yl)phenoxy)-2-oxo-6,9,12,15,18,21,24,27,30,33,36,39-dodecaoxa-3-azahentetracontan-41-oat in DMSO-d_6

^{1}H-NMR 1-(4-(4-(2-(5-amino-2-(furan-2-yl)-7H-pyrazolo[4,3-e][1,2,4]triazolo[1,5-c]pyrimidin-7-yl)ethyl)piperazin-1-yl)phenoxy)-2-oxo-6,9,12,15,18,21,24,27,30,33,36,39,42,45,48,51-hexadecaoxa-3-azatripentacontan-53-oate in DMSO-d_6

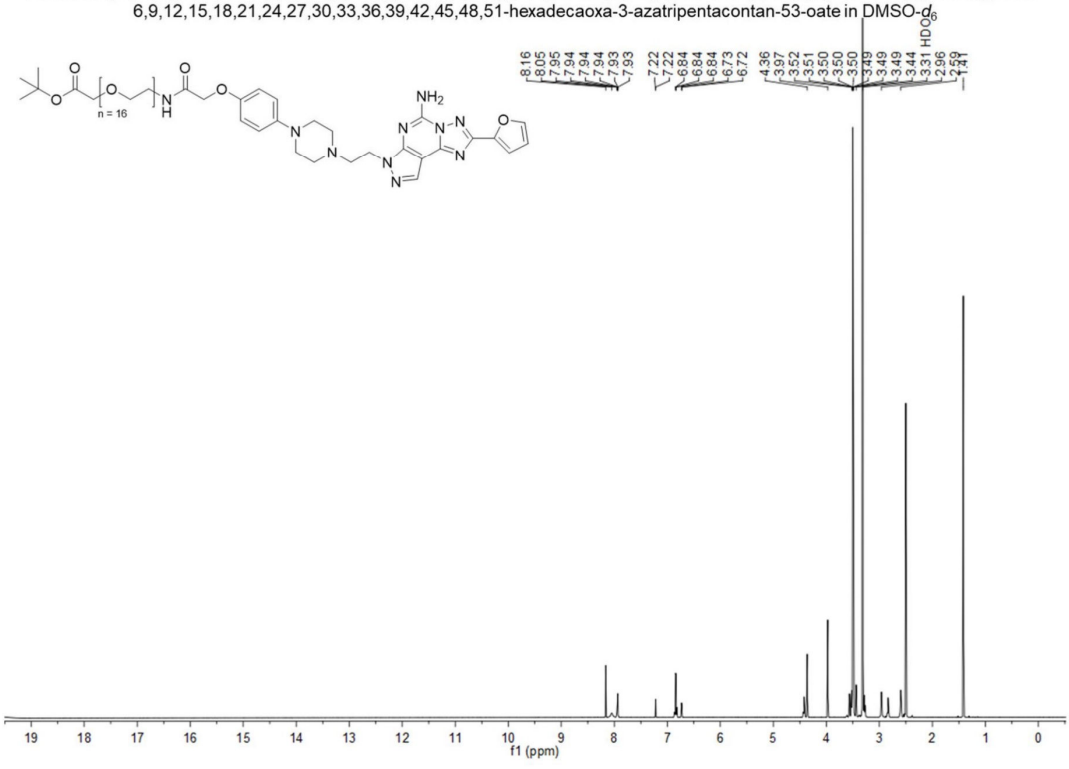

^{13}C-NMR 1-(4-(4-(2-(5-amino-2-(furan-2-yl)-7H-pyrazolo[4,3-e][1,2,4]triazolo[1,5-c]pyrimidin-7-yl)ethyl)piperazin-1-yl)phenoxy)-2-oxo-6,9,12,15,18,21,24,27,30,33,36,39,42,45,48,51-hexadecaoxa-3-azatripentacontan-53-oate in DMSO-d_6

^{1}H-NMR 1-(4-(4-(2-(5-amino-2-(furan-2-yl)-7H-pyrazolo[4,3-e][1,2,4]triazolo[1,5-c]pyrimidin-7-yl)ethyl)piperazin-1-yl)phenoxy)-2-oxo-6,9,12,15,18,21,24,27,30,33,36,39,42,45,48,51,54,57,60,63-icosaoxa-3-azapentahexacontan-65-oate in DMSO-d_6

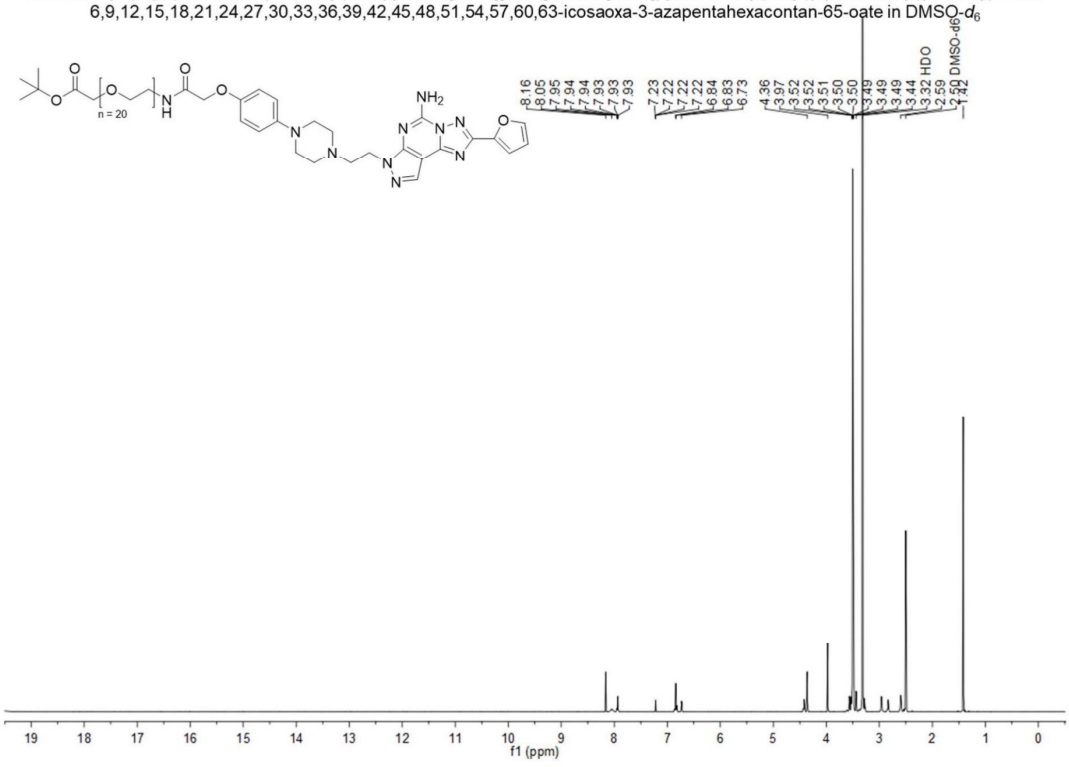

^{13}C-NMR 1-(4-(4-(2-(5-amino-2-(furan-2-yl)-7H-pyrazolo[4,3-e][1,2,4]triazolo[1,5-c]pyrimidin-7-yl)ethyl)piperazin-1-yl)phenoxy)-2-oxo-6,9,12,15,18,21,24,27,30,33,36,39,42,45,48,51,54,57,60,63-icosaoxa-3-azapentahexacontan-65-oate in DMSO-d_6

^{1}H-NMR 1-(4-(4-(2-(5-Amino-2-(furan-2-yl)-7*H*-pyrazolo[4,3-*e*][1,2,4]triazolo[1,5-*c*]pyrimidin-7-yl)ethyl)piperazin-1-yl)phenoxy)-2-oxo-6,9,12,15-tetraoxa-3-azaheptadecan-17-säure in DMSO-d_6

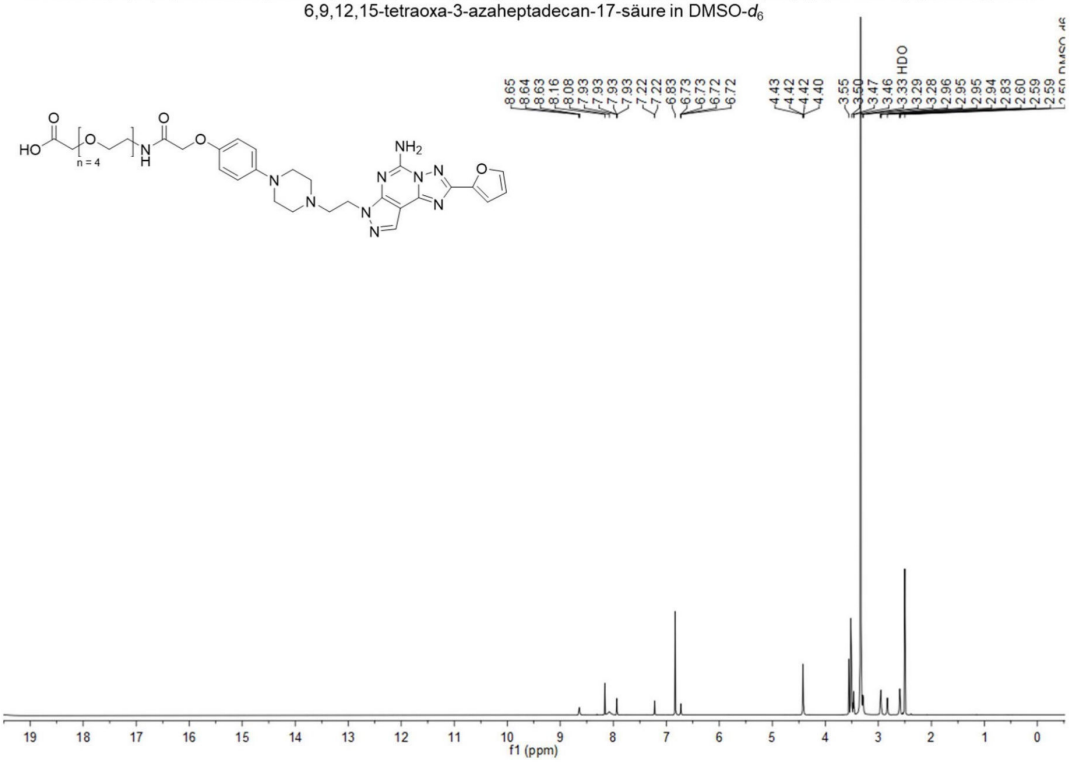

^{13}C-NMR 1-(4-(4-(2-(5-Amino-2-(furan-2-yl)-7*H*-pyrazolo[4,3-*e*][1,2,4]triazolo[1,5-*c*]pyrimidin-7-yl)ethyl)piperazin-1-yl)phenoxy)-2-oxo-6,9,12,15-tetraoxa-3-azaheptadecan-17-säure in DMSO-d_6

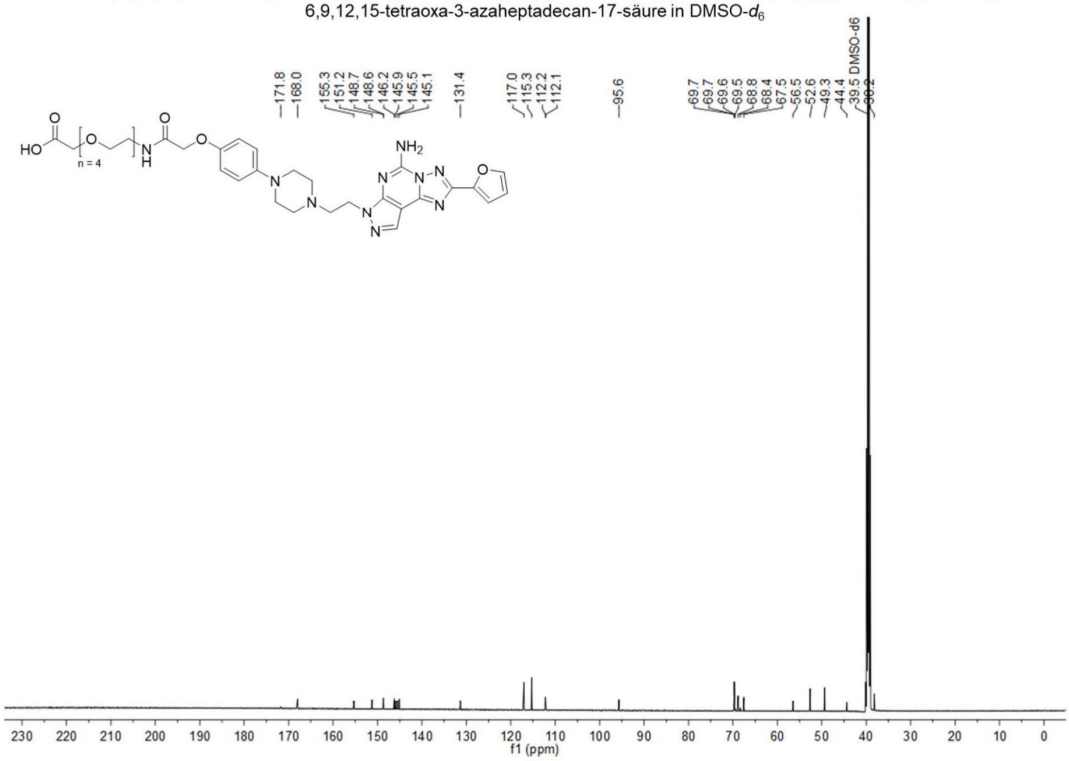

^{1}H-NMR 14-(2-(4-(4-(2-(5-Amino-2-(furan-2-yl)-7*H*-pyrazolo[4,3-*e*][1,2,4]triazolo[1,5-*c*]pyrimidin-7-yl)ethyl)piperazin-1-yl)phenoxy)acetamido)-*N*-(5-(5,5-difluoro-1,3,7,9-tetramethyl-5*H*-4*l*4,5*l*4-dipyrrolo[1,2-*c*:2',1'-*f*][1,3,2]diazaborinin-10-yl)pentyl)-3,6,9,12-tetraoxatetradecanamid in DMSO-d_6

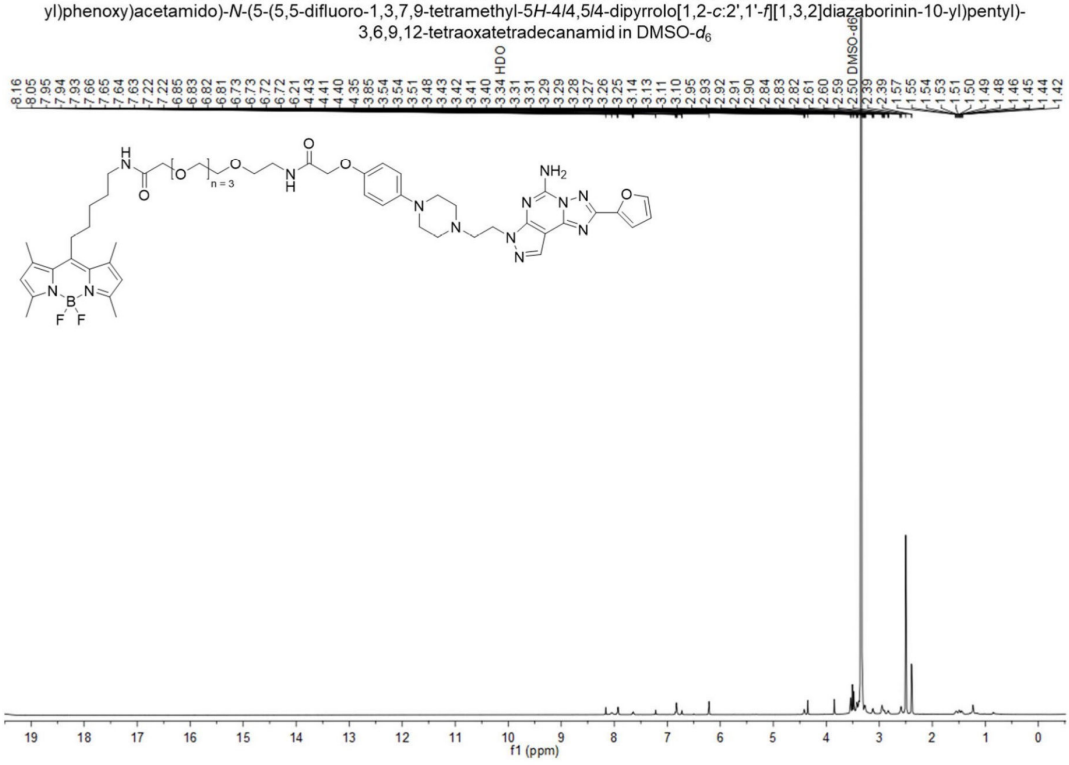

^{13}C-NMR 14-(2-(4-(4-(2-(5-Amino-2-(furan-2-yl)-7*H*-pyrazolo[4,3-*e*][1,2,4]triazolo[1,5-*c*]pyrimidin-7-yl)ethyl)piperazin-1-yl)phenoxy)acetamido)-*N*-(5-(5,5-difluoro-1,3,7,9-tetramethyl-5*H*-4*l*4,5*l*4-dipyrrolo[1,2-*c*:2',1'-*f*][1,3,2]diazaborinin-10-yl)pentyl)-3,6,9,12-tetraoxatetradecanamid in DMSO-d_6

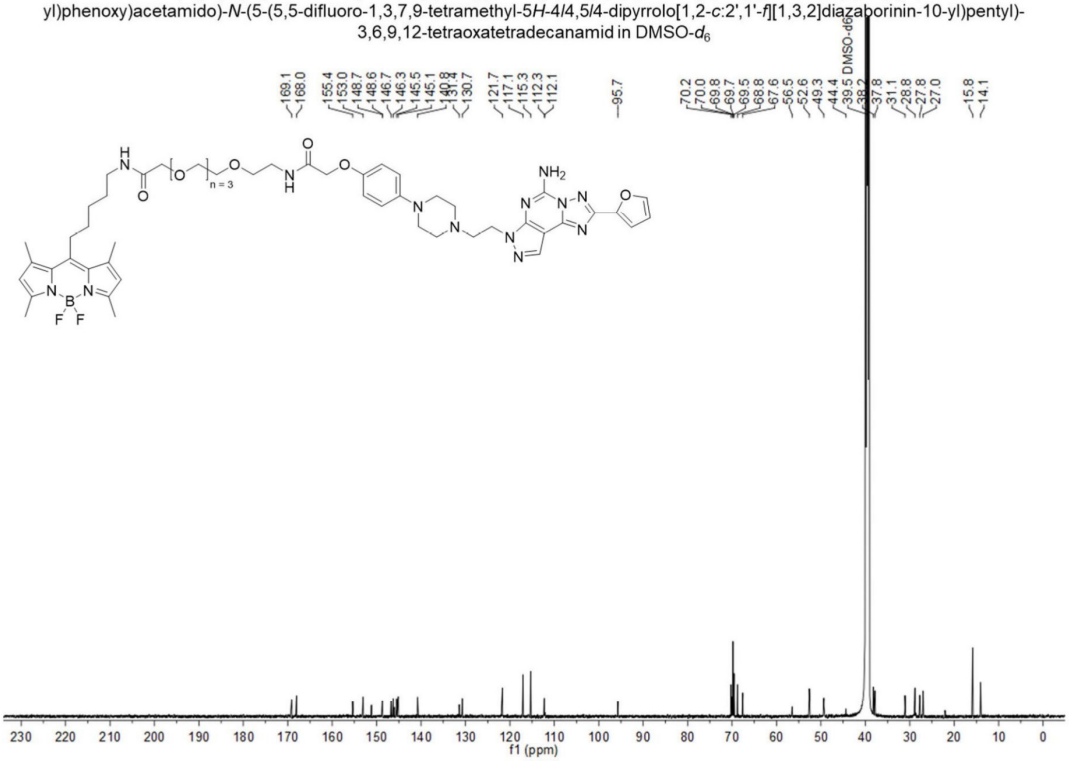

^{1}H-NMR *tert*-Butyl-4-(piperazin-1-yl)benzoat in $CDCl_3$

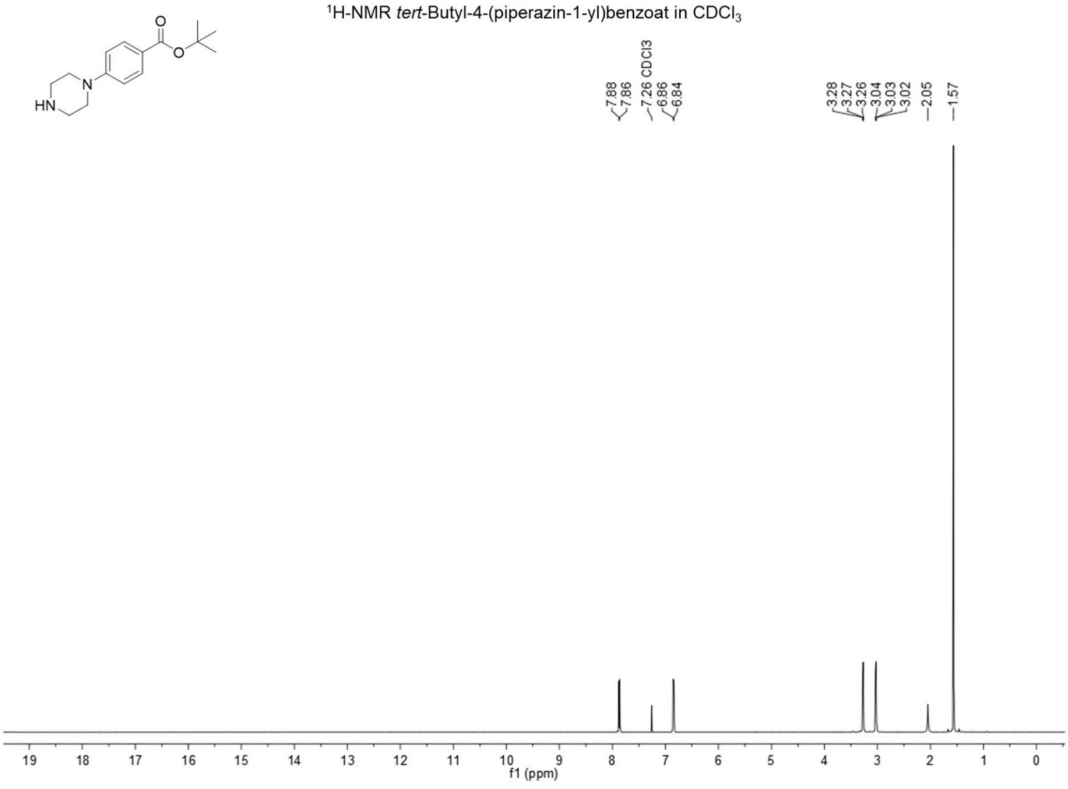

^{13}C-NMR *tert*-Butyl-4-(piperazin-1-yl)benzoat in $CDCl_3$

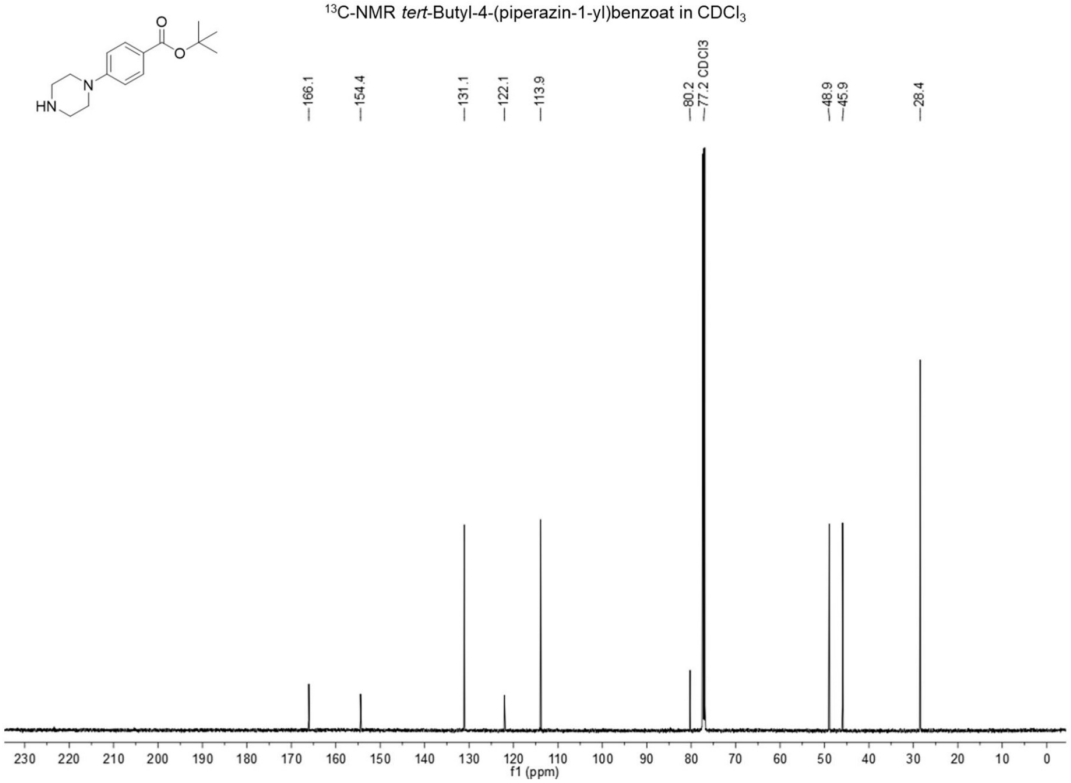

^{1}H-NMR Benzyl-4-(4-(2-(*tert*-butoxy)-2-oxoethoxy)phenyl)piperazin-1-carboxylat in DMSO-d_6

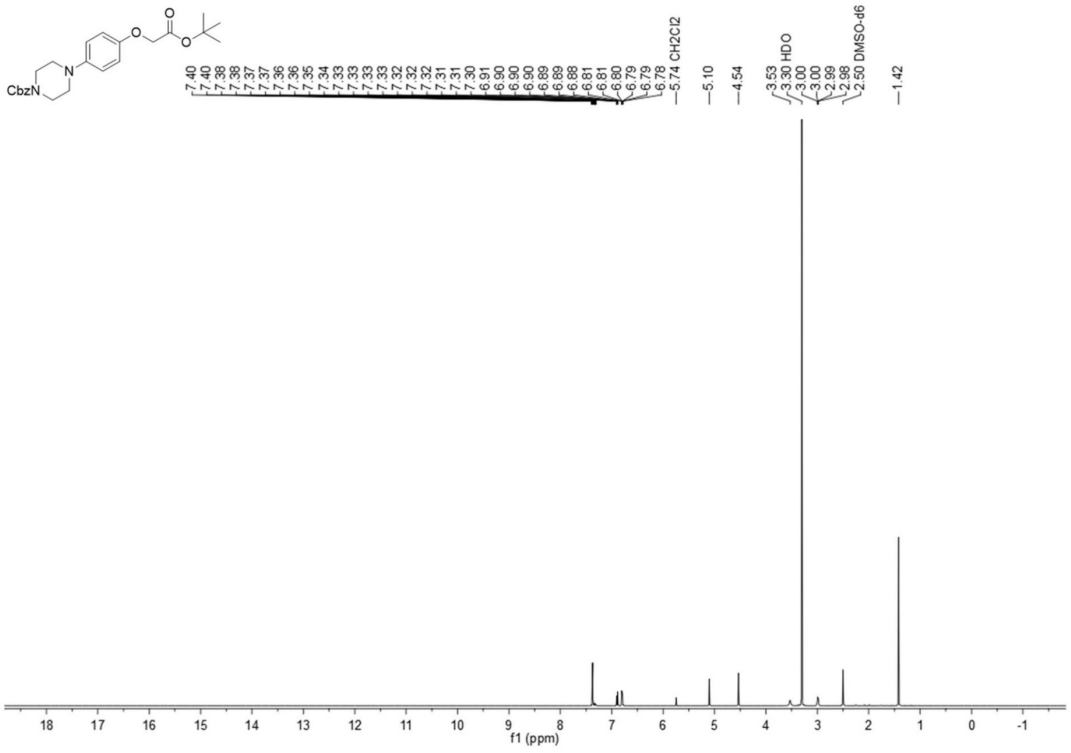

^{13}C-NMR Benzyl-4-(4-(2-(*tert*-butoxy)-2-oxoethoxy)phenyl)piperazin-1-carboxylat in DMSO-d_6

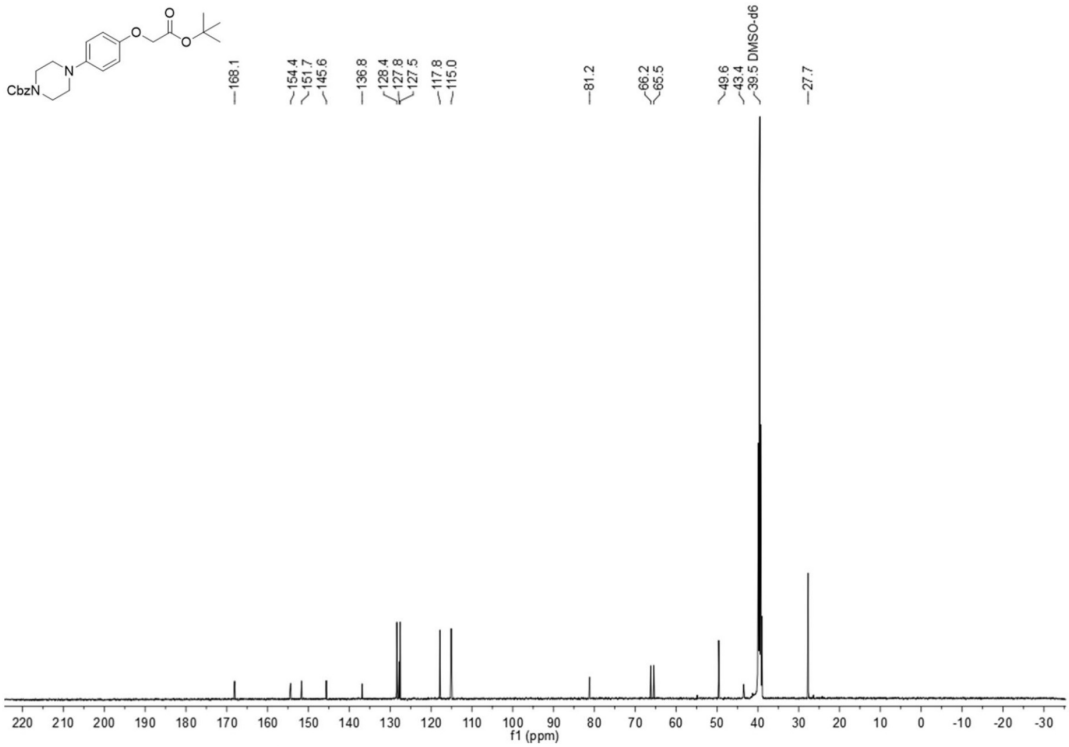

^{1}H-NMR *tert*-Butyl-2-(4-(piperazin-1-yl)phenoxy)acetat in DMSO-d_6

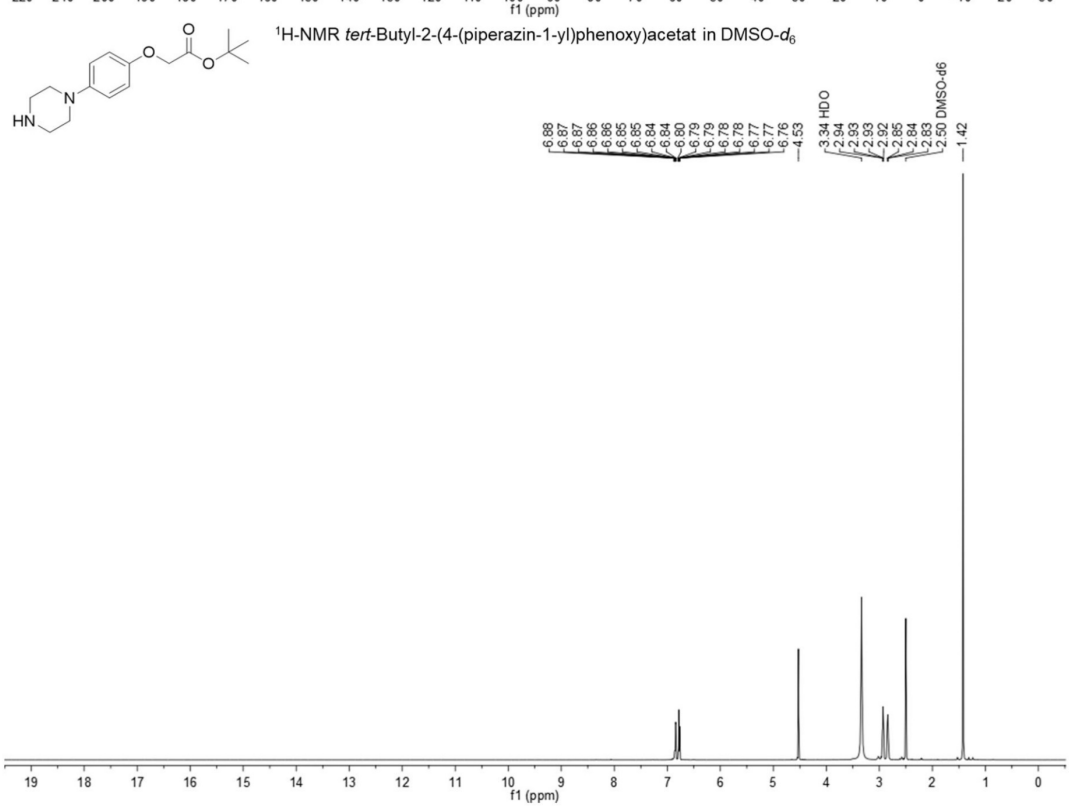

^{13}C-NMR *tert*-Butyl-2-(4-(piperazin-1-yl)phenoxy)acetat in DMSO-d_6

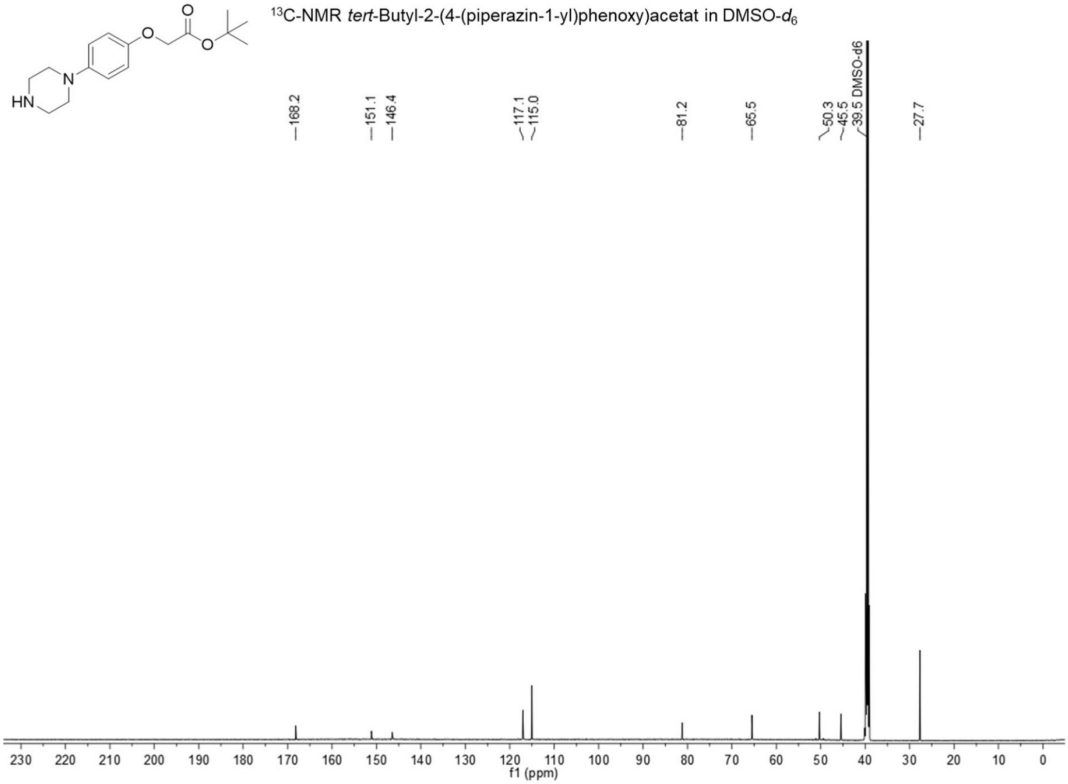

^{1}H-NMR (*E*/*Z*)-*N*'-(6-Chloro-5-formyl-2-imino-2,3-dihydropyrimidin-4(1*H*)-yliden)furan-2-carbohydrazid in DMSO-d_6

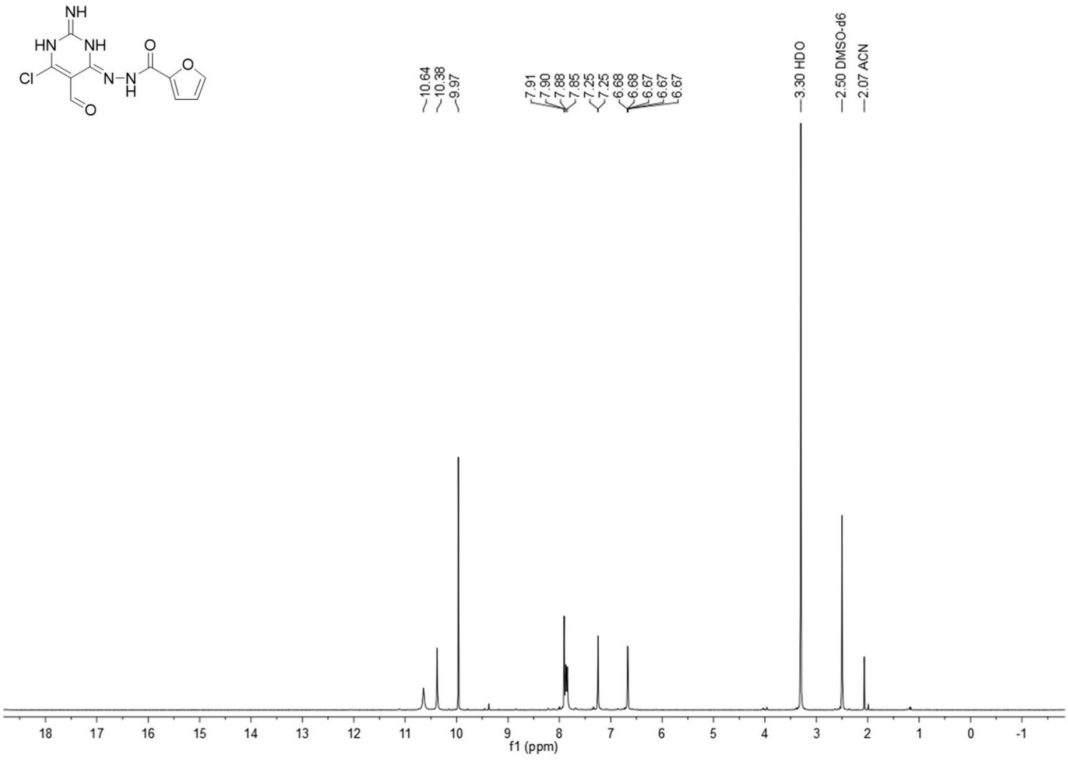

^{13}C-NMR (*E*/*Z*)-*N*'-(6-Chloro-5-formyl-2-imino-2,3-dihydropyrimidin-4(1*H*)-yliden)furan-2-carbohydrazid in DMSO-d_6

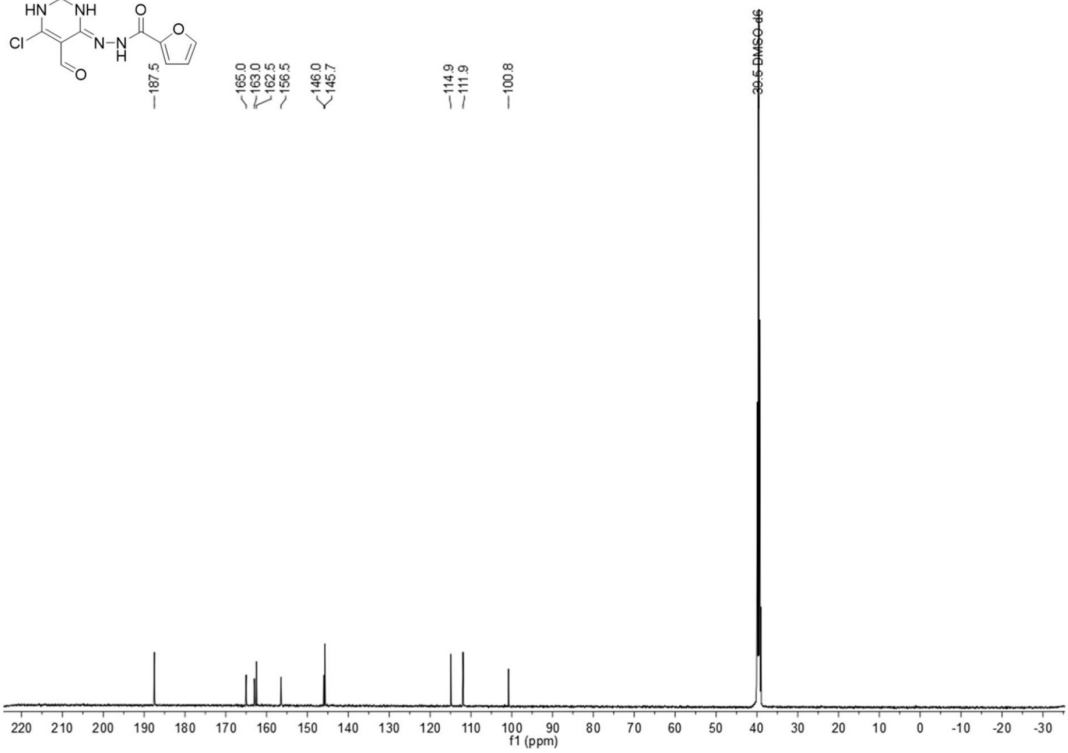

^{1}H-NMR 2-(Furan-2-yl)-7*H*-pyrazolo[4,3-*e*][1,2,4]triazolo[1,5-*c*]pyrimidin-5-amin in DMSO-d_6

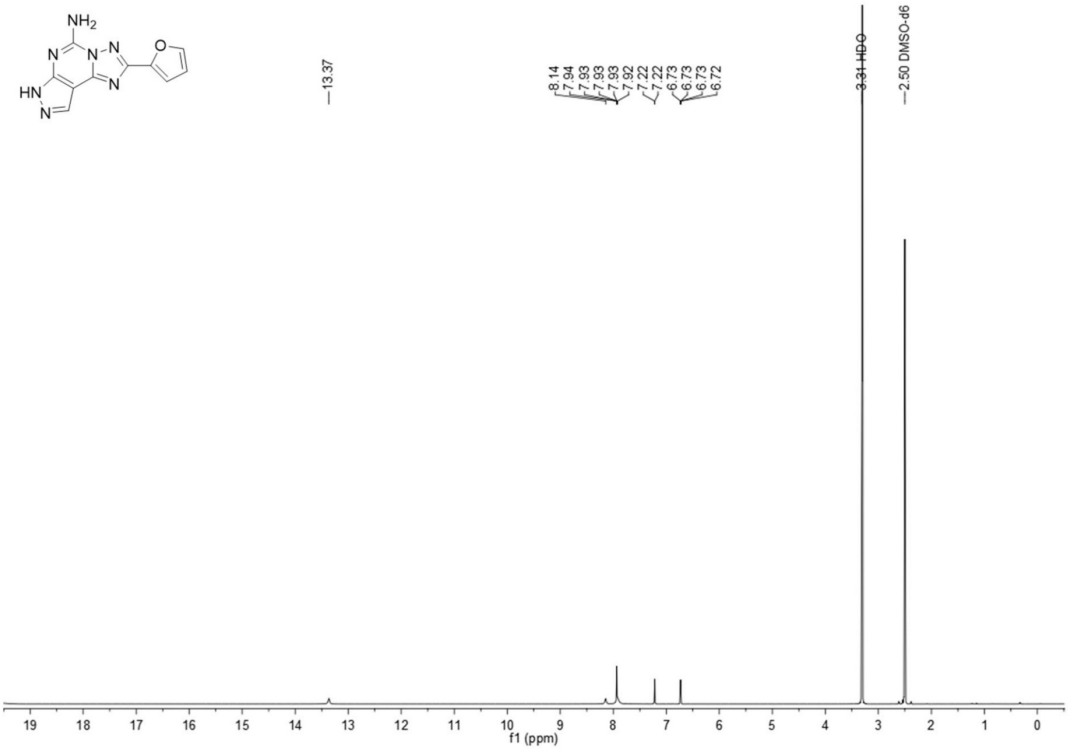

^{13}C-NMR 2-(Furan-2-yl)-7*H*-pyrazolo[4,3-*e*][1,2,4]triazolo[1,5-*c*]pyrimidin-5-amin in DMSO-d_6

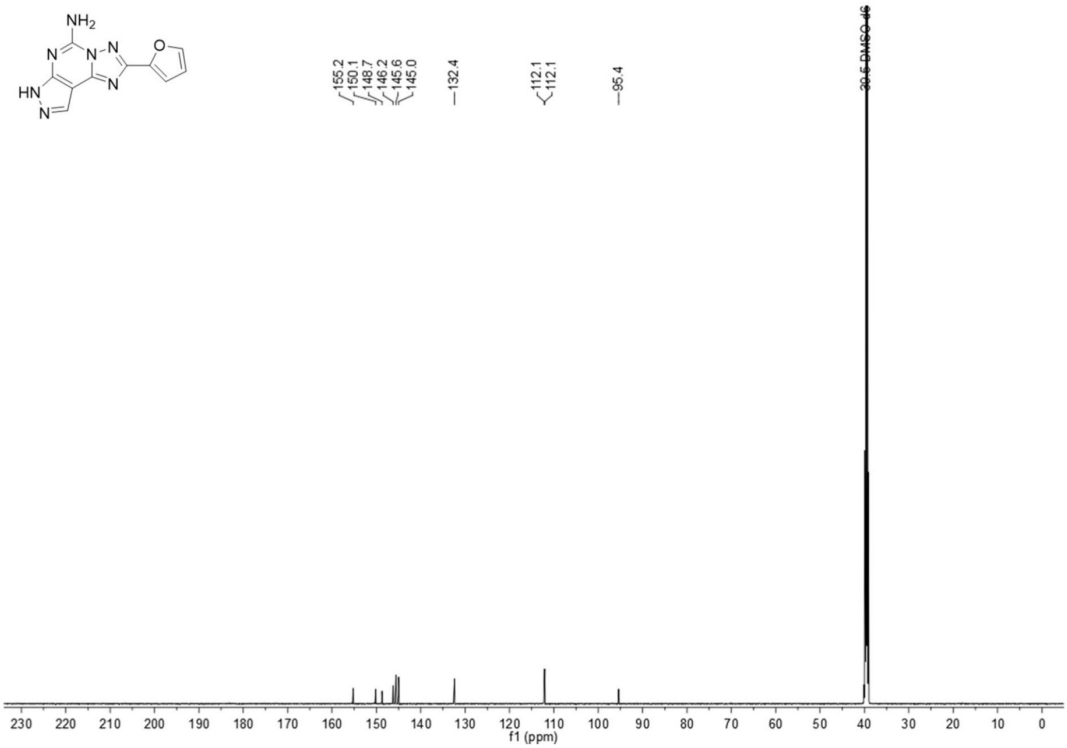

^{1}H-NMR 2-(5-Amino-2-(furan-2-yl)-7*H*-pyrazolo[4,3-*e*][1,2,4]triazolo[1,5-*c*]pyrimidin-7-yl)-ethyl-4-methylbenzenesulfonat in DMSO-d_6

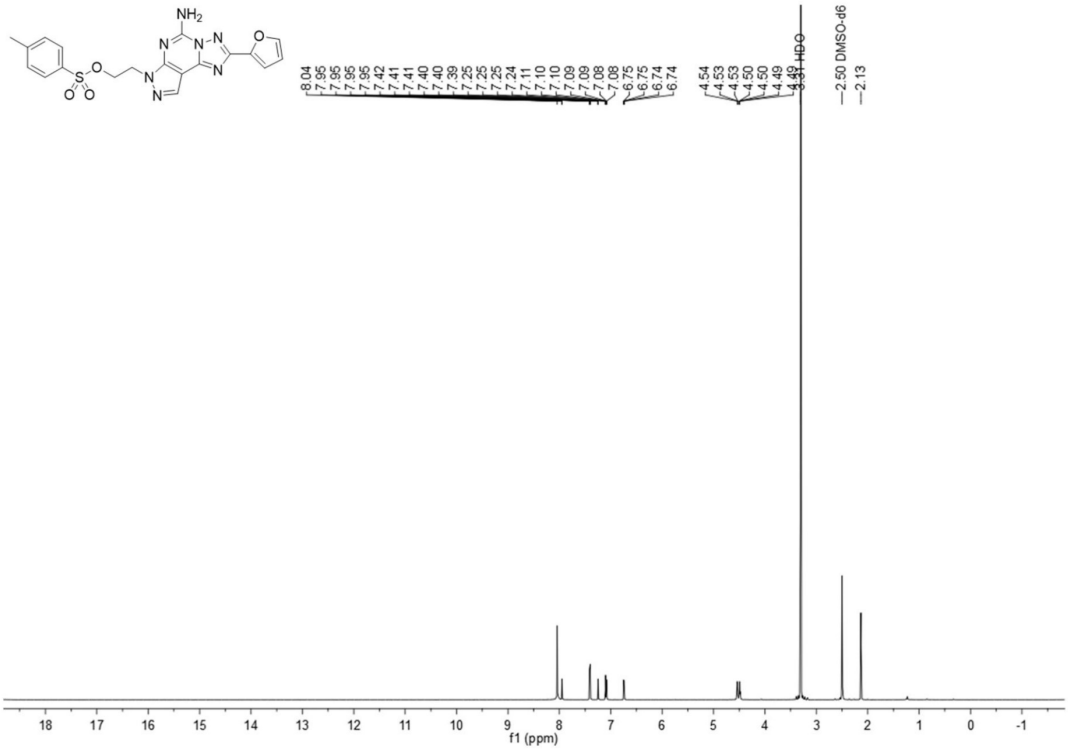

^{13}C-NMR 2-(5-Amino-2-(furan-2-yl)-7*H*-pyrazolo[4,3-*e*][1,2,4]triazolo[1,5-*c*]pyrimidin-7-yl)-ethyl-4-methylbenzenesulfonat in DMSO-d_6

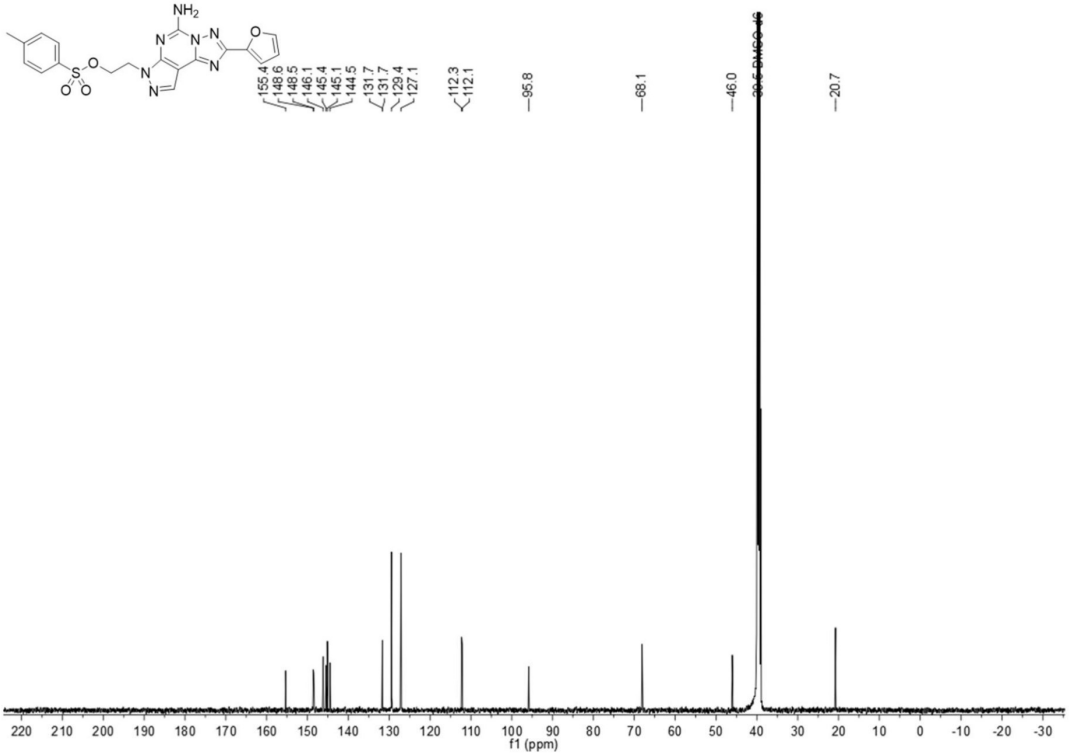

^{1}H-NMR *tert*-Butyl-14-amino-3,6,9,12-tetraoxatetradecanoat in DMSO-d_6

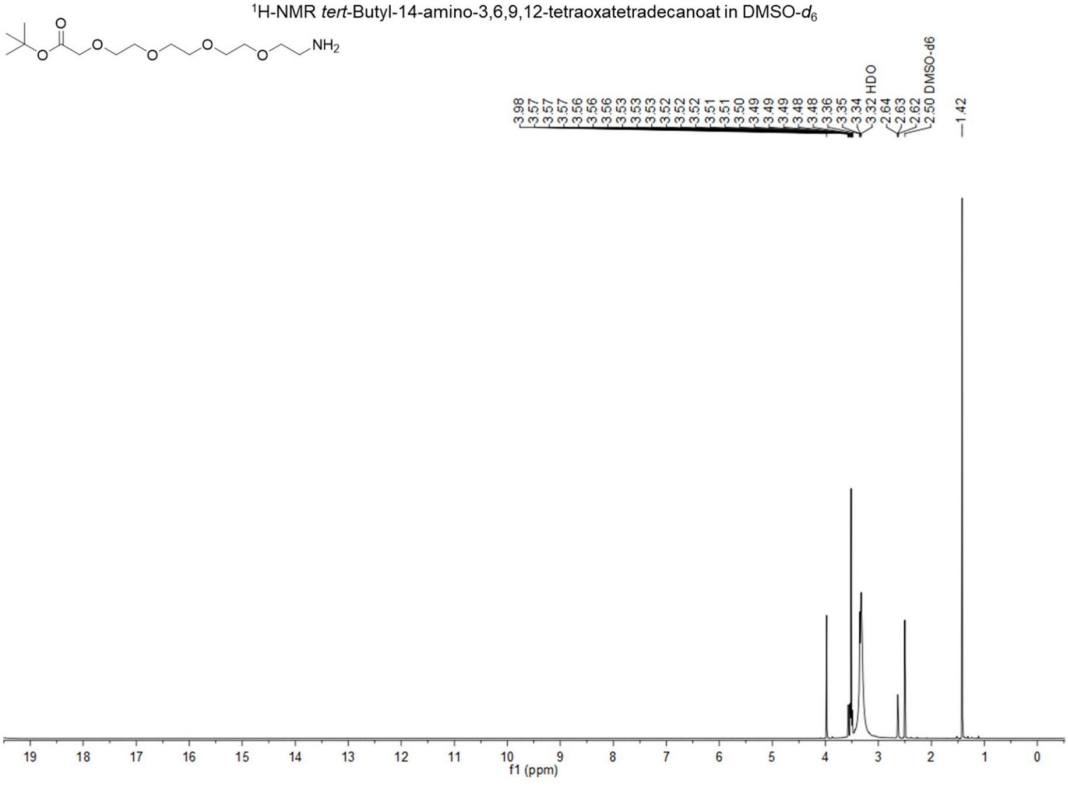

^{13}C-NMR *tert*-Butyl-14-amino-3,6,9,12-tetraoxatetradecanoat in DMSO-d_6

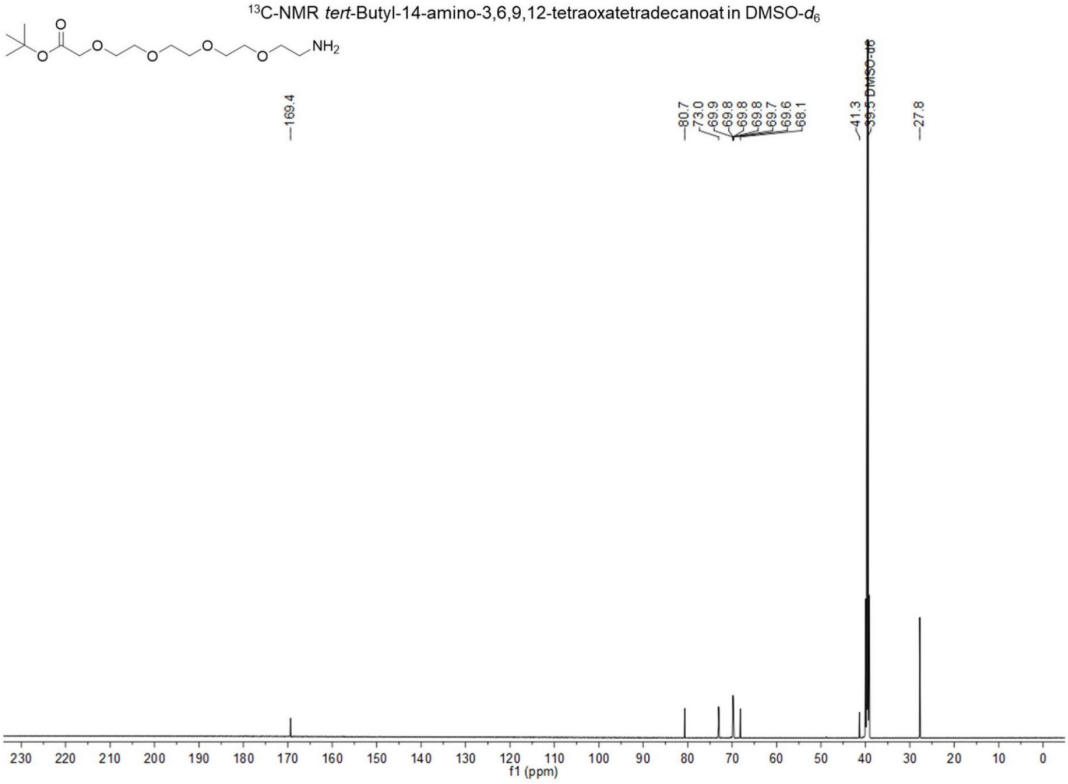

^{1}H-NMR *tert*-Butyl-17-amino-3,6,9,12,15-pentaoxaheptadecanoat in DMSO-d_6

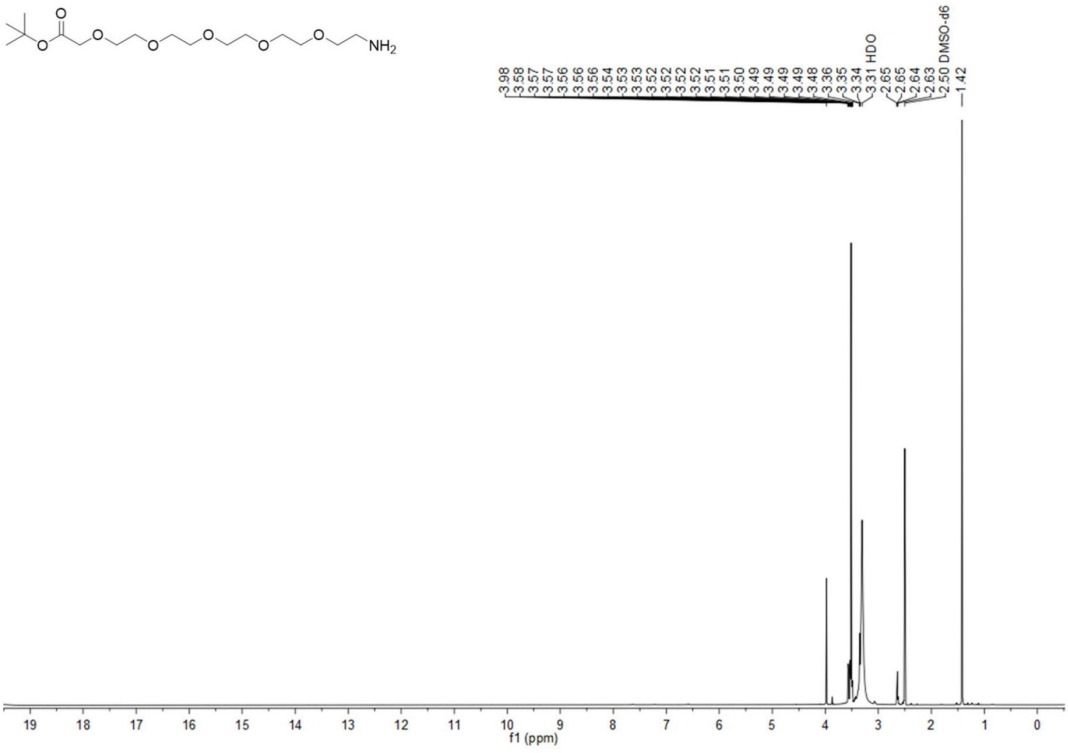

^{13}C-NMR *tert*-Butyl-17-amino-3,6,9,12,15-pentaoxaheptadecanoat in DMSO-d_6

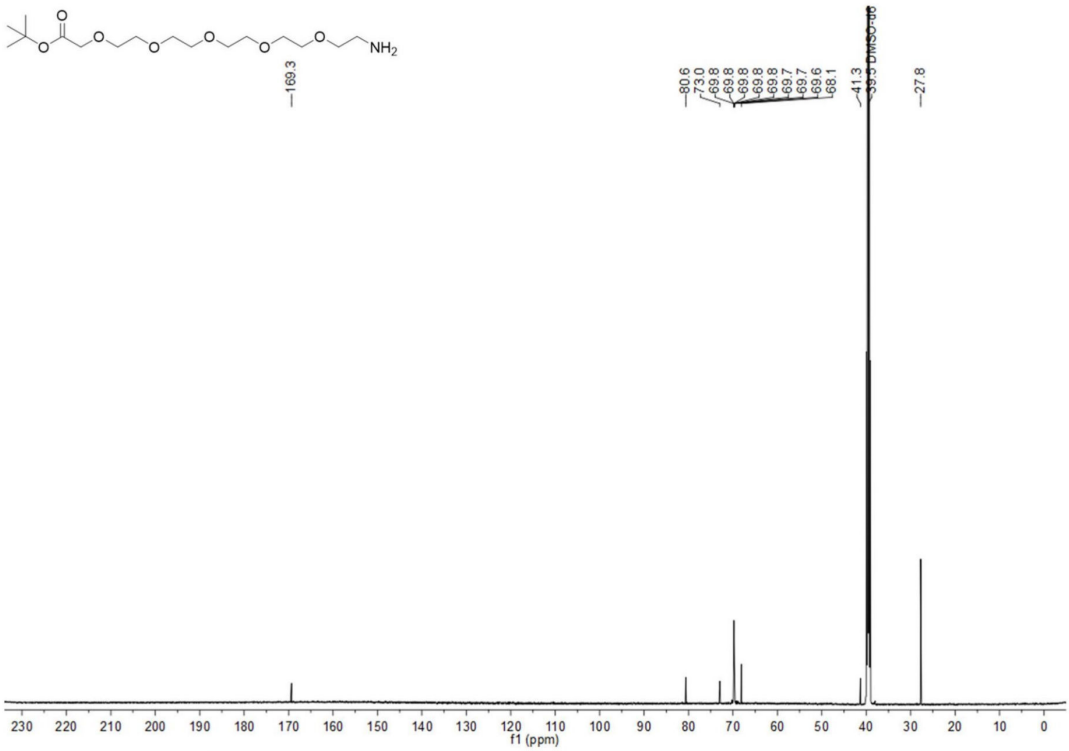

^{1}H-NMR *tert*-Butyl-26-amino-3,6,9,12,15,18,21,24-octaoxahexacosanoat in DMSO-d_6

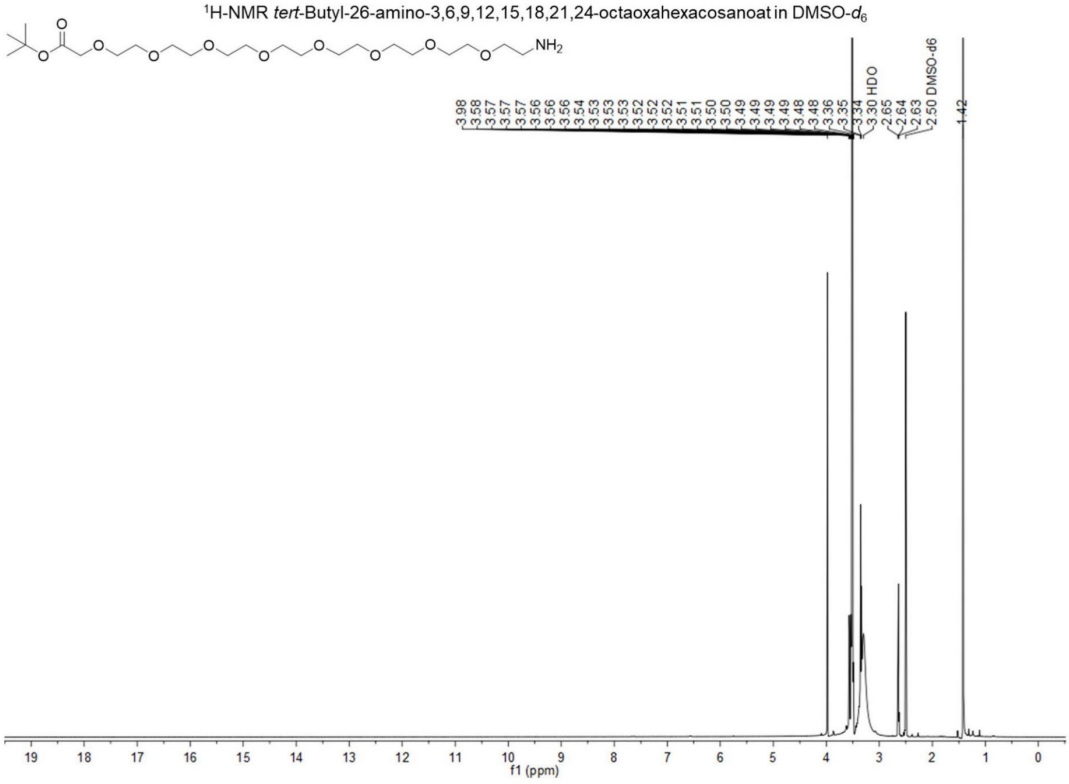

^{13}C-NMR *tert*-Butyl-26-amino-3,6,9,12,15,18,21,24-octaoxahexacosanoat in DMSO-d_6

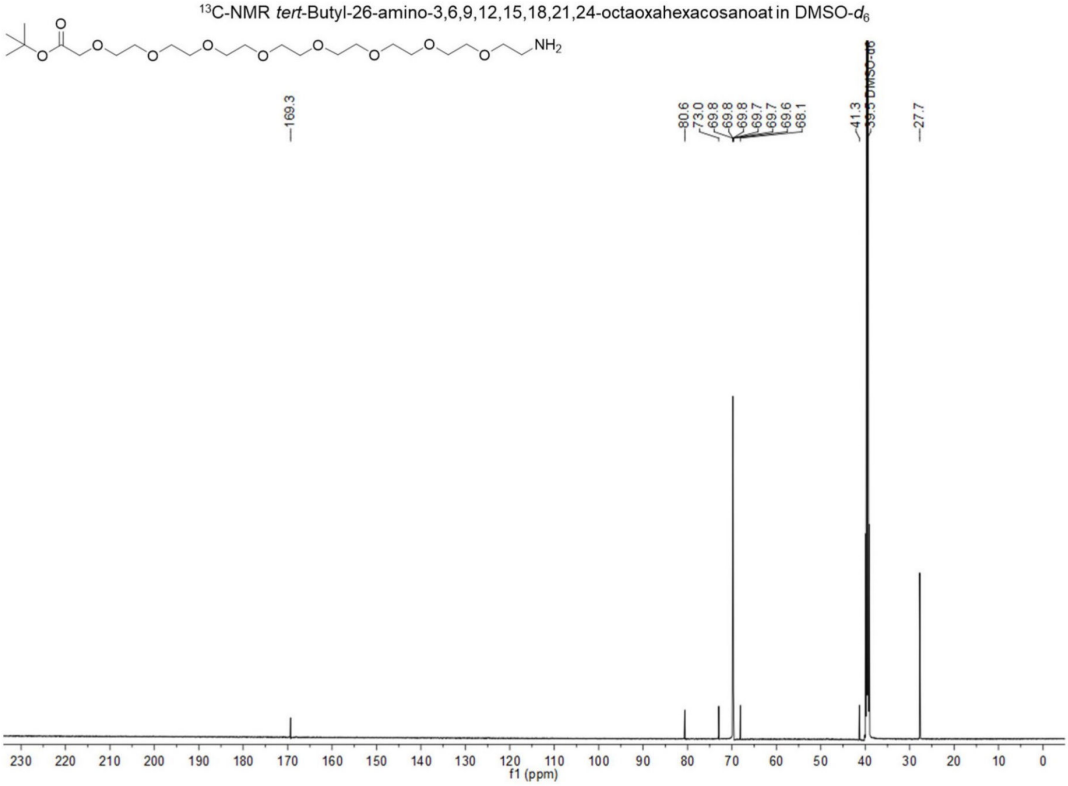

^{1}H-NMR *tert*-Butyl-38-amino-3,6,9,12,15,18,21,24,27,30,33,36-dodecaoxaoctatriacontanoat in DMSO-d_6

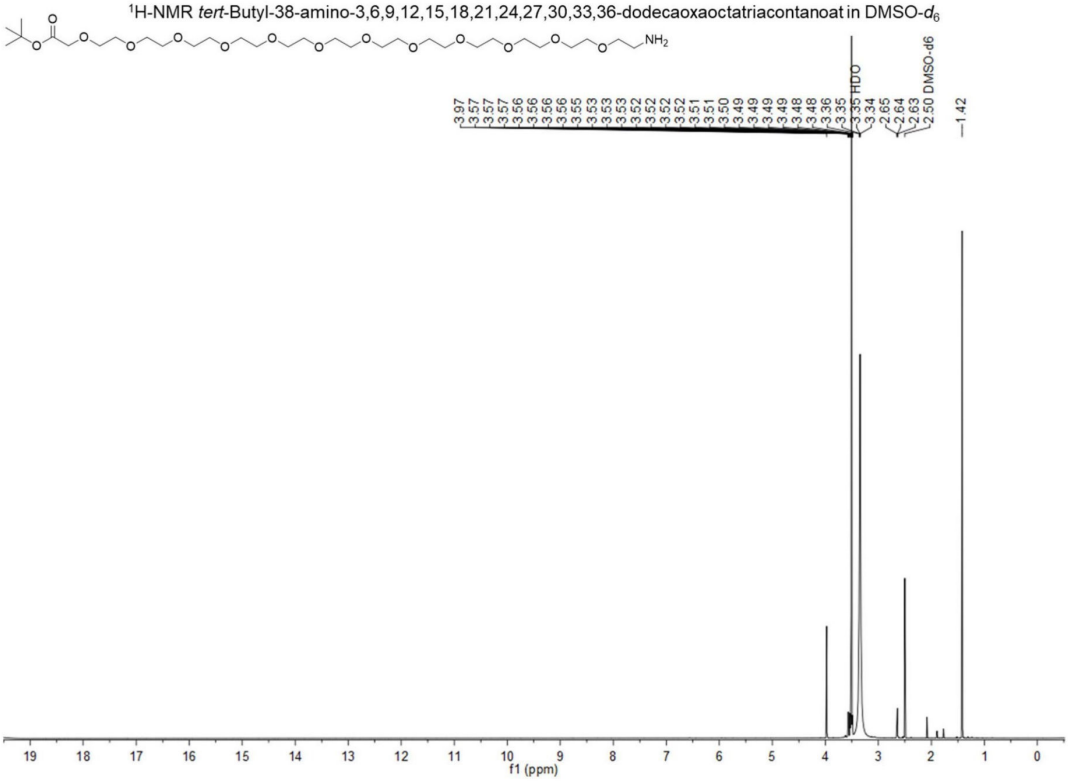

^{13}C-NMR *tert*-Butyl-38-amino-3,6,9,12,15,18,21,24,27,30,33,36-dodecaoxaoctatriacontanoat in DMSO-d_6

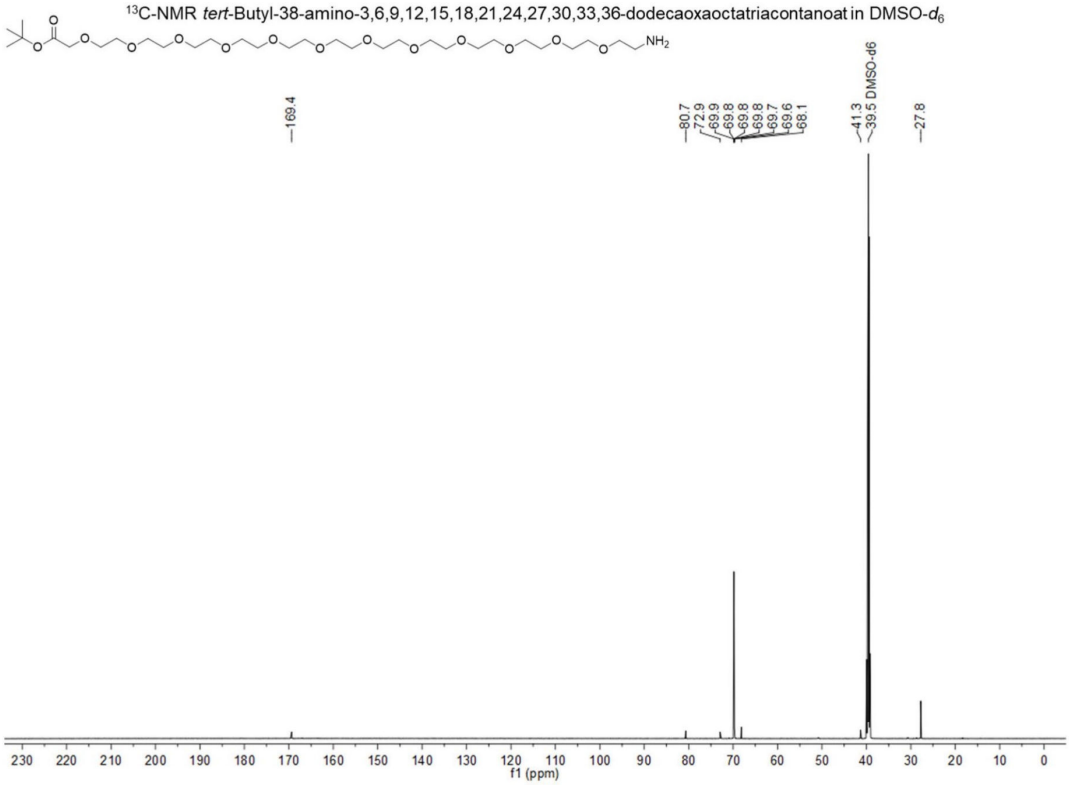

^{1}H-NMR *tert*-Butyl-50-amino-3,6,9,12,15,18,21,24,27,30,33,36,39,42,45,48-hexadecaoxapentacontanoat in DMSO-d_6

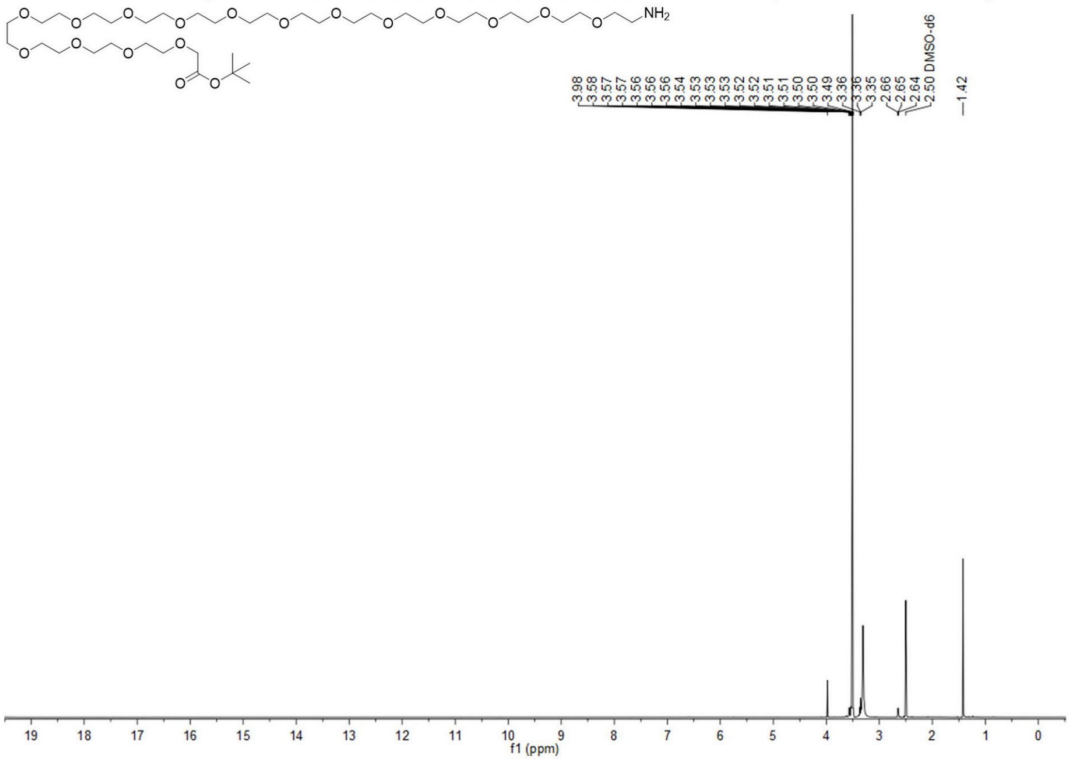

^{13}C-NMR *tert*-Butyl-50-amino-3,6,9,12,15,18,21,24,27,30,33,36,39,42,45,48-hexadecaoxapentacontanoat in DMSO-d_6

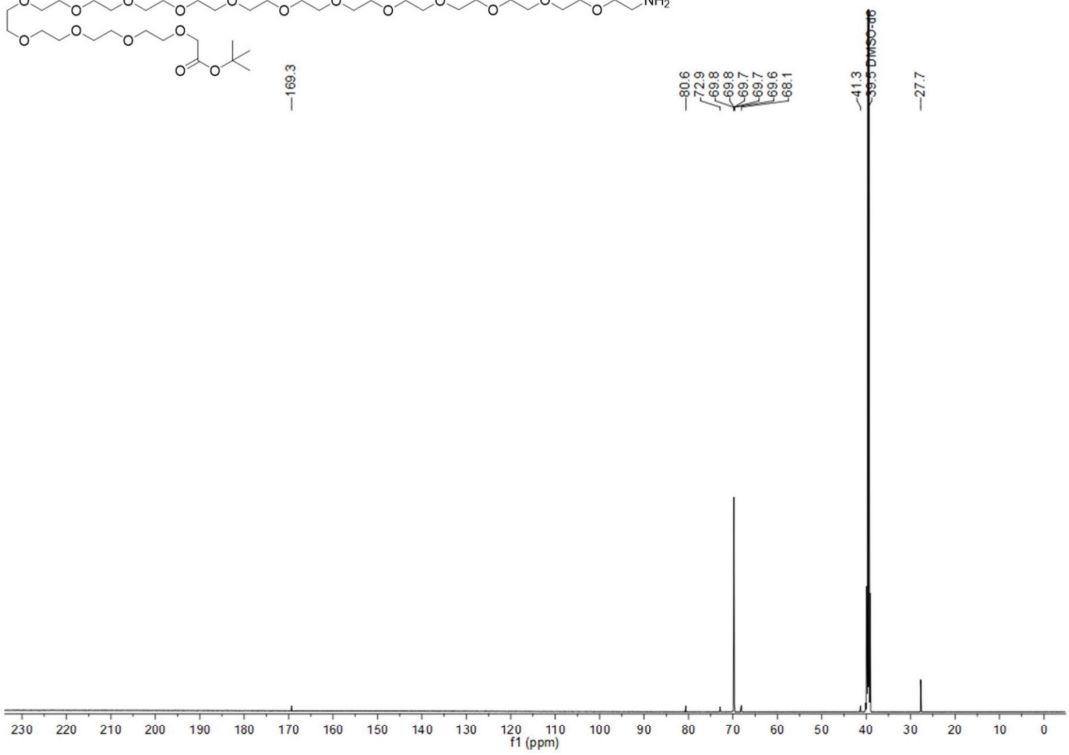

^{1}H-NMR *tert*-Butyl-62-amino-3,6,9,12,15,18,21,24,27,30,33,36,39,42,45,48,51,54,57,60-icosaoxadohexacontanoat in DMSO-d_6

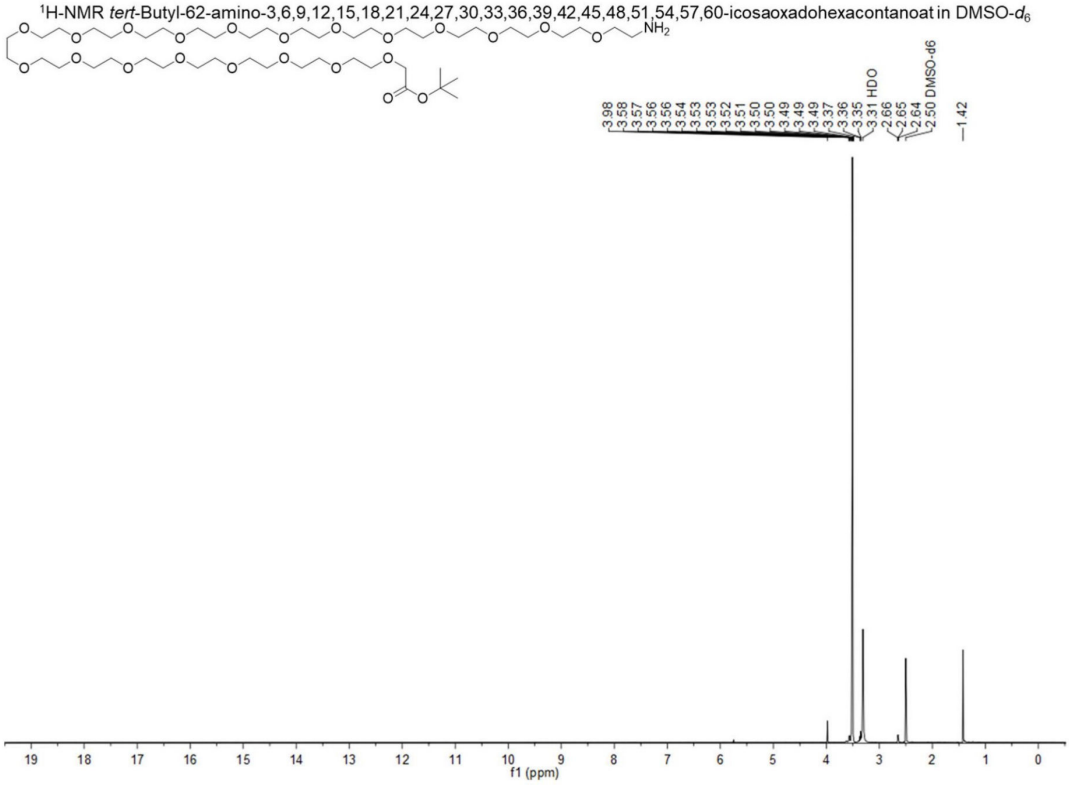

^{13}C-NMR *tert*-Butyl-62-amino-3,6,9,12,15,18,21,24,27,30,33,36,39,42,45,48,51,54,57,60-icosaoxadohexacontanoat in DMSO-d_6

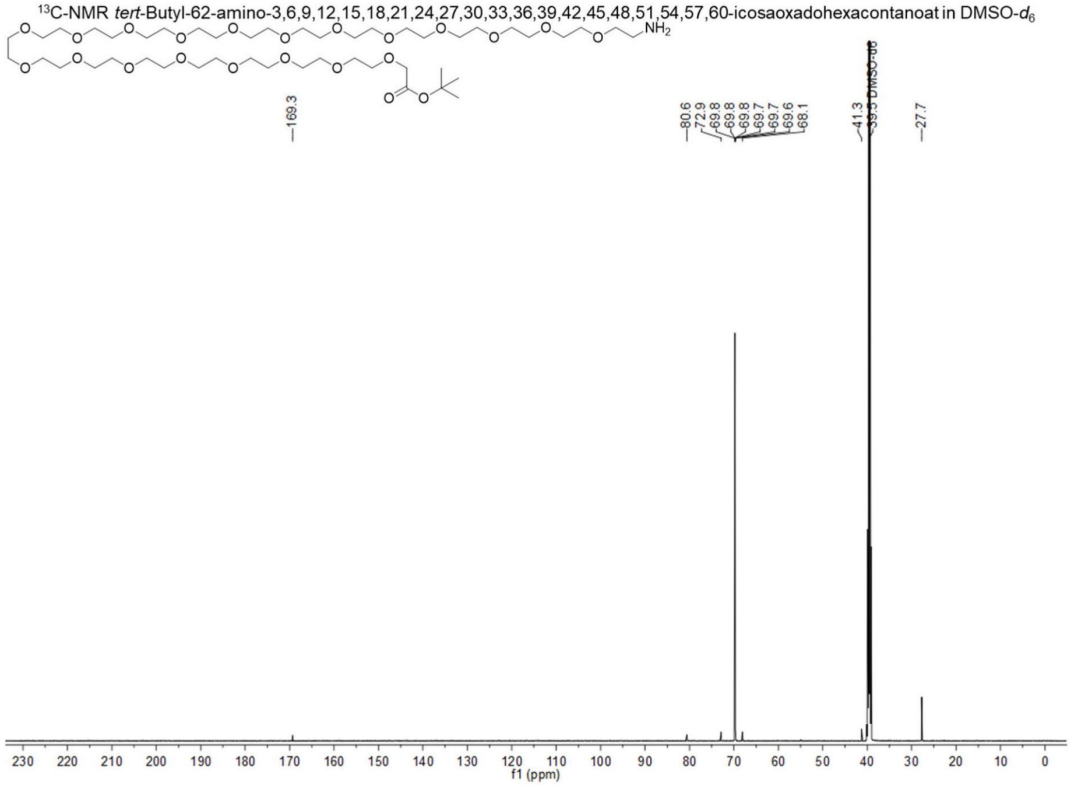

Appendix III. DNA Sequences

Mutations are highlighted in blue. Expression and purification tags are underlined.

DNA Sequence of the A_{2A}-PSB1-bRIL Coding Region

ATGAAGACGATCATCGCCCTGAGCTACATCTTCTGCCTGGTGTTCGCCGACTACAAG
GACGATGATGACGGCGCGCCACCCATCATGGGCTCCTCGGTGTACATCACGGTGGAG
CTGGCCATTGCTGTGCTGGCCATCCTGGGCAATGTGCTGGTGTGCTGGGCCGTGTGG
CTCAACAGCAACCTGCAGAACGTCACCAACTACTTTGTGGTGTCACTGGCGGCGGCC
GACATCGCAGTGGGTGTGCTCGCCATCCCCTTTGCCATCACCATCAGCACCGGGTTC
TGCGCTGCCTGCCACGGCTGCCTCTTCATTGCCTGCTTCGTCCTGGTCCTCACGCAG
AGC**AAG**ATCTTCAGTCTCCTGGCCATCGCCATTGACCGCTACATTGCCATCCGCATC
CCGCTCCGGTACAATGGCTTGGTGACCGGCACGAGGGCTAAGGGCATCATTGCCATC
TGCTGGGTGCTGTCGTTTGCCATCGGCCTGACTCCCATGCTAGGTTGGAACAACTGC
GGTCAGCCAAAGGAGGGCAAGAACCACTCCCAGGGCTGCGGGGAGGGCCAAGTGGCC
TGTCTCTTTGAGGATGTGGTCCCCATGAACTACATGGTGTACTTCAACTTCTTTGCC
TGTGTGCTGGTGCCCCTGCTGCTCATGCTGGGTGTCTATTTGCGGATCTTCCTGGCG
GCGCGACGACAGCTGGCTGATCTGGAAGACAATTGGGAAACTCTGAACGACAATCTC
AAGGTGATCGAGAAGGCTGACAATGCTGCACAAGTCAAAGACGCTCTGACCAAGATG
AGGGCAGCAGCCCTGGACGCTCAGAAGGCCACTCCACCTAAGCTCGAGGACAAGAGC
CCAGATAGCCCTGAAATGAAAGACTTTCGGCATGGATTCGACATTCTGGTGGGACAG
ATTGATGATGCACTCAAGCTGGCCAATGAAGGGAAAGTCAAGGAAGCACAAGCAGCC
GCTGAGCAGCTGAAGACCACCCGGAATGCATACATTCAGAAGTACCTGGAGCGCGCT
CGGTCCACACTGCAGAAGGAGGTCCATGCTGCCAAGTCACTGGCCATCATTGTGGGG
CTCTTTGCCCTCTGCTGGCTGCCCCTACACATCATCAACTGCTTCACTTTCTTCTGC
CCCGACTGCAGCCACGCCCCTCTCTGGCTCATGTACCTGGCCATCGTCCTCTCCCAC
ACCAATTCGGTTGTGAATCCCTTCATCTACGCCTACCGTATCCGCGAGTTCCGCCAG
ACCTTCCGCAAGATCATTCGCAGCCACGTCCTGAGGCAGCAAGAACCTTTCAAGGCA
CACCACCATCACCATCACCATCACCATCACTGA

DNA Sequence of the A_{2A}-PSB2-bRIL Coding Region

ATGAAGACGATCATCGCCCTGAGCTACATCTTCTGCCTGGTGTTCGCCGACTACAAG
GACGATGATGACGGCGCGCCACCCATCATGGGCTCCTCGGTGTACATCACGGTGGAG
CTGGCCATTGCTGTGCTGGCCATCCTGGGCAATGTGCTGGTGTGCTGGGCCGTGTGG
CTCAACAGCAACCTGCAGAACGTCACCAACTACTTTGTGGTGTCACTGGCGGCGGCC
GACATCGCAGTGGGTGTGCTCGCCATCCCCTTTGCCATCACCATCAGCACCGGGTTC
TGCGCTGCCTGCCACGGCTGCCTCTTCATTGCCTGCTTCGTCCTGGTCCTCACGCAG
AGC**AAG**ATCTTCAGTCTCCTGGCCATCGCCATTGACCGCTACATTGCCATCCGCATC
CCGCTCCGGTACAATGGCTTGGTGACCGGCACGAGGGCTAAGGGCATCATTGCCATC
TGCTGGGTGCTGTCGTTTGCCATCGGCCTGACTCCCATGCTAGGTTGGAACAACTGC
GGTCAGCCAAAGGAGGGCAAG**GCT**CACTCCCAGGGCTGCGGGGAGGGCCAAGTGGCC
TGTCTCTTTGAGGATGTGGTCCCCATGAACTACATGGTGTACTTCAACTTCTTTGCC
TGTGTGCTGGTGCCCCTGCTGCTCATGCTGGGTGTCTATTTGCGGATCTTCCTGGCG
GCGCGACGACAGCTGGCTGATCTGGAAGACAATTGGGAAACTCTGAACGACAATCTC
AAGGTGATCGAGAAGGCTGACAATGCTGCACAAGTCAAAGACGCTCTGACCAAGATG
AGGGCAGCAGCCCTGGACGCTCAGAAGGCCACTCCACCTAAGCTCGAGGACAAGAGC
CCAGATAGCCCTGAAATGAAAGACTTTCGGCATGGATTCGACATTCTGGTGGGACAG
ATTGATGATGCACTCAAGCTGGCCAATGAAGGGAAAGTCAAGGAAGCACAAGCAGCC
GCTGAGCAGCTGAAGACCACCCGGAATGCATACATTCAGAAGTACCTGGAGCGCGCT
CGGTCCACACTGCAGAAGGAGGTCCATGCTGCCAAGTCACTGGCCATCATTGTGGGG
CTCTTTGCCCTCTGCTGGCTGCCCCTACACATCATCAACTGCTTCACTTTCTTCTGC
CCCGACTGCAGCCACGCCCCTCTCTGGCTCATGTACCTGGCCATCGTCCTCTCCCAC
ACCAATTCGGTTGTGAATCCCTTCATCTACGCCTACCGTATCCGCGAGTTCCGCCAG
ACCTTCCGCAAGATCATTCGCAGCCACGTCCTGAGGCAGCAAGAACCTTTCAAGGCA
CACCACCATCACCATCACCATCACCATCACTGA

DNA Sequence of the A_{2A}-ΔC Coding Region

ATGAAGACGATCATCGCCCTGAGCTACATCTTCTGCCTGGTGTTCGCCGACTACAAG
GACGATGATGACGGCGCGCCACCCATCATGGGCTCCTCGGTGTACATCACGGTGGAG
CTGGCCATTGCTGTGCTGGCCATCCTGGGCAATGTGCTGGTGTGCTGGGCCGTGTGG
CTCAACAGCAACCTGCAGAACGTCACCAACTACTTTGTGGTGTCACTGGCGGCGGCC
GACATCGCAGTGGGTGTGCTCGCCATCCCCTTTGCCATCACCATCAGCACCGGGTTC
TGCGCTGCCTGCCACGGCTGCCTCTTCATTGCCTGCTTCGTCCTGGTCCTCACGCAG
AGCTCCATCTTCAGTCTCCTGGCCATCGCCATTGACCGCTACATTGCCATCCGCATC
CCGCTCCGGTACAATGGCTTGGTGACCGGCACGAGGGCTAAGGGCATCATTGCCATC
TGCTGGGTGCTGTCGTTTGCCATCGGCCTGACTCCCATGCTAGGTTGGAACAACTGC
GGTCAGCCAAAGGAGGGCAAGAACCACTCCCAGGGCTGCGGGGAGGGCCAAGTGGCC
TGTCTCTTTGAGGATGTGGTCCCCATGAACTACATGGTGTACTTCAACTTCTTTGCC
TGTGTGCTGGTGCCCCTGCTGCTCATGCTGGGTGTCTATTTGCGGATCTTCCTGGCG
GCGCGACGACAGCTGAAGCAGATGGAGAGCCAGCCCCTGCCCGGTGAGCGCGCTCGG
TCCACACTGCAGAAGGAGGTCCATGCTGCCAAGTCACTGGCCATCATTGTGGGGCTC
TTTGCCCTCTGCTGGCTGCCCCTACACATCATCAACTGCTTCACTTTCTTCTGCCCC
GACTGCAGCCACGCCCCTCTCTGGCTCATGTACCTGGCCATCGTCCTCTCCCACACC
AATTCGGTTGTGAATCCCTTCATCTACGCCTACCGTATCCGCGAGTTCCGCCAGACC
TTCCGCAAGATCATTCGCAGCCACGTCCTGAGGCAGCAAGAACCTTTCAAGGCACAC
CACCATCACCATCACCATCACCATCACTGA

DNA Sequence of the A_{2A}-ΔC-bRIL Coding Region

ATGAAGACGATCATCGCCCTGAGCTACATCTTCTGCCTGGTGTTCGCCGACTACAAG
GACGATGATGACGGCGCGCCACCCATCATGGGCTCCTCGGTGTACATCACGGTGGAG
CTGGCCATTGCTGTGCTGGCCATCCTGGGCAATGTGCTGGTGTGCTGGGCCGTGTGG
CTCAACAGCAACCTGCAGAACGTCACCAACTACTTTGTGGTGTCACTGGCGGCGGCC
GACATCGCAGTGGGTGTGCTCGCCATCCCCTTTGCCATCACCATCAGCACCGGGTTC
TGCGCTGCCTGCCACGGCTGCCTCTTCATTGCCTGCTTCGTCCTGGTCCTCACGCAG
AGCTCCATCTTCAGTCTCCTGGCCATCGCCATTGACCGCTACATTGCCATCCGCATC
CCGCTCCGGTACAATGGCTTGGTGACCGGCACGAGGGCTAAGGGCATCATTGCCATC
TGCTGGGTGCTGTCGTTTGCCATCGGCCTGACTCCCATGCTAGGTTGGAACAACTGC
GGTCAGCCAAAGGAGGGCAAGAACCACTCCCAGGGCTGCGGGGAGGGCCAAGTGGCC
TGTCTCTTTGAGGATGTGGTCCCCATGAACTACATGGTGTACTTCAACTTCTTTGCC
TGTGTGCTGGTGCCCCTGCTGCTCATGCTGGGTGTCTATTTGCGGATCTTCCTGGCG
GCGCGACGACAGCTGGCTGATCTGGAAGACAATTGGGAAACTCTGAACGACAATCTC
AAGGTGATCGAGAAGGCTGACAATGCTGCACAAGTCAAAGACGCTCTGACCAAGATG
AGGGCAGCAGCCCTGGACGCTCAGAAGGCCACTCCACCTAAGCTCGAGGACAAGAGC
CCAGATAGCCCTGAAATGAAAGACTTTCGGCATGGATTCGACATTCTGGTGGGACAG
ATTGATGATGCACTCAAGCTGGCCAATGAAGGGAAAGTCAAGGAAGCACAAGCAGCC
GCTGAGCAGCTGAAGACCACCCGGAATGCATACATTCAGAAGTACCTGGAGCGCGCT
CGGTCCACACTGCAGAAGGAGGTCCATGCTGCCAAGTCACTGGCCATCATTGTGGGG
CTCTTTGCCCTCTGCTGGCTGCCCCTACACATCATCAACTGCTTCACTTTCTTCTGC
CCCGACTGCAGCCACGCCCCTCTCTGGCTCATGTACCTGGCCATCGTCCTCTCCCAC
ACCAATTCGGTTGTGAATCCCTTCATCTACGCCTACCGTATCCGCGAGTTCCGCCAG
ACCTTCCGCAAGATCATTCGCAGCCACGTCCTGAGGCAGCAAGAACCTTTCAAGGCA
CACCACCATCACCATCACCATCACCATCACTGA

Appendix IV. Protein Sequences

Mutations are highlighted in blue. Expression and purification tags are underlined.

Primary Sequence of A_{2A}-PSB1-bRIL

MKTIIALSYIFCLVFADYKDDDDGAPPIMGSSVYITVELAIAVLAILGNVLVCWAVW
LNSNLQNVTNYFVVSLAAADIAVGVLAIPFAITISTGFCAACHGCLFIACFVLVLTQ
S**K**IFSLLAIAIDRYIAIRIPLRYNGLVTGTRAKGIIAICWVLSFAIGLTPMLGWNNC
GQPKEGKNHSQGCGEGQVACLFEDVVPMNYMVYFNFFACVLVPLLLMLGVYLRIFLA
ARRQLADLEDNWETLNDNLKVIEKADNAAQVKDALTKMRAAALDAQKATPPKLEDKS
PDSPEMKDFRHGFDILVGQIDDALKLANEGKVKEAQAAAEQLKTTRNAYIQKYLERA
RSTLQKEVHAAKSLAIIVGLFALCWLPLHIINCFTFFCPDCSHAPLWLMYLAIVLSH
TNSVVNPFIYAYRIREFRQTFRKIIRSHVLRQQEPFKAHHHHHHHHHH-

Primary Sequence of A_{2A}-PSB2-bRIL

MKTIIALSYIFCLVFADYKDDDDGAPPIMGSSVYITVELAIAVLAILGNVLVCWAVW
LNSNLQNVTNYFVVSLAAADIAVGVLAIPFAITISTGFCAACHGCLFIACFVLVLTQ
S**K**IFSLLAIAIDRYIAIRIPLRYNGLVTGTRAKGIIAICWVLSFAIGLTPMLGWNNC
GQPKEGK**A**HSQGCGEGQVACLFEDVVPMNYMVYFNFFACVLVPLLLMLGVYLRIFLA
ARRQLADLEDNWETLNDNLKVIEKADNAAQVKDALTKMRAAALDAQKATPPKLEDKS
PDSPEMKDFRHGFDILVGQIDDALKLANEGKVKEAQAAAEQLKTTRNAYIQKYLERA
RSTLQKEVHAAKSLAIIVGLFALCWLPLHIINCFTFFCPDCSHAPLWLMYLAIVLSH
TNSVVNPFIYAYRIREFRQTFRKIIRSHVLRQQEPFKAHHHHHHHHHH-

Primary Sequence of A_{2A}-ΔC

MKTIIALSYIFCLVFADYKDDDDGAPPIMGSSVYITVELAIAVLAILGNVLVCWAVW
LNSNLQNVTNYFVVSLAAADIAVGVLAIPFAITISTGFCAACHGCLFIACFVLVLTQ
SSIFSLLAIAIDRYIAIRIPLRYNGLVTGTRAKGIIAICWVLSFAIGLTPMLGWNNC
GQPKEGKNHSQGCGEGQVACLFEDVVPMNYMVYFNFFACVLVPLLLMLGVYLRIFLA
ARRQLKQMESQPLPGERARSTLQKEVHAAKSLAIIVGLFALCWLPLHIINCFTFFCP
DCSHAPLWLMYLAIVLSHTNSVVNPFIYAYRIREFRQTFRKIIRSHVLRQQEPFKAH
HHHHHHHHH-

Primary Sequence of A_{2A}-ΔC-bRIL

MKTIIALSYIFCLVFADYKDDDDGAPPIMGSSVYITVELAIAVLAILGNVLVCWAVW
LNSNLQNVTNYFVVSLAAADIAVGVLAIPFAITISTGFCAACHGCLFIACFVLVLTQ
SSIFSLLAIAIDRYIAIRIPLRYNGLVTGTRAKGIIAICWVLSFAIGLTPMLGWNNC
GQPKEGKNHSQGCGEGQVACLFEDVVPMNYMVYFNFFACVLVPLLLMLGVYLRIFLA
ARRQLADLEDNWETLNDNLKVIEKADNAAQVKDALTKMRAAALDAQKATPPKLEDKS
PDSPEMKDFRHGFDILVGQIDDALKLANEGKVKEAQAAAEQLKTTRNAYIQKYLERA
RSTLQKEVHAAKSLAIIVGLFALCWLPLHIINCFTFFCPDCSHAPLWLMYLAIVLSH
TNSVVNPFIYAYRIREFRQTFRKIIRSHVLRQQEPFKAHHHHHHHHHH-

Appendix V. Protein Sequence Alignment of A_{2A}-PSB2-bRIL with the Wildtype A_{2A}AR

The A_{2A}-PSB2-bRIL protein sequence is depicted as (1) and the wt A_{2A}AR as (2). Sequences were aligned with Clustal Omega.[251] The bRIL fusion protein is highlighted in orange and point mutations in blue.

```
(1)  MKTIIALSYIFCLVFADYKDDDDGAPPIMGSSVYITVELAIAVLAILGNVLVCWAVWLNS 60
(2)  ------------------------MPIMGSSVYITVELAIAVLAILGNVLVCWAVWLNS 35
                              ********************************

(1)  NLQNVTNYFVVSLAAADIAVGVLAIPFAITISTGFCAACHGCLFIACFVLVLTQSKIFSL 120
(2)  NLQNVTNYFVVSLAAADIAVGVLAIPFAITISTGFCAACHGCLFIACFVLVLTQSSIFSL 95
     ************************************************************.****

(1)  LAIAIDRYIAIRIPLRYNGLVTGTRAKGIIAICWVLSFAIGLTPMLGWNNCGQPKEGKAH 180
(2)  LAIAIDRYIAIRIPLRYNGLVTGTRAKGIIAICWVLSFAIGLTPMLGWNNCGQPKEGKNH 155
     ************************************************************ *

(1)  SQGCGEGQVACLFEDVVPMNYMVYFNFFACVLVPLLLMLGVYLRIFLAARRQLADLEDNW 240
(2)  SQGCGEGQVACLFEDVVPMNYMVYFNFFACVLVPLLLMLGVYLRIFLAARRQLKQMESQP 215
     ************************************************** ::*.:

(1)  ETLNDNLKVIEKADNAAQVKDALTKMRAAALDAQKATPPKLEDKSPDSPEMKDFRHGFDI 300
(2)  ------------------------------------------------------------ 215


(1)  LVGQIDDALKLANEGKVKEAQAAAEQLKTTRNAYIQKYLERARSTLQKEVHAAKSLAIIV 360
(2)  ---------------------------------LPGERARSTLQKEVHAAKSLAIIV 239
                                        ********************

(1)  GLFALCWLPLHIINCFTFFCPDCSHAPLWLMYLAIVLSHTNSVVNPFIYAYRIREFRQTF 420
(2)  GLFALCWLPLHIINCFTFFCPDCSHAPLWLMYLAIVLSHTNSVVNPFIYAYRIREFRQTF 299
     ************************************************************

(1)  RKIIRSHVLRQQEPFKAHHHHHHHHHH-------------------------------- 447
(2)  RKIIRSHVLRQQEPFKAAGTSARVLAAHGSDGEQVSLRLNGHPPGVWANGSAPHPERRPN 359
     ****************     :

(1)  ------------------------------------------------           447
(2)  GYALGLVSGGSAQESQGNTGLPDVELLSHELKGVCPEPPGLDDPLAQDGAGVS         412
```

Danksagung

Zunächst möchte ich mich ganz herzlich bei Prof. Christa Müller bedanken. Liebe Christa, vielen Dank für die hervorragende Betreuung und dass ich das spannende Themenfeld der Strukturbiologie in Bonn mit Deiner Hilfe aufbauen durfte! Es bedeutet mir viel, dass Du mir stets den nötigen Freiraum zur eigenständigen Arbeit gelassen hast und gleichzeitig bei größeren Herausforderungen immer für mich da warst.

Prof. Michael Gütschow danke ich für die Bereitschaft in meiner Prüfungskommission mitzuwirken und insbesondere für die Erstellung des zweiten Gutachtens zu meiner Doktorarbeit.

Außerdem danke ich Prof. Evi Kostenis und Prof. Rainer Manthey für die bereitwillige Mitwirkung in der Prüfungskommission.

Chemisch reine und hochaffine Liganden sind essenziell für die Strukturbiologie von GPCRs. Für dessen Synthese, Bereitstellung und Optimierung danke ich Dr. Tim Klapschinski, Dr. Ahmed Temirak, Dr. Jörg Hockemeyer, Dr. Tim Harms und Angelo Oneto ganz herzlich. Ohne Euch wäre meine Forschung in diesem Umfang nicht möglich gewesen!

Für unzählige Messtage am Deutschen Elektronensynchrotron und die damit verbundene Auswertung der Daten bedanke ich mich bei Prof. Jörg Labahn, Prof. Norbert Sträter, Dr. Udaya Tiruttani Subhramanyam und Dr. Renato Weiße. Außerdem danke ich Prof. Claudia Binda und Andrea Gottinger für die Co-Kristallisation von MAO-B und dessen Strukturaufklärung.

Ein besonderer Dank gilt Victoria und Jonathan. Bei Euch möchte ich mich herzlichst für die gemeinsame Zeit und die tägliche Zusammenarbeit im Labor bedanken. Wir haben uns stets gegenseitig geholfen und ihr standet mir immer zur Seite. So haben wir zusammen jegliche Herausforderung überstanden und eine Freundschaft entwickelt, die ich nicht mehr missen möchte. Vielen Dank!

Für die angenehme Arbeitsatmosphäre im Labor und im Büro, sowie für die unzähligen Gespräche, die auch oft über fachliches hinausgingen, möchte ich mich außerdem bei Jan, Robin, Andhika, Martin, Carina, Christian, Conny, Georg, Jessica, Ghazl und Salahuddin bedanken.

Andhika, Dir möchte ich des Weiteren für die unerschöpfliche Quelle an Nervennahrung danken, die Du immer bereitwillig geteilt hast. Außerdem danke ich Dir herzlichst für Deine einzigartige Hilfsbereitschaft und nicht zuletzt auch für Deine tatkräftige Unterstützung bei der Erstellung von Abbildung 1.

Ein großer Dank gilt Chrisi, Christin und Katharina. Ihr habt mich stets unterstützt und standet mir auch bei außergewöhnlichen Wünschen und Bestellungen immer zur Seite. Vielen Dank für Eure Hilfe! Christin, Dir möchte ich darüber hinaus für die Durchführung zahlreicher Radioligand-Bindungs-Experimente danken.

Des Weiteren danke ich PD Dr. Anke Schiedel und Dr. Dominik Thimm für die stetige Unterstützung und die erstklassige Organisation der Praktika.

Bei Victoria, Jonathan, Georg und Lukas bedanke ich mich herzlich für das gemeinsame Mittagessen-Ritual, das mir täglich neue Energie für den restlichen Tag gegeben hat. Eure Präsenz hat auch die manchmal weniger leckeren Gerichte der Mensa wieder gut gemacht!

Allen weiteren Kolleginnen und Kollegen des AK Müllers möchte ich ausdrücklich für die angenehme Arbeitsatmosphäre und die gute Zusammenarbeit danken.

Mein größter Dank gilt meinen Freunden, meiner Familie und insbesondere meinen Eltern. Vielen Dank, dass ihr mir sowohl privat als auch auf meiner beruflichen Laufbahn immer den Rücken gestärkt habt! Meinem Vater danke ich zusätzlich für die tatkräftige Unterstützung bei der Entwicklung von diversen Programmen, die den Arbeitsalltag von mir deutlich erleichtert haben und auch zukünftigen Doktorandinnen und Doktoranden zur Verfügung stehen werden.